GDAŃSK UNIVERSITY OF TECHNOLOGY

The author of the PhD dissertation: Katarzyna Lisewska
Scientific discipline: Civil Engineering, Geodesy and Transport

DOCTORAL DISSERTATION

Title of PhD dissertation: Modelling anisotropic mechanical properties of stiff soils

Title of PhD dissertation (in Polish): Modelowanie anizotropii właściwości mechanicznych gruntów sztywnych

Supervisor *signature*
dr hab. inż. Marcin Cudny, prof. PG

Gdańsk, year 2025

GDAŃSK UNIVERSITY OF TECHNOLOGY

STATEMENT

The author of the PhD dissertation: Katarzyna Lisewska

I, the undersigned, declare that I am aware that in accordance with the provisions of Art. 27 (1) and (2) of the Act of 4th February 1994 on Copyright and Related Rights (Journal of Laws of 2021, item 1062), the university may use my doctoral dissertation entitled:
Modelling anisotropic mechanical properties of stiff soils
may be used for scientific or didactic purposes.[1]

Gdańsk,..... .....

signature of the PhD student

Aware of criminal liability for violations of the Act of 4th February 1994 on Copyright and Related Rights and disciplinary actions set out in the Law on Higher Education and Science(Journal of Laws 2021, item 478), as well as civil liability, I declare, that the submitted doctoral dissertation is my own work.

I declare, that the submitted doctoral dissertation is my own work performed under and in cooperation with the supervision of dr hab. inż. Marcin Cudny, prof. PG.

This submitted doctoral dissertation has never before been the basis of an official procedure associated with the awarding of a PhD degree.

All the information contained in the above thesis which is derived from written and electronic sources is documented in a list of relevant literature in accordance with Art. 34 of the Copyright and Related Rights Act.

I confirm that this doctoral dissertation is identical to the attached electronic version.

Gdańsk,..... .....

signature of the PhD student

I, the undersigned, agree to include an electronic version of the above doctoral dissertation in the open, institutional, digital repository of Gdańsk University of Technology.

Gdańsk,..... .....

signature of the PhD student

[1] Art 27. 1. Educational institutions and entities referred to in art. 7 sec. 1 points 1, 2 and 4–8 of the Act of 20 July 2018 – Law on Higher Education and Science, may use the disseminated works in the original and in translation for the purposes of illustrating the content provided for didactic purposes or in order to conduct research activities, and to reproduce for this purpose disseminated minor works or fragments of larger works.

2. If the works are made available to the public in such a way that everyone can have access to them at the place and time selected by them, as referred to in para. 1, is allowed only for a limited group of people learning, teaching or conducting research, identified by the entities listed in paragraph 1.

GDAŃSK UNIVERSITY OF TECHNOLOGY

DESCRIPTION OF DOCTORAL DISSERTATION

The Author of the doctoral dissertation: Katarzyna Lisewska

Title of doctoral dissertation: Modelling anisotropic mechanical properties of stiff soils

Title of doctoral dissertation in Polish: Modelowanie anizotropii właściwości mechanicznych gruntów sztywnych

Language of doctoral dissertation: English

Supervision: Marcin Cudny

Date of doctoral defense:

Keywords of doctoral dissertation in Polish: anizotropia krzyżowa, anizotropia sztywności w małych odkształceniach, deformacja gruntu wywołana drążeniem tuneli, deformacja gruntu wywołana wykopem, geotechniczne zagadnienia początkowo-brzegowe, grunty drobnoziarniste o dużej sztywności, grunty prekonsolidowane, hipersprężystość, metoda elementów skończonych, model Brick, modelowanie konstytutywne, nieliniowość sztywności

Keywords of doctoral dissertation in English: Brick-type model, constitutive modelling, cross-anisotropy, excavation-induced deformation, fine-grained stiff soils, finite element method, geotechnical boundary value problems, hyperelasticity, overconsolidated soils, small-strain stiffness anisotropy, stiffness nonlinearity, tunnelling-induced deformation

Katarzyna Lisewska

Modelling anisotropic mechanical properties of stiff soils

A thesis submitted to the Gdańsk University of Technology
In partial fulfilment of the requirements
for the degree of Doctor of Philosophy
in the Faculty of Civil and Environmental Engineering

30/09/2025

Gdańsk University of Technology,
Faculty of Civil and Environmental Engineering
Department of Geotechnical and Hydraulic Engineering

Abstract

Stiff fine-grained soils are usually anisotropic, meaning their properties vary with direction. While anisotropy effects on soil response are known to be important in geotechnics, the related research is still limited due to complex testing and modelling.

Advances in numerical modelling now allow analysis of soil–structure interaction in boundary value problems (BVPs). A key step is selecting a constitutive model that captures soil behaviour, yet most models available in commercial codes are isotropic.

To address this, the anisotropic *AHEBrick* constitutive model was developed. Since strains near well-designed structures are generally small, stiffness anisotropy is implemented in the small-strain range. This is particularly relevant for geotechnical problems related to major unloading, where stress redistribution is significant, making anisotropy in the pre-failure range essential.

This work investigates stiff anisotropic clays with experimental support, focusing on constitutive approaches for simulating anisotropy. The *AHEBrick* model is described, including refinements to its first version. Validation with element tests, geotechnical BVPs, and real case back-analyses highlights the role of stiffness anisotropy and its impact on soil behaviour.

Streszczenie

Sztywne grunty drobnoziarniste są zazwyczaj anizotropowe, czyli ich właściwości zmieniają się w zależności od kierunku. Choć anizotropia silnie wpływa na zachowanie gruntu, badania są ograniczone z powodu złożoności testów laboratoryjnych i modelowania.

Postęp w modelowaniu numerycznym pozwala dziś analizować interakcje grunt–konstrukcja w zagadnieniach brzegowych (BVP). Kluczowe jest zastosowanie modelu konstytutywnego wiernie odwzorowującego zachowanie gruntu, jednak większość modeli w programach komercyjnych zakłada izotropię.

Aby przezwyciężyć te ograniczenia, opracowano anizotropowy model *AHEBrick*. Ponieważ odkształcenia przy dobrze zaprojektowanych konstrukcjach są zwykle małe, anizotropię sztywności wprowadzono w zakresie małych odkształceń. Jest to istotne zwłaszcza przy procesach odciążenia, gdzie następuje redystrybucja naprężeń, a uwzględnienie anizotropii w zakresie przedzniszczeniowym jest kluczowe.

W pracy analizowane są sztywne gliny anizotropowe z wykorzystaniem danych eksperymentalnych i podejść konstytutywnych. Opisano model *AHEBrick* oraz jego ulepszenia. Walidacja poprzez testy elementowe, zagadnienia brzegowe i analizy rzeczywistych przypadków potwierdza znaczenie anizotropii sztywności i jej wpływ na zachowanie gruntu.

To my husband Mateusz

Acknowledgements

I would like to express my sincere gratitude to my supervisor Professor Marcin Cudny for his invaluable guidance and encouragement. I am deeply thankful to Prof. Cudny, his knowledge and experience greatly supported me and allowed me to grow both personally and professionally.

My heartfelt thanks go to my colleagues from the Department of Geotechnical and Hydraulic Engineering for their constant support and kind words.

I am profoundly grateful to my family for their unwavering encouragement, which has been truly invaluable. Finally, I wish to thank my husband Mateusz who has been my greatest source of comfort and support from the very beginning of this journey.

Gdańsk, September 2025 *Katarzyna Lisewska*

Contents

List of symbols

Latin letters

c	effective cohesion
c_1	anisotropy constant in the *AHEBrick* model controlling stress-induced anisotropy, $c_1 = 1.0$
c_2	anisotropy constant in the *AHEBrick* model controlling stress-induced and microstructure anisotropy, $c_2 = 2(\alpha_G - 1)$
$\mathbf{e}, e_{ij}$	deviatoric part of strain tensor, $e_{ij} = \varepsilon_{ij} - \frac{1}{3}\varepsilon_v\,\delta_{ij}$
$\mathbf{C}, C_{ijkl}$	compliance fourth order tensor
$\overline{\mathbf{C}}, \overline{C}_{ij}$	compliance matrix in simplified form 6×6
$\mathbf{D}, D_{ijkl}$	stiffness fourth order tensor
$\overline{\mathbf{D}}, \overline{D}_{ij}$	stiffness matrix in simplified form 6×6
e	void ratio
E	Young's modulus
E_{oed}	oedometer modulus
G	shear modulus
G_{ij}	shear modulus measured in the plane $x_i - x_j$
$\mathbf{I}, I_{ijkl}$	fourth order identity tensor $I_{ijkl} = \frac{1}{2}(\delta_{ik}\delta_{jl} + \delta_{il}\delta_{jk})$
I_1, I_2, I_3	invariants of stress tensor $\boldsymbol{\sigma}$,
K	bulk modulus
K, K_0	stress ratio $(\sigma_h/\sigma_v, \sigma_{11}/\sigma_{22})$, x_2 vertical
$\mathbf{l}, l_i$	generalised loading direction vector
m	power-law exponent
M	bending moment
$\mathbf{M}$	microstructure tensor
M_c, M_e	inclination of the shear strength envelope in the $p - q$ plane for

	axisymmetric compression and extension respectively,
	for Mohr-Coulomb criterion $M_c = \frac{6\sin\phi}{3-\sin\phi}$ and $M_e = \frac{6\sin\phi}{3+\sin\phi}$
n_{ab}	number of active bricks in the *AHEBrick* model
N_{b}	number of bricks in the *AHEBrick* model
p	mean effective stress, $p = -\frac{1}{3}\sigma_{kk}$
p_{pe}	maximum tensile stress
q	invariant of deviatoric part of stress tensor $\mathbf{s}$, $q = \sqrt{\frac{3}{2}s_{ij}s_{ij}}$,
	changed to negative for axisymmetric extension in the $p-q$ diagrams
$Q(\boldsymbol{\sigma})$	stress invariant
$Q_{\mathrm{M}}(\boldsymbol{\sigma}, \mathbf{M})$	joint invariant of stress and microstructure
$\overline{Q}(\boldsymbol{\sigma}, \mathbf{M})$	mixed invariant of stress and microstructure
$\mathbf{s}, s_{ij}$	deviatoric part of stress tensor, $s_{ij} = \sigma_{ij} + p\,\delta_{ij}$
s^j	length of the j-th string in the *AHEBrick* model
t	time
u_x, u_y, u_z	displacement components in directions x, y, z respectively
$\mathbf{v}$	unit vector normal to the plane of isotropy
	defined for the cross-anisotropic materials (axis of symmetry)
$\mathrm{v_s}, \mathrm{v_p}$	propagation velocities of shear and compression waves, respectively
v_L	volume loss, defined as the ratio of the volume of the surface settlement
	trough per meter of tunnel advance to the excavated face area
W	elastic potential function: $W(\boldsymbol{\varepsilon}^e)$ - Helmholtz free energy function,
	$W(\boldsymbol{\sigma})$ - negative Gibbs free energy function
$x_{GE}, x_{G\nu}$	cross-anisotropy exponents, $\alpha_G = \alpha_E^{x_{GE}}$, $\alpha_G = \alpha_\nu^{x_{G\nu}}$

Greek letters

α	Graham-Houlsby cross-anisotropy factor, $\alpha = \sqrt{\frac{E_h}{E_v}} = \frac{G_{hh}}{G_{vh}} = \frac{\nu_{hh}}{\nu_{vh}}$
$\alpha_G, \alpha_E, \alpha_\nu$	cross-anisotropy coefficients, $\alpha_G = \frac{G_{hh}}{G_{vh}}$, $\alpha_E = \frac{E_h}{E_v}$, $\alpha_\nu = \frac{\nu_{hh}}{\nu_{vh}}$
β	parameter in the *AHEBrick* model, which controls the order of barotropy
γ	shear strain, $\gamma = \frac{3}{2}\varepsilon_q = \sqrt{\frac{3}{2}e_{ij}e_{ij}}$
$\boldsymbol{\delta}, \delta_{ij}$	Kronecker's symbol
$\boldsymbol{\varepsilon}, \varepsilon_{ij}$	strain tensor, compression negative
$\overline{\boldsymbol{\varepsilon}}, \overline{\varepsilon}_i$	vector form of $\boldsymbol{\varepsilon}$, $\overline{\varepsilon}_i = [\varepsilon_{11}\ \varepsilon_{22}\ \varepsilon_{33}\ \varepsilon_{12}\ \varepsilon_{23}\ \varepsilon_{31}]^T$
ε_q	invariant of deviatoric strain tensor, $\varepsilon_q = \sqrt{\frac{2}{3}e_{ij}e_{ij}}$
ε_V	volumetric strain, $\varepsilon_V = \varepsilon_{ii}$
$\|\|\boldsymbol{\varepsilon}\|\|_{\mathrm{sh}}$	parameter in the *AHEBrick* model

	defining the shape and steepness of the strain-stiffness S-curve
ϵ	generalised strain, $\epsilon = \sqrt{\Delta\varepsilon_V^2 + \Delta\varepsilon_q^2}$
$\boldsymbol{\epsilon}, \epsilon_i$	strain vector used in the Brick-type models
θ	Lode angle
θ, φ	spherical coordinates defining the direction of the plane of isotropy
ν	Poisson's ratio
ρ	soil bulk density
$\boldsymbol{\sigma}, \sigma_{ij}$	effective Cauchy stress tensor, compression negative
$\sigma_1, \sigma_2, \sigma_3$	major, intermediate and minor principal stress components respectively
$\overline{\boldsymbol{\sigma}}, \overline{\sigma}_i$	vector form of $\boldsymbol{\sigma}$, $\overline{\sigma}_i = [\sigma_{11}\ \sigma_{22}\ \sigma_{33}\ \sigma_{12}\ \sigma_{23}\ \sigma_{31}]^T$
σ_{pp}	pore water pressure, compression negative
τ	shear stress
ϕ	effective friction angle
ψ	dilatancy angle
$\Delta\omega_G$	stiffness proportion defining stiffness drop in the *AHEBrick* model
$\boldsymbol{\Omega}, \Omega_{ij}$	deviatoric measure of the material microstructure, for cross-anisotropic case (x_2 vertical): $\Omega_{11} = \Omega_{33} = -\Omega_{22}/2 = -\Omega_v/2$

Subscripts and superscripts

$()_0, ()^0$	initial values (*e.g.* small strain stiffness moduli or stress)
$()_{\text{ref}}, ()^{\text{ref}}$	reference values (*e.g.* reference tangent stiffness moduli estimated at reference pressure p_{ref})
$()^{\text{e}}$	elastic
$()^{\text{s}}, ()^{\text{t}}$	secant and tangential values respectively
$()_v, ()_h$	vertical and horizontal components respectively (*e.g.* stress components σ_v, σ_h, which on graphs appear with compression positive convention)

Operators

$\cdot$	single contraction, $\mathbf{a} \cdot \mathbf{b} = a_i b_i$ or $\mathbf{A} \cdot \mathbf{b} = A_{ij} b_j$
:	double contraction, $\mathbf{D} : \boldsymbol{\sigma} = D_{ijkl}\sigma_{kl}$ or $\boldsymbol{\sigma} : \boldsymbol{\sigma} = \sigma_{ij}\sigma_{ij}$
$\otimes$	dyadic or outer product, $\mathbf{A} = \mathbf{a} \otimes \mathbf{b} = a_i b_j = A_{ij}$
$\dot{()}$	time derivative, *e.g.* $\dot{\boldsymbol{\sigma}} = d\boldsymbol{\sigma}/dt$
$\| \|$	Euclidean norm, *e.g.* $\|\mathbf{x}\| = \sqrt{x_i x_i}$ or $\|\boldsymbol{\sigma}\| = \sqrt{\sigma_{ij}\sigma_{ij}}$

$\mathrm{tr}\,()$	trace of a tensor, *e.g.* $\mathrm{tr}\,\boldsymbol{\sigma} = \sigma_{ii}$
$()^n$	power of a tensor, *e.g.* $\boldsymbol{\sigma}^n = \overbrace{\boldsymbol{\sigma}\cdot\boldsymbol{\sigma}\cdot\ldots\cdot\boldsymbol{\sigma}}^{n}$ or $\mathrm{tr}\,\boldsymbol{\sigma}^3 = \mathrm{tr}\,(\sigma_{ik}\sigma_{kl}\sigma_{lj}) = \sigma_{ik}\sigma_{kl}\sigma_{li}$

Abbreviation

AHEBrick	Anisotropic Hyperelastic Brick
BVP	boundary value problems
FEM	finite element method
HS	Hardening Soil
HSS	Hardening Soil Small
OCR	overconsolidation ratio

1

Introduction

1.1 Motivation

Due to the geological processes that influence soil microstructure, stiff fine-grained soils are typically anisotropic, which means their properties vary with a direction. This directional dependence may be observed as stiffness anisotropy, strength anisotropy or permeability anisotropy. The influence of anisotropy on soil response has been confirmed in several studies, e.g. [3, 22, 76, 98, 102, 123, 138, 147, 179, 180]. Nevertheless, research on anisotropic soils is relatively recent compared to isotropic soils, mainly because laboratory testing is far more complex. Such tests require advanced equipment capable of measuring soil properties in different directions.

With the development of numerical modelling, it has become possible to analyse soil-structure interaction in boundary value problems (BVP) of the geotechnical cases. A crucial aspect of this process is selecting a material model that reliably reproduces soil behaviour. However, most of the material models, available in commercial software, are isotropic. The closest option for representing stiffness and strength anisotropy is the Jointed-Rock Model, which allows to assign separate strength parameters to discontinuities within the linear elastic cross-anisotropic rock matrix. Furthermore, commercially available material models that incorporate anisotropy into formulation are generally limited or complex, as they require a large number of material parameters. However, the alternative anisotropic material models are available in [153].

1.2 Aim

The initial version of the *AHEBrick* constitutive model, presented in this work, was first formulated at Gdańsk University of Technology and described in [44]. This model introduces

stiffness anisotropy within the small-strain range by implementing a hyperelastic kernel that incorporates joint stress and microstructure invariant into the formulation. The resulting stiffness anisotropy is then extended into the intermediate strain range. Stress history is accurately reproduced with the use of the Brick procedure, proposed by Simpson [149], which is characterised by the nonlinear stepwise stiffness degradation. In contrast, shear strength is modeled using the isotropic Matsuoka-Nakai criterion [106]. The advantage of this model is that the initial parameters can be obtained from laboratory tests.

Although both stiffness anisotropy and strength anisotropy occur in stiff soils, the *AHEBrick* model introduces only stiffness anisotropy in the small-strain range, since strains around well-constructed structures are generally small [34]. Accurate characterization of soil stiffness in this range is therefore essential. Moreover, stiffness anisotropy influences the stress path under undrained conditions, thus also affecting the undrained shear strength of the soil [150]. Due to the fact that the most critical displacement occurs during short-term and undrained conditions, the *AHEBrick* model seems to be suitable for capturing the behaviour of stiff anisotropic soils. Additionally, in this work, soil-structure interaction problems related to soil removal, such as tunnel drilling, deep supported excavations and open-pit excavations are analysed. These processes cause significant unloading, which in turn leads to major stress redistribution. Therefore, for such cases, modeling anisotropy in the pre-failure range is essential.

The aim of this work is to improve and validate the *AHEBrick* model and to investigate whether the model, which accounts for barotropy, stiffness anisotropy and nonlinear stiffness degradation within the pre-failure regime, is able to produce satisfactory results, regardless the applied isotropic shear strength criterion.

1.3 Scope

This work examines the properties of stiff anisotropic fine-grained clays, supported by experimental evidence. The primary focus, however, is on constitutive models and approaches for simulating anisotropy. Considering the characteristics of the *AHEBrick* model, the discussion of anisotropy and its numerical simulation is centered on stiffness anisotropy, which is defined within the small-strain range.

The *AHEBrick* model is described in detail and the refinements added to the initial version are presented. The in-depth parametric analysis is carried out to demonstrate the influence of the material constants on soil response. The model is then validated using element tests, geotechnical BVPs, and back-analyses of real cases. Particular attention is dedicated to ex-

amining the effects of stiffness anisotropy on the selected geotechnical problems. This analysis makes it possible to assess the actual impact of the magnitude of anisotropy on soil behaviour.

This work is arranged in a following way:

Chapter 2: Nonlinear pre-failure stiffness of soils

The magnitude of soil stiffness is highly dependent on the stress level (barotropy) and degrades nonlinearly with strain. This chapter presents experimental evidence of both barotropy and stiffness degradation, followed by a discussion of modeling approaches for pre-failure soil behavior. Barotropy can be incorporated into an elasto-plastic framework by introducing stress dependency into the elastic stiffness. Barotopic models can either be hypoelastic or hyperelasic. Examples of these formulations are presented, with particular emphasis put on the hyperelastic model proposed by Vermeer [163], as it plays later a key role in the *AHEBrick* model. The behaviour of soil within small intermediate and large strain ranges is then described. Nonlinear stiffness can be represented using hysteretic models, however, these often struggle to track stress-strain history of a material, especially concerning stiffness recovery following sharp stress path reversals. To overcome this limitation, models that properly capture stiffness changes during small stress reversals employ the concept of nested yield surfaces. This concept is explained. Finally, a multi-surface Brick-type model, formulated in strain space and proposed by Simpson [149], is presented. A modified version of the Brick procedure is later used in the *AHEBrick* model.

Chapter 3: Anisotropy of soils

In this chapter, the description and origin of anisotropic properties of soils are presented. Two types of anisotropy are distinguished: inherent anisotropy, which is fully dependent on soil microstructure and stress-induced anisotropy, which is influenced by the magnitude and rotation of principal stress components. In general, anisotropic soils exhibit cross-anisotropy, meaning their properties are symmetric about the axis normal to the bedding plane (the plane of isotropy). Subsequently, experimental evidence of mechanical anisotropy is presented: stiffness anisotropy in the small-strain range and strength anisotropy at large strains. Methods for testing anisotropic parameters are discussed. Then the examples of soils that exhibit anisotropic behaviour are provided.

Chapter 4: Constitutive modelling of anisotropy

This chapter presents approaches to modelling anisotropic mechanical properties. Linear elastic models which incorporate anisotropic stiffness are discussed, including their parameters and

the limitations associated with proper model definition. Subsequently, the method for introducing anisotropy into nonlinear models is presented. It is done by the incorporation of joint invariants of stress and microstructure into the formulation [23, 24]. This approach, used to define anisotropic failure criteria, is described for the model proposed by Pietruszczak and Mróz [133, 134]. A quite interesting method of introducing inherent cross-anisotropy into arbitrary isotropic models is proposed by Niemunis and Staszewska [121] is then described. In this approach, cross-anisotropic characteristics of soil microstructure are superimposed on isotropic elastic stiffness tensor or shear strength criterion by a special scaling method.

Chapter 5: Anisotropic hyperelastic-plastic model for stiff soils

In this chapter the *AHEBrick* model is defined. The model description is organised into three parts: the small-strain range, the intermediate strain range, and the yield surface in a form of shear strength envelope. The first section presents the formulation of the anisotropic hyperelastic kernel. All initial stiffness parameters of the *AHEBrick* model are described, along with their functions and limitations. Methods for determining these parameters from laboratory test data are also presented. The marginal influence of parameter c_1 on anisotropy changes has been demonstrated, and its value has therefore been established as a constant ($c_1 = 1.0$). Consequently, parameter c_2 can be directly correlated with the cross-anisotropy coefficient α_G. This reduces the number of required material parameters and simplifies their determination from laboratory tests. Within the intermediate strain range, the nonlinear degradation of stiffness is presented, for which the previously described Brick procedure was used. The selection of an appropriate strain measure is then discussed. Subsequently, the isotropic Matsuoka-Nakai shear strength criterion is introduced. Finally, the procedure for implementing the model into a commercial FE code [26] is described.

Chapter 6: Verification of the *AHEBrick* model in element tests and exemplary BV problems

In this chapter, the *AHEBrick* model is verified. First, the simulations of laboratory tests on a single element is presented. The influence of selected model parameters on soil response is examined. Based on laboratory data, model parameters are then calibrated so the implemented material model reproduces the observed mechanical behaviour of tested soils as closely as possible. The model response is further validated through FE simulations of geotechnical boundary value problems. The aim of BVPs is to investigate material parameter influence on the soil-structure interaction, hence the homogeneous soil layout and basic flow conditions are

considered. The investigations are carried out for tunnel drilling, open excavation and supported excavation cases, where anisotropic properties in the small and intermediate strain ranges play a critical role, as the soil undergoes significant unloading.

Chapter 7: Application of the *AHEBrick* model in case studies

In this chapter the *AHEBrick* model is validated against real geotechnical cases. The purpose of such analysis is to verify the extent to which the adopted material model is able to reflect reality. For this reason, the model geometry and construction procedure are closely based on the data reported in literature. The results are then compared to corresponding field measurements of well documented case studies. The following analyses concern the cases of twin tunnel construction in London Clay [32, 33], FE and HG-A tunnels in Opalinus Clay [102, 115] and trial open-pit excavation in Oxford Clay [70, 132].

Chapter 8: Conslusions

The main conclusions of this work are presented.

2

Nonlinear pre-failure stiffness of soils

Up to 1970s, the discrepancy between the *in situ* stiffness and stiffness tested in laboratory conditions, was thought to be caused by a sample disturbance. As finite element method had become popular in the numerical simulations of geotechnical boundary value problems, it was possible to verify the stiffness parameters obtained from the laboratory tests by the back analyses of real cases and its comparison to the field measurements. When field deformation measurements were juxtaposed with calculation results based on stiffness parameters obtained from the standard laboratory tests, it was quickly discovered that the real soil stiffness is frequently underestimated [34, 42, 154, 172]. It was then established that soil stiffness is highly dependent on the stress level and strain history a material is subjected to [10, 149, 154].

These dependencies are presented in Fig. 2.1 for the example of Hachirougata Clay [145]. The results of the cyclic torsion shear (CTS) tests are presented through the relationship between the secant shear modulus G_{eq}, defined as the slope of the line connecting two peaks of the hysteresis loop, and single amplitude shear strain γ_{SA}. Eight undisturbed soil samples were tested under various values of the isotropic consolidation pressure p_0. The results clearly show the influence of stress level on soil stiffness. The value of stiffness modulus increases along with the increasing effective stress level. This dependence of soil stiffness on stress level is called barotropy. Typically, the stiffness modulus is expressed as a function of the mean stress p or of one of the principal stress components σ_i.

On the other hand, stiffness of a material decreases nonlinearly during straining. As shown in Fig.2.1b, the relationship between shear modulus G_{eq} and strain γ_{SA} can be represented on a logarithmic scale by a characteristic S-shaped curve. Based on a soil behaviour, three strain ranges can be distinguished: small, intermediate, and large. In the literature, the terms very small, small, and large strains are also used interchangeably, eg. [20, 41, 129]. Within the small-strain range, the value of stiffness can be considered constant. For Hachirougata Clay,

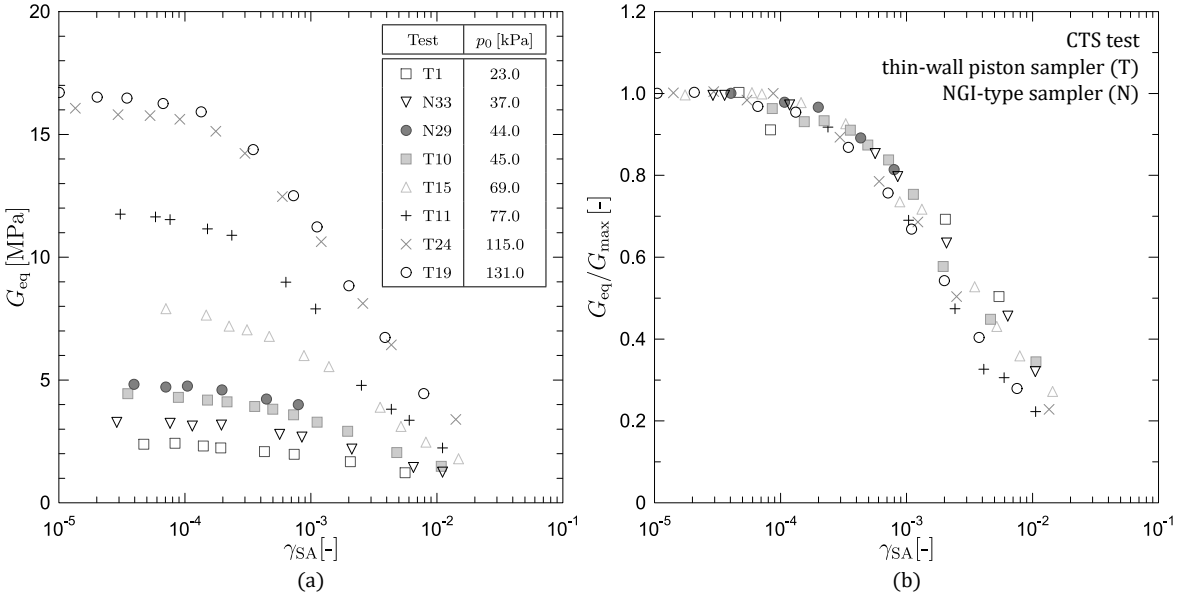

Fig. 2.1: Relation between shear modulus G_{eq} and single amplitude shear strain γ_{SA}, obtained from CTS test on undisturbed Hachirougata Clay samples: a) the variation of shear moduli G_{eq} under different isotropic consolidation pressure, b) shear moduli G_{eq} normalised by $G_{\max}$, after [145]

this phenomenon is observed up to $\gamma_{\mathrm{SA}} = 10^{-4}$. Beyond this point, in the intermediate and large strain ranges, nonlinear degradation of stiffness occurs.

Within the framework of elasto-plasticity, barotropy is mainly taken into consideration in the elastic region, in order to properly determine the value of the initial stiffness modulus. This value is subjected to the stiffness-strain degradation within the intermediate strain range. The description of the influence of stress level and stain history on the current soil stiffness and the modelling approaches of the pre-failure soil behaviour are presented in this chapter.

2.1 Barotropy

Constitutive modelling at small elastic strains is expressed by the following relation between stress and strain:

$$\boldsymbol{\sigma} = \mathbf{D}^{\mathrm{s}} : \boldsymbol{\varepsilon}^{\mathrm{e}}, \quad \dot{\boldsymbol{\sigma}} = \mathbf{D}^{\mathrm{t}} : \dot{\boldsymbol{\varepsilon}}^{\mathrm{e}}, \tag{2.1}$$

in the form of secant relationship between stress and elastic strain or tangent relationship between stress rate and elastic strain rate. The forth order tensors $\mathbf{D}^{\mathrm{s}}$ and $\mathbf{D}^{\mathrm{t}}$ refer to secant and tangent stiffness, respectively. They are related to the forth order secant and tangent compliance tensors $\mathbf{C}^{\mathrm{s}}$, $\mathbf{C}^{\mathrm{t}}$ in a following way: $\mathbf{C}^{\mathrm{s}} = (\mathbf{D}^{\mathrm{s}})^{-1}$ and $\mathbf{C}^{\mathrm{t}} = (\mathbf{D}^{\mathrm{t}})^{-1}$.

The simplest small-strain model is based on the Hooke's linear isotropic elasticity:

$$D^{\mathrm{t}}_{ijkl} = \frac{E_0}{(1+\nu_0)(1-2\nu_0)}\left[\nu_0\delta_{ij}\delta_{kl} + \frac{1-2\nu_0}{2}(\delta_{ik}\delta_{jl}+\delta_{jk}\delta_{il})\right], \tag{2.2}$$

where E is the Young's modulus and ν is the Poisson's ratio. Subscript $()_0$ refers to the initial (small strain) values. In this formulation, the secant and tangent relations have the same constant stiffness.

However, in reality, the magnitude of initial elastic stiffness moduli is highly influenced by the current stress state. Therefore, the dependency of the stress level on the initial soil stiffness needs to implemented within the small strain range.

2.1.1 Hypoelasticity

The application of the empirical correlations to Hooke's law isotropic elasticity is the simplest way to create a nonlinear elastic model with barotropic stiffness, for which Young's modulus $E(\boldsymbol{\sigma})$ is stress dependent and Poisson's ratio ν is constant:

$$D^{\mathrm{t}}_{ijkl}(\boldsymbol{\sigma}) = \frac{E(\boldsymbol{\sigma})}{(1+\nu)(1-2\nu)}\left[\nu\delta_{ij}\delta_{kl} + \frac{1-2\nu}{2}(\delta_{ik}\delta_{jl}+\delta_{jk}\delta_{il})\right]. \tag{2.3}$$

It should be noted that, in the context of hypoelasticity, it is often difficult to determine whether the parameters refer to tangent or secant stiffness. For this reason, the parameters are presented without the subscript $()_0$.

Commonly used barotropic relation is based on power law:

$$E(\boldsymbol{\sigma}) = E^{\mathrm{ref}}\left(\frac{p}{p_{\mathrm{ref}}}\right)^m, \tag{2.4}$$

where m is power law exponent that defines the order of the stress-stiffness relation. Another popular empirical equation was proposed by Ohde [127] and Janbu [80]:

$$E_{\mathrm{oed}}(\boldsymbol{\sigma}) = wE^{\mathrm{ref}}_{\mathrm{oed}}\left(\frac{-\sigma_3+a}{p_{\mathrm{ref}}+a}\right)^n, \tag{2.5}$$

where the tangent oedometric modulus $E^{\mathrm{ref}}_{\mathrm{oed}}$ is measured at the reference pressure p_{ref} and w, $a = c\cot\phi$, n are the material constants.

While empirical relations work well concerning a fit to the experimental data, their incorporation into Hooke's elastic stiffness may result in a non-conservative behaviour, meaning it allows for the accumulation of stress or strain and the generation of energy for some closed strain or stress cycles, respectively [119, 121]. In this regard such models can be called *hypoelastic*.

To evaluate whether the model is conservative, the stress response to a circular strain loop in the principal strain space can be investigated. Such closed strain loop naturally occurs during

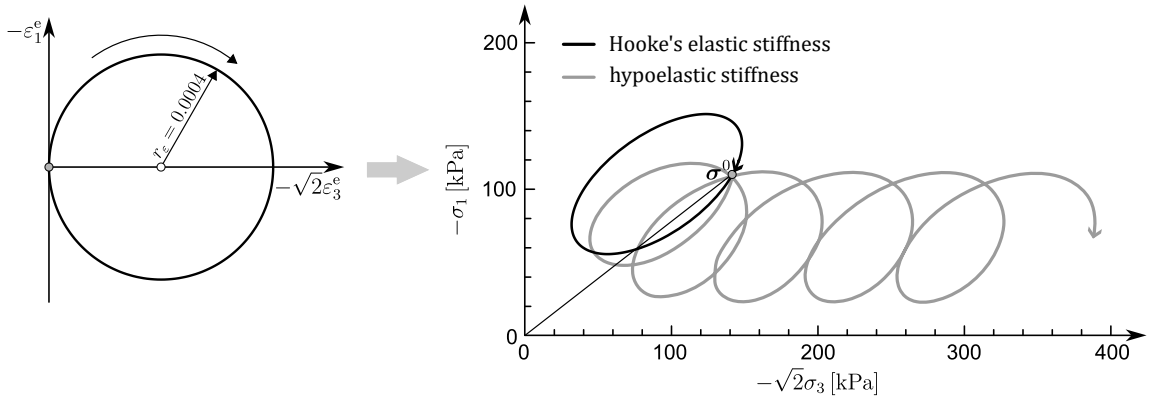

Fig. 2.2: Stress paths obtained for a five-cycle closed circular strain loop in $\sqrt{2}\varepsilon_3^e - \varepsilon_1^e$ plane. In the case of hypoelastic formulation stress accumulation occurs, after [44]

the propagation of a Rayleigh wave. Presented in Fig. 2.2 stress paths are obtained over five cycles of the circular strain path. The analysis is carried out for Hooke's linear elasticity and a hypoelastic stiffness defined with the power law expression in Eq. 2.4. The parameters are chosen so that both models produce the same response envelope at the initial stress state σ^0. If the stress response forms a closed loop in stress space, the model is considered conservative. In contrast, the hypoelastic model produces open loops, where the stress values progressively increase with each cycle.

Based on the preceding analysis, it can be concluded that the application of hypoelastic models to geotechnical problems involving dynamic or cyclic loading may lead to significant computational errors [75, 121]. Nevertheless, if stress or strain does not form a closed loop, the stresses and strains revert to their original values, even when a non-conservative model is used [119].

2.1.2 Hyperelasticity

A conservative elastic material should not assume stress and energy accumulation in closed strain loops [47, 121]:

$$\oint D^{\mathrm{t}}_{ijkl}\mathrm{d}\varepsilon^{\mathrm{e}}_{kl} = 0, \qquad \oint C^{\mathrm{t}}_{ijkl}\mathrm{d}\sigma_{kl} = 0, \qquad \oint \sigma_{ij}\mathrm{d}\varepsilon^{\mathrm{e}}_{ij} = 0, \tag{2.6}$$

where $\mathbf{D}^{\mathrm{t}}$ and $\mathbf{C}^{\mathrm{t}}$ are fourth order tangent stiffness and compliance tensors. This type of relation is called *hyperelastic*. The most straightforward way of formulating a truly hyperelastic material model is to use the elastic potential function W [44, 73, 119]. This elastic potential can be denoted either as negative Gibbs free energy $W(\boldsymbol{\sigma})$ - a scalar function of stress or Helmholtz free energy $W(\boldsymbol{\varepsilon}^{\mathrm{e}})$ - a scalar function of elastic strain. Secant compliance and stiffness tensors

($\mathbf{C}^{\mathrm{s}}$, $\mathbf{D}^{\mathrm{s}}$) can be obtained by the differentiation of stress based and elastic strain based potential functions respectively:

$$\varepsilon^{\mathrm{e}}_{ij} = \frac{\partial W(\boldsymbol{\sigma})}{\partial \sigma_{ij}} = C^{\mathrm{s}}_{ijkl}\sigma_{kl}, \tag{2.7}$$

$$\sigma_{ij} = \frac{\partial W(\boldsymbol{\varepsilon}^{\mathrm{e}})}{\partial \varepsilon^{\mathrm{e}}_{ij}} = D^{\mathrm{s}}_{ijkl}\varepsilon^{\mathrm{e}}_{kl}. \tag{2.8}$$

Whereas tangent compliance and stiffness tensors ($\mathbf{C}^{\mathrm{t}}$, $\mathbf{D}^{\mathrm{t}}$) are obtained as second derivatives of the potential functions:

$$C^{\mathrm{t}}_{ijkl} = \frac{\partial^2 W(\boldsymbol{\sigma})}{\partial \sigma_{ij}\partial \sigma_{kl}}, \tag{2.9}$$

$$D^{\mathrm{t}}_{ijkl} = \frac{\partial^2 W(\boldsymbol{\varepsilon}^{\mathrm{e}})}{\partial \varepsilon^{\mathrm{e}}_{ij}\partial \varepsilon^{\mathrm{e}}_{kl}}. \tag{2.10}$$

It is impossible to directly measure an elastic potential function by any experiments. However, one can formulate it on the basis of trial analysis and inspection, for example, by comparing the response from the model with some test results. An overview of some hyperelastic potentials is provided in [119, 174].

The strain-based elastic potential was proposed by Houlsby *et al.* [74]:

$$W(\boldsymbol{\varepsilon}^{\mathrm{e}}) = \frac{p_{\mathrm{ref}}}{k(2-n)}\left[k(1-n)\right]^{\frac{2-n}{2-2n}}\left\{\left[k(1-n)-\frac{2g}{3}\right]\mathrm{tr}^{\,2}(\boldsymbol{\varepsilon}^{\mathrm{e}}) + 2g\mathrm{tr}\left(\boldsymbol{\varepsilon}^{\mathrm{e2}}_{\mathrm{symm}}\right)\right\}^{\frac{2-n}{2-2n}}, \tag{2.11}$$

where n, k g are dimensionless parameters. Another example was presented by Xiao *et al.* [173]:

$$W(\boldsymbol{\varepsilon}^{\mathrm{e}}) = A\left(\varepsilon^{\mathrm{e}}_V\right)^m)\left[\left(\varepsilon^{\mathrm{e}}_V\right)^2 + \xi\left(\varepsilon^{\mathrm{e}}_s\right)^2\right], \tag{2.12}$$

where A, ξ are elastic constants, $\varepsilon^{\mathrm{e}}_V$ is volumetric elastic strain and $\varepsilon^{\mathrm{e}}_s = \sqrt{e^{\mathrm{e}}_{ij}e^{\mathrm{e}}_{ij}}$ is the second invariant of elastic strain tensor $\varepsilon^{\mathrm{e}}_{ij}$. In both cases, the provided models account for the anisotropic material.

On the other hand, the formulation, proposed by Boyce [25], assumes secant stiffness moduli G^{s}, K^{s} to be functions of stress invariants p, q:

$$G^{\mathrm{s}}(p,q) = g_1 p_{\mathrm{ref}}\left(\frac{p}{p_{\mathrm{ref}}}\right)^{1-n_1} \text{ and } K^{\mathrm{s}}(p,q) = k_1 p_{\mathrm{ref}}\left(\frac{p}{p_{\mathrm{ref}}}\right)^{1-n_1}\left[1-(1-n_1)\frac{k_1}{6g_1}\left(\frac{q}{p}\right)^2\right]^{-1}, \tag{2.13}$$

where g_1, k_1, n_1 are dimensionless parameters.

Usually, the commercial FE codes, eg. [26], are displacement-based, hence in this case tangent stiffness tensor is required. For elastic potentials, defined with the function of strain, $\mathbf{D}^{\mathrm{t}}$ is obtained directly as second derivative. However, if the provided formulation is stress-dependent,

tangent stiffness may be acquired either numerically or analytically by inverting tangent compliance tensor $\mathbf{C}^{\mathrm{t}} = (\mathbf{D}^{\mathrm{t}})^{-1}$. Another approach concerns attaining elastic potential function of strain $W(\boldsymbol{\varepsilon}^{\mathrm{e}})$, that corresponds to the stress based potential, by the Legendre transform applied on a scalar function of stress $W(\boldsymbol{\sigma})$ [74].

The following formulation is very important in the context of this work, which is why it is described here in more detail. The potential presented by Vermeer [163] takes the following form:

$$W(\boldsymbol{\sigma}) = \frac{3p_{\mathrm{ref}}^{1-\beta}}{2G_0^{\mathrm{ref}}(1+\beta)}\left[\frac{2}{3}Q(\boldsymbol{\sigma})\right]^{\frac{1+\beta}{2}}, \quad \text{where} \quad Q(\boldsymbol{\sigma}) = \frac{1}{2}\mathrm{tr}\,\boldsymbol{\sigma}^2 = \frac{1}{2}\sigma_{ab}\sigma_{ab}. \tag{2.14}$$

This function is based on the parameters that can be easily tested in laboratory conditions and are used in engineering practises, where G_0^{ref} is the small-strain tangent shear modulus measured at the reference isotropic stress $p = p_{\mathrm{ref}}$, and β is a material constant dependent on Poisson's ratio:

$$\beta = -2 + \frac{3}{1+\nu_0} \quad \text{and} \quad \nu_0 = \frac{1-\beta}{2+\beta}. \tag{2.15}$$

Tangent compliance is obtained due to differentiation of the function $W(\boldsymbol{\sigma})$ (see Eq. 2.9):

$$C^{\mathrm{t}}_{ijkl} = \frac{1}{2G_0}\left[\frac{1}{2}(\delta_{ik}\delta_{jl} + \delta_{il}\delta_{jk}) - (1-\beta)\frac{\sigma_{ij}\sigma_{kl}}{\sigma_{ab}\sigma_{ab}}\right]. \tag{2.16}$$

Whereas the stiffness matrix can be a result of analytical inversion of the compliance matrix:

$$D^{\mathrm{t}}_{ijkl} = 2G_0\left[\frac{1}{2}(\delta_{ik}\delta_{jl} + \delta_{il}\delta_{jk}) - \frac{(\beta-1)}{\beta}\frac{\sigma_{ij}\sigma_{kl}}{\sigma_{ab}\sigma_{ab}}\right], \tag{2.17}$$

where G_0 is shear modulus dependent on stress:

$$G_0 = G_0^{\mathrm{ref}}\left(\frac{\sqrt{\frac{1}{3}\sigma_{ab}\sigma_{ab}}}{p_{\mathrm{ref}}}\right)^{1-\beta}. \tag{2.18}$$

The influence of stress on the stiffness obtained from Vermeer's hyperelastic potential can be studied in a graphical form of the so-called response envelope [61]. It is a useful tool to study the differences of parameter influence, especially for small strain stiffness formulations. It is described as a polar representation of the tangent compliance or stiffness tensor. It is illustrated in Fig. 2.3 as a closed curve response of material stiffness or compliance to a radial stain or stress probes in the selected stress or strain planes ($\sqrt{2}\sigma_3 - \sigma_1$, $\sqrt{2}\varepsilon_3^{\mathrm{e}} - \varepsilon_1^{\mathrm{e}}$), respectively. It is possible to obtain response envelopes in a laboratory environment, e.g. [64, 90], however the testing is still extremely complex.

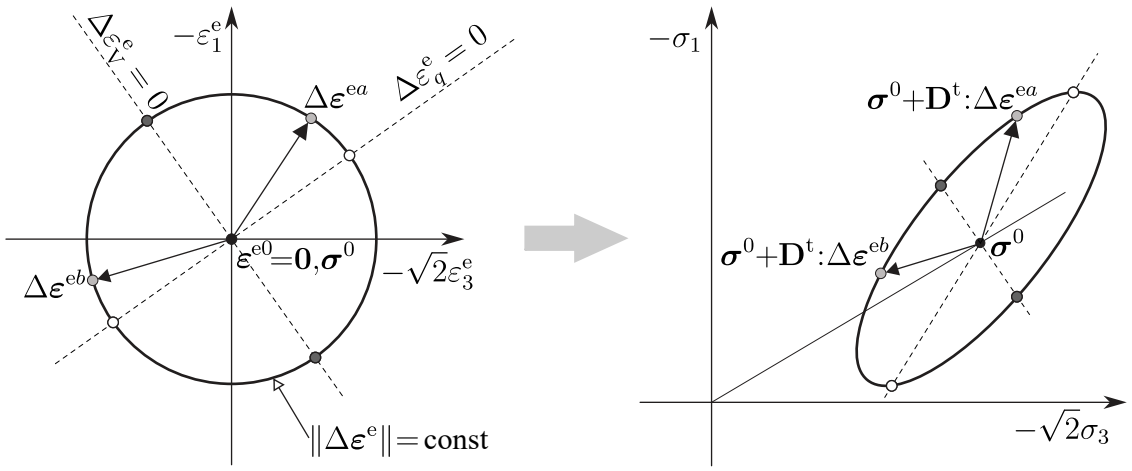

Fig. 2.3: A schematic representation of a response envelope in the triaxial plane ($\sigma_2 = \sigma_3$) to a strain probe. The strain increment controls the size of the ellipses and can be used as a scale. The white and dark grey dots show purely deviatoric and volumetric strain increments, respectively, after [47]

In Fig. 2.4 the response envelopes of the Vermeer's nonlinear hyperelastic stiffness are shown. Three axisymmetric stress ratios ($K = \sigma_3/\sigma_1 = 0.5, 1.0, 2.0$) are considered. If stress state is deviatoric ($K \neq 1.0$), the obtained envelopes are rotated with a respect to the hydrostatic axis $K = 1.0$. Moreover, if the reference pressure p_{ref} increases, the ellipses get larger accordingly. This model is compared to the Hooke's isotropic linear elasticity. The value of the Hooke's law stiffness E_0^{ref} is selected in a way that it correlates to the hyperelastic model parameter G_0^{ref},

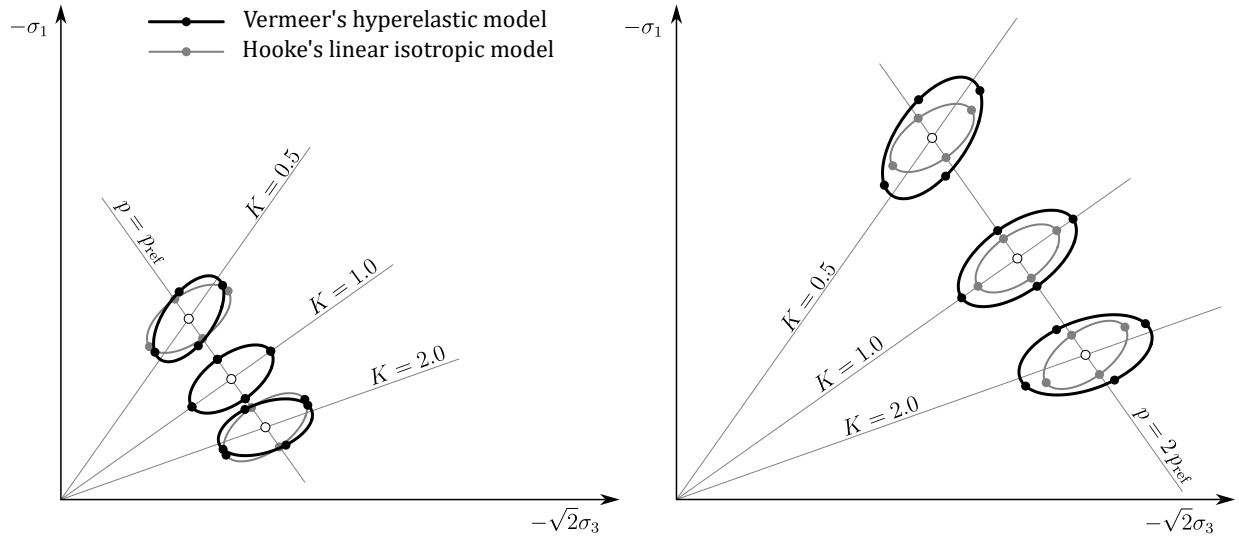

Fig. 2.4: Comparision of the response envelopes for Vermeer's nonlinear hyperelastic and Hooke's linear elastic models. The values of Hooke's stiffness parameters $E_0^{\text{ref}} = 120000$ kPa, $\nu_0 = 0.2$ correspond to the parameters used in Vermeer's model: $G_0^{\text{ref}} = 50000$ kPa, $\beta = 0.5$

following the relation:

$$E_0^{\text{ref}} = 2\,G_0^{\text{ref}}(1+\nu_0), \tag{2.19}$$

where tangent moduli E_0^{ref} and G_0^{ref} are measured at the reference pressure p_{ref} and the value of ν_0, which corresponds to β parameter, is obtained form the expression in Eq. 2.15. Since the Hooke's stiffness is not depended on stress, the size and the position of the envelopes remain the same regardless the stress state.

2.2 Stiffness-strain degradation

A material response to loading can be described by taking into account the kinematic nature of soil stiffness presented by Jardine [82]. As presented in Fig. 2.5, the distinct zones of soil behaviour can be identified corresponding to different soil stiffness ranges. Each zone is restricted by a kinematic surface Y_i. Those surfaces are controlled by strain thresholds. The extensive overview of reported strain thresholds for different soils is featured in [49]. Strain ranges coincide with kinematic zones as follows: small-strain range - zone 1 and zone 2, intermediate strain range - zone 3, large strains - zone 4.

It has been proven in [34], based on numerous practical cases of geotechnical problems [14, 17, 35, 91], that the soil straining around well constructed objects rarely exceed the value of 0.1%. Hence, the proper determination of soil stiffness within the small-strain range is crucial.

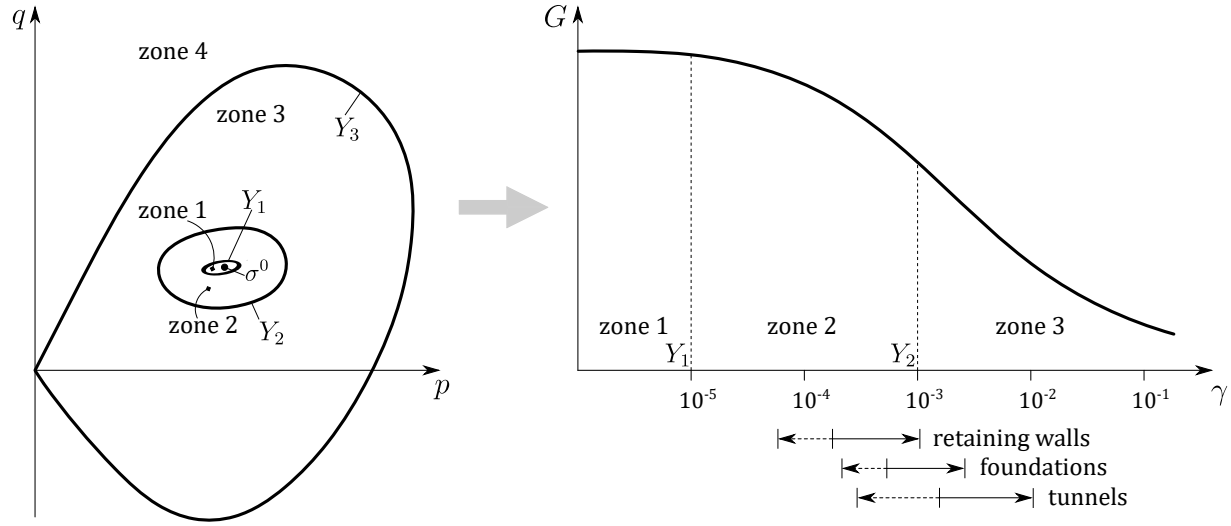

Fig. 2.5: Kinematic behaviour of soil stiffness presented by Jardine [82] in regards to S-shaped stiffness-strain relation. The thresholds of kinematic surfaces Y_i depend on the soil. Typical strain rates around structures rarely exceed 0.1% [13, 104]

Soil stiffness at small strains is measured by the means of dynamic testing. The standard parameter indicating small-strain stiffness rate is the initial shear modulus G_0. In soil dynamics two types of seismic waves can be distinguished: body waves and surface waves. Surface waves propagate on ground face or along the interfaces of soil materials with different stiffness. They are dispersive and originate from the interaction of shear and compressive waves at the surface. Two types of surface waves can be differentiated: Rayleigh waves and Love waves. Rayleigh waves move elliptically in the vertical direction away from a surface energy source, whereas Love waves propagate horizontally form the epicentre [40].

The body waves, shown in Fig. 2.6, travel through a soil at given velocity, controlled by its stiffness and density. Primary compressive waves (P-waves) mainly depend on volumetric compressibility of soil, whereas secondary shear waves (S-waves) account for material shape change with no impact to volume. The values of shear and oedometric moduli can be calculated based on soil wave propagation velocity and material bulk density ρ:

$$E_{\mathrm{oed0}} = \rho \mathrm{v}_{\mathrm{p}}^2, \qquad G_0 = \rho \mathrm{v}_{\mathrm{s}}^2, \tag{2.20}$$

where v_{p} and v_{s} are the velocities of a P-wave and a S-wave, respectively.

Although, it may vary, depending on the investigated material, in general, small strains are considered up to the value of $\gamma = 10^{-3}$. Inside the zone 1 the soil behaviour is considered purely elastic and the strains are fully recoverable. Stiffness moduli are at their maximum and, for practical purposes, these parameters are assumed constant up to the elastic threshold restricted by kinematic surface Y_1. Typically, the elastic limit is contained within the range of $\gamma = 10^{-6} \div 10^{-4}$. In Fig. 2.7 the linear soil behaviour in zone 1 is presented for the example

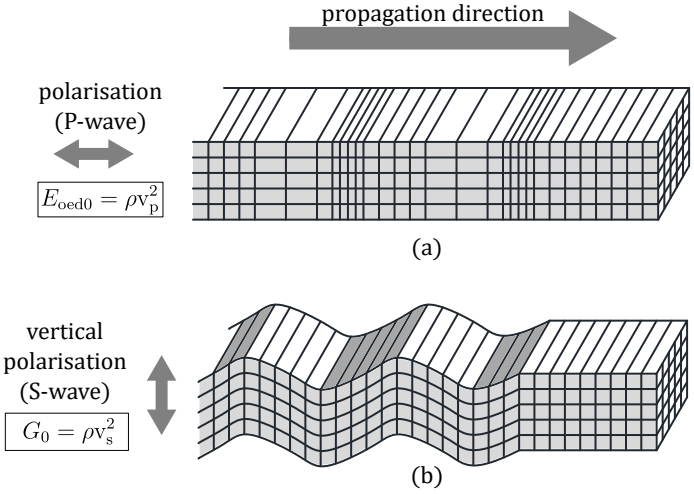

Fig. 2.6: Seismic small-strain stiffness identification of a isotropic soil material: a) compressive P-wave, b) shear S-wave, after [19]

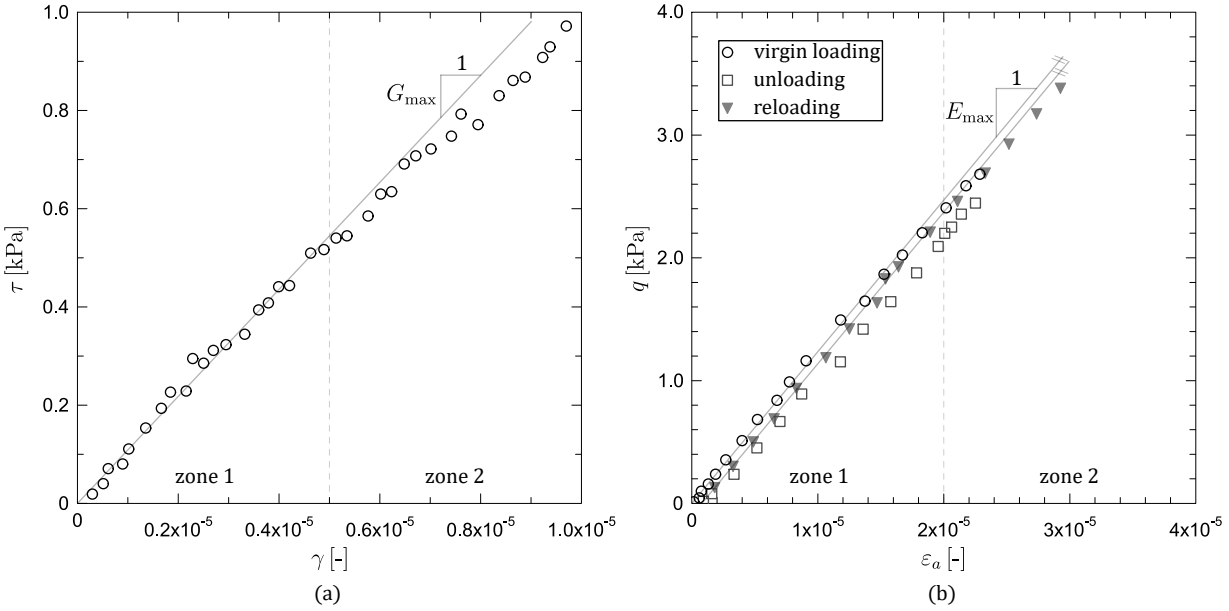

Fig. 2.7: Stress-strain relation of Toyoura Sand. The results of a) a torsional shear test and b) a plane strain compression test show the strain range within which the material response is elastic, after [159]

of Toyoura Sand [159]. For this material the value of the surface Y_1 has been tested to be at $\gamma = 5 \times 10^{-6}$ and $\varepsilon_a = 2 \times 10^{-5}$. The results of the plane strain compression test (Fig. 2.7b) show a non-recoverable response during the first unloading-reloading cycle, suggesting some degree of non-elastic soil behaviour. However, for very small strain values, the secant stiffness modulus measured during unloading-reloading is consistent with the one obtained during the initial loading. Similar trends are observed for the triaxial tests conducted on both kaolin and undisturbed Tokyo Bay Clay samples [114], subjected to isotropic and anisotropic consolidation. These results indicate that, within this strain range, the soil behaviour can be considered truly elastic [82].

When deformation extends into zone 2, it remains fully recoverable, however, the stress-strain relationship of soil becomes nonlinear, and load-unload cycles form closed hysteresis loops. According to [82], the energy dissipation reflected in these hysteretic loops arises from localized, small-scale yielding at particle contacts.

One of the key features of soil behaviour within this kinematic zone is the strong dependence of soil stiffness on the recent stress history [12, 141]. This effect is illustrated in Fig. 2.8 for reconstituted London Clay samples, subjected to drained compression or extension tests [12]. The samples were loaded along a constant p path (0A), but the initial stress point (0) was approached from different directions ($\theta = -90°$, $0°$, $90°$, $180°$). Depending on the path rotation θ, the corresponding tangent shear stiffness G_t changes. In case of drained compression, the

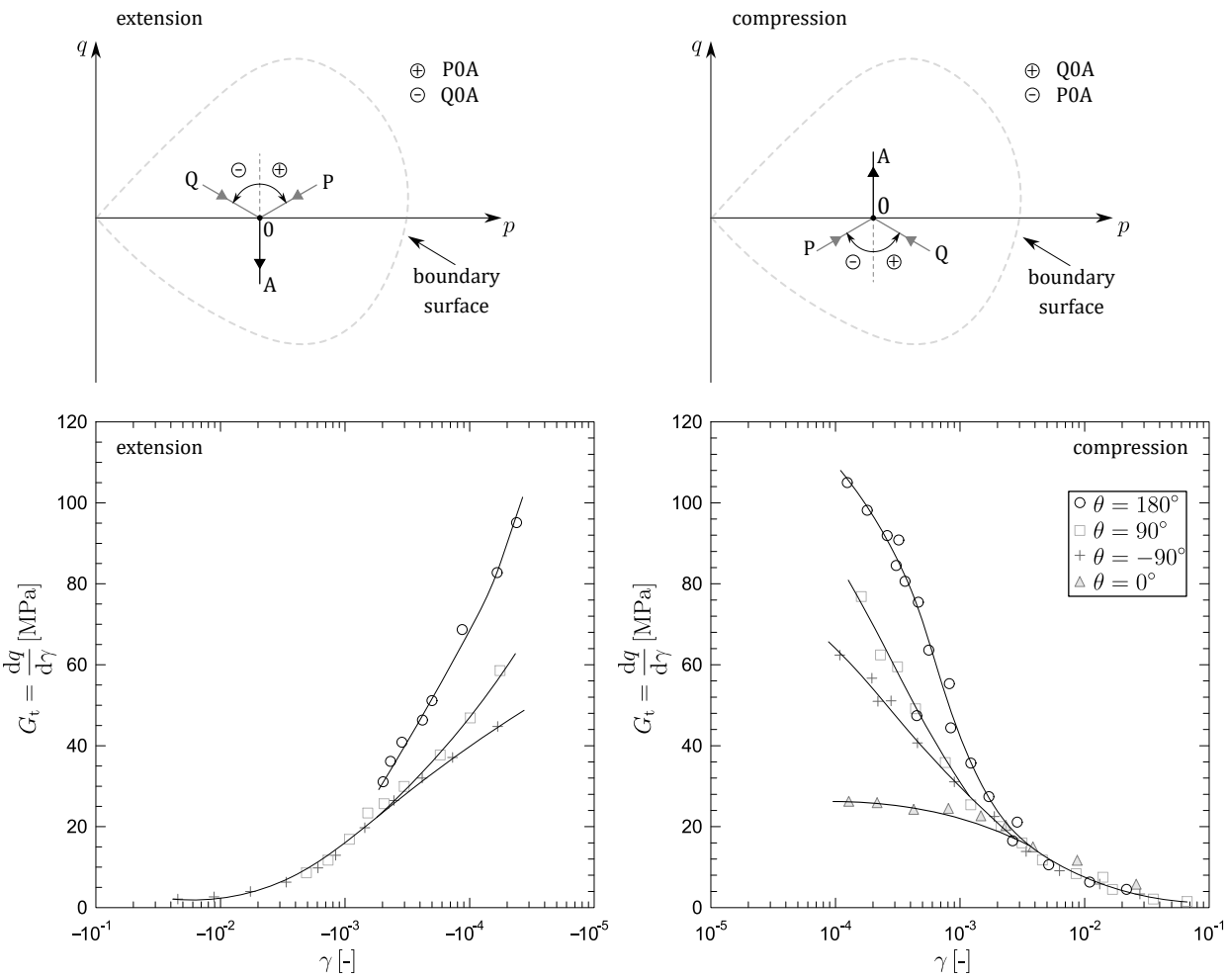

Fig. 2.8: The influence of stress history on the reconstituted London Clay stiffness. Triaxial drained extension and compression tests for constant p paths (0A) preceded by stress paths at different angle θ, after [12]

highest value of G_t was obtained for $\theta = 180°$, whereas the tangent shear stiffness of a sample subjected to $\theta = 0°$ path is almost six times smaller. Similar trend is evident for the drained extension tests. This effect diminishes at larger strains, where the stiffness converges to the same value regardless of stress history.

Kinematic surface Y_2 denotes the plastic threshold of soil. Reported values of elastic threshold range from 10^{-4} to 10^{-3} for overconsolidated stiff clays, e.g. [81]. Beyond this boundary, connections between particles fail and as a result particle movements follow.

Transition from zone 2 to zone 3 entails further development of deformation albeit of the unrecoverable one, which can be distinguished by open hysteresis loops. Such change is illustrated in Fig. 2.9 showing the stress-strain behaviour of reconstituted Magnus till subjected to undrained triaxial test. The three load-unload cycles were performed. After the first stage, the

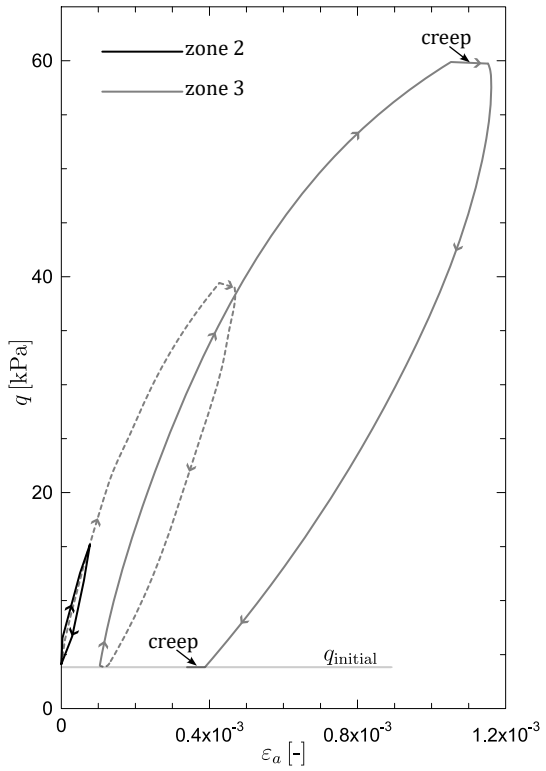

Fig. 2.9: The load-unload cycles of a Magnus till sample, showing transition from zone 2 to zone 3 (dashed line), after [82]

obtained response is clearly within the zone of recoverable strains, characterised by nonlinear hysteretic loop. However, as the deviator load increases, in two next cycles, the permanent strains become notable, as well as creep at constant q.

Within zone 3 the biggest drop of soil stiffness can be noted (Fig. 2.5), hence the modelling of soil behaviour within this strain range has crucial practical applications in geotechnical structural serviceability evaluations [44]. Further loading can lead to reaching kinematic surface Y_3 - yield surface. Beyond this border large plastic strains occur and soil attain the state of normal consolidation [60].

2.2.1 Stiffness degradation modelling

Nonlinear approach to stiffness modelling, described in Sec. 2.1, properly reflects initial stiffness and its depth-dependent distribution. Soil stiffness increases with the mean stress level p, however it simultaneously decreases with strain. Therefore, to accurately model the pre-failure behavior of soil, it is necessary to account for both barotropy and stiffness degradation.

In literature one can find numerous proposals of stiffness-strain modelling. In order to maintain a realistic nature of material stiffness, a chosen stiffness-strain relation should properly simulate soil behaviour under cyclic load. This can be fulfilled by incorporating the effects of hysteresis into a model - a material response to load cycle forms a closed hysteretic loop in stress-strain space. One of the most commonly used hysteretic models, which describes secant shear modulus degradation, was proposed by Hardin and Drnevich [63]:

$$\frac{G_{\mathrm{s}}^{\mathrm{ref}}}{G_{0}^{\mathrm{ref}}} = \frac{1}{1 + |\gamma/\gamma_{\mathrm{r}}|}, \tag{2.21}$$

where γ is shear strain, $\gamma_{\mathrm{r}} = \tau_{\mathrm{failure}}/G_{0}^{\mathrm{ref}}$ denotes threshold strain. Santos and Correia [142] suggested the modified version of the Eq. 2.21:

$$\frac{G_{\mathrm{s}}^{\mathrm{ref}}}{G_{0}^{\mathrm{ref}}} = \frac{1}{1 + \frac{3}{7}\gamma/\gamma_{0.7}}. \tag{2.22}$$

Here, the threshold strain $\gamma_{0.7}$ corresponds to the value of secant shear modulus $G_{\mathrm{s}}^{\mathrm{ref}}$ reduced to $0.7\,G_{0}^{\mathrm{ref}}$.

The main drawback of the aforementioned expressions is the potential difficultly in tracking stress-strain history of a material, especially concerning stiffness recovery following sharp stress path reversals. For example, the relation in Eg. 2.22 is used in the small-strain constitutive model (Hardening Soil-Small model) proposed by Benz [19]. The HSS model was developed as a refinement of the popular Hardening Soil [143] model used in commercial FE codes, as it extends the HS model with small-strain stiffness definition. However, in case of HSS model, if a small unloading-reloading cycle occurs during monotonic loading (caused, for example, by dynamic disturbance), the stress history may be erased and, as a result, the obtained stiffness becomes much greater than in reality [120]. This phenomenon is known as overshooting. A proposed solution to the problem of overshooting in the HSS model is presented in [48].

Models, which properly control stiffness changes during small stress reversals are based on the concept of nested yield surfaces. This idea was first presented in works by Mróz [113] and Iwan [78]. The general assumption of a model is to define a finite number of yield loci in stress or strain space. The innermost surface corresponds to the range of small-strain elastic stiffness, whereas the outermost surface is associated with a conventional bounding surface. In theory, every loci can be subjected to kinematic or anisotropic hardening, meaning its shape and size can change with increasing stress. However, it would result in an introduction of additional state variables and a complex formulation and implementation. Hence, in numerous models, the inner surfaces are only capable of movement, and any hardening effects are applied to the bounding surface.

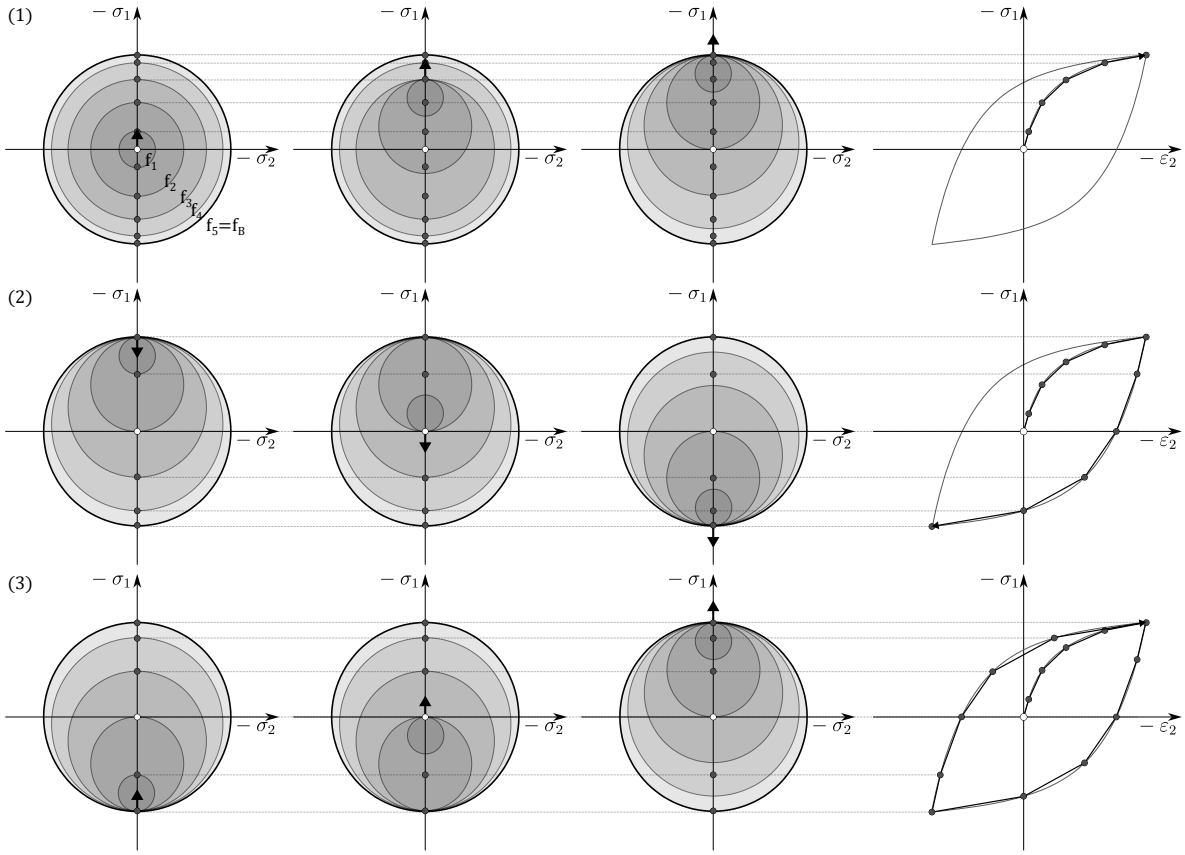

Fig. 2.10: Schematic presentation of the concept of nested yield surfaces f_i in stress space for the case of uniaxial compression, after [113, 118]: (1) loading, (2) unloading, (3) reloading

The schematic example of a multi-surface model performance, in stress space, is presented in Fig. 2.10 for a uniaxial compression. The initial stress point is in the middle of the innermost nested yield surface, determining the elastic behaviour of the soil. With the increasing stress, the boundary of the first surface is approached. When the value of the current stress exceeds this limit, the response of soil becomes elasto-plastic, and the first plane gets pulled along. As stress continues to increase, the consecutive surfaces are activated. This action is directly related to stiffness degradation of the soil. Additionally, along with the change of location of the nested yield surfaces, the stress history is established. The movement of the loci continues up to the immovable bounding surface. This surface is reached once the shear strength criterion is satisfied. In certain cases, the surface may coincide with the state of normal consolidation, but only in the absence of hardening. A stress path reversal occurs in case of unloading. It results in the deactivation of the all surfaces. In consequence the soil response is elastic again and stiffness regains its initial value.

The concept of nested yield surfaces was utilised in so-called *bubble* models [5, 6]. In this case a singular surface is implemented (*a bubble*) defining small-strain elastic behaviour of soil. In another model, presented in [137], three yield surfaces are described, which subsequently correspond to kinematic zones proposed by Jardine [82].

A multi-surface model, formulated in strain space, was proposed by Simpson *et al.* [149], and later validated with the numerical simulation of retaining structures [147]. In order to describe this model, an analogy of a person pulling a number of bricks around a room is used. A schematic explanation of this comparison is presented in Fig. 2.11. The room represents strain space and the person walking around it symbolises a current strain state. Bricks are tied to the person with a set of strings. Each string has a different length that corresponds to the radius of a consecutive nested yield surface. At initial state, the position of the man and the bricks is close to each other and every rope is slack. The value of soil stiffness modulus is then considered to be at its maximum. The moment the person starts to move the bricks gradually follow the same path, beginning with the ones tied to the shortest strings. Every time the man begins to pull the next brick, the soil stiffness degrades in stepwise fashion. The minimum stiffness is obtained when all bricks are in motion. In case of a sudden change of a loading direction

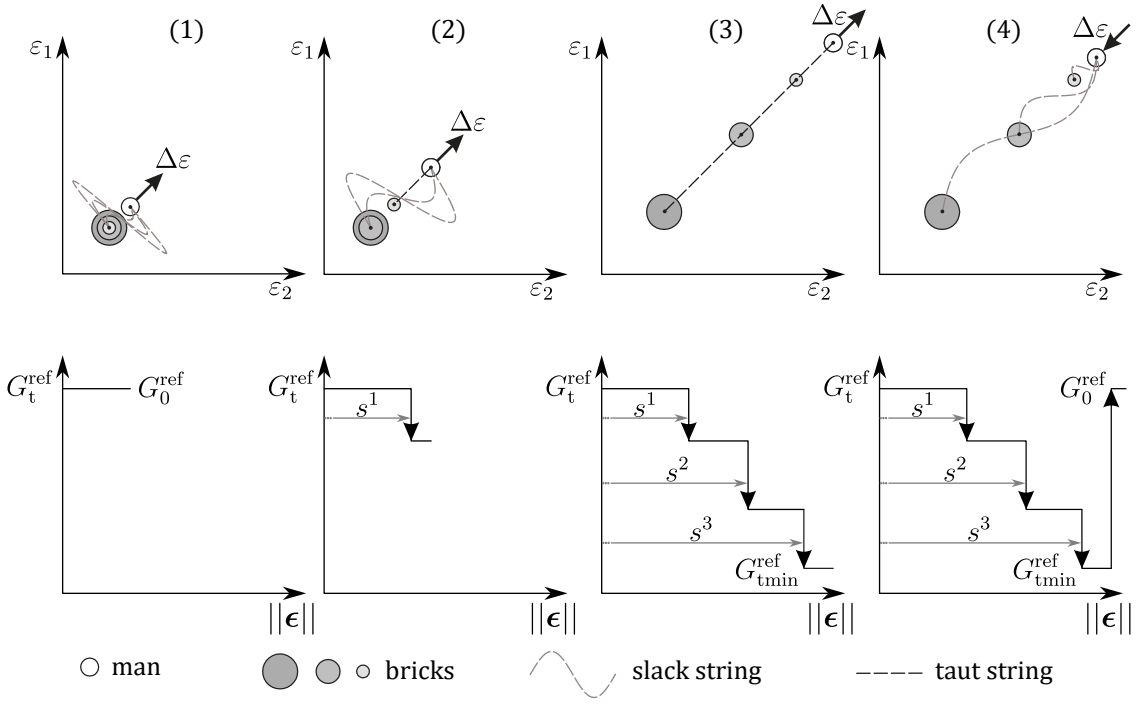

Fig. 2.11: An analogy of a man pulling bricks used to describe Brick model proposed by Simpson [147]. Stiffness degrades in stepwise fashion during the monotonic strain path (1-3) but its initial value is recovered due to the sudden unloading (4)

in strain space, *i.e.* the person turns back or stops, the string go slack and the initial value of shear modulus is attained.

In the original formulation of Simpson's Brick model, the magnitude of each stiffness drop, so-called stiffness proportion, is strictly related to the sting length s^j and the ratio of the actual reference tangent shear modulus $G_{\mathrm{t}}^{\mathrm{ref}}$ to the reference initial shear modulus G_0^{ref}. The measure of the string length is specified in strain space. This distance, given plane strain conditions ($\varepsilon_{31} = \varepsilon_{23} = \varepsilon_{33} = 0$), can be expressed as Euclidean norm:

$$||\boldsymbol{\epsilon}|| = \sqrt{\epsilon_i \epsilon_i} = \sqrt{\varepsilon_V^2 + (\varepsilon_{22} - \varepsilon_{11})^2 + 4\varepsilon_{12}^2} = \sqrt{\varepsilon_V^2 + \gamma_M^2}, \tag{2.23}$$

where three strain space components ϵ_i are:

$$\epsilon_1 = \varepsilon_V = \varepsilon_{11} + \varepsilon_{22}, \quad \epsilon_2 = \varepsilon_{22} - \varepsilon_{11}, \quad \epsilon_3 = \gamma_{12} = 2\varepsilon_{12} \tag{2.24}$$

and $\gamma_M = \sqrt{(\varepsilon_{22} - \varepsilon_{11})^2 + 4\varepsilon_{12}^2}$ is the diameter of Mohr's circle.

Later, the Brick model was extended to operate in three dimensional space, defined with six stain components ϵ_i [39, 99]:

$$\begin{aligned} \epsilon_1 = \varepsilon_V = \varepsilon_{11} + \varepsilon_{22} + \varepsilon_{33}, \quad \epsilon_2 = \varepsilon_{33} - \varepsilon_{11}, \quad \epsilon_3 = \frac{2\varepsilon_{22} - \varepsilon_{11} - \varepsilon_{33}}{\sqrt{3}}, \\ \epsilon_4 = \gamma_{12} = 2\varepsilon_{12}, \quad \epsilon_5 = \gamma_{23} = 2\varepsilon_{23}, \quad \epsilon_6 = \gamma_{31} = 2\varepsilon_{13}. \end{aligned} \tag{2.25}$$

In this case, the Euclidean norm takes the following form:

$$||\boldsymbol{\epsilon}|| = \sqrt{\sum_{i=1}^{6} \epsilon_i \epsilon_i} = \sqrt{\varepsilon_V^2 + (\epsilon_2^2 + ... + \epsilon_6^2)} = \sqrt{\varepsilon_V^2 + 3\varepsilon_q^2} = \sqrt{\varepsilon_V^2 + \frac{3}{2}\gamma_{\mathrm{oct}}^2}, \tag{2.26}$$

where ε_V and ε_q are volumetric and deviatioric strain, respectively and

$$\begin{aligned} \gamma_{\mathrm{oct}} &= \sqrt{\frac{4}{3} e_{ij} e_{ij}} = \\ &= \frac{2}{3}\sqrt{(\varepsilon_{11} - \varepsilon_{22})^2 + (\varepsilon_{22} - \varepsilon_{33})^2 + (\varepsilon_{33} - \varepsilon_{11})^2 + 6(\varepsilon_{12}^2 + \varepsilon_{23}^2 + \varepsilon_{31}^2)} \end{aligned} \tag{2.27}$$

is the octahedral shear strain.

The Brick procedure itself is only responsible for the description of stiffness-strain relation. Hence, an advanced elastic law that determines soil response within small-strain range is required to obtain a properly formulated constitutive model. The Brick-type models are found to be especially effective considering the simulation of clayey soil behaviour, e.g. [4, 39, 45, 48, 99, 148].

3

Anisotropy of soils

Soil deposits have been formed, over millions of years, due to geological, chemical, biological processes and climate changes (glacial periods). Weathering products of a parent material are transported to other regions through agents (e.g. water, wind, landslides) and then subjected to sedimentation and deposition. All postdepositional processes concerning changes in a sediment, such as diagenesis, cementation and consolidation affect directly soil microstructure and its physical, mechanical and hydraulic properties [110, 112].

In the early stages of deposition, particles of fine grained cohesive soils tend to align edge-to-face, which is caused by their magnetic properties; an edge of a singular clay shale is charged positively, whereas a face - negatively [18, 128]. This so-called *honeycomb* structure exhibit isotropic properties and is characterised by relatively high porosity. Such soils typically originate from young Holocene marine and lake deposits [160]. These are usually very compressible soft soils.

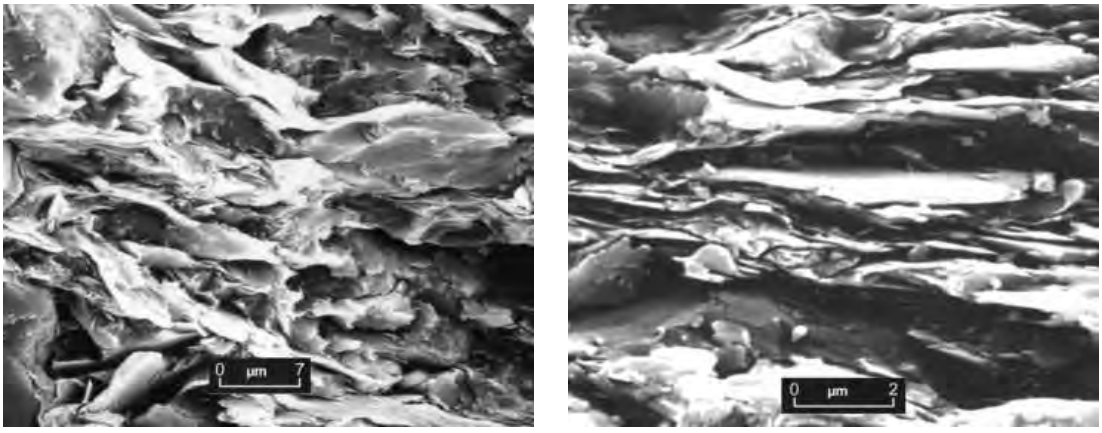

(a) (b)

Fig. 3.1: SEM images of shale microstructure contacts: a) edge-to-face, b) face-to-face, from [170]

While undergoing consolidation process, soil microstructure is subjected to volumetric straining, in consequence creating more compacted face-to-face arrangement of clay particles oriented normal to the stress direction. This laminate structure is especially a characteristic of stiff overconsolidated clay soils, subjected to one-dimensional consolidation, which mechanical properties depend on particle orientation. Due to material packing, void ratio decreases and small fissure-like pores form along distinctive layers resulting in anisotropic hydraulic nature of such clays [170]. Both honeycomb and laminar type of microstructure, captured using scanning electron microscopy technique (SEM), are presented in Fig. 3.1.

Permeability of a soil deposit may vary due to local changes of soil mineralogy, microstructure and material discontinuities. It is possible that dissipation of pore water can occur at a slower rate than the sedimentation process. In result, upward water migration can be prevented by compacted soil layers with reduced permeability. Zones, in which high excess pore water pressure is generated, exhibit the behaviour of normally consolidated, thus maintaining edge-to-face microstructure. Such soil behaviour under locally varying hydraulic properties is portrayed in Fig. 3.2. This process, however, is temporary, as under growing overburden load, the particle structure collapses creating face-to-face contacts [144].

Soil structure, geological history and *in situ* stress state induce either isotropy, cross-anisotropy or orthotropy in a soil material. Granular soils and normally consolidated clays with a random particle orientation are typically isotropic - their properties do not change with orientation. A cross-anisotropic (transversely isotropic) material exhibits direction-dependent properties that are symmetric about the axis normal to the bedding plane arrangement, so-called *plane of isotropy*. A more detailed description of such soils is presented later in this

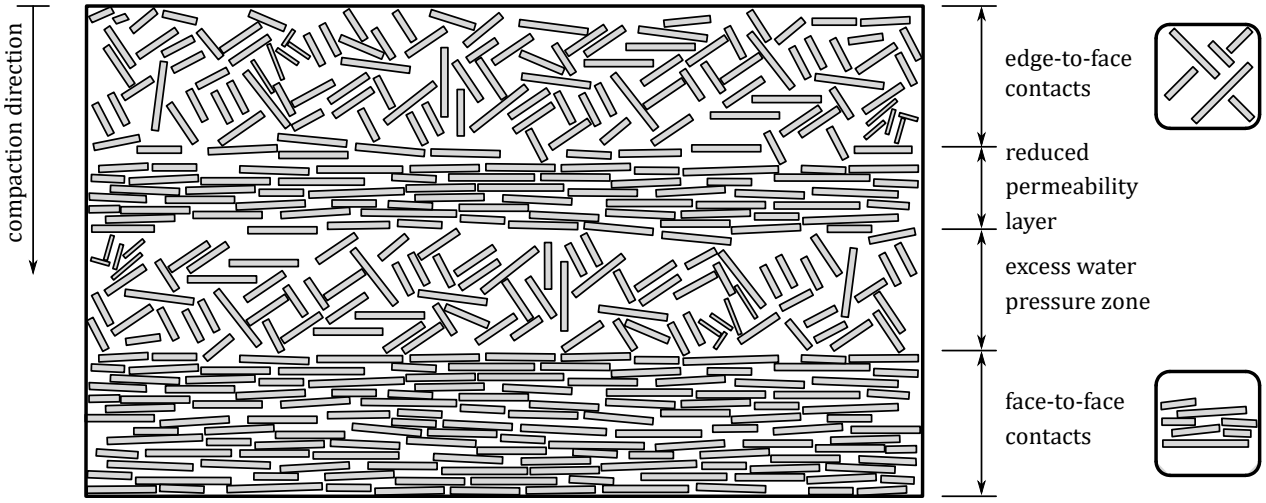

Fig. 3.2: Scheme of soil compaction disruption caused by local permeability changes, after [144]

chapter. The most complex soil behaviour, orthotropy, assumes different parameter values for all three mutually perpendicular directions. It usually can be applied for rock masses with prominent joints and discontinuities. Directional dependency of isotropic, cross-anisotropic and orthotropic material is shown in Fig. 3.3.

The mechanical behaviour of soils assumed as isotropic has been well studied over years. In contrast, the response of both cross-anisotropic and orthotropic soils are yet to be fully understood, due to the complex and expensive laboratory testing. In this work the analysis of the directional-depended behaviour of the soils is limited to overconsolidated fine-grained clays and those are mostly cross-anisotropic. Hence, in this chapter the emphasis is mostly put on the description of the cross-anisotropy.

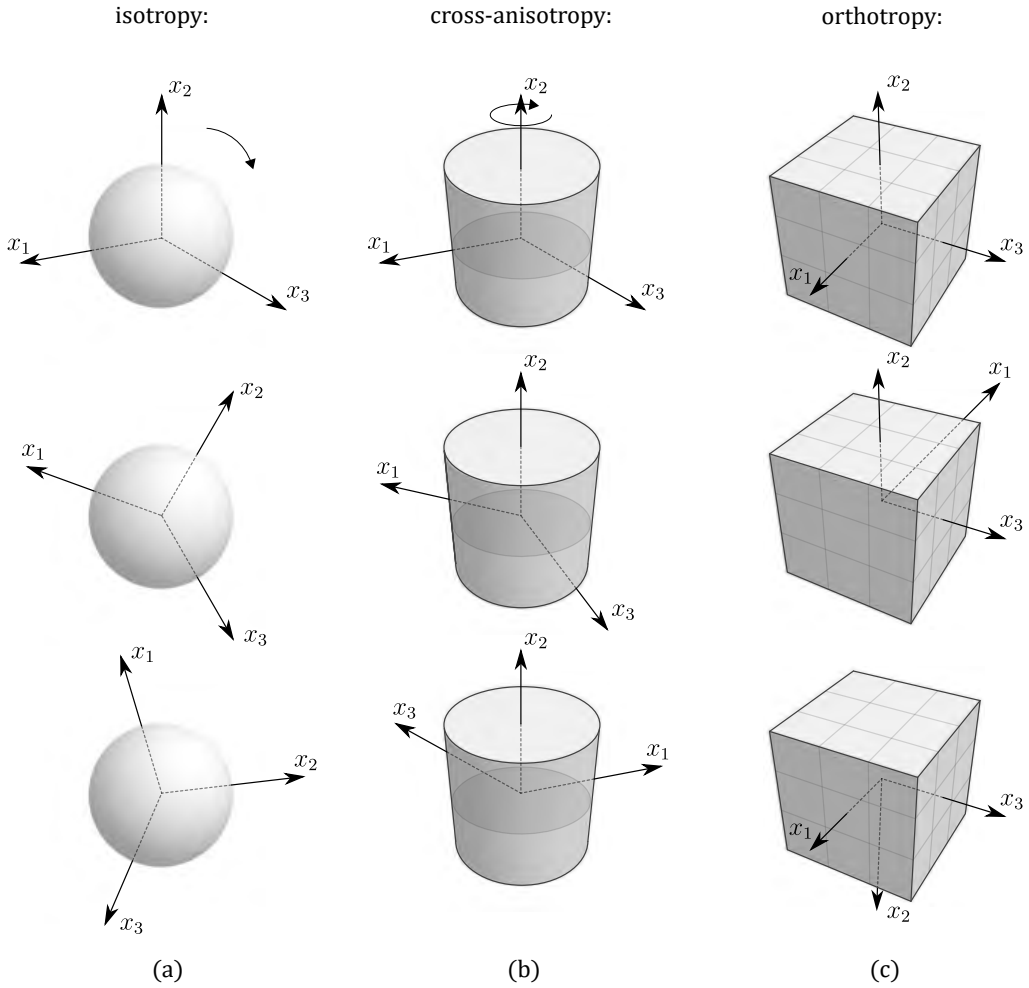

Fig. 3.3: Schematic description of a isotropic, cross-anisotropic and orthotropic materials. Soil properties remain unchanged in terms of: a) isotropy - regardless of axis orientation, b) cross-anisotropy - symmetric about normal to plane of isotropy, c) orthotropy - for the mirroring axes, after [118]

3.1 Inherent and stress-induced anisotropy

Two types of anisotropy in natural soil deposits can be distinguished: inherent and stress-induced. Geological processes, which influence soil microstructure and, consequently, the orientation of the microstructure coordinate system, directly affect the so-called inherent anisotropy. Typically, inherent anisotropy exhibits characteristics of cross-anisotropy, meaning that soil properties remain unchanged about the axis normal to the plane of isotropy. This axis, denoted by the unit vector **v** (Fig. 3.4), corresponds to the direction of material deposition. For overconsolidated, fine-grained, stiff soils, the plane of isotropy is defined by the prevailing particle arrangement, which creates distinctive bedding planes. As shown in Fig. 3.5, bedding planes are usually formed horizontally, however, an inclination of the plane of isotropy is possible, especially in older stiff clayey sediments. Inherent anisotropy depends only on the orientation of the material microstructure and, in the case of heavily overconsolidated natural clays, remains constant and insensitive to significant changes in stresses and strains. Reconstituted

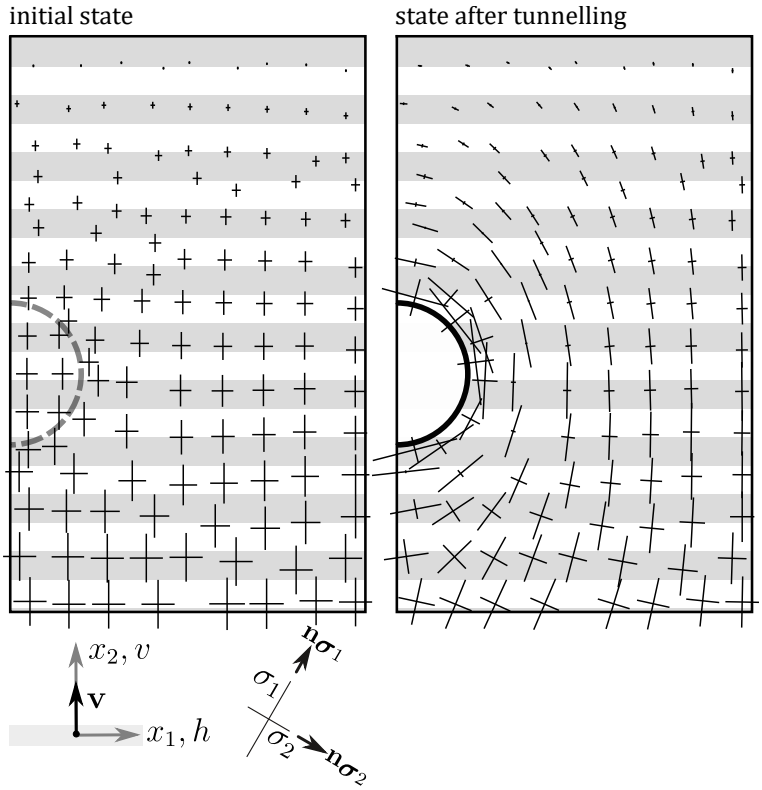

Fig. 3.4: The definition of axes in cross-anisotropic natural soil shown for the example of tunnel drilling. The geometrical axes (x_1, x_2) corresponds to material coordinate system representing plane of isotropy (h) and axis of symmetry ($\mathbf{v}$, v), respectively. The components of principal stress σ_i and principal stress axes directions n_{σ_i} change due to unloading, after [46]

(a) (b)

Fig. 3.5: Distinctive layered particle arrangement corresponding to a material's plane of isotropy: a) horizontal bedding planes of a boulder clay, own source, b) inclined bedding planes of a boulder clay in Gutio mine, own source

and slightly overconsolidated soils may undergo microstructural changes during extensive, irreversible strains, hence, in this instance, the anisotropy of the microstructure may evolve [40, 47, 108]. Pure inherent anisotropic behaviour of soil can be properly measured only under isotropic stress conditions, as the stress-controlled component of anisotropy is deactivated.

Stress-induced anisotropy of soil material depends in part on stress history and its *in situ* state. The most common indicator of the initial *in situ* stress state is denoted as the coefficient of earth pressure at rest K_0. It describes the relationship between horizontal effective stress component and a vertical one: $K_0 = \frac{\sigma_h}{\sigma_v}$. Soil material subjected to loading and unloading due to geotechnical processes may experience enhancement of the stress-induced anisotropy as all the values of principal stress components could be different and their rotation may occur.

Anisotropy of natural soils is rather complex as it includes the superposition of inherent and stress-induced anisotropy. Its definition depends on three principal axes, as shown in Fig. 3.4. Geometrical coordinates x_i are usually collinear with the direction of gravity. In this dissertation, unless stated otherwise, axis x_2 is determined as vertical. Microstructural axes $x_{\mathrm{m}i}$ correspond to prevailing particle arrangement of soil. In terms of horizontally distributed sediment, the analysis is simplified as both geometrical and microstructure coordinate systems align. Orientation of principle axes of stress $\mathbf{n}_{\boldsymbol{\sigma}i}$ is independent in relation to microstructure coordinates, and may rotate due to introduction of additional loads and undergoing geotechnical engineering processes. Ultimately, the anisotropy of stiffness and strength depends on the orientation of three axes: geometric, microstructural, and principal stress directions.

3.2 Experimental evidence of mechanical anisotropy

Anisotropic behaviour of soils is especially noticeable in the range of small strains (soil stiffness) and large strains (shear strength). Overconsolidated clays, with the prevailing particle arrangement, are mostly anisotropic in terms of stiffness and strength. However, it is important to mention that anisotropic stiffness tested in undrained conditions influences the stress paths, so it also affects the undrained shear strength of a tested specimen [150]. Strength anisotropy can also be evident for soft clays and sands but it is mostly due to its stress-induced component, as it can develop in previously isotropic material subjected to plastic deformation and loading [38]. Inherent anisotropy in sand depends on particle contacts and there have been reported cases of sands showcasing cross-anisotropic fabric, e.g. [9, 126]. In rock mechanics, a material is generally anisotropic in case of stiffness and strength, however, due to so-called planes of weakness, induced by e.g. bedding planes or discontinuities, the the influence of strength anisotropy seems to be especially important.

Laboratory testing of anisotropic properties of soils can be quite difficult, as it is required to examine the sample in different directions. Hence, the advanced laboratory equipment is needed, as well as, the specific testing procedures should be followed to properly obtain anisotropic parameters. It could be very expensive and time consuming. However, as the importance of anisotropic mechanical properties of soils has been recognised for numerous geotechnical engineering cases e.g. [3, 4, 22, 83, 123, 138, 147, 179, 180], the need to properly define material anisotropic properties has become evident.

3.2.1 Small-strain stiffness anisotropy

Soil stiffness can be tested either *in situ* or using high accuracy laboratory equipment. Schematic examples of various small-strain stiffness surveying techniques are illustrated in Fig. 3.6. In the case of field seismic analysis, wave propagation velocity of compressive and shear waves can be measured with such methods: cross-hole, down-hole and CPTU seismic tests, whereas the surface waves - Rayleigh waves - are used for Spectral Analysis of Surface Waves (SASW) and Continuous Surface Wave System (CSWS) method [19, 40, 44, 107].

Compared to field investigations, laboratory testing is expensive, time consuming, complex and additionally carries a risk of sample disturbance. Still, it provides more detailed data of small-strain stiffness and its nonlinear degradation [19]. The small-strain stiffness of soils is usually measured in laboratory environment by advanced triaxial devices, equipped with seismic elements or local displacement transducers, a resonant column or a torsional shear instrumentation [40, 47, 65, 146]. Determination of anisotropic small strain stiffness parameters

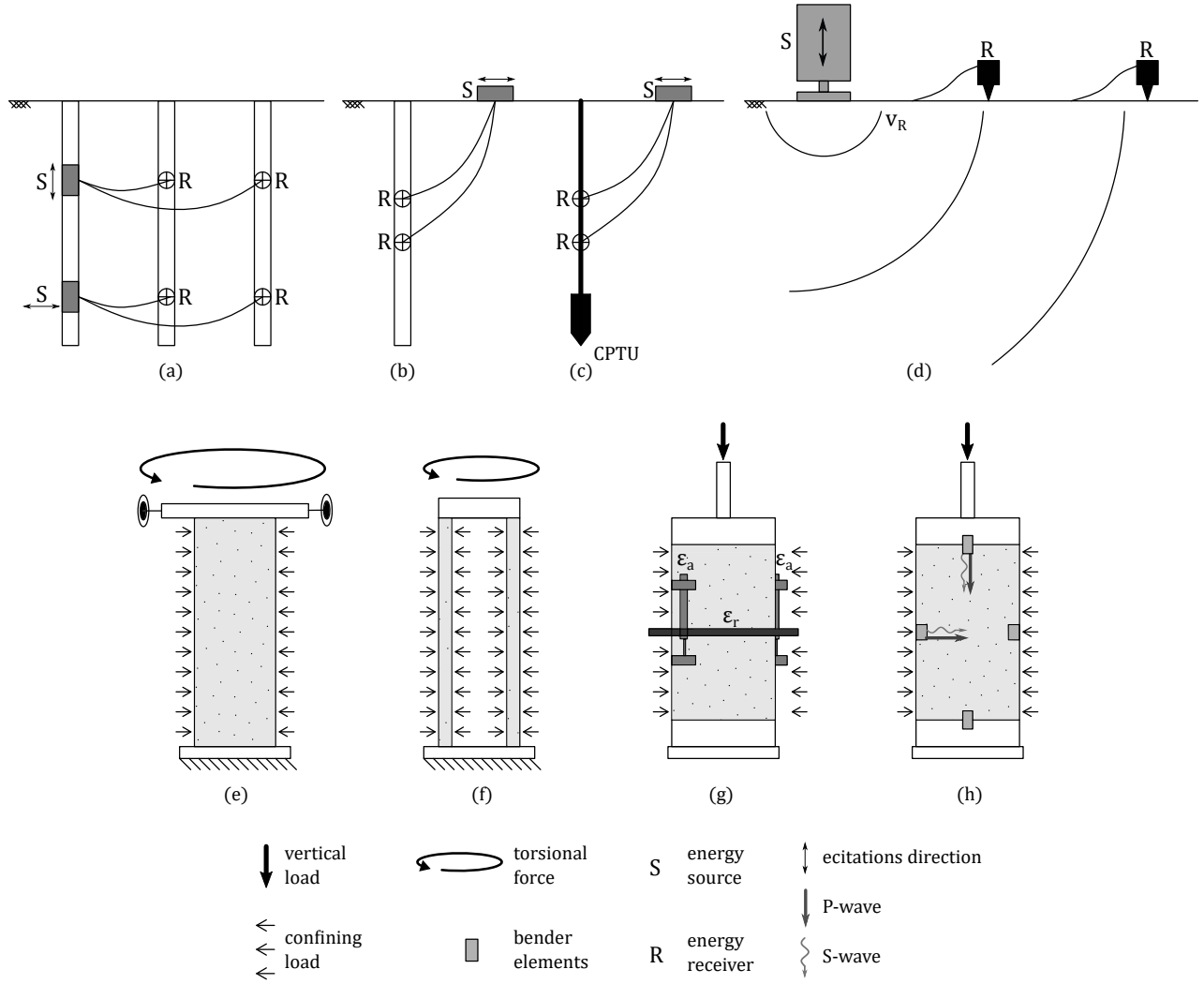

Fig. 3.6: Schematic representation of the typical field (a-d) [19, 40, 44] and laboratory (e-h) [40, 47, 65, 146] seismic tests: a) cross-hole, b) down-hole, c) seismic CPTU test, d) Continuous Surface Wave System (CSWS) - measured with dispersive Rayleigh waves v_R, e)resonant column, d)hollow cylinder apparatus, e-f) triaxial apparatus with displacement transducers and bender elements, respectively

is, in the most cases, performed in the triaxial apparatus with seismic bender elements, which are designed to measure the velocity of shear wave. The standard setup, shown in Fig. 3.7, assumes a cross-anisotropic soil sample to be trimmed in the direction parallel to the symmetry axis. The bender elements are oriented in such way that the polarization of the generated shear wave corresponds to the plane of isotropy [85]. Generally, the bedding planes of an anisotropic specimen in the triaxial device should be oriented horizontally or vertically, otherwise shear deformation during the compression occurs [7] and the test cannot be classified as an element test.

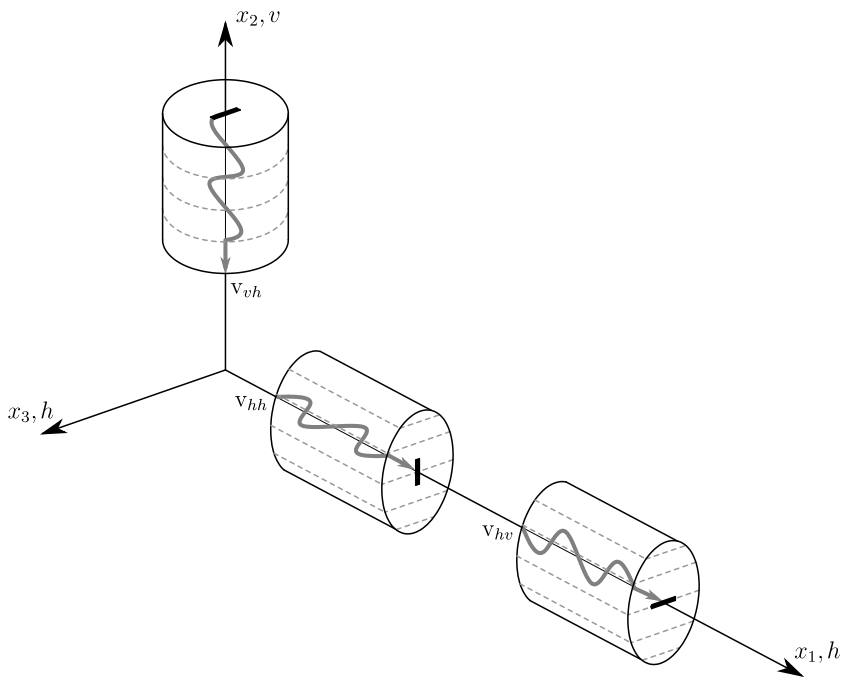

Fig. 3.7: Examples of soil sample trimming and applicable shear wave velocity measurements, after [85]

Assuming cross-anisotropic characteristics of soil, in order to obtain the proper small-strain behaviour description, five independent material constants are required. Most commonly used parameter set contains: Young's modulus in vertical direction E_v, Young's modulus in horizontal direction E_h, Poisson's ratio due to the vertical stress on the horizontal strain ν_{vh}, Poisson's ratio due to the horizontal stress on the horizontal strain ν_{hh} and shear modulus in vertical plane G_{vh} [103]. Due to the simplicity of, the subscript $()_0$, which specifies initial or small-strain parameter values is here omitted. Overall, the determination of all five parameters from the laboratory testing is very difficult, however it has been reported [52] that, using the triaxial apparatus with multi-directional piezoelectric sensors installed, as illustrated in Fig. 3.8, it is possible to obtain substitute set of five seismic stiffness parameters from one soil sample. The stiffness matrix for such obtained parameters is as follows:

$$\begin{Bmatrix} \dot{\sigma}_{11} \\ \dot{\sigma}_{22} \\ \dot{\sigma}_{33} \\ \dot{\sigma}_{12} \\ \dot{\sigma}_{23} \\ \dot{\sigma}_{31} \end{Bmatrix} = \begin{bmatrix} E_{\mathrm{oed}h} & D_{23} & E_{\mathrm{oed}h} - 2G_{hh} & 0 & 0 & 0 \\ D_{23} & E_{\mathrm{oed}v} & D_{23} & 0 & 0 & 0 \\ E_{\mathrm{oed}h} - 2G_{hh} & D_{23} & E_{\mathrm{oed}h} & 0 & 0 & 0 \\ 0 & 0 & 0 & G_{vh} & 0 & 0 \\ 0 & 0 & 0 & 0 & G_{vh} & 0 \\ 0 & 0 & 0 & 0 & 0 & G_{hh} \end{bmatrix} \begin{Bmatrix} \dot{\varepsilon}_{11} \\ \dot{\varepsilon}_{22} \\ \dot{\varepsilon}_{33} \\ \dot{\gamma}_{12} \\ \dot{\gamma}_{23} \\ \dot{\gamma}_{31} \end{Bmatrix}, \tag{3.1}$$

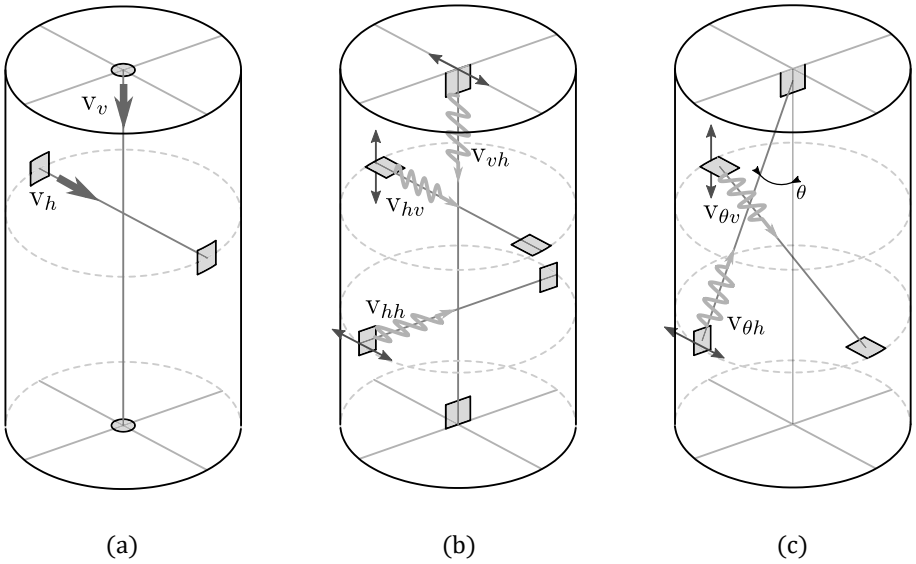

Fig. 3.8: Schematic representation of wave propagation velocity measurements using multi-directional piezoelectric sensors: a) compressive waves, b) shear waves, c) oblique waves, after [52]

where $E_{\mathrm{oed}h}$ and $E_{\mathrm{oed}v}$ correspond to constrained oedometric moduli acquired from compressive P-waves propagated in horizontal and vertical directions respectively, G_{vh} and G_{hh} are shear moduli in vertical and horizontal planes accordingly using shear S-waves; stiffness component D_{23} vastly depends on propagation velocity of oblique P-wave $v_{\theta v}$. Both oedometric and shear moduli can be calculated according to Eq. 2.20:

$$E_{\mathrm{oed}h} = \rho v_h^2, \qquad E_{\mathrm{oed}v} = \rho v_v^2, \tag{3.2}$$

$$G_{hh} = \rho v_{hh}^2, \qquad G_{vh} = \rho v_{vh}^2, \tag{3.3}$$

whereas the value of D_{23} can be obtained from the Stokoe solution [157, 158]:

$$v_{\theta v} = \sqrt{\frac{A-B}{2\rho}}, \tag{3.4}$$

for which:

$$A = E_{\mathrm{oed}h}\sin^2\theta + E_{\mathrm{oed}v}\cos^2\theta + G_{vh}, \tag{3.5}$$

$$B = \sqrt{[(E_{\mathrm{oed}h} - G_{vh})\sin^2\theta - (E_{\mathrm{oed}v} - G_{vh})\cos^2\theta]^2 + 4(D_{23} - G_{vh})^2\sin^2\theta\cos^2\theta}. \tag{3.6}$$

Given seismic parameters in Eq. 3.1 the conversion to standard cross-anisotropic parameters can be done as follows:

$$E_v = \frac{D_{23}^2}{G_{hh} - E_{\mathrm{oed}h}} + E_{\mathrm{oed}v}, \tag{3.7}$$

$$E_h = \frac{4G_{hh}(D_{23}^2 + (G_{hh} - E_{\mathrm{oed}h})E_{\mathrm{oed}v})}{D_{23}^2 - E_{\mathrm{oed}h}E_{\mathrm{oed}v}}, \tag{3.8}$$

$$\nu_{hh} = \frac{D_{23}^2 + 2G_{hh}E_{\mathrm{oed}v} - E_{\mathrm{oed}h}E_{\mathrm{oed}v}}{D_{23}^2 - E_{\mathrm{oed}h}E_{\mathrm{oed}v}}, \tag{3.9}$$

$$\nu_{vh} = \frac{D_{23}}{2(-G_{hh} + E_{\mathrm{oed}h})}. \tag{3.10}$$

Following [58], three anisotropy coefficients, indicating the degree of soil inherent anisotropy, has been proposed [108]:

$$\alpha_G = \frac{G_{hh}}{G_{vh}}, \tag{3.11}$$

$$\alpha_E = \frac{E_h}{E_v}, \tag{3.12}$$

$$\alpha_\nu = \frac{\nu_{hh}}{\nu_{vh}}, \tag{3.13}$$

where G_{hh} is the shear modulus in the plane of isotropy:

$$G_{hh} = \frac{E_h}{2(1 - \nu_{hh})}. \tag{3.14}$$

In terms of cross-anisotropy G_{vh} and G_{hv} are assumed equal, as confirmed by laboratory testing shown in Fig. 3.9.

In addition to the anisotropy coefficients α_G, α_E, α_ν, two anisotropy exponents x_{GE} and $x_{G\nu}$ has been introduced, following the relations:

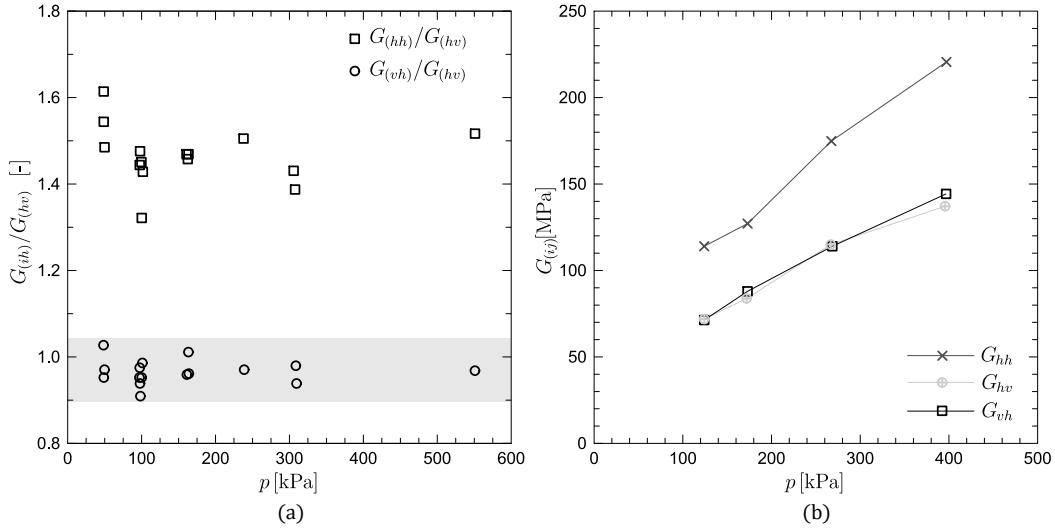

Fig. 3.9: Relations of soil stiffness parameters in case of: a) Gault Clay, after [129], b) London Clay, after [85]

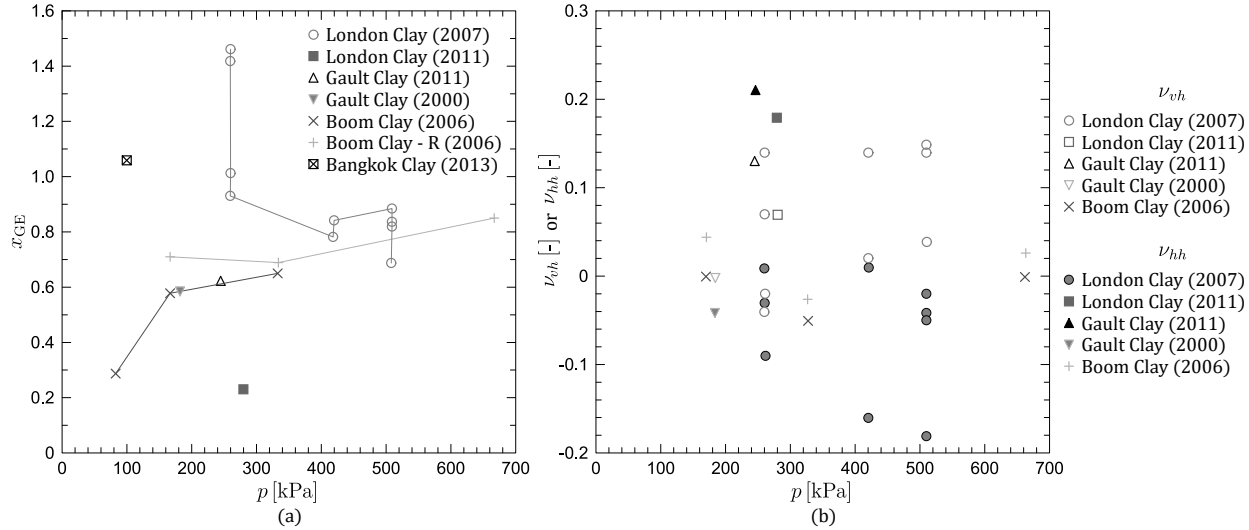

Fig. 3.10: The overview [108] of the laboratory results of cross-anisotropic parameters conducted for different clays [57, 100, 136, 140, 175]: a) the relation between the anisotropy exponent x_{GE} and the mean stress p, b) Poisson's ratio in vertical and horizontal plane; due to the big data scatter it is impossible to determine the value of $x_{G\nu}$

$$\alpha_G = \alpha_E^{x_{GE}}, \qquad \alpha_G = \alpha_\nu^{x_{G\nu}}. \tag{3.15}$$

Based on the overview of experimental tests on anisotropic stiffness parameters presented in [108] and illustrated in Fig. 3.10, the average value of the exponent x_{GE} is approximately 0.8. The value of $x_{G\nu}$ is unknown, as the laboratory test results of ν_{vh} and ν_{hh} show a large scatter.

The joint effect of inherent and stress-induced anisotropy on initial soil stiffness can be expressed [62] as:

$$G_{0ij} = S_{(ij)} F(e) (\mathrm{OCR})^k p_{\mathrm{ref}}^{(1-ni-nj)} \sigma_i^{ni} \sigma_j^{nj}, \tag{3.16}$$

for which, indexes i and j correspond to directions of seismic wave propagation and polarisation, respectively, and principal stresses σ_i, σ_j indicate the plane of measured soil stiffness G_{0ij} and $S_{(ij)}$ is dimensionless elastic stiffness coefficient. The function $F(e)$ describes material void ratio, material constant k is associated with plasticity index PI and overconsolidation ratio (OCR), whereas ni and nj are the empirical exponents. Soil stiffness is calculated for reference mean pressure p_{ref}. This expression has been validated for numerous clayey soils [79]. In another laboratory triaxial testing on the reconstituted clay [111], the samples were subjected to isotropic ($K_0 = 1.0$) and anisotropic ($K_0 \neq 1.0$) loading. For such paths, the shear moduli were tested in the vertical and horizontal directions and the value of anisotropy coefficients α_G were calculated. Obtained values of α_G differed based on the value of K_0, clearly showing that stress-induced anisotropy influences the shear moduli G_{0ij}.

The review of cross-anisotropic elastic parameters of reconstituted and natural stiff clays based on the literature study is summarised in Tab. 3.1. The values of cross-anisotropy coefficients in the case of overconsolidated natural stiff clays tend to be greater than 1.0, meaning that the soil stiffness is generally higher in the plane of isotropy corresponding to the direction of the symmetry axis ($G_{hh} > G_{vh}$, $E_h > E_v$). However, it should be noted that stiffness measured *in situ* or under anisotropic stress conditions $K_0 \neq 1.0$ displays mixed situation of both inherent and stress-induced anisotropy, as the pure microstructure effect can be measured under isotropic stress state only. Poisson's ratio is quite difficult to study experimentally, so there is still a lack of high quality laboratory evidence on the coefficient α_ν. Contrary to common knowledge on the isotropic Poisson's ratios, in the case of cross-anisotropy, the negative values of Poisson's ratio are possible, especially in the case of ν_{hh}.

3.2.2 Shear strength anisotropy

Shear strength of soil and its anisotropic characteristics are particularly important in situations where ground movement needs to be considered, such as slope stability problems. The loading, unloading or reloading of the subsoil leads to the rotation of the principal stress directions. The influence of principal stress rotation on shear strength parameters has been proven in e.g. [11, 30, 96, 124]. Hence, strength anisotropy is tested with the regard to the angle α between the direction of major principal stress σ_1 and vertical direction.

Standard equipment used to determine shear strength anisotropy parameters is either triaxial apparatus or hollow cylinder apparatus. In the case of triaxial apparatus, the sample can only be tested for the α values being equal to 0° or 90°, whereas for the HCA it is possible to test sample at any α angle [178]. Fig. 3.11 illustrates the components of stress and strain in the hollow cylinder apparatus. The values of the principal stress components σ_1, σ_2, σ_3 and the angle α can be controlled independently through the separate application of inner and outer cell pressures, axial force and torque [68].

The relation between principal stress values is controlled by the intermediate principal stress ratio b:

$$b = \frac{\sigma_2 - \sigma_3}{\sigma_1 - \sigma_3}. \tag{3.17}$$

The b value varies from 0 to 1 where $b = 0$ is triaxial compression and $b = 1$ is triaxial extension. In the case of the torsion shear test with the same inside and outside cell pressures, the b value relates to the angle α such that [96]:

$$b = \sin^2 \alpha. \tag{3.18}$$

Table 3.1: Review of laboratory results on cross-anisotropic elastic parameters of reconstituted and natural stiff clays.

Reference	Soil	Test	α_E	ν_{vh}	ν_{hh}	α_G	Remark
[166] (1959) Ward *et al.*	London Clay (N)	TX	$1.16-1.54$	–	–	–	$K_0 = 1.0$
[11] (1975) Atkinson	London Clay (N)	PS, TX	2.0	0.19	0.0	1.9	$K_0 = 1.0$
[66] (1997) Hight *et al.*	London Clay (N)	c-h,d-h, HCA,TX,RC	0.95	–	–	$1.45-2.3$	*in situ*, $K_0 > 1.0$
[66] (1997) Hight *et al.*	Thanet Beds Clay (N)	c-h,d-h, HCA,TX,RC	$0.9-1.1$	–	–	$1.3-1.6$	*in situ*, $K_0 > 1.0$
[129] (1997) Pennington *et al.*	Gault Clay (N)	TX+BE	–	–	–	$2.25-2.75$	$K_0 = 2.1$
[129] (1997) Pennington *et al.*	Gault Clay (R)	TX+BE	–	–	–	$1.3-1.6$	$K_0 = 1.0$
[85] (1998) Jovičič & Coop	London Clay (N)	TX+BE	–	–	–	$1.5-1.6$	$K_0 = 1.0$
[85] (1998) Jovičič & Coop	London Clay (R)	TX+BE	–	–	–	$1.4-1.5$	$K_0 = 1.0$
[92] (1999) Kuwano	Kaolin (R)	TX+BE	–	–	–	$1.75-2.0$	$K_0 = 1.0$
[100] (2000) Lings *et al.*	Gault Clay (N)	TX+BE, TX+DT	3.97	0.00	-0.04	$1.8-2.25$	$K_0 = 2.0$
[122] (2005) Nishimura	London Clay (N)	TX+BE, RC, HC	1.9	–	–	$1.8-2.2$	$K_0 = 1.0$
[122] (2005) Nishimura	London Clay (N)	TX+BE, RC,HC	1.9	–	–	$1.8-2.2$	*in situ*, $K_0 > 1.0$
[175] (2005) Yamashita	NSF Clay (R)	TX+BE	$1.4-2.0$	–	–	$1.5-2.3$	$K_0 = 1.0$
[97] (2006) Landon & DeGroot	Boston Blue Clay (N)	BE	–	–	–	1.68	unloaded
[136] (2006) Piriyakul	Boom Clay (N)	TX+BE	–	–	–	$1.4-1.6$	$K_0 = 1.0$
[136] (2006) Piriyakul	Boom Clay (R)	TX+BE	–	–	–	$1.2-1.5$	$K_0 = 1.0$
[136] (2006) Piriyakul	Boom Clay (N)	TX+BE+DT	–	0.0	0.03	$1.4-2.0$	$K_0 = 2.0$
[57] (2007) Gasparre *et al.*	London Clay (N)	TX+BE	$1.5-2.8$	$0.1-0.25$	$-0.19-(-0.02)$	$1.8-2.2$	*in situ*, $K_0 > 1.0$
[177] (2011) Yimsiri & Soga	Gault Clay (N)	TX+BE+DT	2.32	0.13	0.21	1.68	$K_0 = 1.0$
[177] (2011) Yimsiri & Soga	London Clay (N)	TX+BE+DT	2.18	0.07	0.18	1.2	$K_0 = 1.0$
[29] (2017) Brosse *et al.*	Gault Clay (N)	TX, HCA	3.13	–	–	1.9	$K_0 = 1.8$
[29] (2017) Brosse *et al.*	Kimmeridge Clay (N)	TX, HCA	2.4	–	–	1.68	$K_0 = 1.7-1.8$
[29] (2017) Brosse *et al.*	Oxford Clay (N)	TX, HCA	2.8	–	–	2.3	$K_0 = 1.8$

(N)/(R) - natural/reconstituted clay, TX - triaxial test, HC - hollow cylinder apparatus, RC - resonant column, c-d/d-h - cross/down hole, BE - bender elements, PS - plane strain test, DT - displacement transducers, *in situ* - stress state

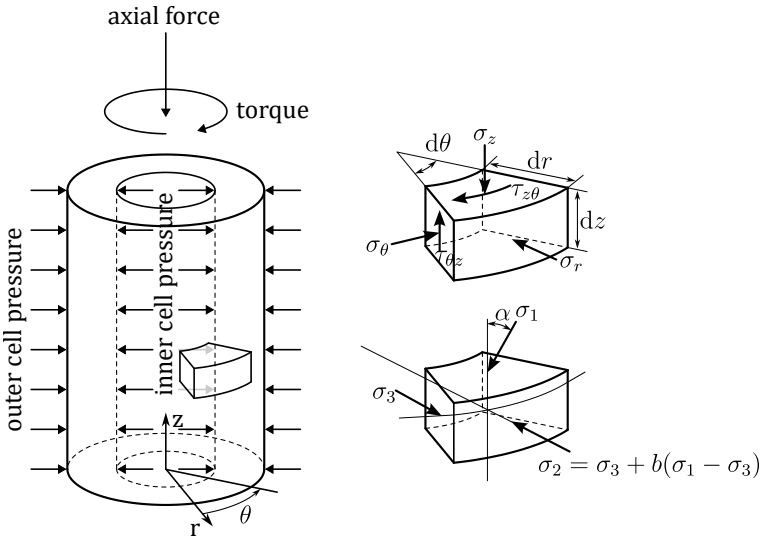

Fig. 3.11: Components of stress and strain in hollow cylinder apparetus, after [68, 178]

The shape of the failure surface for cross-anisotropic material has been experimentally determined in [2, 88, 89]. In Fig. 3.12 the shape of the failure surface, obtained from drained true triaxial test, is shown for the example of the San Francisco Bay Mud. The experimental data is shown on the octahedral plane, with three sectors distinguished based on the Lode angle θ, sector I: $\theta \in [0°, 60°]$, sector II: $\theta \in [60°, 120°]$, sector III: $\theta \in [120°, 180°]$. The results were obtained with the control of the b value for each sector. Two triaxial compression tests were conducted at angles $\theta = 0°$ and $\theta = 120°$ and two triaxial extension tests at $\theta = 90°$ and $\theta = 180°$. Due to cross-anisotropic nature of the soil, it is assumed that the surface is symmetric around the axis normal to the plane of isotropy, in this case inclined horizontally. The data was compared to the isotropic Mohr-Coulomb and Lade [93] failure criteria. It is evident that cross-anisotropy of the fabric influences the shear strength of a soil.

In rock mechanics anisotropy of rock masses is common. In fact, purely isotropic rocks rarely occur and are regarded as exceptions [28]. At micro level, anisotropy is mainly influenced by a material fabric, its schistosity, bedding, foliation and fissility [76, 162]. At macro scale, however, the material anisotropy is depended on joints, so-called discontinuities, developed in rock mass. In [71] the strength of jointed rocks is determined as completely relying on the degree of rock interlocking. A rock material showcases a highly anisotropic behaviour if one set of joint is considered. Alternatively, if at least three joint sets intersect each other, the strength of rock is regarded as isotropic and homogenous.

Due to the general anisotropy of rock masses, the strength obtained from laboratory testing should be referred to the angle β between the plane of weakness and the loading direction σ_1.

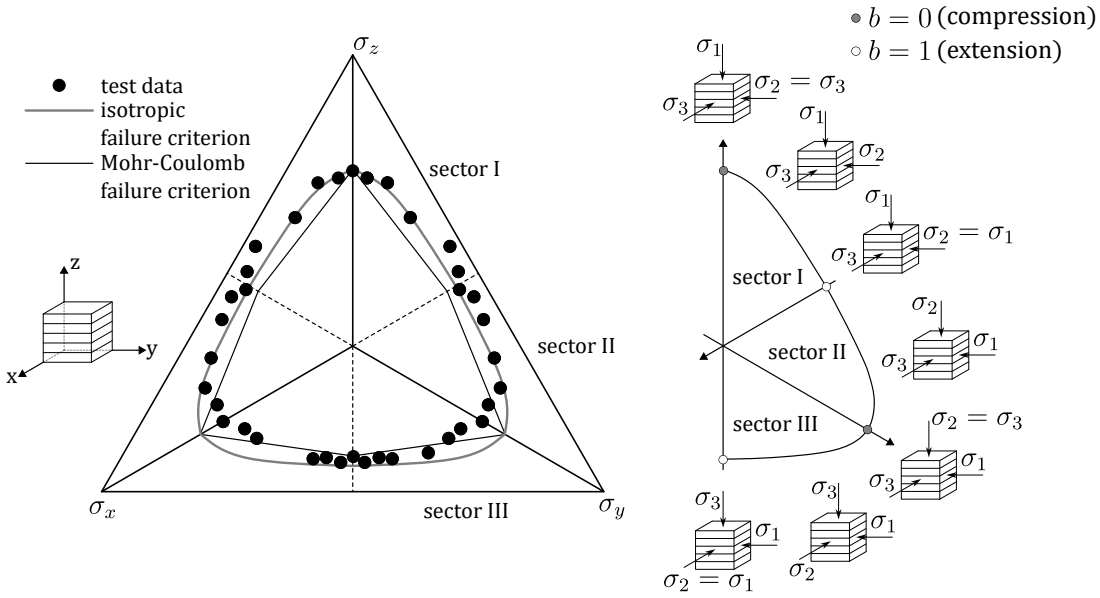

Fig. 3.12: Experimental failure surface obtained from the drained true triaxial tests conducted on the San Francisco Bay Mud samples [2]. Three sectors have based on the Lode angle θ have been distinguished. Tests were controlled by the value of the intermediate principal stress ratio b [95]

The values that are of the most interest are the maximum and the minimum rock strength. The ratio between these extreme strength values is regarded as the maximum strength anisotropy of a rock [139]:

$$R_{\mathrm{c}} = \frac{\sigma_{\mathrm{c(max)}}}{\sigma_{\mathrm{c(min)}}}, \tag{3.19}$$

where the R_{c} ratio refers to uniaxial compressive strength. As shown in Fig. 3.13, the uniaxial compressive strength of a rock mass depends on the planes of weakness and β angle. The maximum value of strength $\sigma_{\mathrm{c(max)}}$ is obtained when the loading direction is perpendicular or parallel to the weakness plane ($\beta_{(\max)} = 0°, \beta_{(\max)} = 90°$), whereas the lowest strength is reported to be reached for $\beta_{(\min)} = 30° - 45°$, due to the additional shearing along the bedding planes occurring.

Strength anisotropy of rocks can also be classified with the commonly used point-load anisotropy index I_α, adopted by the International Society for Rock Mechanics [53]:

$$I_\alpha = \frac{I_{\mathrm{s(50)}\perp}}{I_{\mathrm{s(50)}\parallel}}, \tag{3.20}$$

where $I_{\mathrm{s(50)}\perp}$ and $I_{\mathrm{s(50)}\parallel}$ are the point-load strength indexes of a sample with bedding plane orientation perpendicular and parallel to the load, respectively. The point-load index $I_{\mathrm{s(50)}}$ is described as:

$$I_{\mathrm{s(50)}} = \frac{P}{D^2}, \tag{3.21}$$

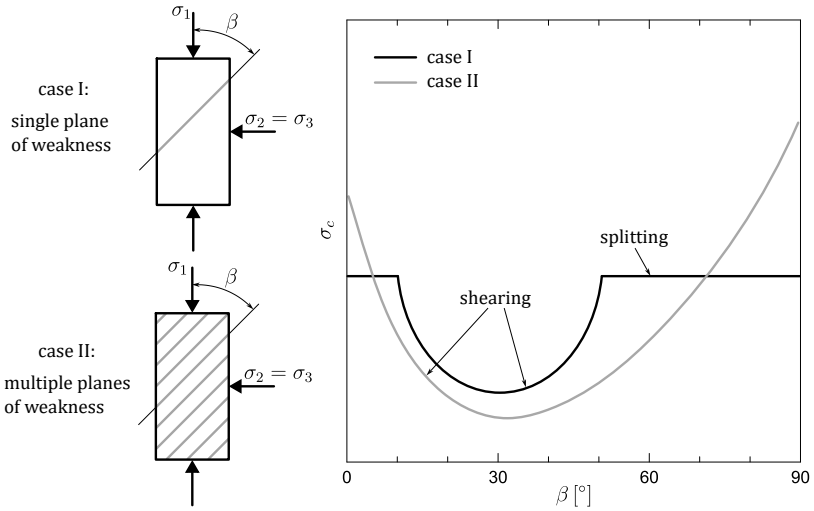

Fig. 3.13: The theoretical uniaxial compressive strength σ_c of a rock mass depending on the plane of weakness and the angle β. The maximum values of the compressive strength are obtained when $\beta_{\max} = 0^\circ$ or $\beta_{(\max)} = 90^\circ$, the minimum strength when $\beta_{(\min)} = 30^\circ - 45^\circ$, after [139]

where P is a load needed for the failure to occur, and D is a core diameter of a specimen. A standard size of the sample diameter has been adopted to be $D = 50\,\text{mm}$. As shown in Fig. 3.14, when the sample, with the foliation distribution perpendicular to the load, is tested, the obtained $I_{s(50)}$ index is at its maximum. The minimum value of $I_{s(50)}$ is found for the sample with bedding planes oriented parallel to the loading, due to splitting that occurs along the plane of weakness.

The classification of rock masses based on their anisotropic ratio R_c and point load anisotropy index I_α is shown in Tab. 3.2. Low strength anisotropy can be attributed to metamorphic rocks of a medium irregular grain size. Fine-grained rocks with the distinctive bedding planes are usually highly anisotropic.

Table 3.2: The classification of strength anisotropy for various rock masses, after [161, 162].

Anisotropy classification	Rock types	Anisotropy ratio R_c	Point load anisotropy index I_α
Quasi-isotropic	Hornfels, granulite, quartzite	$1.0 - 1.1$	< 1.1
Fairly anisotropic	Mylonite, shales, granitic gneiss	$1.1 - 2.0$	$1.1 - 1.5$
Moderately anisotropic	Quartz schist, schistose gneiss	$2.0 - 4.0$	$1.5 - 2.5$
Highly anisotropic	Hornblende schist, mica schist	$4.0 - 6.0$	$2.5 - 3.5$
Very highly anisotropic	Phyllite, slate	> 6.0	> 3.5

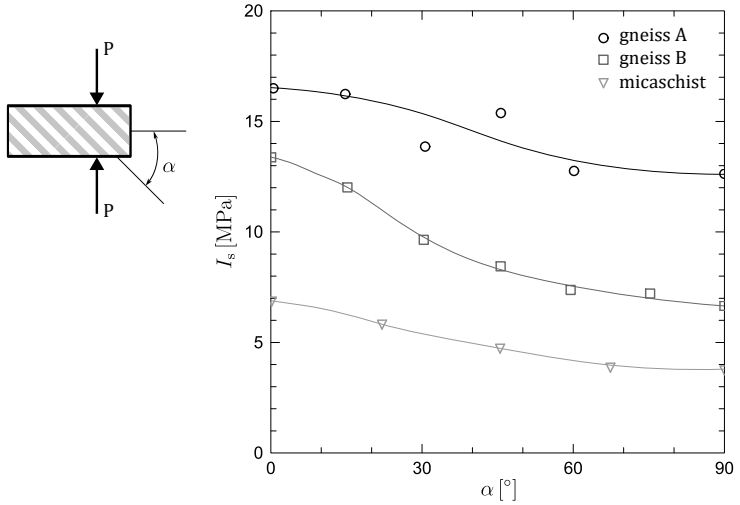

Fig. 3.14: Point-load strength index of three rocks with the regard to the angle α between horizontal core axis and the plane of weakness, after [1]

4

Constitutive modelling of anisotropy

It has become both popular and convenient to analyse geomechanical initial boundary value problems using numerical methods. In practice, material models are typically implemented within the finite element method (FEM), where soil is treated as a continuum. The use of finite element codes enables reliable analysis of complex multi-phase engineering problems involving the interaction between geotechnical structures and the soil. Numerical simulations are also valuable for calibrating the material parameters of advanced constitutive models by comparing element test results with laboratory data.

Nowadays, available commercial FE computer programs include a wide selection of constitutive models designed to simulate different aspects of soil behaviour (barotropy, stiffness strain degradation, softening, creep, shear strength, anisotropy). However, the choice of the proper material model needs to be done by a designer, based on the experience and knowledge, taking into consideration such factors as: structural problem or soil material parameters availability. For example, applying basic Mohr-Coulomb model for normally consolidated clay deposits could potentially generate higher undrained strength of the soil that it is in reality. Moreover, yielding effects of soils, which are important to take into account in slope or foundation stability analyses, may be not crucial for structural designing where prefailure soil behaviour is generally more important.

Commercial computational programmes, by default, offer only the isotropic material models. Numerical implementation of isotropic models is simpler and more straightforward, compared to complex anisotropic and orthotropic models, as parameter directional dependency does not need to be taken into account. In the case of isotropic linear elastic modelling, only two material constants are required (e.g. Young's modulus E and Poisson's ratio ν or bulk modulus K and shear modulus G).

In comparison, to define cross-anisotropic material, five soil independent parameters are needed, or in the case of the orthotropic material - nine independent constants. The inclusion of

anisotropic soil stiffness or strength in the material model previously developed as isotropic may be quite complex. It is due to the fact that isotropic models are often implemented considering three-dimensional stress or strain invariants space and not six-dimensional stress or strain space which is needed in the case of anisotropy. Due to convenience, simplicity and also costs of soil laboratory testing, isotropic models are a preferred choice.

However, the experimental evidence has shown that soils, especially overconsolidated fine-grained soils, tend to be highly anisotropic (see Sec. 3.2). The importance of anisotropy has been proven in numerous analyses of practical geotechnical cases, especially including the tunnelling and excavation problems. For example, Fig. 4.1 compares settlement troughs obtained from numerical simulations with those measured in the field. For the isotropic linear elastic model and the two isotropic nonlinear models L4 and J4, the simulated settlement troughs are excessively wide and shallow. In contrast, the soil response is captured more accurately with the nonlinear models AJ4i and AJ4ii, which incorporate stiffness anisotropy. It proves that, neglecting anisotropic behaviour in numerical modelling may result in unrealistic, as compared to further field monitoring, deformation and may lead to potential structural problems, especially in the case of tunnel drilling simulations in urban areas.

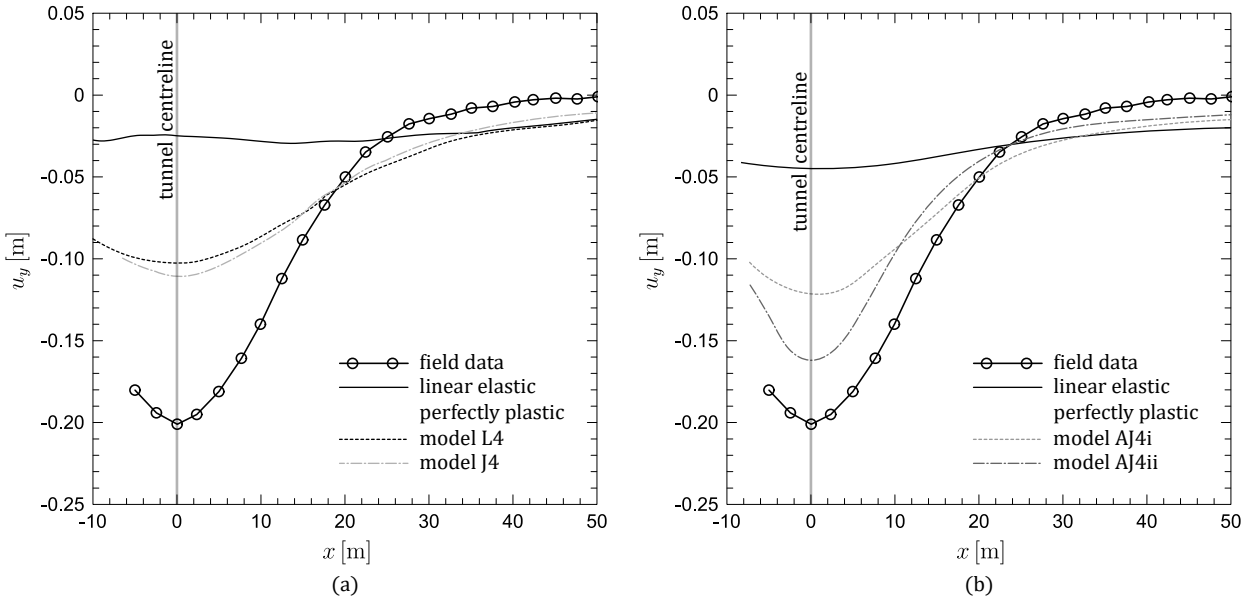

Fig. 4.1: Surface settlement profiles obtained from the numerical simulation of a tunnel drilling problem [4] with the use of a) isotropic material models, b) anisotropic material models. The soil response was compared to the field data [156]. In the case of isotropic model analysis, the settlement troughs are too shallow and too wide compared to the field data. With the use of anisotropic material models, it was possible to improve soil response

The elements of the constitutive model, which need to be taken into consideration to simulate properly anisotropic soil behaviour, are stiffness nonlinearity (barotropy and strain degradation), inherent anisotropy, stress-induced anisotropy and shear strength criterion.

4.1 Small-strain

4.1.1 Linear elastic models

The most basic form of modelling elastic anisotropy is to use linear elastic orthotropy. Stiffness matrix, written in 6×6 Voigt notation, contains 36 independent stiffness component. Taking into account the Cauchy stress tensor symmetry the number of components is reduced to 21. However, for most materials, anisotropy is limited due to assumed planes of symmetry. Hence, the number of needed parameters can be reduced. For the orthotropic material description the Hooke's law compliance matrix can be written as:

$$\begin{Bmatrix} \dot{\varepsilon}_{11} \\ \dot{\varepsilon}_{22} \\ \dot{\varepsilon}_{33} \\ \dot{\gamma}_{12} \\ \dot{\gamma}_{23} \\ \dot{\gamma}_{31} \end{Bmatrix} = \begin{bmatrix} \frac{1}{E_1} & \frac{-\nu_{12}}{E_1} & \frac{-\nu_{13}}{E_1} & 0 & 0 & 0 \\ \frac{-\nu_{12}}{E_1} & \frac{1}{E_2} & \frac{-\nu_{23}}{E_2} & 0 & 0 & 0 \\ \frac{-\nu_{13}}{E_1} & \frac{-\nu_{23}}{E_2} & \frac{1}{E_3} & 0 & 0 & 0 \\ 0 & 0 & 0 & \frac{1}{G_{12}} & 0 & 0 \\ 0 & 0 & 0 & 0 & \frac{1}{G_{23}} & 0 \\ 0 & 0 & 0 & 0 & 0 & \frac{1}{G_{13}} \end{bmatrix} \begin{Bmatrix} \dot{\sigma}_{11} \\ \dot{\sigma}_{22} \\ \dot{\sigma}_{33} \\ \dot{\sigma}_{12} \\ \dot{\sigma}_{23} \\ \dot{\sigma}_{31} \end{Bmatrix}. \tag{4.1}$$

To obtain a stable material description, the following conditions must be fulfilled [118]:

$$E_i, G_{ij} > 0, \tag{4.2}$$

$$(\nu_{ij})^2 < \frac{E_i}{E_j}, \tag{4.3}$$

$$\frac{1}{\gamma} = 1 - \nu_{12}\nu_{21} - \nu_{13}\nu_{31} - \nu_{23}\nu_{32} - \nu_{12}\nu_{23}\nu_{31} - \nu_{13}\nu_{21}\nu_{32} \quad \text{and} \quad \gamma > 0. \tag{4.4}$$

It is important to note that the Poisson's ratio components are not interchangeable ($\nu_{ij} \neq \nu_{ji}$) but, since a orthotropic material has three orthogonal planes of symmetry, the expression $\frac{\nu_{ij}}{E_i} = \frac{\nu_{ji}}{E_j}$ is true. Taking this into account, the stress rate-strain rate relation can be reduced to nine independent parameters, as shown in Fig. 4.2. Those elastic constants are Young's moduli: E_1, E_2, E_3, shear moduli G_{12}, G_{23}, G_{13} and Poisson's ratio $\nu_{12}, \nu_{23}, \nu_{13}$.

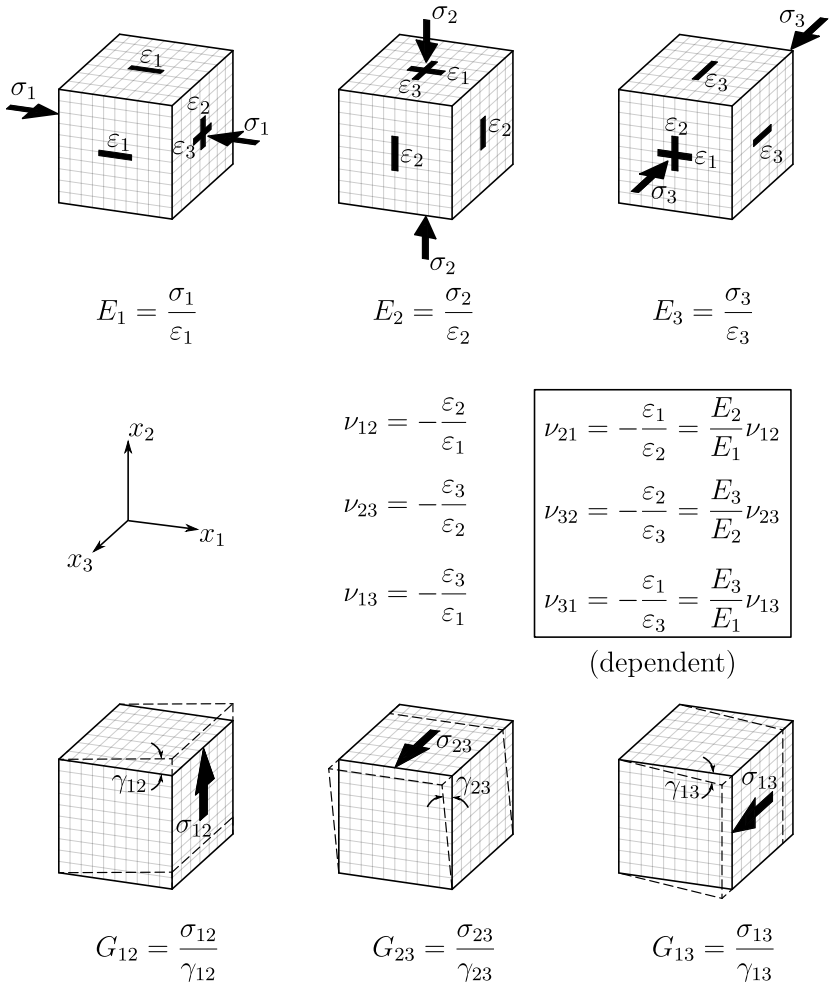

Fig. 4.2: Elastic constants in orthotropic material, nine independent parameters: E_1, E_2, E_3, G_{12}, G_{23}, G_{13}, ν_{12}, ν_{23}, ν_{13}, after [171]

The influence of the individual orthotropic parameters on soil stiffness can be visualised with the use of the orientation distribution function [165]:

$$\varrho^{-1C}(\mathbf{C}^{\mathrm{t}}, \mathbf{n}) = (n_i n_j C^{\mathrm{t}}_{ijkl} n_k n_l)^{-1}. \tag{4.5}$$

The result gives a scalar value of a Young's modulus in the direction described by the unit vector $\mathbf{n}$ and it is related to the fourth-order compliance tensor $\mathbf{C}^{\mathrm{t}}$. The spherical plots of directional distribution of stiffness are shown in Fig. 4.3. In Fig. 4.3a the values of the parameters do not depend on the direction, hence the obtained response corresponds to the Hooke's law isotropic elastic stiffness. The the influence of orthotropic parameters on soil stiffness is tested by the change of the parameter value in the relation to the initial isotropic state, as shown for the Figs. 4.3(b-d). All nine parameters affect the obtained soil stiffness. For example, if the value of

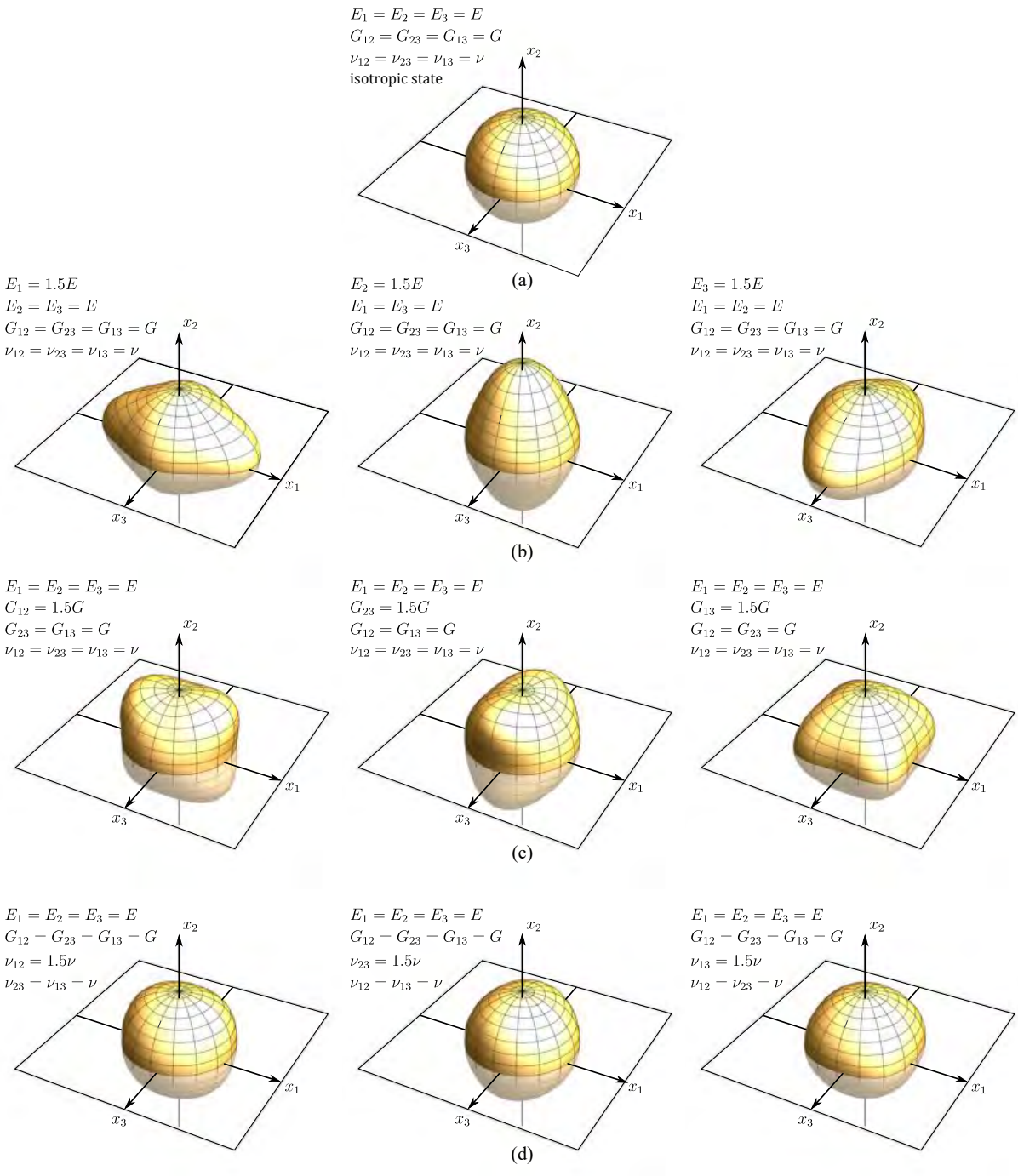

Fig. 4.3: Spherical plots illustrating the influence of the nine elastic constants in orthotropic material on the dimensional distribution of stiffness: a) isotropic state, b) change of Young's modulus E_i c) change of shear modulus G_{ij}, d) change of Poisson's ratio ν_{ij}

E_i increases, then the stiffness distribution is larger along the corresponding x_i axis. Similarly, the changes of G_{ij} and ν_{ij} are noticeable on ij plane.

In the case of cross-anisotropy, the material model can be described using five independent elastic constants, as shown in Fig. 4.4. The corresponding stress rate-strain rate relationship is expressed as:

$$\begin{Bmatrix} \dot{\varepsilon}_{11} \\ \dot{\varepsilon}_{22} \\ \dot{\varepsilon}_{33} \\ \dot{\gamma}_{12} \\ \dot{\gamma}_{23} \\ \dot{\gamma}_{31} \end{Bmatrix} = \begin{bmatrix} \frac{1}{E_h} & \frac{-\nu_{vh}}{E_v} & \frac{-\nu_{hh}}{E_h} & 0 & 0 & 0 \\ \frac{-\nu_{vh}}{E_v} & \frac{1}{E_v} & \frac{-\nu_{vh}}{E_v} & 0 & 0 & 0 \\ \frac{-\nu_{hh}}{E_h} & \frac{-\nu_{vh}}{E_v} & \frac{1}{E_h} & 0 & 0 & 0 \\ 0 & 0 & 0 & \frac{1}{G_{vh}} & 0 & 0 \\ 0 & 0 & 0 & 0 & \frac{1}{G_{vh}} & 0 \\ 0 & 0 & 0 & 0 & 0 & \frac{2(1+\nu_{hh})}{E_h} \end{bmatrix} \begin{Bmatrix} \dot{\sigma}_{11} \\ \dot{\sigma}_{22} \\ \dot{\sigma}_{33} \\ \dot{\sigma}_{12} \\ \dot{\sigma}_{23} \\ \dot{\sigma}_{31} \end{Bmatrix}. \tag{4.6}$$

Assuming a standard horizontal position of the plane of isotropy, the geometric axis x_i coincides with the microstructural axis x_{mi}. Under this assumption, the stiffness parameters can be directly related to values measured in the vertical and horizontal directions. The definitions of the individual material constants are also illustrated in Fig. 4.4.

In order to fulfil thermodynamic laws, elastic strain energy must be positive. In this terms the following limits must be satisfied [131]:

$$E_h, E_v, G_{vh} \geq 0, \tag{4.7}$$

$$-1 \leq \nu_{hh} \leq 1, \tag{4.8}$$

$$\frac{E_v}{E_h}(1 - \nu_{hh}) - 2\nu_{vh}^2 \geq 0, \tag{4.9}$$

$$\frac{E_h}{E_v}(1 - \nu_{hh}) - 2\nu_{hv}^2 \geq 0. \tag{4.10}$$

The influence of five cross-anisotropic elastic parameters on directional distribution of stiffness is shown in Fig. 4.5 in a form of spherical plots. The coordinate system is defined so the axis x_2 is vertical. The parameters are tested analogously to the orthotropic elastic constants from Fig. 4.3. The seemingly no influence of Poisson's ratio ν_{hh} on the dimensional distribution of stiffness results from the function ϱ^{-1C}. The expression reduces in a way that is completely not depended on ν_{hh}.

It is quite uncommon to obtain all five elastic parameters of cross-anisotropic materials by the means of standard laboratory testing (see Tab. 3.1). Graham and Houlsby [58] proposed an alternative in the form of simplified set of three elastic parameters: modified Young's modulus

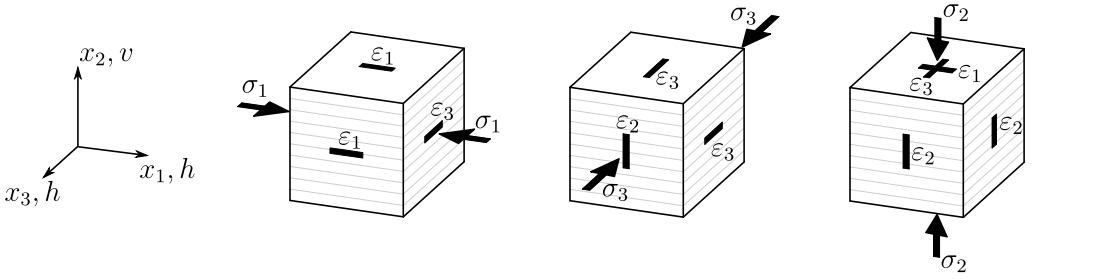

$$E_1 = \frac{\sigma_1}{\varepsilon_1} = E_3 = \frac{\sigma_3}{\varepsilon_3} = E_h \qquad E_2 = \frac{\sigma_2}{\varepsilon_2} = E_v$$

$$\nu_{13} = -\frac{\varepsilon_3}{\varepsilon_1} = \nu_{hh} \qquad \nu_{21} = -\frac{\varepsilon_2}{\varepsilon_1} = \nu_{23} = -\frac{\varepsilon_3}{\varepsilon_2} = \nu_{vh}$$

$$\boxed{\nu_{32} = -\frac{\varepsilon_2}{\varepsilon_3} = \frac{E_1}{E_2}\nu_{21} = \nu_{hv}}$$

(dependent)

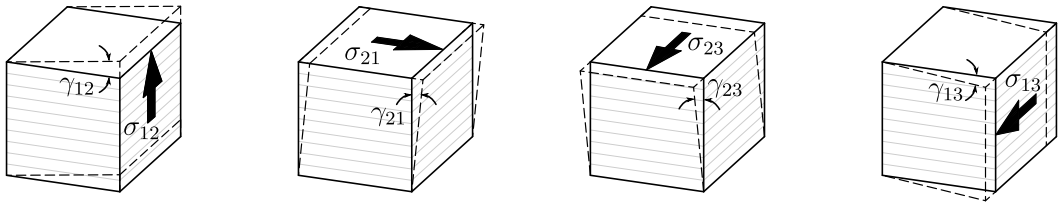

$$G_{12} = \frac{\sigma_{12}}{\gamma_{12}} = G_{hv} \qquad G_{23} = \frac{\sigma_{23}}{\gamma_{23}} = G_{21} = \frac{\sigma_{21}}{\gamma_{21}} = G_{vh}$$

$$\boxed{G_{13} = \frac{\sigma_{13}}{\gamma_{13}} = \frac{E_1}{2(1+\nu_{13})} = G_{hh}}$$

$$G_{vh} = G_{hv}$$

(dependent)

Fig. 4.4: Elastic constants in cross-anisotropic material, five independent parameters: E_v, E_h, G_{vh}, ν_{vh}, ν_{hh}, after [44, 171]

E^*, modified Poisson's ratio ν^* and coefficient of cross-anisotropy $\alpha = \alpha_G$. This method is based on an assumption of the following correlations:

$$E^* = E_v, \qquad \nu^* = \nu_{hh}, \qquad \alpha = \sqrt{\frac{E_h}{E_v}} = \frac{G_{hh}}{G_{vh}} = \frac{\nu_{hh}}{\nu_{vh}}. \tag{4.11}$$

In the regard of, mentioned in Eq. 3.15, anisotropy exponents x_{GE} and $x_{G\nu}$, the relation proposed by Graham and Houlsby gives them the values: $x_{GE} = 0.5$ and $x_{G\nu} = 1.0$. The remaining of cross-anisotropic parameters can be determined as follows:

$$E_h = \alpha^2 E^*, \tag{4.12}$$

$$G_{vh} = \alpha \frac{E^*}{2(1+\nu^*)} \tag{4.13}$$

$$\nu_{vh} = \frac{\nu^*}{\alpha}. \tag{4.14}$$

The five-parameter strain rate-stress rate including cross-anisotropic compliance matrix reduced to Graham-Houlsby three-parameter description is denoted as:

$$\begin{Bmatrix} \dot{\varepsilon}_{11} \\ \dot{\varepsilon}_{22} \\ \dot{\varepsilon}_{33} \\ \dot{\gamma}_{12} \\ \dot{\gamma}_{23} \\ \dot{\gamma}_{31} \end{Bmatrix} = \begin{bmatrix} \frac{1}{\alpha^2 E^*} & \frac{-\nu^*}{\alpha E^*} & \frac{-\nu^*}{\alpha^2 E^*} & 0 & 0 & 0 \\ \frac{-\nu^*}{\alpha E^*} & \frac{1}{E^*} & \frac{-\nu^*}{\alpha E^*} & 0 & 0 & 0 \\ \frac{-\nu^*}{\alpha^2 E^*} & \frac{-\nu^*}{\alpha E^*} & \frac{1}{\alpha^2 E^*} & 0 & 0 & 0 \\ 0 & 0 & 0 & \frac{2(1+\nu^*)}{\alpha E^*} & 0 & 0 \\ 0 & 0 & 0 & 0 & \frac{2(1+\nu^*)}{\alpha E^*} & 0 \\ 0 & 0 & 0 & 0 & 0 & \frac{2(1+\nu^*)}{\alpha^2 E^*} \end{bmatrix} \begin{Bmatrix} \dot{\sigma}_{11} \\ \dot{\sigma}_{22} \\ \dot{\sigma}_{33} \\ \dot{\sigma}_{12} \\ \dot{\sigma}_{23} \\ \dot{\sigma}_{31} \end{Bmatrix}. \tag{4.15}$$

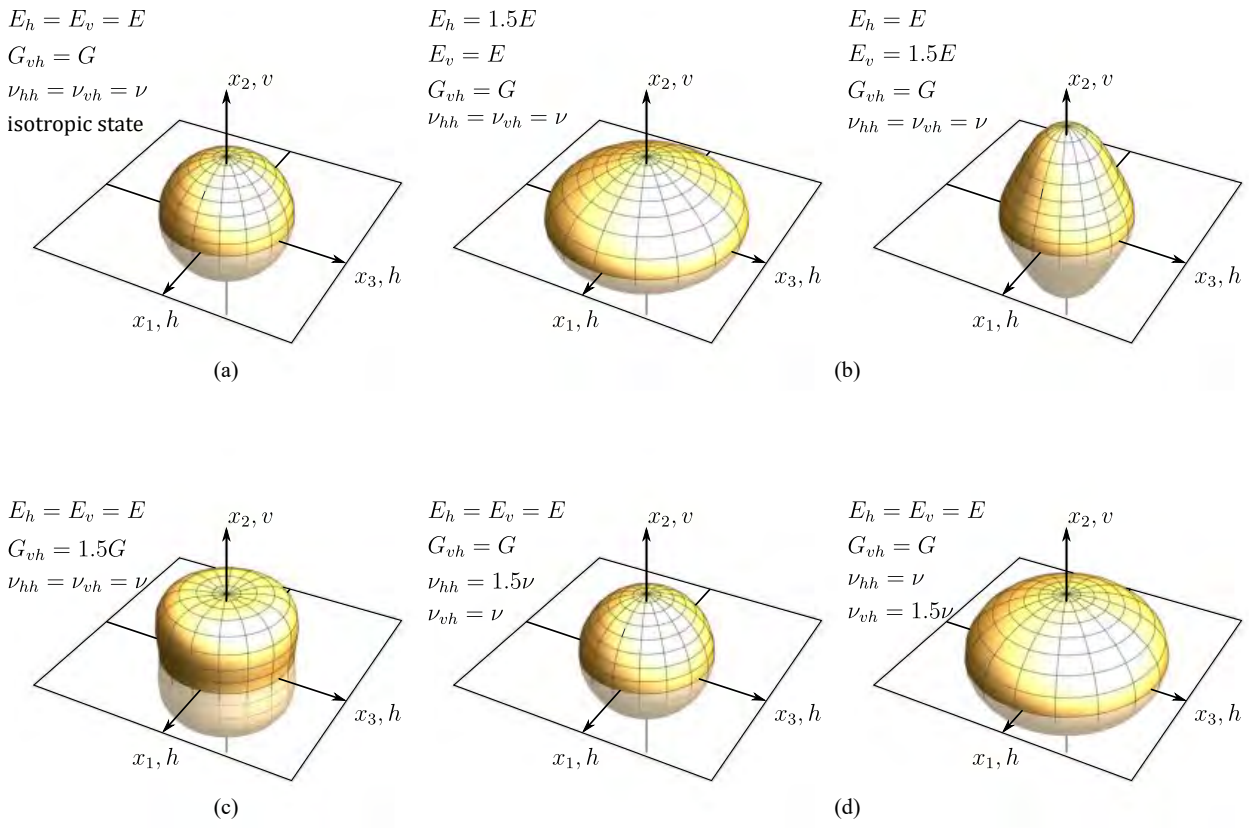

Fig. 4.5: Spherical plots illustrating the influence of the elastic constants in cross-anisotropic material on the dimensional distribution of stiffness: a) isotropic state, b) change of Young's moduli E_h and E_v, c) change of shear modulus G_{vh}, d) change of Poisson's ratio ν_{hh} and ν_{vh}

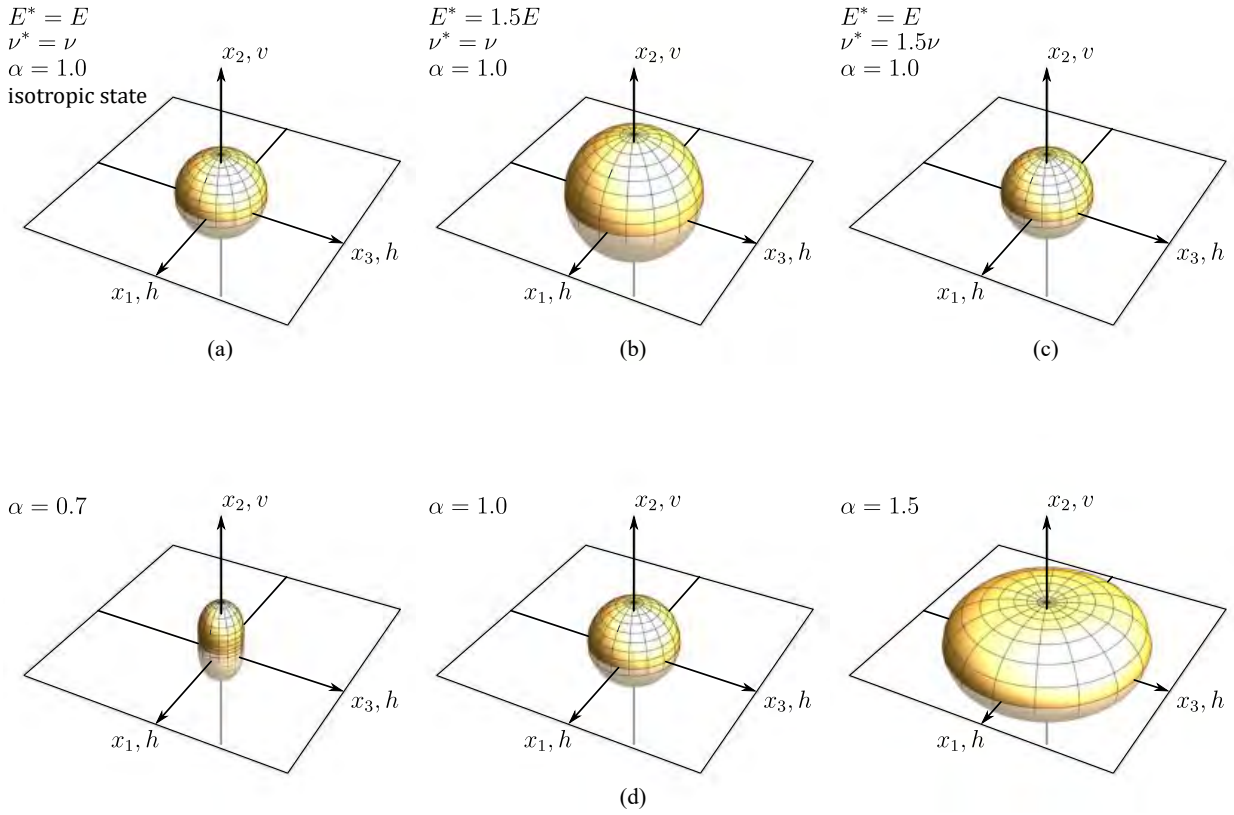

Fig. 4.6: Spherical plots illustrating the influence of the elastic constants in three parameter cross-anisotropic material on the dimensional distribution of stiffness: a) isotropic state, b) change of the modified Young's modulus E^*, c) change of the modified Poisson's ratio ν^*, d) change of the anisotropy coefficient α

It is unwise to treat parameters E^* and ν^* as isotropic, and then implement anisotropy with the use of α coefficient. If the value of α is different than 1.0, only Young's modulus E_v and Poisson's ratio ν_{hh} stay constant. The overall soil stiffness is different, as the values of the remaining cross-anisotropic parameters E_h, G_{vh} and ν_{vh} change in accordance to Eq. (4.12-4.14). This is shown in Fig. 4.6. The sphere, obtained in Fig. 4.6b, is enlarged in a constant manner in every direction, as compared to the isotropic case. Since the anisotropy factor $\alpha = 1.0$, the Graham-Houlsby material model assumes the Hooke's law isotropic stiffness properties. The modified Poisson's ratio ν^* corresponds to ν_{hh}, so again there is no influence of this parameter on the dimensional distribution function ϱ^{-1C}. In Fig. 4.6d the impact of the anisotropy coefficient is shown, for the cases of $\alpha = 0.7$, $\alpha = 1.0$ and $\alpha = 1.5$. The stiffness distribution in vertical direction remains the same for each example, however stiffness changes

notably in horizonal direction. If $\alpha < 1.0$, then $E_v > E_h$, hence the volume of the sphere decreases along the plane of isotropy. The situation is reversed when $\alpha > 1.0$.

4.1.2 Nonlinear models

Models described in Chapter 2 are sensitive to stress changes but are isotropic in their nature. The most straightforward way of obtaining a model that is both nonlinear and anisotropic would be the implementation of inherent anisotropy into a nonlinear isotropic formulation.

A microstructure of a cross-anisotropic material can be defined by the second-order tensor $\mathbf{M}$, obtained from the dyadic product [24]:

$$\mathbf{M} = \mathbf{v} \otimes \mathbf{v} \qquad \text{or} \qquad M_{ij} = v_i \otimes v_j. \tag{4.16}$$

A plane of isotropy is defined with the use of the unit vector $\mathbf{v}$. This vector determines the symmetry axis of a cross-anisotropic material.

The general approach that introduces microstructure tensor into a nonlinear formulation was proposed in [23, 24]. It operates based on the theory of tensor functions. If a scalar is a function of two symmetric tensors, then it can be described as a function of three different types of scalar invariants. Hence, for any function $f(\boldsymbol{\sigma}, \mathbf{M})$, these are the invariants of stress, microstructure and mixed stress-microstructure, respectively:

$$\operatorname{tr}\boldsymbol{\sigma},\ \operatorname{tr}\boldsymbol{\sigma}^2,\ \operatorname{tr}\boldsymbol{\sigma}^3, \tag{4.17}$$

$$\operatorname{tr}\mathbf{M},\ \operatorname{tr}\mathbf{M}^2,\ \operatorname{tr}\mathbf{M}^3, \tag{4.18}$$

$$\operatorname{tr}(\boldsymbol{\sigma}\cdot\mathbf{M}),\ \operatorname{tr}(\boldsymbol{\sigma}^2\cdot\mathbf{M}),\ \operatorname{tr}(\boldsymbol{\sigma}\cdot\mathbf{M}^2),\ \operatorname{tr}(\boldsymbol{\sigma}^2\cdot\mathbf{M}^2). \tag{4.19}$$

Assuming a cross-anisotropic material, all microstructure invariants (Eq. 4.18) are the same $\mathbf{M} = \mathbf{M}^2 = \mathbf{M}^3$. In order to incorporate the influence of microstructure into this function, joint invariants of stress and microstructure $\operatorname{tr}(\boldsymbol{\sigma}\cdot\mathbf{M})$ and $\operatorname{tr}(\boldsymbol{\sigma}^2\cdot\mathbf{M})$ are sufficient.

A general form of a elastic potential that includes stress and microstructure tensors can be expressed as follows:

$$\overline{W}(\boldsymbol{\sigma}, \mathbf{M}) = \overline{W}([\xi_1 \operatorname{tr}\boldsymbol{\sigma} + \xi_2 \operatorname{tr}(\boldsymbol{\sigma}\cdot\mathbf{M})], [\xi_3 \operatorname{tr}\boldsymbol{\sigma}^2 + \xi_4 \operatorname{tr}(\boldsymbol{\sigma}^2\cdot\mathbf{M})], \operatorname{tr}\boldsymbol{\sigma}^3), \tag{4.20}$$

where ξ_i are scalar multipliers. The symbol $\overline{()}$ denotes functions of mixed stress-microstructure invariants.

In literature one can find various material models capable of simulating anisotropic stiffness, e.g. [4, 16, 55]. A general method showing the implementation of inherent anisotropy into hyperelasticity has been presented in [74] and later validated in [8].

4.1.3 Stiffness scaling

A quite interesting method of introducing inherent cross-anisotropy into arbitrary isotropic model is proposed by Niemunis and Staszewska [121]. In this approach, cross-anisotropic characteristics of soil microstructure is superimposed on isotropic elastic stiffness tensor $\mathbf{D}^{\mathrm{iso}}$ by special scaling method. Stiffness tensor $\mathbf{D}^{\times\mathrm{A}}$ including inherent cross-anisotropic component is obtained from the following operation:

$$\mathbf{D}^{\times\mathrm{A}} = \mathbf{Q}^{\mathrm{T}} : \mathbf{D}^{\mathrm{iso}} : \mathbf{Q}, \tag{4.21}$$

where $\mathbf{Q}$ is anisotropy tensor used to scale isotropic stiffness tensor $\mathbf{D}^{\mathrm{iso}}$. Anisotropy tensor $\mathbf{Q}$ is obtained based on soil sedimentation direction $\mathbf{m} = [0, 0, 1]$ and additional constants which relate to the coefficients of cross-anisotropy. Components of $\mathbf{Q}$ tensor do not depend on strain, stress or isotropic material parameters. Hence, it represents a pure cross-anisotropic characteristics.

Three types of cross-anisotropic scaling of isotropic stiffness tensor are described, denoted as $\times$A1, $\times$A2, $\times$A3. The first is delivering the cross-anisotropic stiffness as in the Graham-Houlsby model [58]. The third is just to show impossibility of obtaining three independent coefficient of cross-anisotropy via proposed scaling. However, the second one ($\times$A2) is interesting and worth of application. The scaling of $\times$A2 is proposed with two anisotropy constants $\alpha = \alpha_G$ and β:

$$\alpha = \alpha_G = \alpha_E^{\frac{\beta}{2}} = \alpha_\nu^{\beta}, \tag{4.22}$$

meaning the β parameter is referred to anisotropic exponents [108] as follows:

$$x_{GE} = \frac{\beta}{2} \quad \text{and} \quad x_{G\nu} = \beta. \tag{4.23}$$

If $\beta = 1.0$, then the obtained expression reduces to $\times$A1 scaling corresponding to Graham-Houlsby model [58].

The $\times$A2 anisotropy tensor $\mathbf{Q}$ is defined as:

$$Q_{ijkl} = \mu_{ik}\mu_{jl} + cI_{ijlk} \quad \text{and} \quad \mu_{ij} = a\delta_{ij} + bM_{ij}. \tag{4.24}$$

The functions a, b, c depend on the cross-anisotropic parameters α_G and β, while the microstructure tensor M_{ij} is obtained from the dyadic product (see Eq. 4.16). Consequently, the anisotropy tensor $\mathbf{Q}$ can be expressed as a function $\mathbf{Q}(\alpha_G, \beta, \mathbf{M})$. The value of parameter β have been estimated, taking into account recent literature evidence [108]. In particular, for stiff clays, parameter β tends to remain constant, with $x_{GE} \approx 0.8$ leading to $\beta \approx 1.6$.

The main advantage of the stiffness scaling method is that the pure cross-anisotropy in a form of ×A2 can be applied to any stiffness or compliance matrix without violating thermodynamic laws. Hence, it is easy to implement it into any existing constitutive models. For example, the Hardening Soil model, refined with the Brick-type stiffness degradation (*HSBrick*), has been further extended to account for stiffness cross-anisotropy. A detailed parametric analysis and validation of the model are provided in [45].

4.2 Shear strength anisotropy

The classification of the various anisotropic failure criteria was proposed in [50]. The described models were divided into 3 groups: continuous, discontinuous and empirical. In the case of empirical models, the parameters used in basic isotropic criteria, are described as a function of the loading orientation, calibrated in a way that they fit the experimental data. They are not formulated based on any physical or mathematical laws, hence it is not recommended to use them.

For *discontinuous weakness plane* or *critical plane* models, a material is typically assumed as isotropic at the micro scale, however, on macro level discontinuities, that develop in a body, are also analysed. A failure can happen in the rock matrix, due to the generation of a possible failure plane, or along the predetermined joints. As such two distinct criteria for the material and the joints should be used. This approach is used in so-called Jointed-Rock Model that is available in various commercial geotechnical computational programmes.

In the case of continuous models, strength anisotropy can be introduced into a material model through the kinematic hardening. It allows to modify the shape, size and movement of the yield surface, which is sensitive to the change of stress paths, as well as to the rotation of the principal stresses. The examples of such models were developed at MIT for normally consolidated clays and sands [130] and overconsolidated clays [167]. Overall, this type of method could be quite complicated to formulate, as it operates strictly within the stress space and is depended on multiple parameters, which are not easily tested in laboratory environment. In addition, these models do not incorporate the influence of the anisotropic microstructure on strength.

The implementation of inherent anisotropy into a failure criterion may be conducted with the use of mixed invariants method, described in Sec. 4.1.2. The anisotropic failure criterion was proposed by Pietruszczak and Mróz [133, 134]. Here, the microstructure tensor **a** takes the following form:

$$a_{ij} = a_1 m_{ij}^{(1)} + a_2 m_{ij}^{(2)} + a_3 m_{ij}^{(3)}, \tag{4.25}$$

where $m_{ij}^{(\alpha)} = e_i^{(\alpha)} e_j^{(\alpha)}$ are structure-oriented tensors defined at the respective directions $\alpha = 1, 2, 3$. The description of the coordinate system is shown in Fig. 4.7. The loading orientation is determined by a unit vector $\mathbf{l}$, specified with the respect to the principal directions $e^{(\alpha)}$:

$$l_i = \frac{L_i}{\sqrt{L_k L_k}}, \tag{4.26}$$

where $\mathbf{L}$ is a generalised loading vector:

$$L_i = L_1 e_i^{(1)} + L_2 e_i^{(2)} + L_3 e_i^{(3)}. \tag{4.27}$$

The magnitudes of the individual traction moduli are defined as follows:

$$L_1 = \sqrt{\sigma_{11}^2 + \sigma_{12}^2 + \sigma_{13}^2}, \quad L_2 = \sqrt{\sigma_{12}^2 + \sigma_{22}^2 + \sigma_{23}^2}, \quad L_3 = \sqrt{\sigma_{13}^2 + \sigma_{23}^2 + \sigma_{33}^2}. \tag{4.28}$$

The failure criterion for anisotropic materials is formulated as:

$$F(\boldsymbol{\sigma}, \mathbf{a}) = \eta = \eta_0 (1 + \Omega_{ij} l_i l_j). \tag{4.29}$$

The parameter η is a description of the three-dimensional directional distribution of a scalar. In this case η_0 is simply an isotropic value of η. Tensor $\boldsymbol{\Omega}$ defines the deviatoric part of the microstructure tensor $\mathbf{a}$:

$$\Omega_{ij} = \frac{\left(a_{ij} - \frac{1}{3}\delta_{ij} a_{kk}\right)}{\left(\frac{1}{3} a_{kk}\right)}. \tag{4.30}$$

This tensor is symmetric and traceless, meaning $\Omega_{kk} = 0$. Given an isotropic material, the tensor $\boldsymbol{\Omega} = 0$, so $\eta = \eta_0 = \text{const}$. To describe an orthotropic fabric two distinct eigenvalues are needed. However, for the case of cross-anisotropy only one scalar value is enough for the proper material definition. Assuming a horizontal bedding plane distribution (x_2 is vertical, $x_1 = x_3$ are horizontal), the tensor $\boldsymbol{\Omega}$ takes the following form:

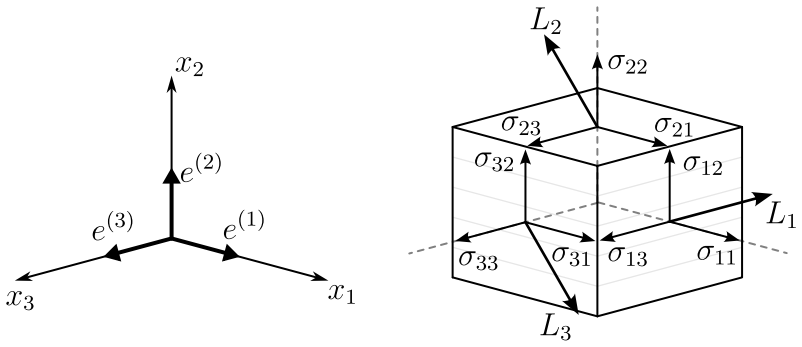

Fig. 4.7: Definition of principal axes and loading direction components, after [134, 95]

$$\Omega_{ij} = \begin{bmatrix} \frac{-\Omega_v}{2} & 0 & 0 \\ 0 & \Omega_v & 0 \\ 0 & 0 & \frac{-\Omega_v}{2} \end{bmatrix}. \tag{4.31}$$

For such material the strength in the plane of isotropy is constant, hence $\Omega_1 = \Omega_3$. Since $\Omega_1 + \Omega_2 + \Omega_3 = 0$ and $l_1^2 + l_2^2 + l_3^2 = 1$, the failure criterion for a cross-anisotropic fabric can be written as:

$$\eta = \eta_0 \left[1 + \frac{\Omega_v}{2}(1 - 3l_2^2)\right]. \tag{4.32}$$

In Fig. 4.8 the spherical plots of the directional distribution of a cross-anisotropic material and the influence of Ω_v are shown. As previously mentioned, if the value of $\Omega_v = 0$, then the soil response is isotropic. However, as Ω_v increases, the anisotropic properties of the yield surface get more prominent.

The undeniable advantage of this model is the fact that the directional distribution function can be implemented in any model and individual parameters can be made direction-dependent. For example, the influence of cross-anisotropic fabric on strength was introduced to the isotropic Lade criterion [94, 95]:

$$f = \left(\frac{I_1^3}{I_3} - 27\right)\left(\frac{I_1}{p_\mathrm{a}}\right)^m = \eta_0 \left[1 + \Omega_1(1 - 3l_2^2)\right], \tag{4.33}$$

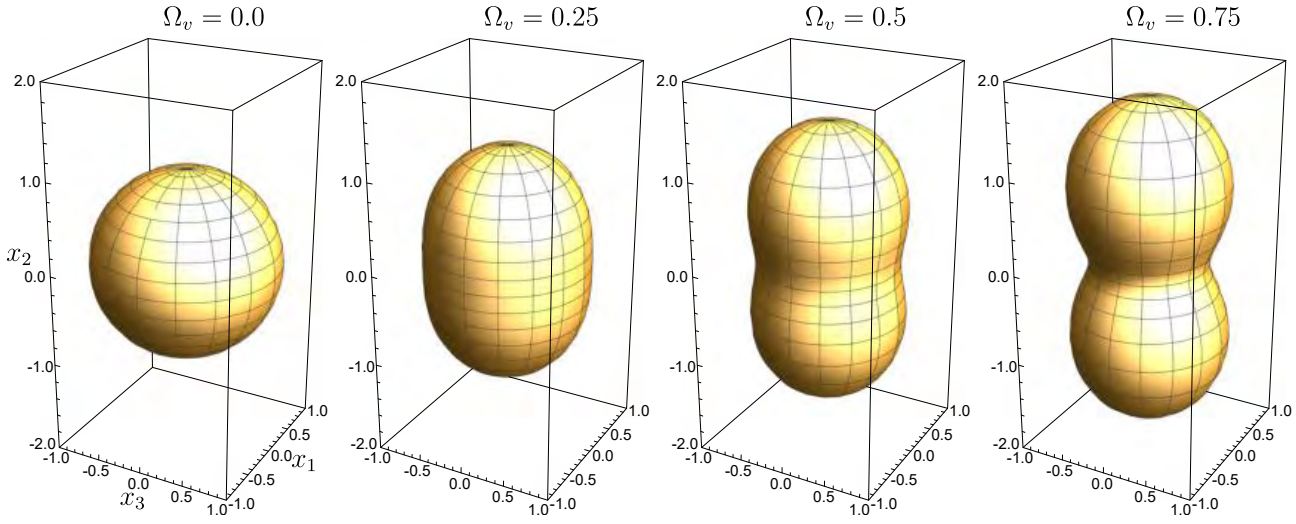

Fig. 4.8: Spherical plots illustrating the distribution of cross-anisotropic material. The shape of the spheres is depended on the value of Ω_v. The bigger the value of Ω_v the larger the spacial variation form the isotropic state that is attained when $\Omega_v = 0$

where I_1 I_3 are the stress tensor invariants, p_a denotes an atmospheric pressure expressed with the same unit as the tensor invariant I_1 and exponent m depends on the type and the density of a given soil.

Additionally, this approach can incorporated into a multi-laminate framework. In [135] the tangent of the internal friction angle $m = \tan\phi$ and effective cohesion c of Mohr-Coulomb failure criterion were assumed anisotropic:

$$F(\boldsymbol{\sigma}) = \tau - m\sigma - c = 0, \quad \text{where} \quad m = m_0(1 + \Omega^m_{ij} l_i l_j) \quad \text{and} \quad c = c_0(1 + \Omega^c_{ij} l_i l_j). \tag{4.34}$$

The scaling method, described in Sec. 4.1.3, can also be implemented into any isotropic yield criterion $F(\boldsymbol{\sigma}) \leq 0$, by incorporating scaling tensor $\mathbf{Q}$ into stress in a following way:

$$F(\boldsymbol{\sigma})^{\times A} = F(\mathbf{Q}\boldsymbol{\sigma}). \tag{4.35}$$

Fig. 4.9 illustrates the application of this method to the Matsuoka-Nakai yield surface [106], defined in Eq. 5.72. Scaling is performed according to approach $\times A1$, where:

$$Q_{ijkl} = \mu_{ik}\mu_{jl}, \quad \text{and} \quad \mu_{ij} = \sqrt{\alpha}\delta_{ij} + (1 - \sqrt{\alpha})M_{ij}. \tag{4.36}$$

Parameter α is defined in Eq. 4.22, based on the Graham-Houlsby model [58].

The isotropic surface ($\alpha = 1.0$) is compared with two anisotropic cases ($\alpha = 0.8$ and $\alpha = 1.2$). For the anisotropic surfaces, the strength parameters are adjusted in such way that the response

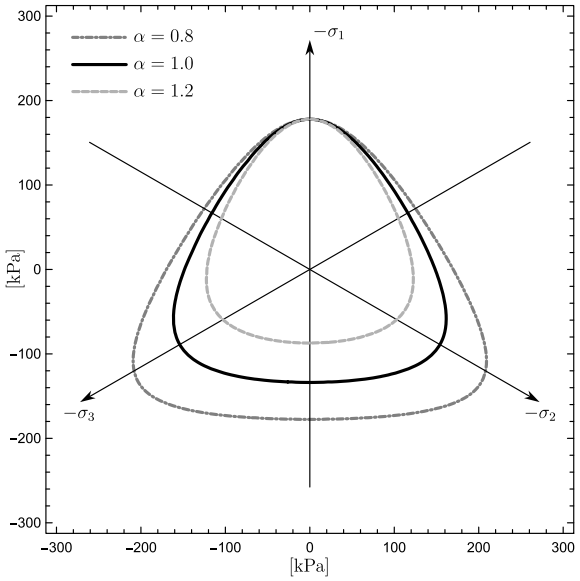

	$\alpha = 1.0$	$\alpha = 0.8$	$\alpha = 1.2$
$\phi^{\times A1}$ [°]	25	31	20
$c^{\times A1}$ [kPa]	10	13	8

Fig. 4.9: The comparison between isotropic Matsuoka-Nakai yield surface [106] and two anisotropic surfaces obtained with $\times A1$ scaling procedure [121]. The strength parameters are adjusted such that the response under triaxial compression remains unchanged. The approximated values of the scaled ϕ and c parameters are provided in the table

under triaxial compression remains unchanged. The corresponding modified values are provided in Fig. 4.9.

Unlike stiffness anisotropy, the strength in horizontal direction gets higher along with the decreasing value of the α parameter.

5

Anisotropic hyperelastic-plastic model for stiff soils

In this section the anisotropic hyperelastic-plastic (*AHEBrick*) constitutive model is described. It was first introduced in [44] and has since been the subject of detailed analysis, refinement, and validation, e.g. [46, 47, 101]. The model accounts for both inherent and stress-induced anisotropy of stiffness, as well as barotropy. It can also properly model stiffness changes due to stress history. Currently, only stiffness anisotropy has been implemented. However, the attempts are made to introduce strength anisotropy with the use of scaling method, presented in [121].

The model description is divided into three sections depending on the strain range. Stiffness anisotropy is introduced within the elastic part. It is then propagated to the intermediate strain range. Here, the procedure of stiffness degradation due to strain is described. Lastly, the applied shear strength criterion is presented. The model is implemented in the commercial FE code [26]. Its application is explained in a form of a simplified algorithm.

5.1 Small-strain range: hyperelastic part

In order to implement inherent cross-anisotropy of microstructure, the symmetry axis normal to the plane of isotropy, defined by unit vector $\mathbf{v}$, needs to be introduced. Its geometric description, based on two spherical coordinates θ and φ, is shown in Fig. 5.1. Depending on the definition of the geometrical axes x_i, the Cartesian coordinates of $\mathbf{v}$ are:

$$\mathbf{v} = [\sin\theta \sin\varphi, \cos\theta, \sin\theta \cos\varphi]^T, \tag{5.1}$$

$$\mathbf{v} = [\sin\theta \cos\varphi, \sin\theta \sin\varphi, \cos\theta]^T. \tag{5.2}$$

In the commercial FE code [26], the vertical axis is defined as x_2 in plane strain and axisymmetric conditions and as x_3 for the three dimensional case. Hence, the definition of second-order microstructure tensors $\mathbf{M}$, which components are calculated from the dyadic product (Eq. 4.16), is as follows:

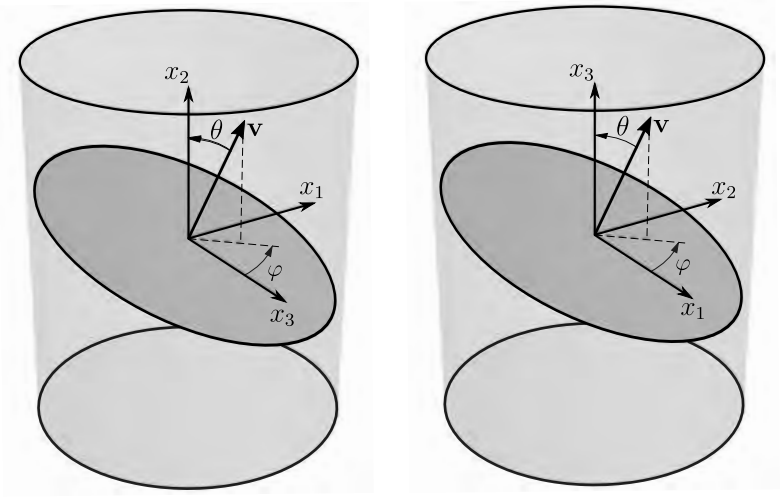

Fig. 5.1: The position of the symmetry axis normal to the plane of isotropy, defined by the unit vector $\mathbf{v}$, depending on the geometric system x_i and spherical coordinates φ, θ

$$\mathbf{M} = \begin{bmatrix} \sin^2\theta\sin^2\varphi & \cos\theta\sin\theta\sin\varphi & \cos\varphi\sin^2\theta\sin\varphi \\ \cos\theta\sin\theta\sin\varphi & \cos^2\theta & \cos\theta\cos\varphi\sin\theta \\ \cos\varphi\sin^2\theta\sin\varphi & \cos\theta\cos\varphi\sin\theta & \cos^2\varphi\sin^2\theta \end{bmatrix}, \tag{5.3}$$

$$\mathbf{M} = \begin{bmatrix} \cos^2\varphi\sin^2\theta & \cos\varphi\sin^2\theta\sin\varphi & \cos\theta\cos\varphi\sin\theta \\ \cos\varphi\sin^2\theta\sin\varphi & \sin^2\theta\sin^2\varphi & \cos\theta\sin\theta\sin\varphi \\ \cos\theta\cos\varphi\sin\theta & \cos\theta\sin\theta\sin\varphi & \cos^2\theta \end{bmatrix}, \tag{5.4}$$

where the respective unit vectors $\mathbf{v}$ are presented in Eqs. 5.1-5.2.

If the plane of isotropy is horizontally oriented, the unit vector $\mathbf{v}$ is in vertical direction ($\theta = 0°$), which leads to:

$$\mathbf{v} = [0,1,0]^T,\ \mathbf{v} = [0,0,1]^T, \tag{5.5}$$

and corresponding microstructure tensors $\mathbf{M}$:

$$\mathbf{M} = \begin{bmatrix} 0 & 0 & 0 \\ 0 & 1 & 0 \\ 0 & 0 & 0 \end{bmatrix},\ \mathbf{M} = \begin{bmatrix} 0 & 0 & 0 \\ 0 & 0 & 0 \\ 0 & 0 & 1 \end{bmatrix}. \tag{5.6}$$

The base for the anisotropic hyperelastic kernel is the isotropic model proposed by Vermeer [163], see Eq. 2.14. It is a function of one stress invariant Q. As described in Sec. 4.2, in

order to incorporate inherent anisotropy into hyperelastic potential, joint invariant of stress and microstructure can be used [23, 24]:

$$Q_{\mathrm{M}}(\boldsymbol{\sigma}, \mathbf{M}) = \frac{1}{2}\mathrm{tr}\,(\boldsymbol{\sigma}^2 \cdot \mathbf{M}) = \frac{1}{2} M_{ab}\sigma_{bc}\sigma_{ca}. \tag{5.7}$$

Hence, analogously to Eq. 4.20, mixed invariant $\overline{Q}$ is obtained based on Q and Q_{M}:

$$\overline{Q}(\boldsymbol{\sigma}, \mathbf{M}) = c_1 Q + c_2 Q_{\mathrm{M}} = \frac{1}{2}\overbrace{(c_1\delta_{ij} + c_2 M_{ab})}^{m_{ab}}\sigma_{bc}\sigma_{ca} = \frac{1}{2} m_{ab}\sigma_{bc}\sigma_{ca}. \tag{5.8}$$

Parameters c_1 and c_2 are the new material constants. Their influence is described in depth later in this chapter.

To acquire the modified hyperelastic potential, that is able to simulate both stress-induced and inherent anisotropy, the stress invariant Q is simply replaced by the mixed expression $\overline{Q}$:

$$\overline{W}(\boldsymbol{\sigma}, \mathbf{M}) = \frac{3 p_{\mathrm{ref}}^{1-\beta}}{2\, G_0^{\mathrm{ref}}(1+\beta)} \left(\frac{2}{3}\overline{Q}(\boldsymbol{\sigma}, \mathbf{M})\right)^{\frac{1+\beta}{2}}. \tag{5.9}$$

By calculating the patrial derivative of the mixed stress-microstructure invariant $\overline{Q}$:

$$\frac{\partial \overline{Q}(\boldsymbol{\sigma}, \mathbf{M})}{\partial \sigma_{ij}} = \frac{1}{2}(\sigma_{aj} m_{ai} + \sigma_{bi} m_{bj}), \tag{5.10}$$

secant stress-strain relation is obtained:

$$\varepsilon_{ij}^{\mathrm{e}} = \frac{\partial \overline{W}(\boldsymbol{\sigma}, \mathbf{M})}{\partial \sigma_{ij}} = \frac{1}{4\overline{G}_0}(\sigma_{aj} m_{ai} + \sigma_{bi} m_{bj}), \tag{5.11}$$

where

$$\overline{G}_0 = G_0^{\mathrm{ref}} \left(\frac{\sqrt{\frac{2}{3}\overline{Q}(\boldsymbol{\sigma}, \mathbf{M})}}{p_{\mathrm{ref}}}\right)^{1-\beta}. \tag{5.12}$$

Finally, the second stress derivative of the modified hyperelastic potential $\overline{W}(\boldsymbol{\sigma}, \mathbf{M})$ gives the following tangent compliance tensor $\mathbf{C}^{\mathrm{t}}$:

$$C_{ijkl}^{\mathrm{t}} = \frac{\partial^2 \overline{W}(\boldsymbol{\sigma}, \mathbf{M})}{\partial \sigma_{ij} \partial \sigma_{kl}} = \frac{1}{4\,\overline{G}_0} A_{ijkl}, \tag{5.13}$$

for which

$$A_{ijkl} = (\delta_{jl} m_{ki} + \delta_{il} m_{jk})^{\mathrm{symm}} - (1-\beta)\frac{(\sigma_{al} m_{ak} + \sigma_{bk} m_{bl})(\sigma_{aj} m_{ai} + \sigma_{bi} m_{bj})}{4\overline{Q}} \tag{5.14}$$

and

$$(m_{ki}\delta_{jl} + m_{jk}\delta_{il})^{\text{symm}} = \frac{1}{2}(m_{ki}\delta_{jl} + m_{li}\delta_{jk} + m_{jk}\delta_{il} + m_{lj}\delta_{ik}). \tag{5.15}$$

For the detailed description of all operations conducted in order to calculate tangent compliance matrix from the hyperelastic potential, see Appendix A.1.

In numerical implementation tangent stiffness matrix $\mathbf{D}^{\text{t}}$ is needed. Hence, the tangent stiffness matrix is obtained by analytical or numerical inversion of the tangent compliance $\mathbf{C}^{\text{t}}$, transformed from 4-th order tensor to the Voigt notation [117].

The basic set of the model input stiffness parameters are: G_0^{ref}, c_1, c_2, β and p_{ref}. The level of the barotropy and stress-induced anisotropy of soil is controlled by the constant c_1. The influence of the c_1 parameter on the stress-stiffness relation is conduced as a proportional stiffness scaling. It has been tested that the impact of c_1 on the stiffness directional dependency is negligible and its magnitude is mostly dependent on the parameter c_2. It is shown in Fig. 5.2 as an elastic distribution of the potential $\overline{W}(\boldsymbol{\sigma}, \mathbf{M})$. In order to test the pure influence of c_1 on stiffness, the condition $c_2 = 0$ is assumed. Isolines represent the same value of the potential $\overline{W}(\boldsymbol{\sigma}, \mathbf{M})$ and are strictly related to the stiffness directional distribution. If the isolines form circles and the stress distances between the subsequent isolines are the same in every direction, then the material is isotropic. As it can be noticed, the change of c_1 value is responsible for the intensity of barotropy but does not induce any anisotropic response in a soil. Hence, due to the simplicity, the constant value $c_1 = 1.0$ has been established, so it has no influence on the stiffness anisotropy.

The parameter c_2 is responsible for the introduction of the stiffness inherent cross-anisotropy. Given $c_1 = 1.0$, if $c_2 > 0$, then the stiffness distribution is higher in the direction defined by the

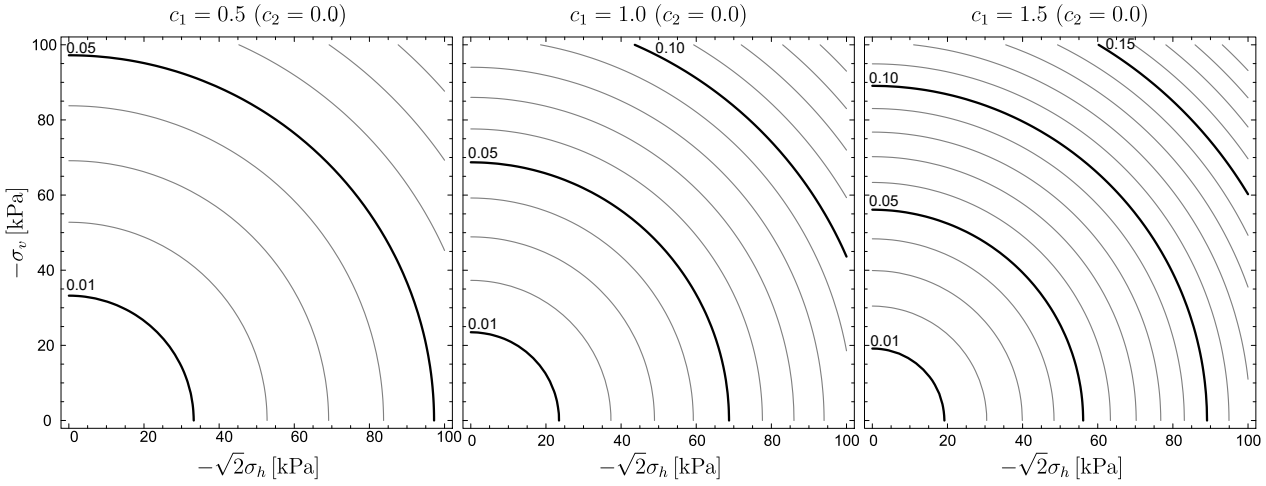

Fig. 5.2: Isolines of the constant values of the potential function $\overline{W}(\boldsymbol{\sigma}, \mathbf{M})$ in the triaxial plane related to c_1 parameter. Negligible influence on stiffness anisotropy has been noted

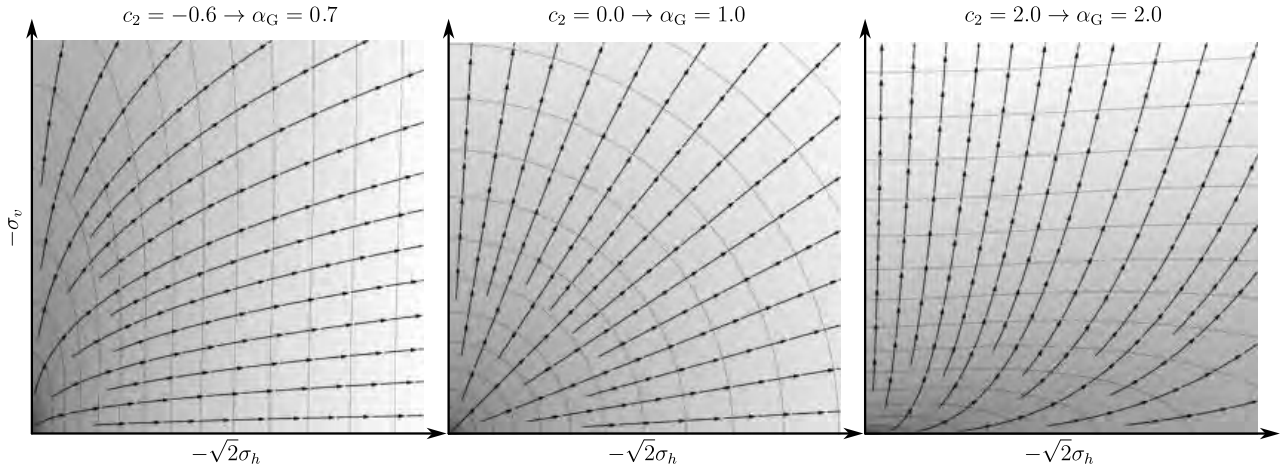

Fig. 5.3: Elastic strain distribution of Eq. 5.11 in triaxial stress plane. The influence of c_2 is manifested as the stress distance of the $||\partial\overline{W}/\partial\boldsymbol{\sigma}||$ isolines along the vector streams directions $[\partial\overline{W}/\partial\sigma_h, \partial\overline{W}/\partial\sigma_v]^T$

plane of isotropy and corresponds to the anisotropy coefficients in a following way: $\alpha_G, \alpha_E > 1.0$. In case of the negative value of c_2, the condition $\alpha_G, \alpha_E < 1.0$ is true. However, if $c_2 = 0$, then the component of inherent anisotropy deactivates and the hyperelastic potential is regained in its isotropic form in Eq. 2.14.

The influence of the parameter c_2 on the elastic strain distribution, defined in Eq. 5.11, is presented in Fig. 5.3. Three different values of c_2, corresponding to the conditions $\alpha_G < 1.0$, $\alpha_G = 1.0$ and $\alpha_G > 1.0$, are considered. For all cases, $c_1 = 1.0$ and the reference shear modulus G_{vh}^{ref} is kept constant. The distances between $||\partial\overline{W}/\partial\boldsymbol{\sigma}||$ isolines correspond to the directional stiffness. At the isotropic case, the isolines form uniform response. However, if the condition $c_2 \neq 1.0$ is considered, the span between the constant $||\partial\overline{W}/\partial\boldsymbol{\sigma}||$ values can be higher along the vertical ($c_2 < 1.0$) or horizontal ($c_2 > 1.0$) axis.

The parameter β controls the order of stiffness-stress dependency. It can be related to the power law (Eq. 2.4) exponent m in a way that $m = 1 - \beta$. At the same time this constant is strictly dependent on the isotropic Poisson's ratio (see Eq. 2.15).

Due to the direct coupling between m and ν paramters, the application of the described model is limited. Based on the Eq. 2.17, to avoid the infinite stiffness value, the following condition $\beta \neq 0$ must be satisfied. However, if $\beta \neq 0$, then $m \neq 1.0$, meaning it is impossible to introduce the linear relation between stress and stiffness, which is apparent in normally consolidated clays. As such, the model is applicable for fine-grained overconsolidated clays and granular soils, for which m is reported to be in the range of $0.3 - 0.7$ [19].

In Fig. 5.4 the relation between the parameter β, the power law exponent m and Poisson's ratio ν is shown. For the marked range of analysed β and m constants, the limit values of

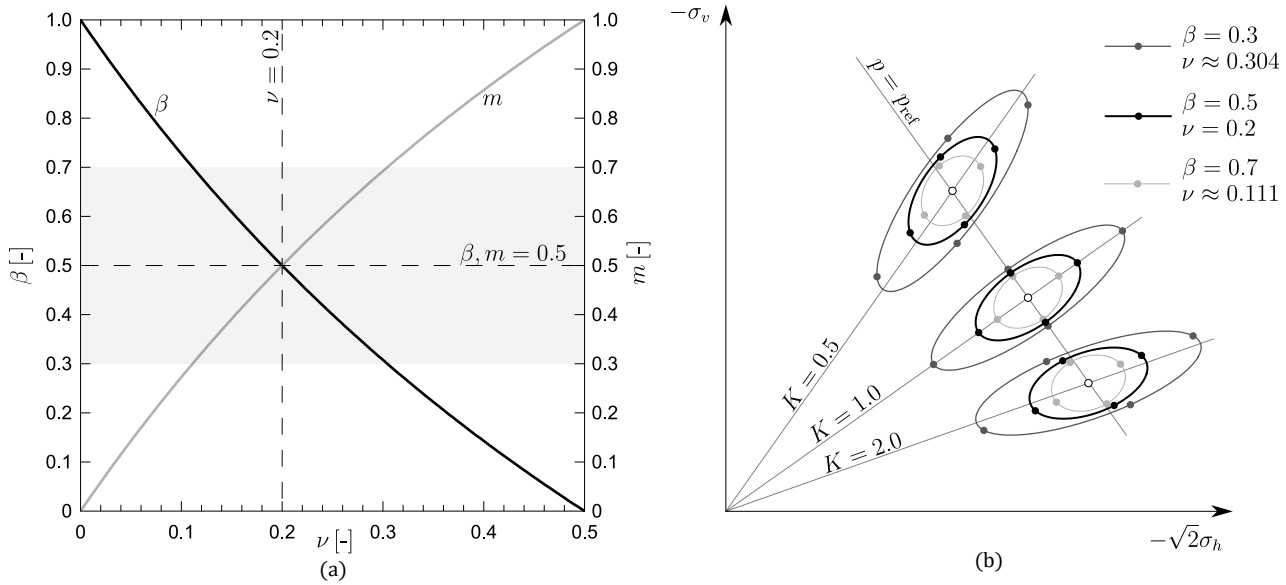

Fig. 5.4: The coupling between parameter β, the stress-stiffness dependency parameter m and isotropic Hooke's law Poisson's ratio ν: (a) the direct relationship between β and m, (b) the response envelopes of the isotropic Vermeer's model [163] for $\beta = 0.3$, 0.5, 0.7 and $K = 0.5$, 1.0, 2.0

Poisson's ratio are $\nu = 0.11$ and $\nu = 0.3$. Considering the relation $\beta = m = 0.5$, the obtained Poisson's ratio is then $\nu = 0.2$. The response envelopes presented in Fig. 5.4b correspond to the aforementioned values of the β parameter. The elongation of the obtained ellipses along the $K = \text{const}$ path strictly depends on β. It shows that this constant can also influence the distribution of stiffness in a stress space.

The initial soil stiffness is determined with the reference shear modulus G_0^{ref}. However, this is an isotropic parameter. Given the material that is anisotropic in its nature, the proper estimation of G_0^{ref} is very difficult. Hence, it would be most optimal to refer the aforementioned set of elastic constants to the parameters that can be tested in laboratory, e.g. the basic cross-anisotropic stiffness moduli: G_{vh}, G_{hh}, E_v, E_h and Poisson's ratios: ν_{vh}, ν_{hh}.

5.1.1 Inherent anisotropy at isotropic stress state

The value of G_0^{ref} is equal to G_{vh}^{ref} only if the considered material is isotropic ($\alpha_G = 1.0$). Otherwise, the proper relation between model constants and stiffness parameters can be obtained from the study of stress and strain increments related to the compliance tensor from Eq. 5.13:

$$\Delta\boldsymbol{\varepsilon}^{\text{e}} = \mathbf{C}^{\text{t}}(\boldsymbol{\sigma}^0, \mathbf{M}) : \Delta\boldsymbol{\sigma}. \tag{5.16}$$

Given the inherent inverse isotropy, the tests can only be conducted under isotropic stress conditions. Additionally, in this analysis axis x_2 is considered vertical, so:

$$\boldsymbol{\sigma}^0 = \begin{bmatrix} -p_0 & 0 & 0 \\ 0 & -p_0 & 0 \\ 0 & 0 & -p_0 \end{bmatrix} \quad \text{and} \quad \mathbf{M} = \begin{bmatrix} 0 & 0 & 0 \\ 0 & 1 & 0 \\ 0 & 0 & 0 \end{bmatrix}. \tag{5.17}$$

To calculate shear moduli G_{vh}, G_{hh}, the respective stress increment are needed:

$$\Delta\boldsymbol{\sigma} = \begin{bmatrix} 0 & \Delta\sigma_{vh} & 0 \\ \Delta\sigma_{vh} & 0 & 0 \\ 0 & 0 & 0 \end{bmatrix}, \quad \Delta\boldsymbol{\sigma} = \begin{bmatrix} 0 & 0 & \Delta\sigma_{hh} \\ 0 & 0 & 0 \\ \Delta\sigma_{hh} & 0 & 0 \end{bmatrix}, \tag{5.18}$$

whereas in terms of Young's moduli E_v, E_h the following states are considered:

$$\Delta\boldsymbol{\sigma} = \begin{bmatrix} 0 & 0 & 0 \\ 0 & \Delta\sigma_v & 0 \\ 0 & 0 & 0 \end{bmatrix}, \quad \Delta\boldsymbol{\sigma} = \begin{bmatrix} \Delta\sigma_h & 0 & 0 \\ 0 & 0 & 0 \\ 0 & 0 & 0 \end{bmatrix}. \tag{5.19}$$

Based on Eq. 5.16, the cross-anisotropic parameters are obtained:

$$G_{vh} = \frac{\Delta\sigma_{vh}}{2\Delta\varepsilon^{\mathrm{e}}_{12}} = G_0^{\mathrm{ref}} \frac{\left(\frac{p_0}{p_{\mathrm{ref}}}\sqrt{c_1 + \frac{1}{3}c_2}\right)^{1-\beta}}{c_1 + \frac{1}{2}c_2}, \tag{5.20}$$

$$G_{hh} = \frac{\Delta\sigma_{hh}}{2\Delta\varepsilon^{\mathrm{e}}_{13}} = G_0^{\mathrm{ref}} \frac{\left(\frac{p_0}{p_{\mathrm{ref}}}\sqrt{c_1 + \frac{1}{3}c_2}\right)^{1-\beta}}{c_1}, \tag{5.21}$$

$$E_v = \frac{\Delta\sigma_v}{\Delta\varepsilon^{\mathrm{e}}_{22}} = 2G_0^{\mathrm{ref}} \frac{(3c_1 + c_2)\left(\frac{p_0}{p_{\mathrm{ref}}}\sqrt{c_1 + \frac{1}{3}c_2}\right)^{1-\beta}}{(c_1 + c_2)[c_2\beta + c_1(2+\beta)]}, \tag{5.22}$$

$$E_h = \frac{\Delta\sigma_h}{\Delta\varepsilon^{\mathrm{e}}_{11}} = 2G_0^{\mathrm{ref}} \frac{(3c_1 + c_2)\left(\frac{p_0}{p_{\mathrm{ref}}}\sqrt{c_1 + \frac{1}{3}c_2}\right)^{1-\beta}}{c_1[c_2 + c_1(2+\beta)]}, \tag{5.23}$$

$$\nu_{vh} = \frac{-\Delta\varepsilon^{\mathrm{e}}_{11}}{\Delta\varepsilon^{\mathrm{e}}_{22}} = \frac{c_1(1-\beta)}{c_2\beta + c_1(2+\beta)}, \tag{5.24}$$

$$\nu_{hh} = \frac{-\Delta\varepsilon^{\mathrm{e}}_{33}}{\Delta\varepsilon^{\mathrm{e}}_{11}} = \frac{c_1(1-\beta)}{c_2 + c_1(2+\beta)}. \tag{5.25}$$

Next, the values of anisotropic coefficients α_G, α_E, α_ν can be derived:

$$\alpha_E = \frac{E_h}{E_v} = \frac{(c_1 + c_2)[c_2\beta + c_1(2+\beta)]}{c_1[c_2 + c_1(2+\beta)]}, \tag{5.26}$$

$$\alpha_G = \frac{G_{hh}}{G_{vh}} = 1 + \frac{c_2}{2c_1}, \tag{5.27}$$

$$\alpha_\nu = \frac{\nu_{hh}}{\nu_{vh}} = \frac{c_2\beta + c_1(2+\beta)}{c_2 + c_1(2+\beta)}. \tag{5.28}$$

The coefficient α_G is only influenced by constants c_1 and c_2. Since the condition $c_1 = 1.0$ has been adopted, then $c_2 = 2(\alpha_G - 1)$. Following this relation and the assumption that the samples are tested under the isotropic stress state $p_0 = p_{\text{ref}}$, the Eqs. 5.20-5.25 can be written in a simplified form:

$$G_{vh}^{\text{ref}} = G_0^{\text{ref}} \frac{\left(\sqrt{1 + \frac{2}{3}(\alpha_G - 1)}\right)^{1-\beta}}{\alpha_G}, \tag{5.29}$$

$$G_{hh}^{\text{ref}} = G_0^{\text{ref}} \left(\sqrt{1 + \frac{2}{3}(\alpha_G - 1)}\right)^{1-\beta}, \tag{5.30}$$

$$E_v^{\text{ref}} = 2G_0^{\text{ref}} \frac{(1+2\alpha_G)\left(\sqrt{1 + \frac{2}{3}(\alpha_G - 1)}\right)^{1-\beta}}{(2\alpha_G - 1)[(2\alpha_G - 1)\beta + 2]}, \tag{5.31}$$

$$E_h^{\text{ref}} = 2G_0^{\text{ref}} \frac{(1+2\alpha_G)\left(\sqrt{1 + \frac{2}{3}(\alpha_G - 1)}\right)^{1-\beta}}{2\alpha_G + \beta}, \tag{5.32}$$

$$\nu_{vh} = \frac{1-\beta}{(2\alpha_G - 1)\beta + 2}, \tag{5.33}$$

$$\nu_{hh} = \frac{1-\beta}{2\alpha_G + \beta}. \tag{5.34}$$

The values of Poisson's ratios ν_{vh} and ν_{hh} are dependent on both α_G and β, which imposes certain limits on their values, as presented in Fig. 5.5. In the case of ν_{vh}, the maximum value that can be obtained, limited by the thermodynamic laws, is $\nu_{vh} = 0.5$, regardless of the applied α_G coefficient. However, considering the β values for overconsolidated soils, $\beta = 0.3 - 0.7$, the extreme values of ν_{vh} for isotropic material ($\alpha_G = 1.0$) are $\nu_{vh} \approx 0.11$ and $\nu_{vh} \approx 0.3$. Along with the increasing α_G, the possible values of ν_{vh} decrease and, in the case $\alpha_G = 2.0$, are $\nu_{vh} \approx 0.07$ and $\nu_{vh} \approx 0.24$. Conversely, the highest ν_{vh} values are obtained for $\alpha_G = 0.7$, $\nu_{vh} \approx 0.13$, $\nu_{vh} \approx 0.33$. Additionally, as α_G decreases, the relationship between ν_{vh} and β becomes increasingly linear. For isotropic material, the same curve is obtained, $\nu_{hh} = \nu_{vh}$. However, as α_G increases, the maximum possible value of ν_{hh} decreases significantly, in this case $\nu_{hh} = 0.25$. Conversely, for decreasing α_G, the minimum value of β parameter increases, once $\nu_{hh} = 0.5$ is reached. Similar to the Poisson's ratio ν_{vh}, higher values of ν_{hh} are obtained as α_G decreases. In this case, however, those differences are considerably more pronounced. For

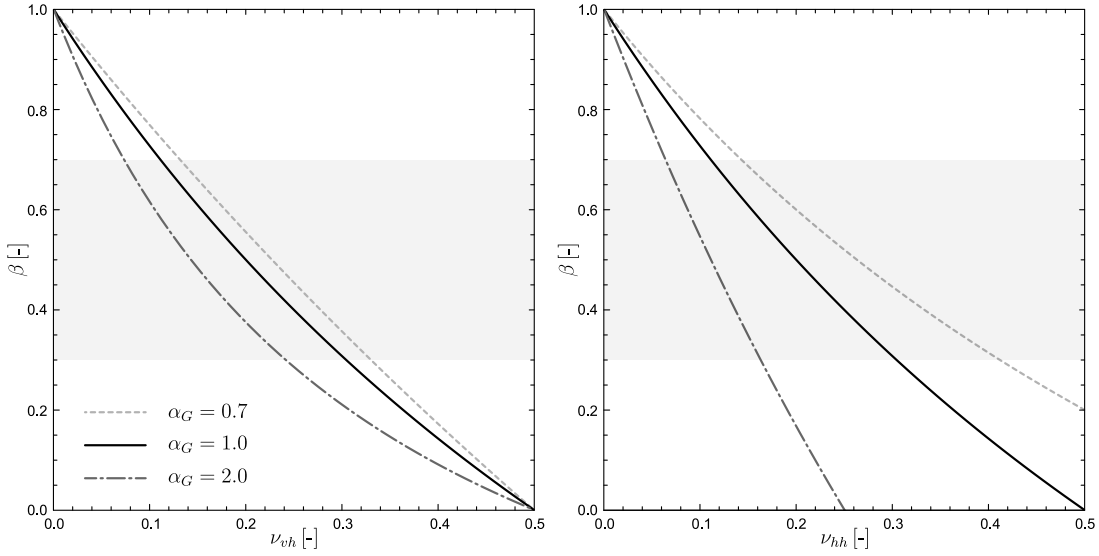

Fig. 5.5: The influence of cross-anisotropy coefficient α_G and β parameter on Poisson's ratios ν_{vh} and ν_{hh}. The values of β reported in overconsolidated stiff soils are marked

overconsolidated soils, the threshold values are $\nu_{vh} \approx 0.06$, $\nu_{vh} \approx 0.16$ when $\alpha_G = 2.0$, and $\nu_{vh} \approx 0.14$, $\nu_{vh} \approx 0.41$ when $\alpha_G = 0.7$.

Based on Eqs. 5.29-5.32 , the reference shear modulus G_0^{ref} can be calculated in the following way:

$$G_0^{\text{ref}}(G_{vh}^{\text{ref}}, \alpha_G, \beta) = G_{vh}^{\text{ref}} \alpha_G \left(\sqrt{\frac{1+2\alpha_G}{3}} \right)^{\beta-1}, \tag{5.35}$$

$$G_0^{\text{ref}}(G_{hh}^{\text{ref}}, \alpha_G, \beta) = G_{hh}^{\text{ref}} \left(\sqrt{\frac{1+2\alpha_G}{3}} \right)^{\beta-1}, \tag{5.36}$$

$$G_0^{\text{ref}}(E_v^{\text{ref}}, \alpha_G, \beta) = E_v^{\text{ref}} \frac{1-2\alpha_G}{1+2\alpha_G} \left(\frac{1-2\alpha_G}{2}\beta - 1 \right) \left(\sqrt{\frac{1+2\alpha_G}{3}} \right)^{\beta-1}, \tag{5.37}$$

$$G_0^{\text{ref}}(E_h^{\text{ref}}, \alpha_G, \beta) = E_h^{\text{ref}} \frac{(2\alpha_G + \beta)\left(\sqrt{\frac{1+2\alpha_G}{3}}\right)^{\beta-1}}{2(1+2\alpha_G)}. \tag{5.38}$$

Considering a soil sample tested in a triaxial apparatus, the cross-anisotropic moduli that are especially feasible to be properly measured are: G_{vh}^{ref} and E_v^{ref}. In this work, shear modulus in vertical direction G_{vh}^{ref} is established as a default. Hence, the alternative set of model stiffness constants are: G_{vh}^{ref}, α_G, β and p_{ref}.

As such, the joint stress-microstructure invariant from Eq. 5.8, can be defined as:

$$\overline{Q}(\boldsymbol{\sigma}, \mathbf{M}) = \frac{1}{2} \overbrace{\left[\delta_{ij} + 2(\alpha_G - 1) M_{ab}\right]}^{m_{ab}} \sigma_{bc}\sigma_{ca} = \frac{1}{2} m_{ab}\sigma_{bc}\sigma_{ca} \tag{5.39}$$

and by substituting G_0^{ref} with the expression in Eq. 5.35, the updated hyperelastic potential is obtained:

$$\overline{W}(\boldsymbol{\sigma}, \mathbf{M}) = \frac{\left(p_{\mathrm{ref}}\sqrt{\frac{1}{2}+\alpha_G}\right)^{1-\beta}}{\alpha_G\, G_{vh}^{\mathrm{ref}}(1+\beta)}\overline{Q}(\boldsymbol{\sigma}, \mathbf{M})^{\frac{1+\beta}{2}}. \tag{5.40}$$

5.1.2 Mixed anisotropy at axisymmetric stress state

It is possible to expand the definitions of inherent cross-anisotropic stiffness parameters to take asisymmetric stress state ($K \neq 1.0$) into consideration. By doing so, the actual influence of the stress conditions on the soil stiffness can be demonstrated. The study of the material response to stress increments shown in Eqs. 5.18 and 5.19 is carried out analogously as in Eq. 5.16, based on the following initial stress state:

$$\boldsymbol{\sigma}^0 = \begin{bmatrix} -\frac{3p_0}{1+2K} & 0 & 0 \\ 0 & -\frac{3Kp_0}{1+2K} & 0 \\ 0 & 0 & -\frac{3Kp_0}{1+2K} \end{bmatrix}. \tag{5.41}$$

The analysis conducted with the standard model parameter set: G_0^{ref}, c_1, c_2, β, K, p_0, p_{ref} returns the following stiffness parameters:

$$G_{vh} = \frac{2G_0^{\mathrm{ref}}}{2c_1+c_2}\left(\frac{\frac{p_0}{p_{\mathrm{ref}}}\sqrt{3(c_1+c_2+2c_1K^2)}}{1+2K}\right)^{1-\beta}, \tag{5.42}$$

$$G_{hh} = \frac{G_0^{\mathrm{ref}}}{c_1}\left(\frac{\frac{p_0}{p_{\mathrm{ref}}}\sqrt{3(c_1+c_2+2c_1K^2)}}{1+2K}\right)^{1-\beta}, \tag{5.43}$$

$$E_v = 2G_0^{\mathrm{ref}}\left(\frac{\frac{p_0}{p_{\mathrm{ref}}}\sqrt{3(c_1+c_2+2c_1K^2)}}{1+2K}\right)^{1-\beta}\frac{c_1+c_2+2c_1K^2}{(c_1+c_2)[2c_1K^2+(c_1+c_2)\beta]}, \tag{5.44}$$

$$E_h = 2G_0^{\mathrm{ref}}\left(\frac{\frac{p_0}{p_{\mathrm{ref}}}\sqrt{3(c_1+c_2+2c_1K^2)}}{1+2K}\right)^{1-\beta}\frac{c_1+c_2+2c_1K^2}{c_1[c_1+c_2+c_1K^2(1+\beta)]}, \tag{5.45}$$

$$\nu_{vh} = \frac{c_1K(1-\beta)}{2c_1K^2+(c_1+c_2)\beta}, \tag{5.46}$$

$$\nu_{hh} = \frac{c_1K^2(\beta-1)}{c_1+c_2+c_1K^2(1+\beta)}. \tag{5.47}$$

The anisotropy coefficients that include stress conditions are defined as follows:

$$\alpha_E = \frac{(c_1+c_2)[2c_1K^2+(c_1+c_2)\beta]}{c_1[c_1+c_2+c_1K^2(1+\beta)]}, \tag{5.48}$$

$$\alpha_\nu = \frac{K[2c_1K^2+(c_1+c_2)\beta]}{c_1+c_2+c_1K^2(1+\beta)}, \tag{5.49}$$

while the value of α_G remains the same as in Eq. 5.27. This shows the model's key characteristic that, under axisymmetric stress circumstances, α_G remains constant and unaffected by the degree of stress obliquity. As such, the conditions $c_1 = 1.0$ and $c_2 = 2(\alpha_G - 1)$ are utilised in the further calculations. The cross-anisotropic stiffness parameters, that are depended on α_G, are defined as:

$$G_{vh} = \frac{G_0^{\text{ref}}}{\alpha_G}\left(\frac{\frac{p_0}{p_{\text{ref}}}\sqrt{6K^2+6\alpha_G-3}}{1+2K}\right)^{1-\beta}, \tag{5.50}$$

$$G_{hh} = G_0^{\text{ref}}\left(\frac{\frac{p_0}{p_{\text{ref}}}\sqrt{6K^2+6\alpha_G-3}}{1+2K}\right)^{1-\beta}, \tag{5.51}$$

$$E_v = 2G_0^{\text{ref}}\left(\frac{\frac{p_0}{p_{\text{ref}}}\sqrt{6K^2+6\alpha_G-3}}{1+2K}\right)^{1-\beta}\frac{2K^2+2\alpha_G-1}{(2\alpha_G-1)[2K^2+(2\alpha_G-1)\beta]}, \tag{5.52}$$

$$E_h = 2G_0^{\text{ref}}\left(\frac{\frac{p_0}{p_{\text{ref}}}\sqrt{6K^2+6\alpha_G-3}}{1+2K}\right)^{1-\beta}\frac{2K^2+2\alpha_G-1}{K^2(1+\beta)+2\alpha_G-1}, \tag{5.53}$$

$$\nu_{vh} = \frac{K(1-\beta)}{2K^2+(2\alpha_G-1)\beta}, \tag{5.54}$$

$$\nu_{hh} = \frac{K^2(\beta-1)}{K^2(1+\beta)+2\alpha_G-1}. \tag{5.55}$$

Given the constants α_G, β, K, p_0, p_{ref}, the reference shear modulus G_0^{ref} can be related to the cross-anisotropic stiffness moduli in a following way:

$$G_0^{\text{ref}}(G_{vh}^{\text{ref}},\alpha_G,\beta,K,p_0,p_{\text{ref}}) = \alpha_G G_{vh}^{\text{ref}}\left(\frac{\frac{p_0}{p_{\text{ref}}}\sqrt{6K^2+6\alpha_G-3}}{1+2K}\right)^{\beta-1}, \tag{5.56}$$

$$G_0^{\text{ref}}(G_{hh}^{\text{ref}},\alpha_G,\beta,K,p_0,p_{\text{ref}}) = G_{hh}^{\text{ref}}\left(\frac{\frac{p_0}{p_{\text{ref}}}\sqrt{6K^2+6\alpha_G-3}}{1+2K}\right)^{\beta-1}, \tag{5.57}$$

$$G_0^{\mathrm{ref}}(E_v^{\mathrm{ref}}, \alpha_G, \beta, K, p_0, p_{\mathrm{ref}}) = \\ = E_v^{\mathrm{ref}} \left(\frac{\frac{p_0}{p_{\mathrm{ref}}}\sqrt{6K^2 + 6\alpha_G - 3}}{1 + 2K} \right)^{\beta - 1} \frac{(2\alpha_G - 1)[2K^2 + (2\alpha_G - 1)\beta]}{2(2K^2 + 2\alpha_G - 1)}, \tag{5.58}$$

$$G_0^{\mathrm{ref}}(E_h^{\mathrm{ref}}, \alpha_G, \beta, K, p_0, p_{\mathrm{ref}}) = \\ = E_h^{\mathrm{ref}} \left(\frac{\frac{p_0}{p_{\mathrm{ref}}}\sqrt{6K^2 + 6\alpha_G - 3}}{1 + 2K} \right)^{\beta - 1} \frac{K^2(1 + \beta) + 2\alpha_G - 1}{2(2K^2 + 2\alpha_G - 1)}. \tag{5.59}$$

In Fig. 5.6 the influence of mixed stiffness anisotropy on the soil response is shown, in a form of orientation distribution function ϱ^{-1C} (Eq. 4.5). The parameters G_{vh}^{ref} and p_0 are kept constant. Their magnitude affects the size of the spheres and here are selected to fulfill the visual purposes only. Three different values of anisotropy coefficient α_G and initial stress condition K_0 are considered. The effect of pure inherent anisotropy is presented for $K_0 = 1.0$, whereas the influence of independent stress-induced anisotropy is shown when $\alpha_G = 1.0$. It should be highlighted, based on this study, that the stiffness distribution of soil appears to be primarily influenced by the anisotropy coefficient α_G.

5.1.3 Anisotropy coefficients

Out of the analysed anisotropy coefficients of stiffness, the α_G parameter is the only constant that is fully independent and its value is not influenced, in any way, by stress. The remaining anisotropy coefficients α_E and α_ν, described in Eqs. 5.26, 5.28, can be defined as functions of parameters α_G and β:

$$\alpha_E(\alpha_G, \beta) = \frac{(2\alpha_G - 1)[(2\alpha_G - 1)\beta + 2]}{2\alpha_G + \beta}, \tag{5.60}$$

$$\alpha_\nu(\alpha_G, \beta) = \frac{(2\alpha_G - 1)\beta + 2}{2\alpha_G + \beta}. \tag{5.61}$$

Following these correlations, the values of the anisotropy exponents x_{GE} and $x_{G\nu}$ are also dependent on α_G and β. In Fig. 5.7, the relations described in Eqs. 5.60 and 5.61, are presented for three different β parameters, that correspond to the values reported for overconsolidated clays. The model response is compared to the anisotropy exponents established in the model proposed by Graham and Houlsby ($x_{GE} = 0.5$, $x_{G\nu} = 1.0$) [58], as well as the value based on the experimental data and suggested by Mašín and Rott ($x_{GE} = 0.8$) [108]. In case when stiffness is greater in the vertical direction ($\alpha_G = 0.7 - 1.0$), the value of coefficient β has very little effect on the obtained relationship $\alpha_G(\alpha_E)$ and the model response especially correlates to

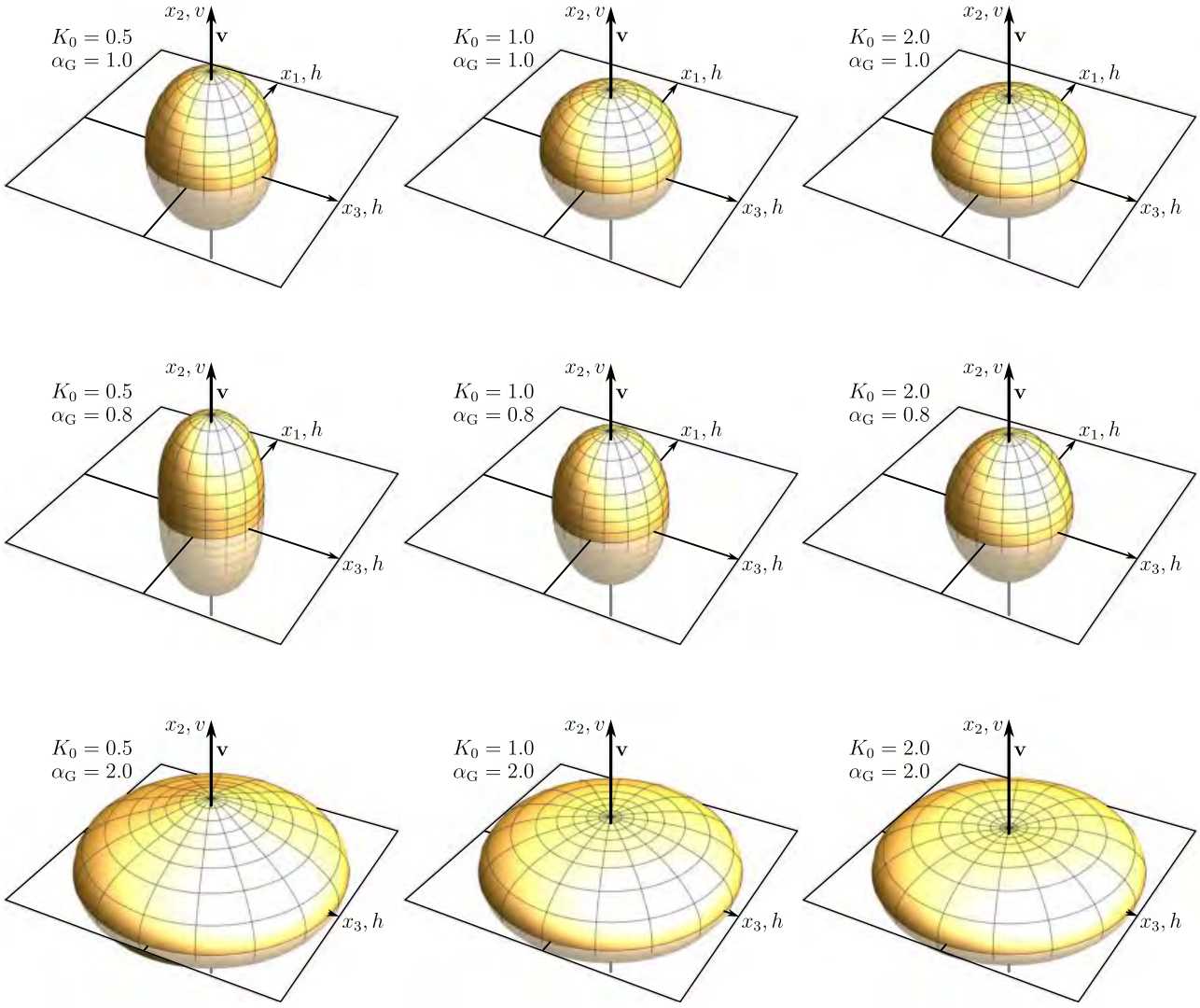

Fig. 5.6: Spherical plots showing the influence of mixed anisotropy on the directional stiffness distribution in regard to different values of $\alpha_G = (0.8, 1.0, 2.0)$ and $K_0 = (0.5, 1.0, 2.0)$

$x_{GE} = 0.5$. However, the typical values of anisotropy coefficient α_G for overconsolidated clays, reported in Tab. 3.1, are within the range of $\alpha_G = 1.1 - 2.5$. The response obtained for $\beta = 0.5$ seems to be the most optimal. In terms of $\alpha_\nu(\alpha_G)$, the calculated results highly deviate from the relation $\alpha_\nu = \alpha_G$. Subsequently, it is impossible to assess whether these functions correlate with laboratory studies due to the extreme data scatter.

The relation between the β parameter and the anisotropy coefficients α_E and α_ν is shown in Fig. 5.8. The changes of α_E and α_ν are determined for three values of $\alpha_G = 0.7, 1.0, 2.0$.

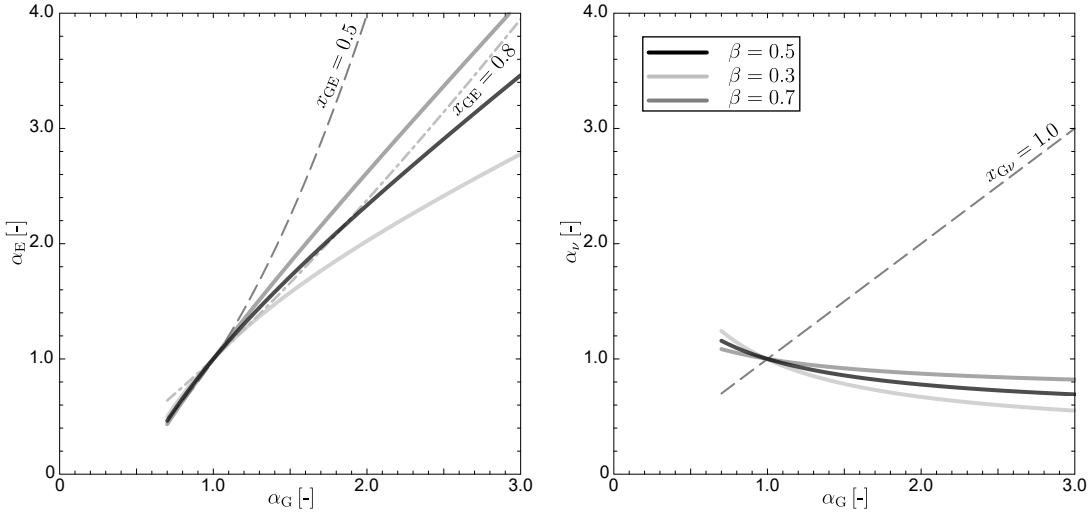

Fig. 5.7: The relations between anisotropy coefficients: $\alpha_E(\alpha_G)$ and $\alpha_\nu(\alpha_G)$. The response obtained from the calculations conducted with the hyperelastic model for $\beta = 0.3, 0.5, 0.7$. The results are compared to anisotropy exponents $x_{GE} = 0.5, 0.8$ and $x_{G\nu} = 1.0$

Since α_G is the independent constant, it is plotted for comparison. If $\alpha_G > 1.0$, then the value of coefficients α_E and α_ν increases with β. The opposite situation is true for $\alpha_G < 1.0$. In addition, when comparing α_G with the other anisotropy coefficients, the following relationships are observed: for $\alpha_G > 1.0$, the cross-anisotropy coefficient α_G is higher than α_ν but its value is lower than α_E. In contrast, when $\alpha_G < 1.0$, the opposite trend is apparent: $\alpha_G < \alpha_\nu$ and $\alpha_G > \alpha_E$. This implies that for $\alpha_G > 1.0$, the value of anisotropy exponents are: $x_{GE} < 1.0$ and $x_{G\nu} > 1.0$, whereas for $\alpha_G < 1.0$, these conditions are reversed: $x_{GE} > 1.0$, $x_{G\nu} < 1.0$. However, the moment the isotropic coefficient $\alpha_G = 1.0$ is introduced, α_E and α_ν are also isotropic and are no longer dependent on β.

Defined in Eqs. 5.48 and 5.49, anisotropic coefficients, that incorporate axisymmetric stress state, can be rewritten so they depend on three parameters: α_G, β and K:

$$\alpha_E(\alpha_G, \beta, K) = \frac{(2\alpha_G - 1)[2K^2 + (2\alpha_G - 1)\beta]}{2\alpha_G + K^2(1+\beta) - 1}, \tag{5.62}$$

$$\alpha_\nu(\alpha_G, \beta, K) = \frac{2K^3 + K(2\alpha_G - 1)\beta}{K^2(1+\beta) + 2\alpha_G - 1}. \tag{5.63}$$

In Fig. 5.9, the changes in the mixed anisotropy at axisymmetric stress states, based on the stress condition K and α_G ratio, are demonstrated using the broader definitions of anisotropy coefficients provided in Eqs. 5.62 and 5.63. The examples are considered for $\beta = 0.5$ and three values of α_G. Given the isotropic stress state ($K = 1.0$), the parameters α_E and α_ν exhibit

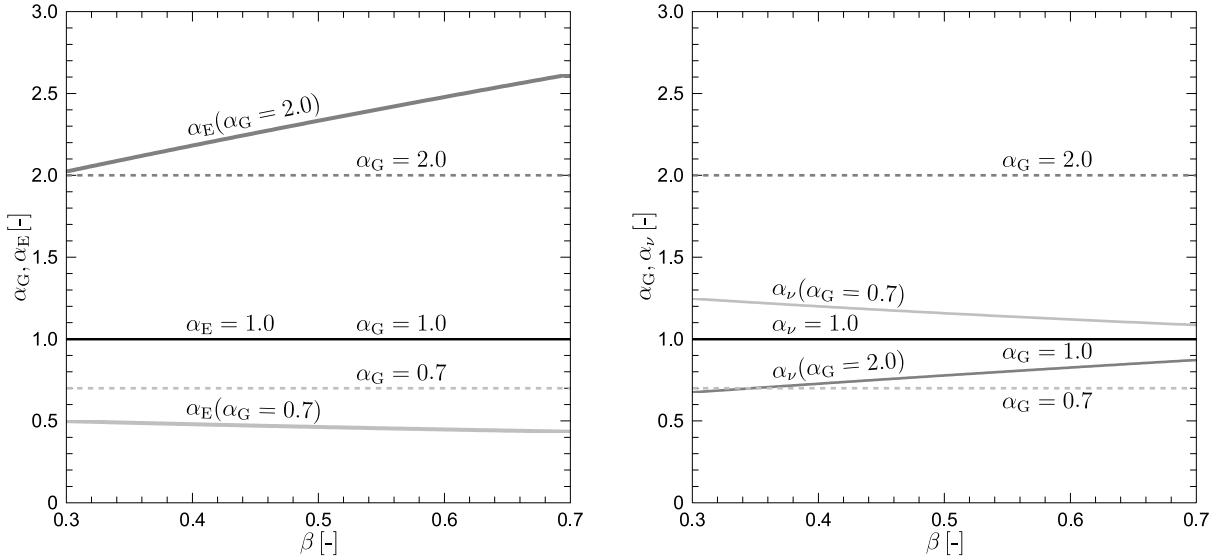

Fig. 5.8: The influence of β on the value of the anisotropy coefficients α_E and α_ν for three different cases of α_G = 0.7, 1.0, 2.0

pure inherent anisotropic behaviour and the expressions from Eqs. 5.60 and 5.61 are regained. Under anisotropic stress conditions ($K \neq 1.0$), the anisotropy ratios increase along with K.

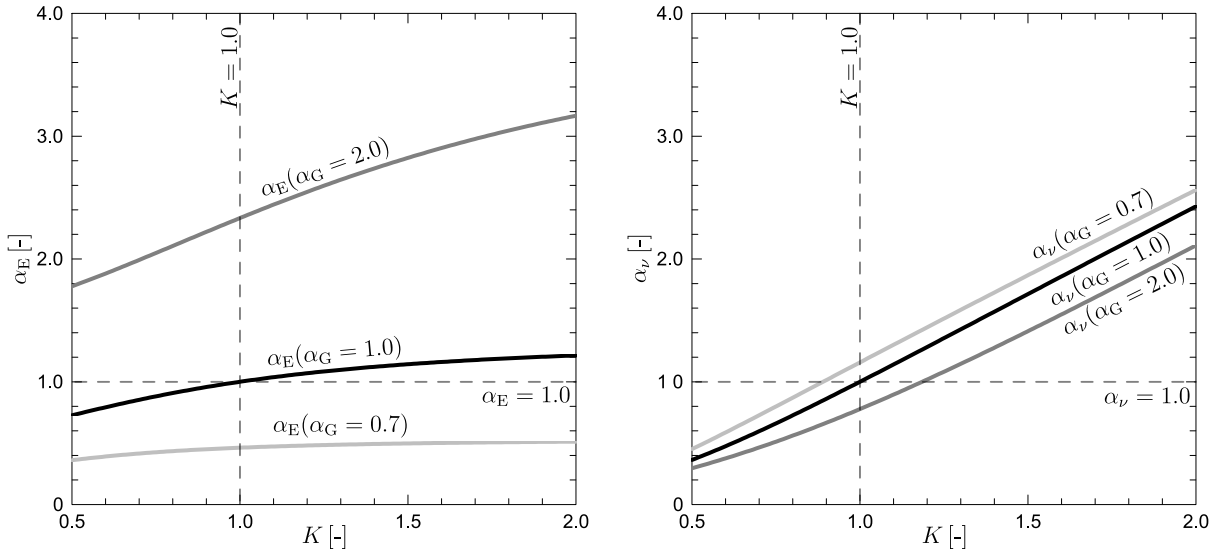

Fig. 5.9: Anisotropy coefficients α_E and α_ν at various stress conditions K

5.2 Intermediate strain range: stiffness degradation

The pre-failure stiffness degradation with strain is simulated, in six-dimensional strain space, with the use of the Brick-type procedure, in depth described in Sec. 2.2.1. In the proposed *AHEBrick* model, the relationship between stiffness modulus and strain is based on the S-curve equation by Santos and Correia [142], see Eq.2.22. In the original expression, the decay of the secant shear modulus $G_{\mathrm{s}}^{\mathrm{ref}}/G_0^{\mathrm{ref}}$ is determined. However, as numerical analysis is based on incremental loading, the definition of the tangent shear modulus degradation is required:

$$\frac{G_{\mathrm{t}}^{\mathrm{ref}}}{G_0^{\mathrm{ref}}} = \left(\frac{\gamma_{0.7}}{\gamma_{0.7} + \frac{3}{7}\gamma} \right)^2 . \tag{5.64}$$

The relative strain distance of each stiffness drop - the string length s^j, is measured with the shear strain invariant $\gamma = \sqrt{\frac{3}{2} e_{ij} e_{ij}}$. However, if a constitutive model is not limited by any additional surfaces, i.e. cap yield surfaces, it is unwise to use shear strain invariant γ as a measure of strain. This especially is apparent during a triaxial compression test on an isotropic sample ($\alpha_G = 1.0$). In such case shear strain is not generated ($\gamma = 0$), and consequently, no stiffness degradation may occur, despite the increasing value of mean stress p.

In the original Brick formulation [149], the Euclidean norm $||\boldsymbol{\epsilon}||$ is defined in strain space and its axes (ε_V and γ_M in plane strain model, or ε_V and γ_{oct} in case of three-dimensional formualtion) are specially selected in such a way that it is possible to define a realistic value of K_0 of a tested material. Additionally, the model is not constrained by any conventional yield surfaces, so the selected norm allows to limit shear strength of soil.

Ultimately, in the *AHEBrick* model, the Euclidean norm of strain tensor $||\boldsymbol{\varepsilon}|| = \sqrt{\varepsilon_{ij}\varepsilon_{ij}}$ has been chosen as a strain distance measure between a person and bricks. It has been decided to use this strain norm due to its straightforward definition, as compared to the original norm proposed by Simpson. In addition, it accounts for stiffness degradation during isotropic compression, with no need for cap surfaces. The relation between tangent shear modulus and the Euclidean norm of strain tensor $||\boldsymbol{\varepsilon}||$ is obtained by modifying Eq. 5.64:

$$\frac{G_{\mathrm{t}}^{\mathrm{ref}}}{G_0^{\mathrm{ref}}} = \left(\frac{||\boldsymbol{\varepsilon}||_{\mathrm{sh}}}{||\boldsymbol{\varepsilon}||_{\mathrm{sh}} + \frac{3}{7}||\boldsymbol{\varepsilon}||} \right)^2 , \tag{5.65}$$

where $||\boldsymbol{\varepsilon}||_{\mathrm{sh}}$ is a parameter that determines the steepness and shape of S-curve.

The differences of stiffness changes due to applied strain measure can be presented in a form of drained triaxial radial paths. This test allows the influence of the stress path direction on soil stiffness to be examined. It involves performing stress probes, from a fixed initial stress point, and measuring the obtained increments of deviatoric ε_q and volumetric ε_V strain. The magnitude of the changes in stiffness can be then visualised using isolines of generalised strain:

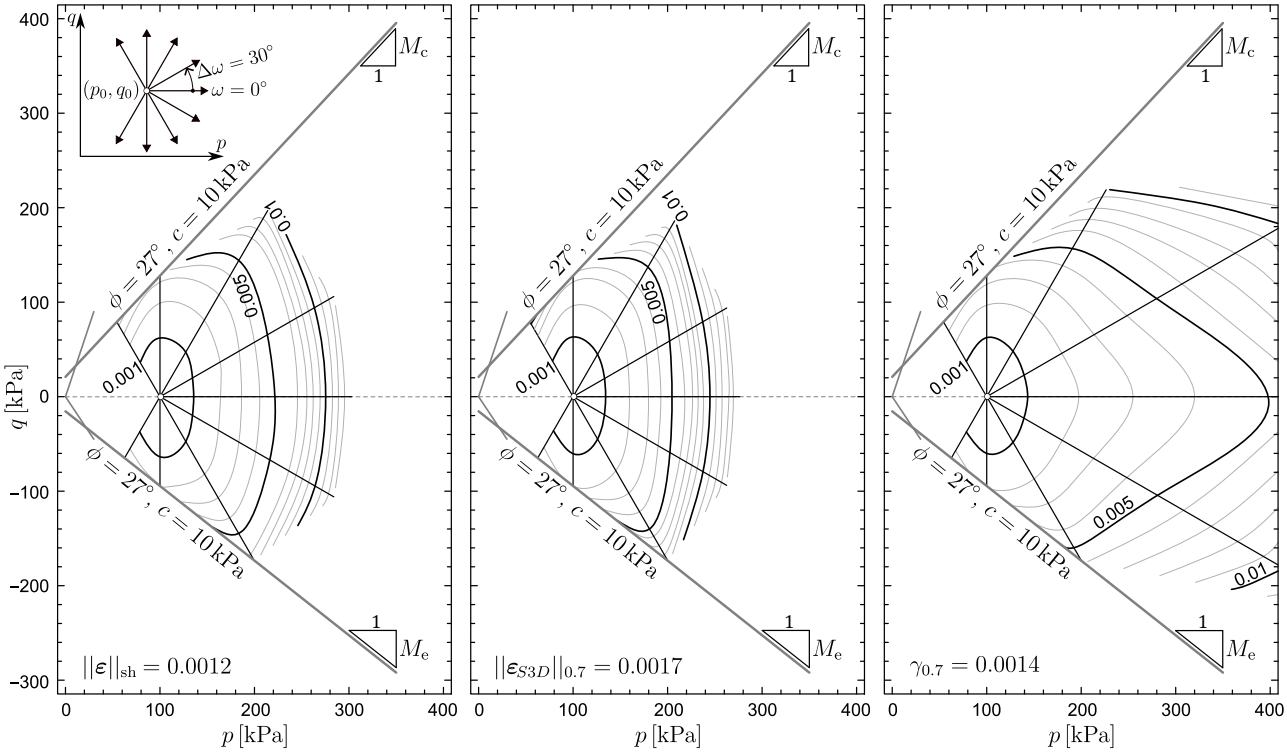

Fig. 5.10: Isolines of accumulated generalised strain ϵ obtained from the simulation of drained triaxial radial stress paths. The influence of strain measure on stiffness changes is presented for Euclidean norm of strain tensor $||\boldsymbol{\varepsilon}||$, Simpson's Euclidean norm for the three-dimensional model $||\boldsymbol{\varepsilon}_{\mathrm{S3D}}||$, and shear strain invariant γ

$$\epsilon = \sqrt{\Delta\varepsilon_V^2 + \Delta\varepsilon_q^2}. \tag{5.66}$$

This test was conducted experimentally for natural Pisa Clay and results were reported in [37].

The graphs, presented in Fig. 5.10, show the results of drained triaxial radial stress paths simulation. The influence of the strain norm on the directional changes of stiffness is conduced for Euclidean norm of strain tensor $||\boldsymbol{\varepsilon}||$, Simpson's Euclidean norm for the three-dimensional model $||\boldsymbol{\epsilon}|| = ||\boldsymbol{\varepsilon}_{\mathrm{S3D}}||$, and shear strain invariant γ. The tested material is isotropic ($\alpha_G = 1.0$) and the input parameters are the same for the each example. The values of S-curve shape parameters $||\boldsymbol{\varepsilon}||_{\mathrm{sh}}$, $\gamma_{0.7}$ and $||\boldsymbol{\varepsilon}_{\mathrm{S3D}}||_{0.7}$ (defined analogously as in Eqs. 5.64 and 5.65) are calibrated in the way that, for the case of conventional drained triaxial compression test (CID), soil stiffness degradation is comparable. The analysed material is tested at the initial isotropic stress state $p_0 = 100\,\mathrm{kPa}$. The schematic diagram of stress path procedure is illustrated in Fig. 5.10. The stress space is limited by the compression M_c and extension M_e shear failure lines and Rankine criterion prevents tensile stress generation.

The results show the significant effect the selection of a strain measure has on changes in soil stiffness of the samples, subjected to the same stress. It is particularly apparent when the

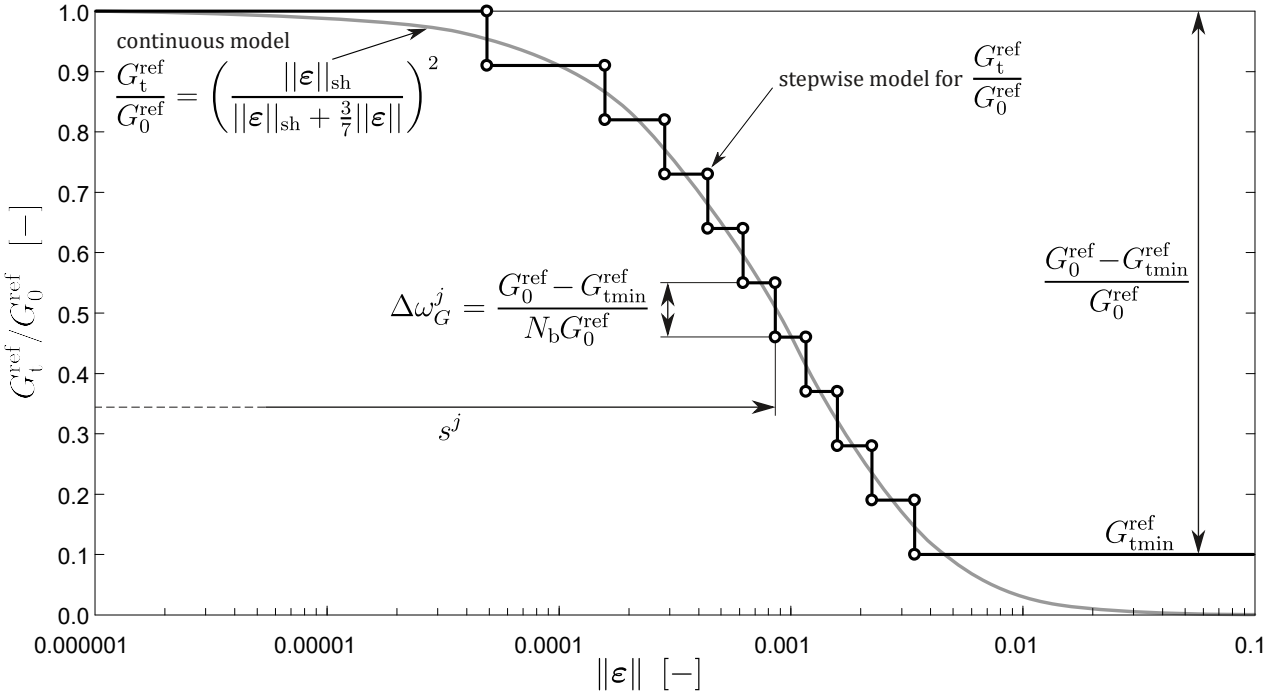

Fig. 5.11: The stepwise description of the S-shaped curve equation proposed by Santos and Correia [142], after [46]

magnitude of stiffness degradation depends on the shear strain invariant γ, especially considering the soil response to the drained stress path, inclined $\omega = 0°$ to the p axis. In this case the values of the load components are equal, $\sigma_{11} = \sigma_{22} = \sigma_{33} = \text{const}$. Hence, the shearing of the sample is minimal and, as a result, stiffness degrades accordingly, e.g. the generalised strain $\epsilon = 0.005$ is obtained for the value of mean stress $p \approx 400\,\text{kPa}$. In comparison, if stiffness decay of a sample is dependent on strain norms $||\boldsymbol{\varepsilon}||$ or $||\boldsymbol{\varepsilon}_{\text{S3D}}||$, the same magnitude of the stiffness change $\epsilon = 0.005$ is reached for the significantly lower stress level $p \approx 200\,\text{kPa}$.

Based on the stiffness-strain relation in Eq. 5.65, the Brick-type stepwise degradation, applied in the model, is presented in Fig. 5.11. The strain history is traced with $N_\text{b} = 10$ bricks. Each brick represents one step, which height, so-called stiffness proportion, has a constant value:

$$\Delta\omega_G = \frac{G_0^{\text{ref}} - G_{\text{tmin}}^{\text{ref}}}{N_\text{b}\, G_0^{\text{ref}}}. \tag{5.67}$$

To avoid a situation where shear modulus G_t^{ref} degrades to zero, which is problematic in numerical modeling, a minimum value of tangent shear modulus $G_{\text{tmin}}^{\text{ref}}$ is applied. This value is reached when all the bricks are pulled. The value of $G_{\text{tmin}}^{\text{ref}}$ can be estimated based on the S-shaped curve obtained from the laboratory testing. Otherwise, it can be assumed as $0.1\ G_0^{\text{ref}}$.

The length of a string s^j for a j-th brick ($j = 1, 2, 3...N_\text{b}$) is calculated from the following expression:

$$s^j = \frac{7}{3}||\boldsymbol{\varepsilon}||_{\mathrm{sh}} \left(\sqrt{\frac{1}{1.0 - j\Delta\omega_G + 0.5\Delta\omega_G}} - 1 \right). \tag{5.68}$$

If the model is implemented into a displacement-based FE software, e.g [26], then the value of strain increment $\Delta\boldsymbol{\varepsilon}$ is known in the stress integration procedure. During the initial step, the location of a man $\boldsymbol{\varepsilon}$ and bricks $\boldsymbol{\varepsilon}^{\mathrm{b}j}$ is usually at the origin of a strain space ($\boldsymbol{\varepsilon} = \boldsymbol{\varepsilon}^{\mathrm{b}j} = 0$). In every next iteration the following condition is reviewed, for each j-th brick:

$$d^j = ||\boldsymbol{\varepsilon} + \Delta\boldsymbol{\varepsilon} - \boldsymbol{\varepsilon}^{\mathrm{b}j}|| > s^j, \tag{5.69}$$

where d^j is the strain distance from the initial position. The moment the condition from Eq. 5.69 is fulfilled for a given j-th brick, this brick is assumed active. Its location is then updated using the strain increment:

$$\Delta\boldsymbol{\varepsilon}^{\mathrm{b}j} = (\boldsymbol{\varepsilon} + \Delta\boldsymbol{\varepsilon} - \boldsymbol{\varepsilon}^{\mathrm{b}j}) \frac{d^j - s^j}{d^j}. \tag{5.70}$$

At the end of each step the number of active bricks n_{ab} is counted and the actual tangent shear modulus $G_{\mathrm{t}}^{\mathrm{ref}}$ can be calculated:

$$G_{\mathrm{t}}^{\mathrm{ref}} = G_0^{\mathrm{ref}}(1 - n_{\mathrm{ab}}\Delta\omega_G). \tag{5.71}$$

Based on this value, it is possible to determine the components of the hyperelastic stiffness matrix and, as result, obtain the stress increment $\Delta\boldsymbol{\sigma}$.

Due to the Brick procedure the *AHEBrick* model poses the ability to accurately reflect the influence of recent stress history on soil stiffness. Fig. 5.12 shows the results of a numerical simulation presenting a simplified analysis of an experimental study performed on London Clay [12, 141], described in Sec. 2.2. The sample loaded at the constant mean stress $p = 200\,\mathrm{kPa}$ (0X) up to the failure is preceded by paths, which start in different stress points in $p-q$ space. Four paths are taken into consideration:

- A0X, starting at point $p_0 = 250\,\mathrm{kPa}$, $q_0 = 0\,\mathrm{kPa}$; q = const unloading to $p = 200\,\mathrm{kPa}$; final path 0X up to the failure,
- B0X, starting at point $p_0 = 200\,\mathrm{kPa}$, $q_0 = -50\,\mathrm{kPa}$; p = const loading to $p = 200\,\mathrm{kPa}$; final path 0X up to the failure,
- C0X, starting at point $p_0 = 150\,\mathrm{kPa}$, $q_0 = 0\,\mathrm{kPa}$; q = const loading to $p = 200\,\mathrm{kPa}$; final path 0X up to the failure,
- D0X, starting at point $p_0 = 200\,\mathrm{kPa}$, $q_0 = 50\,\mathrm{kPa}$; q = const unloading to $p = 200\,\mathrm{kPa}$; final path 0X up to the failure.

The analysed material is isotropic, $\alpha_G = 1.0$. Stiffness-strain relationship is defined as a change of derivatives $\mathrm{d}q/\mathrm{d}\varepsilon_q$ with deviatoric strain ε_q. The presented S-curves are plotted for the last

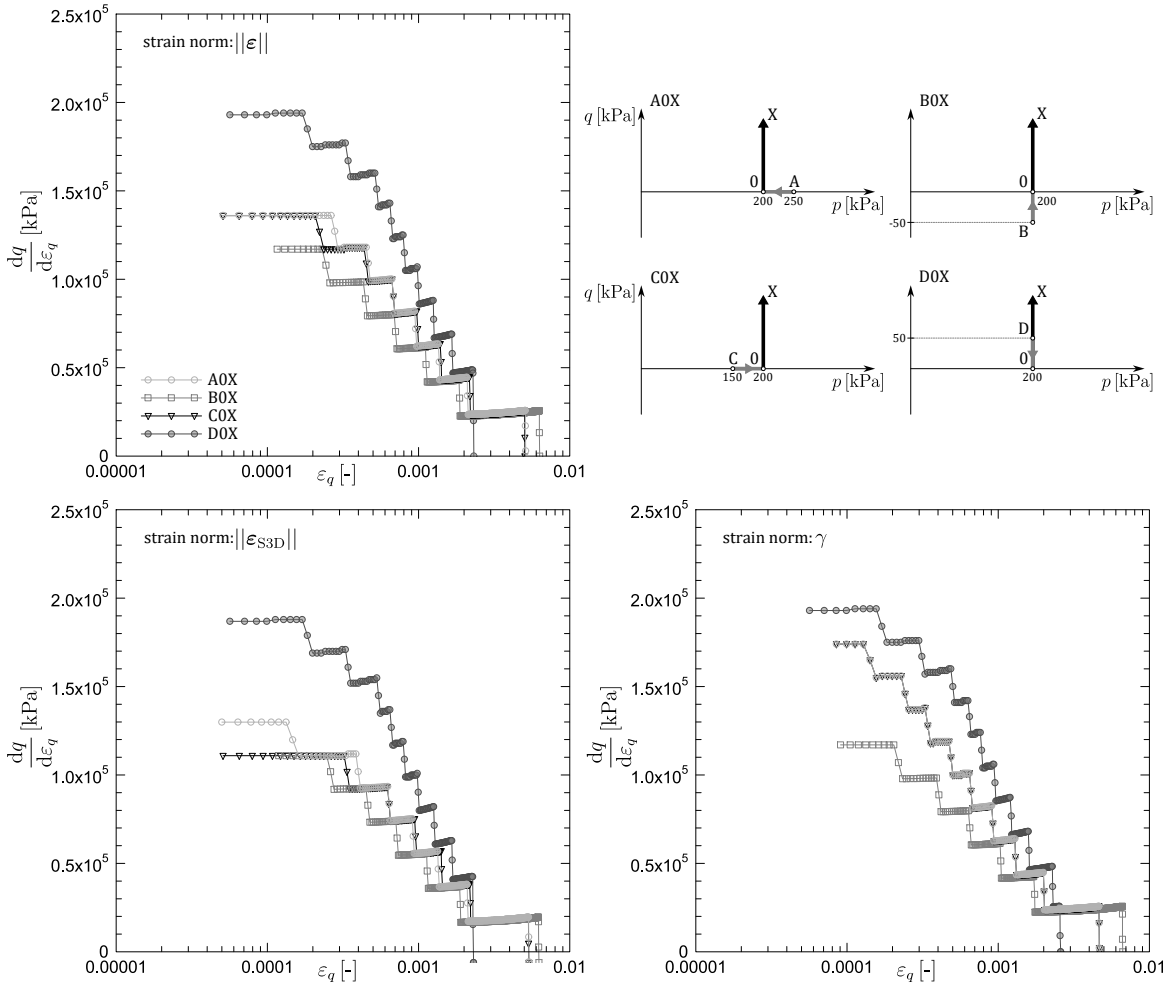

Fig. 5.12: The influence of the recent stress history on the stiffness degradation, presented as a relation between derivatives $\mathrm{d}q/\mathrm{d}\varepsilon_q$ and deviatoric strain ε_q. Three strain measures $||\boldsymbol{\varepsilon}||$, $||\varepsilon_{\mathrm{S3D}}||$, γ are considered

stage of tests, the 0X path. The simulation is conducted considering three strain measures: $||\boldsymbol{\varepsilon}||$, $||\varepsilon_{\mathrm{S3D}}||$, γ.

Overall, the results show the similar pattern as the experimental data presented in Fig. 2.8. Among the analysed strain norms, the closest match is observed for the Euclidean norm of strain tensor $||\boldsymbol{\varepsilon}||$. The highest initial stiffness is obtained from the D0X test. Soil stiffness regains its maximum value due to unloading occurring before the final 0X path. The material response to A0X and C0X simulations is similar, as the preceding A0 and C0 loading paths are subjected to the same stress increment ($q = \mathrm{const} = 0\,\mathrm{kPa}$, $\Delta p = 50\,\mathrm{kPa}$). In contrast, the lowest stiffness is observed in the B0X test. Here, no change in stress direction or unloading occurs, and as a result stiffness degrades significantly before the final 0X path is conducted.

In the case of the other two strain measures, the most notable differences are observed for the A0X and C0X tests. Using the Simpson's Euclidean norm $||\boldsymbol{\varepsilon}_{\mathrm{S3D}}||$, the stiffness obtained from the simulation of the C0X path is comparable to B0X test. This suggests that the greatest degradation occurs when the 0X path is preceded by compression loading. Conversely, when stiffness degradation is controlled by the shear strain invariant γ, the stiffness calculated for A0X and C0X analyses is identical and significantly higher than for other strain norms. This behaviour can be explained by the definition of the shear strain measure, where stiffness degrades with the accumulation of shear strains, which do not develop under isotropic conditions. As a result, the observed soil response reflects the final stage of the test: loading at constant stress $p = 200\,\mathrm{kPa}$.

5.3 Yield surface: isotropic strength criterion

Simpson's original Brick model accurately reproduces shear strength; that is, the mobilized friction angle cannot be greater than the maximum specified friction angle. The shear strength in the suggested *AHEBrick* formulation is determined via the traditional stress-based isotropic Matsuoka-Nakai criterion [106]:

$$F_{\mathrm{MN}}(\boldsymbol{\sigma}) = I_1 I_2 - \frac{9 - \sin^2\phi}{-1 + \sin^2\phi} I_3 \leq 0, \tag{5.72}$$

where I_1, I_2, I_3 are the stress invariants:

$$I_1 = \sigma_{kk}, \quad I_2 = \frac{1}{2}\left[\sigma_{ij}\sigma_{ij} - (I_1)^2\right], \quad I_3 = \det(\boldsymbol{\sigma}), \tag{5.73}$$

and ϕ is the effective maximum friction angle.

To include the effective cohesion c within the failure criterion, the stress invariants in Eq. 5.73 should be calculated for the stress state $\boldsymbol{\sigma} - p_{\mathrm{c}}\boldsymbol{\delta}$, for which compressive stress is defined as: $p_{\mathrm{c}} = c\cot\phi$. Furthermore, the range of the permissible stress states is limited due to the Rankine tension cut-off criterion $p \geq p_{\mathrm{te}}$.

In the flow rule, the Drucker-Prager function is applied as the plastic potential:

$$G_{\mathrm{GP}}(\boldsymbol{\sigma}) = q - \frac{6\sin\psi}{3 - \sin\psi}\, p, \tag{5.74}$$

ψ being the dilatancy angle.

5.4 Implementation

In this section of the implementation of the *AHEBrick* model into a commercial displacement-based FE software is presented. In Plaxis [26] environment, the described material model is programmed as a special `Fortran90` subroutine "User-Defined Soil Model" UDSM. The subroutine is compiled into the dynamic link library file (DLL) and added to the main program directory. Within the program the following six tasks need to be performed:

1. Initialisation of state variables;
2. Calculation of constitutive stresses;
3. Return of the state variables;
4. Return of attributes matrix;
5. Creation of effective material stiffness matrix;
6. Creation of elastic material stiffness matrix.

The detailed description of every task can be found in Plaxis Material Models Manual [27].

As a simplification, in the numerical code, the tangent compliance and tangent stiffness fourth order tensors $(\mathbf{C}^{\mathrm{t}}, \mathbf{D}^{\mathrm{t}})$ are reduced to 6×6 Voigt notation matrices $\left(\left[\mathbf{D}^{\mathrm{t}}\right], \left[\mathbf{C}^{\mathrm{t}}\right]\right)$. This operation can be conduced due to the symmetries of the fourth order tensors calculated from the elastic potential function. The reduced compliance and stiffness matrices are obtained from the stress and strain tensors defined in a simplified manner as 6×1 vectors:

$$\{\boldsymbol{\sigma}\} = \{\sigma_{11}\ \sigma_{22}\ \sigma_{33}\ \sigma_{12}\ \sigma_{23}\ \sigma_{31}\}^{\mathrm{T}} \quad \text{and} \quad \{\boldsymbol{\varepsilon}\} = \{\varepsilon_{11}\ \varepsilon_{22}\ \varepsilon_{33}\ \gamma_{12}\ \gamma_{23}\ \gamma_{31}\}^{\mathrm{T}}. \tag{5.75}$$

In general, in UDSM models the user introduces the information about current stresses and state variables, as well as the required model parameters. Provided input parameters of the *AHEBrick* model are shown in Tab. 5.1 In the model the state variables array `StVar` contains the information about the current position of a person $\boldsymbol{\varepsilon}$ and bricks $\boldsymbol{\varepsilon}^{\mathrm{b}j}$ which is determined by 66 strain components. In the first step the `StVar0` array only contains zeros. In every next step it is automatically updated and the resulting state variables `StVar` calculated in a previous step is transferred to the next one and used as the initial value `StVar0`.

In numerical calculations the current position of a person $\{\boldsymbol{\varepsilon}\}$ and bricks $\left\{\boldsymbol{\varepsilon}^{\mathrm{b}j}\right\}$ is determined based on the strain increments, supplied by Plaxis. It should be noted that in the program's nomenclature, "increment" refers to the total added value within the current step. The information about intermediate increments of each iteration is not stored in the memory. Since the main program may typically produce large strain increments, it could generate the problem of the nonlinear stiffness changes overshooting. Hence, it is crucial to incorporate a substepping

Table 5.1: Input parameters of the *AHEBrick* model

No.	Parameter	Description
1	G_0^{ref} [kPa]	reference small-strain shear modulus
2	β [-]	parameter controlling the order of barotropy
3	p_{ref} [kPa]	reference stress
4	c_1 [-]	anisotropy constant - stress-induced anisotropy
5	c_2 [-]	anisotropy constant - stress-induced and microstructure anisotropy
6	ϕ [°]	effective maximum friction angle
7	c [kPa]	effective cohesion
8	ψ [°]	dilatancy angle
9	p_{te} [kPa]	maximum tensile stress
10	$G_{\text{tmin}}^{\text{ref}}$ [kPa]	minimum reference tangent shear modulus
11	$\|\|\boldsymbol{\varepsilon}\|\|_{\text{sh}}$ [-]	parameter controlling the shape and steepness of the S-curve

scheme into the algorithm. In the model the substepping is applied, if the strain increment of the Euclidean norm $||\Delta\boldsymbol{\varepsilon}^{\text{tot}}||$ is greater than $||\Delta\boldsymbol{\varepsilon}_{\max}|| = 10^{-5}$.

The simplified algorithm of the *AHEBrick* model numerical code implementation is presented in Box 5.1. The stiffness matrix is obtained by the inversion of the compliance matrix $[\mathbf{C}^{\text{e}}] = [\mathbf{D}^{\text{e}}]^{-1}$. If the calculated stress increment (see point IV.) does not fulfill the shear strength criterion, calculated in Eq. 5.72, then it is returned to the yield surface $F_{\text{MN}}(\boldsymbol{\sigma}) = 0$. For this, the implicit return mapping algorithm, explained in [84], is used.

Box 5.1. Algorithm presenting the implementation of the *AHEBrick* model in the commercial FE code [26]

I. $\{\boldsymbol{\sigma}^0\}$, $\{\Delta\boldsymbol{\varepsilon}^{\,\mathrm{tot}}\}$ and `StVar0` are given

II. Calculation of the S-shaped curve parameters s^j and $\Delta\omega_G$, based on Eqs. 5.67-5.68

III. Calulation of the substepping scheme parameters:

1. Calculation of $||\Delta\boldsymbol{\varepsilon}^{\,\mathrm{tot}}||$
2. Calculation of the substepping variable xn_{sub}:
   $xn_{\mathrm{sub}} = \frac{||\Delta\boldsymbol{\varepsilon}^{\,\mathrm{tot}}||}{||\Delta\boldsymbol{\varepsilon}_{\mathrm{max}}||}$, $||\Delta\boldsymbol{\varepsilon}_{\mathrm{max}}|| = 10^{-5}$
3. `IF`: $xn_{\mathrm{sub}} > 1.0$ `THEN`:
   a) $\{\Delta\boldsymbol{\varepsilon}\} = \frac{1}{xn_{\mathrm{sub}}} \cdot \{\Delta\boldsymbol{\varepsilon}^{\,\mathrm{tot}}\}$
   b) $n_{\mathrm{sub}} = \mathtt{FLOOR}(xn_{\mathrm{sub}})$
   c) $\mathrm{rest} = 1.0 - \frac{n_{\mathrm{sub}}}{xn_{\mathrm{sub}}}$
   d) `IF`: $\mathrm{rest} > 0.0$ `THEN`:
   $\{\Delta\boldsymbol{\varepsilon}_{\mathrm{rest}}\} = \mathrm{rest} \cdot \{\Delta\boldsymbol{\varepsilon}^{\,\mathrm{tot}}\}$, $n_{\mathrm{sub}} \coloneqq n_{\mathrm{sub}} + 1$

IV. Calculation of the constitutive stress increments $\{\Delta\boldsymbol{\sigma}\}$:

1. Initial data: $\{\Delta\boldsymbol{\sigma}\} = 0$, $\{\boldsymbol{\sigma}_i^0\} = \{\boldsymbol{\sigma}_0\}$, $i = 1$
2. `DO`:
   a) $\{\boldsymbol{\varepsilon}\} = \{\boldsymbol{\varepsilon}^0\} + \{\Delta\boldsymbol{\varepsilon}\}$
   b) Calculation of the actual tangent shear modulus $G_{\mathrm{t}}^{\mathrm{ref}}$ from the Eq. 5.71
   c) Determination of the hyperelastic stiffness matrix $[\mathbf{D}^{\,\mathrm{e}}(\boldsymbol{\sigma}_i^0)]$ for the actual $G_{\mathrm{t}}^{\mathrm{ref}}$ and the remaining constant parameters $c_1, c_2, \beta, p_{\mathrm{ref}}$
   d) Calculation of stress predictor
   $\{\boldsymbol{\sigma}_i^{\mathrm{e}}\} = \{\boldsymbol{\sigma}_i^0\} + [\mathbf{D}^{\,\mathrm{e}}(\boldsymbol{\sigma}_i^0)] \cdot \{\Delta\boldsymbol{\varepsilon}\}$
   e) `IF`: $F(\{\boldsymbol{\sigma}_i^{\mathrm{e}}\}) > 0$ `THEN`: return mapping algorithm; calculation of $\{\boldsymbol{\sigma}_i\}$, $\{\Delta\boldsymbol{\sigma}_i\}$
   `ELSE`: $\{\boldsymbol{\sigma}_i\} \coloneqq \{\boldsymbol{\sigma}_i^{\mathrm{e}}\}$, $\{\Delta\boldsymbol{\sigma}_i\} \coloneqq \{\Delta\boldsymbol{\sigma}_i^{\mathrm{e}}\}$
   f) $\{\Delta\boldsymbol{\sigma}\} = \{\Delta\boldsymbol{\sigma}\} + \{\Delta\boldsymbol{\sigma}_i\}$, $\{\boldsymbol{\sigma}_i^0\} = \{\boldsymbol{\sigma}_i\}$
   `IF`: $i < n_{\mathrm{sub}}$ `THEN`: $i = i + 1$
   `ELSE IF`: $i = n_{\mathrm{sub}}$ `AND` $\{\Delta\boldsymbol{\varepsilon}_{\mathrm{rest}}\} > 0$ `THEN`:
   $\{\Delta\boldsymbol{\varepsilon}\} = \{\Delta\boldsymbol{\varepsilon}_{\mathrm{rest}}\}$, $i = i + 1$
   `WHILE` $i \leq n_{\mathrm{sub}}$

6

Verification of the *AHEBrick* model in element tests and exemplary BV problems

In the following chapter the model performance is investigated. At the most basic level it is carried out as a laboratory test simulation on a single element. The element test analysis allows to examine the model functionality and the influence of individual input parameters on the material response, either in plane strain or in three-dimensional cases. Additionally, based on the results of laboratory research, it is possible to perform non-standard parameters calibration, aiming to obtain performance of implemented material model close to the investigated mechanical behaviour of soils.

Model response is also validated through FE numerical calculations of geotechnical boundary value problems (BVP). The aim of BVPs is to investigate material parameter influence on the soil-structure interaction, hence the homogeneous soil layout and basic flow conditions are considered. The investigations are carried out for tunnel drilling, open excavation and supported excavation cases. These examples are considered due to significant unloading occurring during the construction and, as a result, stresses within subsoil undergoing substantial redistribution. The directions of the principal stresses are subjected to large rotations, and the corresponding principal stress components change considerably, which strongly affect stiffness of anisotropic soils.

The numerical simulations are carried out with a use of own element test level programs, written in Fortran 90 and Mathematica environments (element tests), and with commercial FE [26] code in plane strain (element tests and BVPs) and 3D conditions (BVPs).

6.1 Element tests

The influence of selected material parameters on the soil response is examined using element testing. This study involves the simulation of triaxial compression tests, under both drained

and undrained conditions, as well as drained radial path tests. Furthermore, the influence of stress history on the material behaviour is presented.

A soil sample with the predetermined set of material parameters listed in Tab. 6.1 was used for the analysis. The values of the listed parameters are selected to be representative of parameter values obtained for preconsolidated clays, (i.e. London Clay or Oxford Clay, see Sec. 6.1.4). The parametric study is conducted on the following parameters: α_G, β, $||\boldsymbol{\varepsilon}||_{\text{sh}}$ and K_0. Tab. 6.1 provides their range. It should be noted that each parameter is tested separately and the remaining variables assume the default value marked as bolded. Any changes in this regard are always indicated in the text.

The model validation is also conducted based on laboratory test results of some stiff over-consolidated fine-grained soils, repotted in literature.

Table 6.1: Set of the *AHEBrick* model parameters used in element test simulations

	Parameter	Clay
Small strain stiffness	G_{vh}^{ref} [kPa]	50000
	β [-]	0.4, **0.5**, 0.6
	α_G [-]	0.7, **1.0**, 2.0, 3.0
	p_{ref} [kPa]	100
Stiffness degradation	$G_{vh\text{tmin}}^{\text{ref}}$ [kPa]	5000
	$||\boldsymbol{\varepsilon}||_{\text{sh}}$ [-]	0.0005, **0.0007**, 0.0009
Shear strength criterion	ϕ [°]	27
	c [kPa]	10
	ψ [°]	5
	p_{te} [kPa]	0
Initial stress state	K_0 [-]	0.5 **1.0**, 2.0

6.1.1 Triaxial compression tests

The simulation of triaxial compression tests at the initial isotropic stress $p_0 = p_{\text{ref}} = 100\,\text{kPa}$, is conducted for undrained (CIU) and drained (CID) conditions. The influence of cross-anisotropy coefficient α_G on material response is presented in Fig. 6.1. The top-left graph (Fig. 6.1a) illustrates the influence of the stiffness anisotropy coefficient α_G on the initial inclination of the undrained stress path in the $p - q$ plane.

For isotropic material ($\alpha_G = 1.0$) the path is initially vertical. In contrast, the path is inclined to the right for $\alpha_G = 0.7$ and to the left if $\alpha_G = 2.0$. The material response for $\alpha_G > 1.0$ correlates with the laboratory data on the overconsolidated stiff clays, presented in Sec. 6.1.4. As the value of deviatoric stress q increases, all paths begin to lean slightly to the

right, which is related to the stress-induced anisotropy of soil stiffness but also, after reaching shear strength criterion, to the dilatancy, which can be described with Skempton's parameter of pore pressure A [151]. Due to the initial inclination of the stress paths, the obtained shear strength decreases proportionally with the α_G value. Hence, it should be noted that both stress-induced and inherent stiffness anisotropy of soil significantly influences shear strength of a material in undrained conditions, which has important practical implications. The stress path under drained conditions is also presented, as a comparison. In this case, stiffness anisotropy does not affect the shear strength of the soil.

The influence of α_G value on soil response is further evident for undrained compression curves $\varepsilon_v - q$, presented in Fig. 6.1b. These curves are plotted alongside with the step-wise line

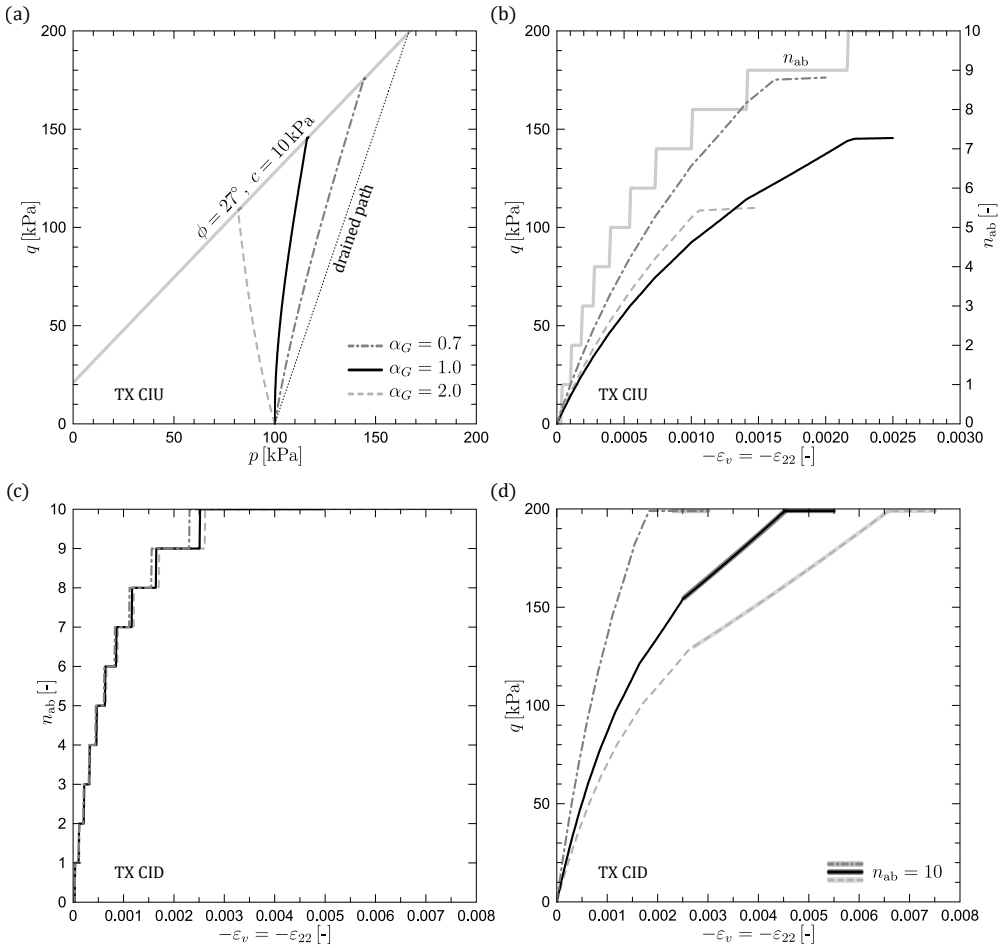

Fig. 6.1: The influence of anisotropy coefficient α_G on soil response subjected to the simulated triaxial CIU and CID tests: a) stress paths in $p-q$ plane, b) undrained compression curves $\varepsilon_v - q$ plotted with brick activation line $\varepsilon_v - n_{ab}$, c) activation of bricks $\varepsilon_v - n_{ab}$ in drained conditions, d) drained compression curves $\varepsilon_v - q$. The minimum stiffness G^{ref}_{vhtmin}, corresponding to $n_{ab} = 10$ is marked for each drained compression curve

indicating the activation of bricks n_{ab} in the *AHEBrick* model. In modelling, the undrained compression is controlled with strains, so the activation of bricks remains unaffected by changes in α_G.

In contrast, drained compression is stress-controlled and the effect of α_G on stiffness degradation is shown in Fig. 6.1c in a form of three separate $\varepsilon_v - n_{\mathrm{ab}}$ curves. Notable differences can be observed at higher strain levels, here for $n_{\mathrm{ab}} = 8, 9, 10$.

Presented in Fig. 6.1d, axial stiffness of soil, in drained conditions, increases with the decreasing α_G value. The minimum stiffness $G^{\mathrm{ref}}_{vh\mathrm{tmin}}$, corresponding to $n_{\mathrm{ab}} = 10$ is marked for each compression curve. This shows that as α_G increases the activation of all bricks occurs quicker

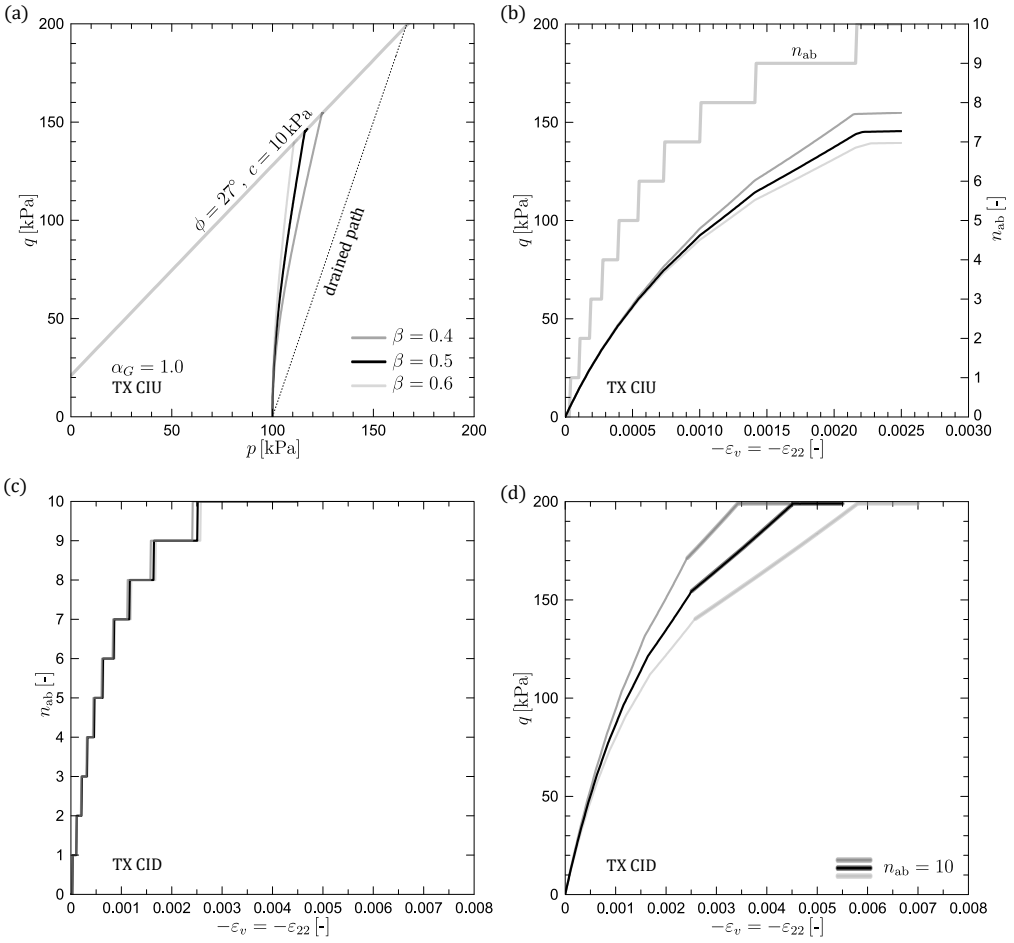

Fig. 6.2: The influence of β parameter on soil response subjected to the simulated triaxial CIU and CID tests: a) stress paths in $p - q$ plane, b) undrained compression curves $\varepsilon_v - q$ plotted with brick activation line $\varepsilon_v - n_{\mathrm{ab}}$, c) activation of bricks $\varepsilon_v - n_{\mathrm{ab}}$ in drained conditions, d) drained compression curves $\varepsilon_v - q$. The minimum stiffness $G^{\mathrm{ref}}_{vh\mathrm{tmin}}$, corresponding to $n_{\mathrm{ab}} = 10$ is marked for each drained compression curve

before the shear strength envelope is reached. In the case of $\alpha_G = 1.0$ and $\alpha_G = 2.0$ this is manifested as a monotonically increasing straight up line until failure.

The same set of tests, presented in Fig. 6.2, was performed in order to study the effect of β on an isotropic sample, $\alpha_G = 1.0$. The values of $\beta = 0.4, 0.5, 0.6$, covered by the study, have been reported to occur for overconsolidated clays [19]. The effect of β on undrained stress paths, in $p-q$ plane, is presented in Fig. 6.2a. This parameter controls the order of dependency of stress on stiffness, so the differences in material response become more noticeable as the deviatoric stress level q increases. Taking into consideration the expression $m = 1 - \beta$, the lower β value is, the greater influence of stress on soil stiffness is obtained, which in turn leads to higher mean stress p.

Additionally, the β parameter affects the shear strength of the material under undrained conditions, as presented in a form of compression curves $\varepsilon_v - q$, in Fig. 6.2b. The initial inclina-

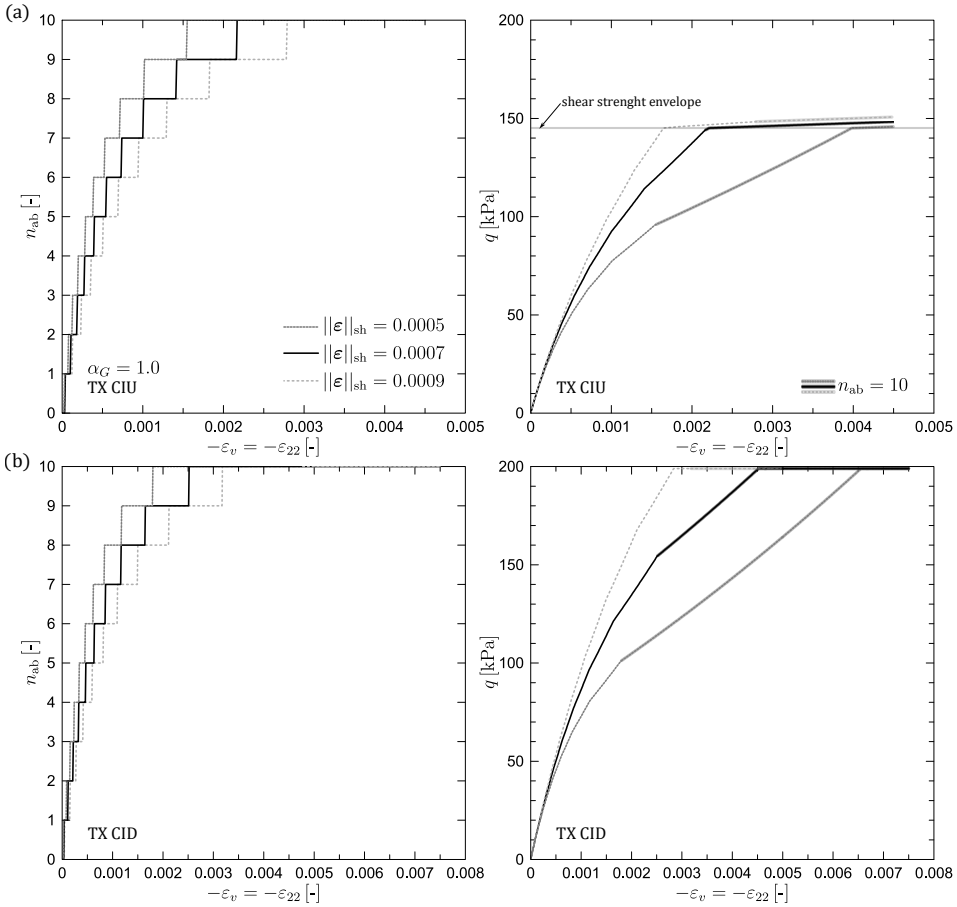

Fig. 6.3: The influence of the shape parameter $||\boldsymbol{\varepsilon}||_{\mathrm{sh}}$ on soil response subjected to the simulated a) undrained and b) drained triaxial compression tests. Brick activation curves $\varepsilon_v - n_{\mathrm{ab}}$ and compression curves $\varepsilon_v - q$ are presented. The minimum stiffness $G^{\mathrm{ref}}_{vh\mathrm{tmin}}$, corresponding to $n_{\mathrm{ab}} = 10$ is marked for each compression curve

tion of all three curves is the same, since according to Eq. 5.35, if material is isotropic($\alpha_G = 1.0$) the initial shear stiffness G_0^{ref} is independent of β. In addition this parameter does not affect stiffness degradation, hence a single $\varepsilon_v - n_{\text{ab}}$ line is plotted.

Figs. 6.2c and 6.2d show the material response to drained compression. Under these conditions the β parameter influences soil stiffness and its degradation but has no effect on shear strength. Furthermore, similarly to α_G, the higher the value of β is, the minimum stiffness, which corresponds to the activation of all bricks $n_{\text{ab}} = 10$ is reached at quicker rate.

The influence of the shape parameter $||\boldsymbol{\varepsilon}||_{\text{sh}}$ on soil response is presented in Fig. 6.3. This parameter determines the steepness of the strain-stiffness degradation curve, meaning it controls the transition from high initial stiffness to nonlinear tangent stiffness changes up to the moment the minimal stiffness becomes stress dependent and shear failure is reached. Along with the increase of $||\boldsymbol{\varepsilon}||_{\text{sh}}$ value, the rate of stiffness degradation decreases. However, this constant does not affect the stress paths and, consequently, does not influence the strength of the sample.

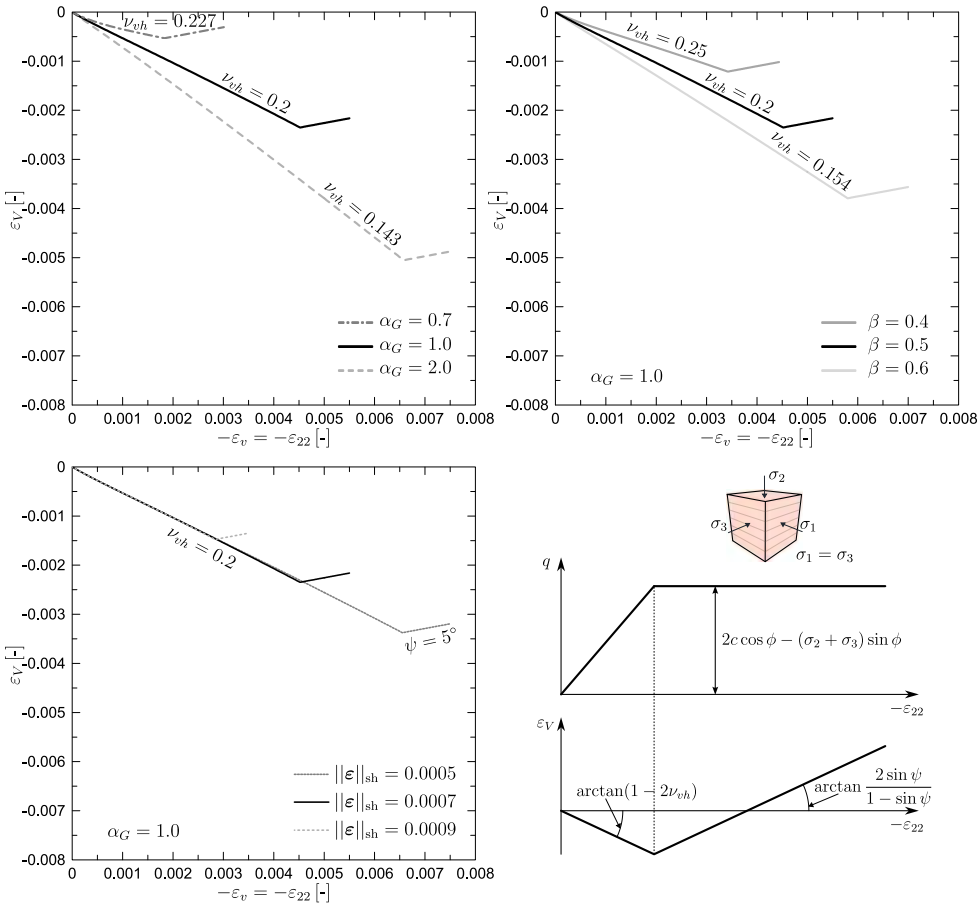

Fig. 6.4: The influence of α_G, β, $||\boldsymbol{\varepsilon}||_{\text{sh}}$ on Poisson's ratio ν_{vh} presented as axial and volumetric strain relation $\varepsilon_v - \varepsilon_V$

Hence only compression curves $\varepsilon_v - q$ and brick activation plots $\varepsilon_v - n_{\mathrm{ab}}$ under undrained and drained conditions are illustrated.

The influence of the parameters α_G, β, $||\boldsymbol{\varepsilon}||_{\mathrm{sh}}$ on the relationship between axial and volumetric strain ($\varepsilon_v - \varepsilon_V$) is illustrated in Fig. 6.4. This relationship, represented as an idealised, theoretical bilinear response of soil to drained compression, allows the determination of Poisson's ratio ν_{vh}. The first line corresponds to the elastic behaviour of the soil and its inclination is dependent on Poisson's ratio, as shown in Fig. 6.4. The second segment represents the post-yield plastic behaviour, with its slope determined by the dilatancy angle [164].

In the obtained results the relation between axial and volumetric strain is nonlinear, due to stiffness barotropy. Therefore, the values of Poisson's ratio must be determined based on the initial inclination of the plotted curves. The presented values of ν_{vh} correspond to the definition provided in Eq. 5.33. Poisson's ratio ν_{vh} is inversely proportional to the applied values of α_G and β. Conversely, the parameter $||\boldsymbol{\varepsilon}||_{\mathrm{sh}}$ does not affect the elastic constants, therefore, the obtained value $\nu_{vh} = 0.2$ is determined by the assumed values of $\alpha_G = 1.0$ and $\beta = 0.5$.

6.1.2 Radial stress path tests

The influence of the initial inherent cross-anisotropy α_G and the initial stress state K_0 on stiffness is studied through triaxial radial tests in drained conditions. Stiffness changes are presented in a form of isolines of accumulated generalised strain ϵ (Eq. 5.66). The procedure of the test is analogous to that described in Sec. 5.2.

The effect of α_G on stiffness changes is shown in Fig. 6.5. Radial drained paths start at the isotropic stress point $p = 100\,\mathrm{kPa}$. Three values of the cross-anisotropic coefficient $\alpha_G = 0.7, 1.0, 2.0$ are taken into consideration. In the case of the isotropic material ($\alpha_G = 1.0$), the soil response is generally uniform, with the greatest changes in stiffness being noticeable when the sample is subjected to significant isotropic loading. In contrast, for anisotropic samples, considerable influence of α_G on soil stiffness is visible. In the case of $\alpha_G = 0.7$, where the stiffness is greater in the vertical direction, the smallest change in strain is observed for the path inclined $\omega = 60^\circ$ to the p axis. This path almost reflects the conditions of triaxial compression, where the highest axial stiffness is obtained when $\alpha_G = 0.7$ (see Fig. 6.1d). For $\alpha_G = 2.0$, the lowest strain generation is conducted for paths inclined $\omega = -30^\circ, -60^\circ$ to the p axis, for which horizontal stress predominates. For the path $\omega = 60^\circ$, the obtained stiffness changes are the largest as compared to other cases, $\alpha_G = 0.7, 1.0$.

The influence of stress-induced anisotropy on stiffness is presented in Fig. 6.6. The sample is subjected to the initial isotropic ($K_0 = 1.0$), anisotropic active ($K_0 = 0.5$) and anisotropic

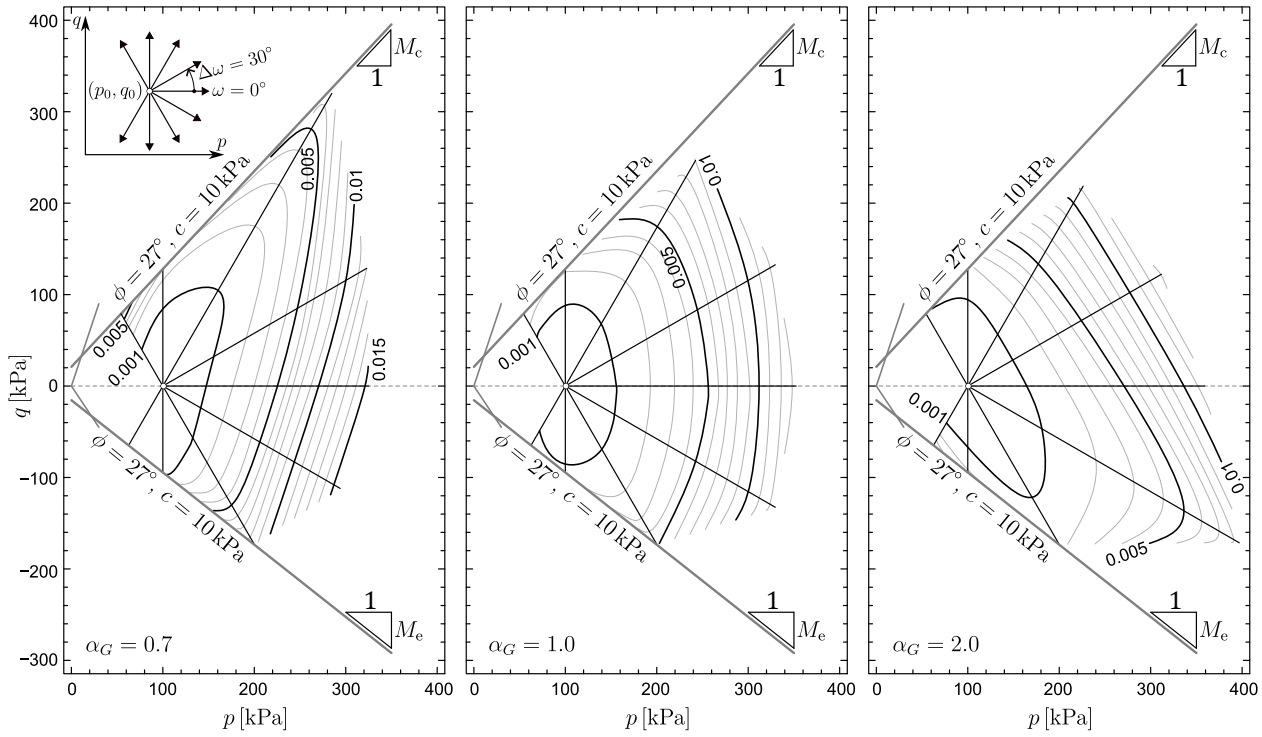

Fig. 6.5: The influence of initial inherent stiffness cross-anisotropy α_G on stiffness changes presented in a form of accumulated generalised strain ϵ obtained from the simulation of drained triaxial radial stress paths

passive ($K_0 = 2.0$) stress conditions. It is apparent that the initial stress state affect the stiffness changes as the obtained isolines patterns centre around the respective K_0 lines.

6.1.3 Stress history tests

The influence of the recent stress history on stiffness degradation is presented in Fig. 6.7 for different values of cross-anisotropy coefficient $\alpha_G = 0.7, 1.0, 2.0$. The obtained S-curves present the soil response to the last 0X path. Stiffness is described in a form of the derivative $\mathrm{d}q/\mathrm{d}\varepsilon_q$, which decays with deviatoric strain ε_q. The analysis includes a simulation of four different stress paths, which are presented in Fig. 6.7. The exact course of each path is described in Sec. 5.2.

The influence of cross-anisotropy coefficient α_G on stiffness degradation induced by recent stress history is evident. The stiffness calculated for the D0X path is the highest in all cases due to unloading occurring before the final 0X loading. However, the soil response to the remaining tests is highly dependent on α_G. In the case of the isotropic material, $\alpha_G = 1.0$, stiffness degradation curves obtained from A0X and C0X simulations are similar, as the path 0X is preceded by isotropic loading of the same stress increment $\Delta p = 50\,\mathrm{kPa}$. Since no direction changes occur in the stress space, the lowest value of stiffness is obtained for the B0X analysis.

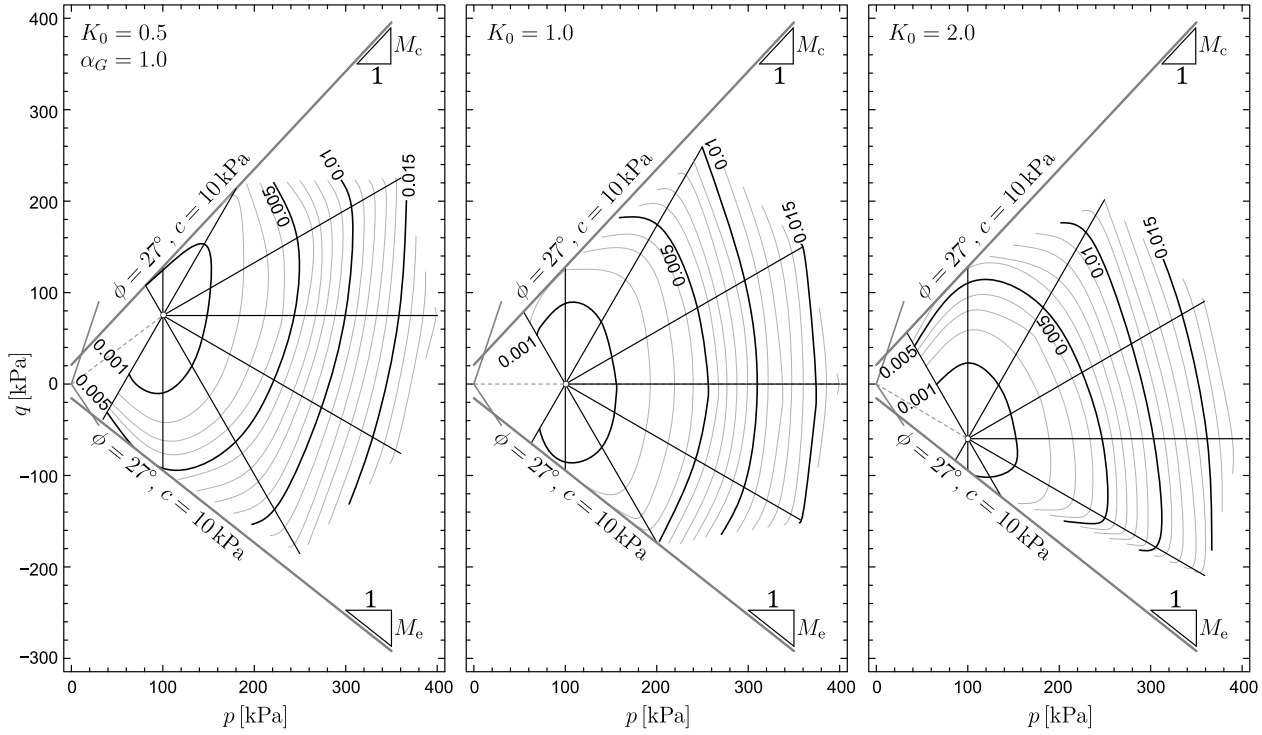

Fig. 6.6: The influence of initial stress conditions K_0 on stiffness changes presented in a form of accumulated generalised strain ϵ obtained from the simulation of drained triaxial radial stress paths

For $\alpha_G = 2.0$, the value of stiffness obtained for the A0X test is much higher, as compared to the isotropic case. Moreover, the stiffness degradation calculated from the C0X and B0X analyses is analogous and significantly lower than for the A0X and D0X. This behaviour suggest that, in the case of high horizontal stiffness, greater stiffness degradation is obtained when the sample is subjected to the compressive loading prior to the final shearing.

When the sample exhibits greater vertical stiffness, $\alpha_G = 0.7$, this pattern is completely different. The soil response to the C0X test is much greater than in other cases and is comparable to the D0X simulation. The lowest stiffness is obtained for the A0X path, with slightly higher values calculated from the B0X test. This behaviour can be explained by the shape of the isolines of accumulated generalised stain ϵ in Fig. 6.5. For a small compressive isotropic stress increment Δp, changes in stiffness are insignificant, but with isotropic unloading, strain is generated rapidly.

The influence of α_G is also notable in the shape of the calculated S-curves. The degradation of isotropic material occurs evenly - there is no increase in stiffness just before the stepwise degradation, as in the case of $\alpha_G = 2.0$. In contrast, for $\alpha_G = 0.7$, this trend is reversed - the stiffness degrades continuously up to the drop. The highest stiffness values for all paths are

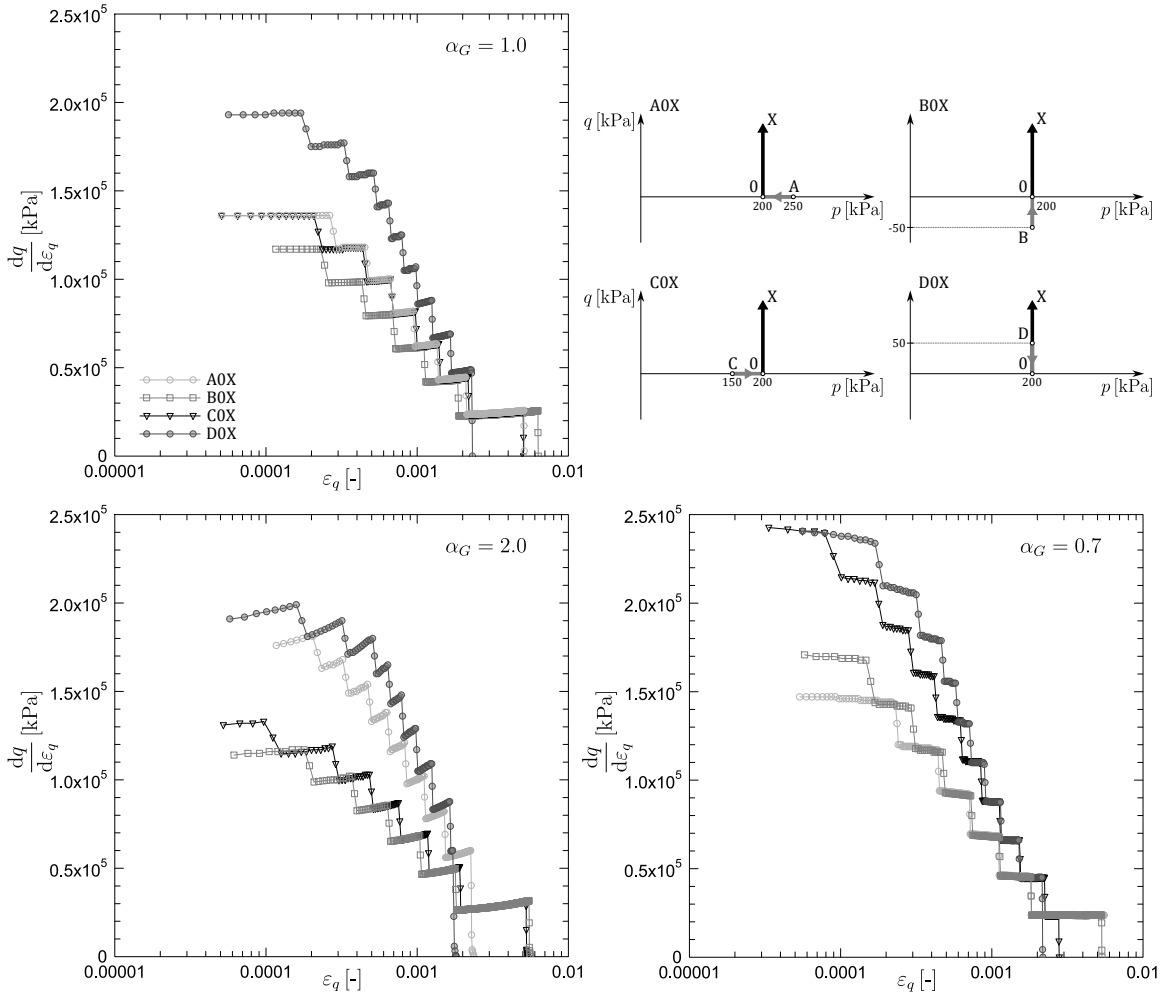

Fig. 6.7: The influence of the recent stress history on the stiffness degradation, presented as a relation between derivatives $\mathrm{d}q/\mathrm{d}\varepsilon_q$ and deviatoric strain ε_q. Three different values of the initial inherent cross-anisotropy coefficients $\alpha_G = 0.7, 1.0, 2.0$ are considered

obtained when $\alpha_G = 0.7$, and the lowest when $\alpha_G = 2.0$. However, the stiffness of the isotropic sample is approximately the same as that for $\alpha_G = 2.0$.

6.1.4 Validation of the model with some laboratory test results

Model validation is additionally carried out through non-standard parameter calibration. It is performed by simulating laboratory tests on singular material element and then adjusting the soil response so it corresponds to the measured results. Adopted parameter values of a tested soil are given in the corresponding figure. Presented in Fig. 6.8, calibration performed for two London Clay units, B2 and A3, is based on the laboratory test results presented in [67]. By

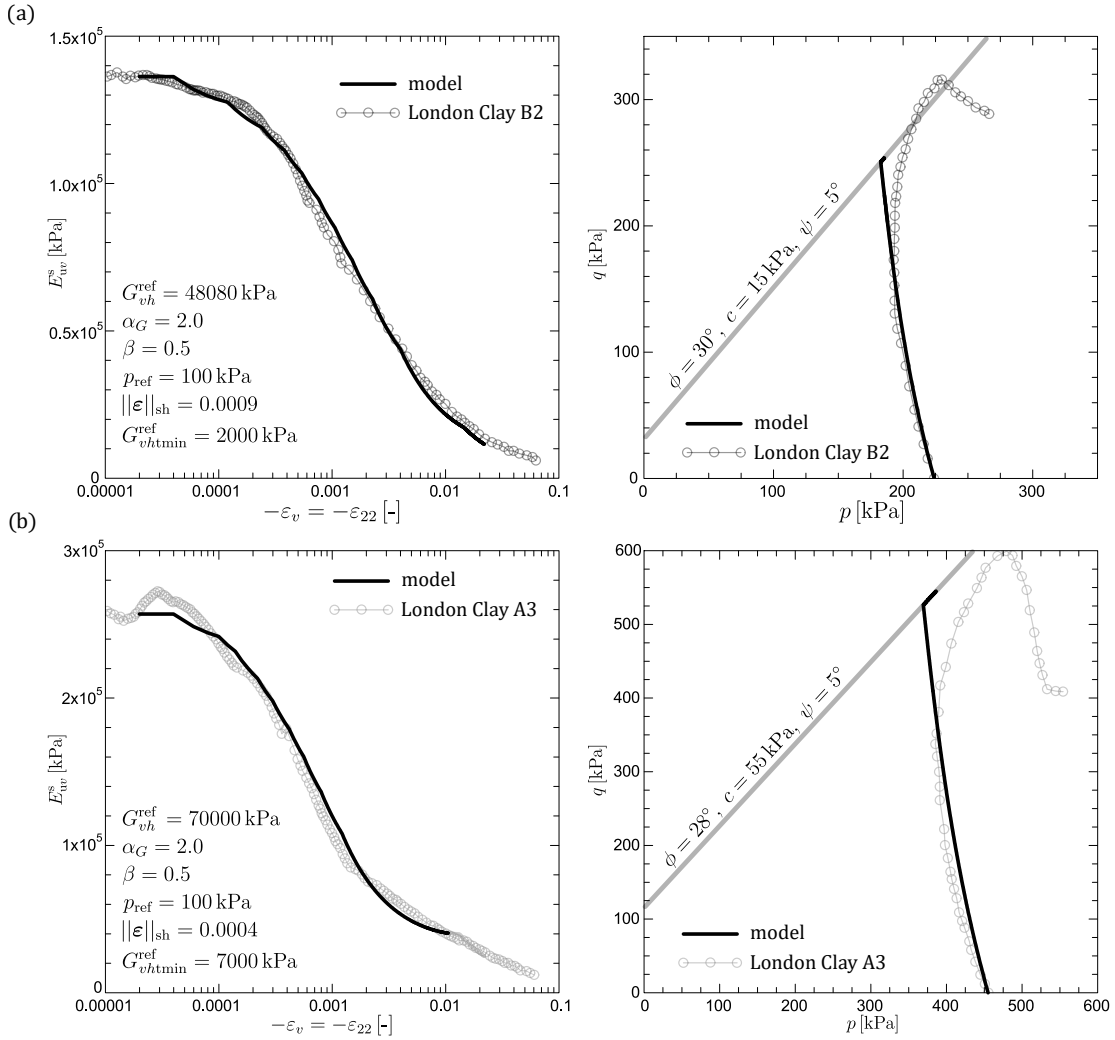

Fig. 6.8: Calibrations of the *AHEBrick* model stiffness and strength parameters for two units of London Clay: a) unit B2, b) unit A3. The obtained calculations are compared to the undrained triaxial compression test results [67]

matching the S-shaped curves, defining degradation of the secant undrained Young's modulus $E^{\mathrm{s}}_{\mathrm{uv}}$ with vertical strain ε_v it is possible to obtain the values of the following stiffness parameters: G^{ref}_{vh}, p_{ref}, $||\boldsymbol{\varepsilon}||_{\mathrm{sh}}$, $G^{\mathrm{ref}}_{vh\mathrm{tmin}}$. Anisotropy parameters α_G, β and shear strength constants c, ϕ, ψ are determined through simulation of undrained stress path in $p - q$ plane. The overall results obtained from numerical simulations show a very good agreement to the laboratory data. The calculated value of the inherent cross-anisotropy coefficient $\alpha_G = 2.0$ is consistent with the values of α_G presented in Tab. 3.1. Furthermore, according to [67], the average value of α_G, obtained from laboratory tests is considered to be $\alpha_G = 2.0$.

The results of analysis conducted on Vallerrica Clay and Todi Clay are shown in Fig. 6.9. Both soils were tested as part of the same research project, described in [36]. Undrained com-

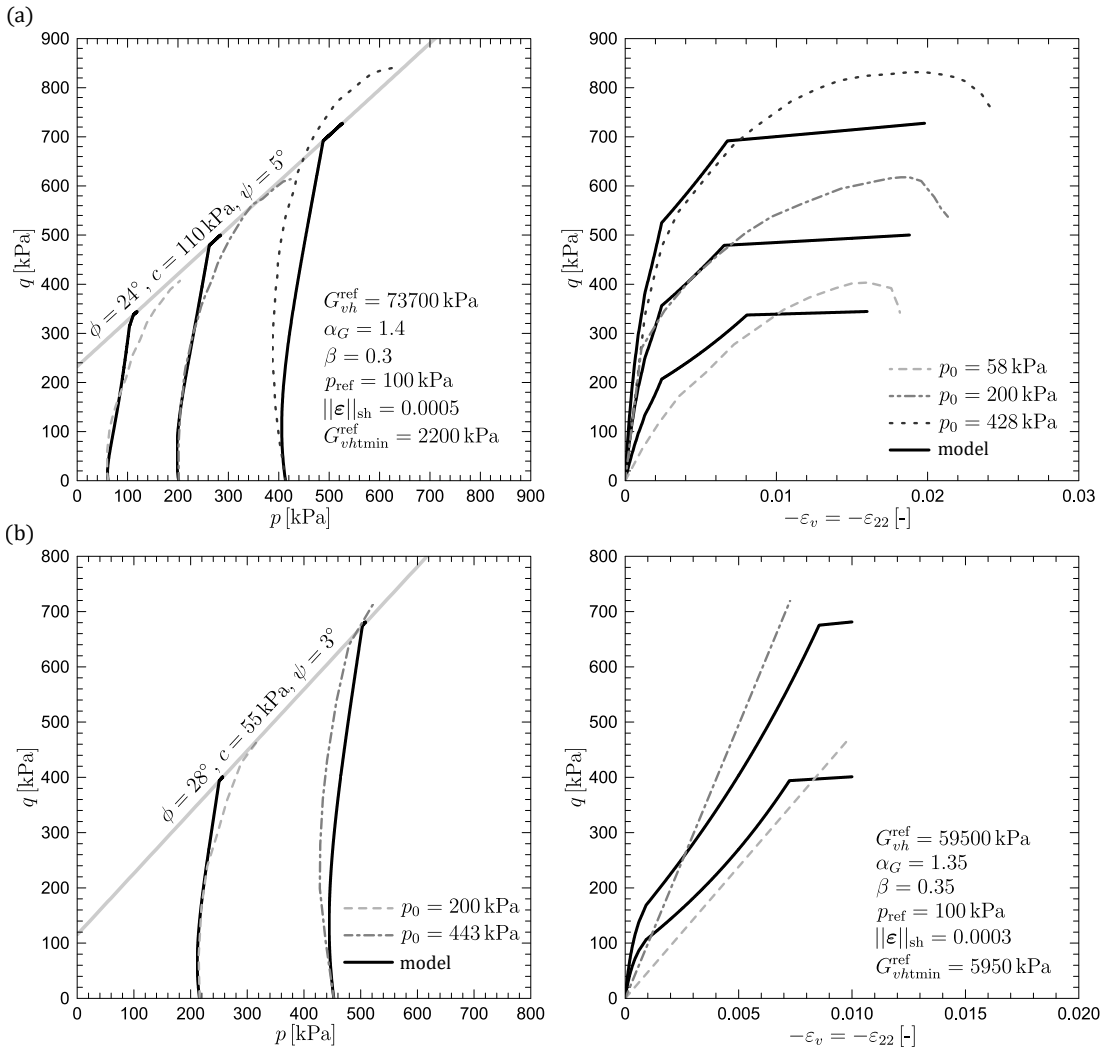

Fig. 6.9: Calibrations of the *AHEBrick* model stiffness and strength parameters compared to the undrained triaxial compression test results conducted on a) Vallerrica Clay, b) Todi Clay [36]

pression tests on Vallerrica Clay were carried out for three samples subjected to different initial isotropic stress: $p_0 = 58\,\text{kPa}$, $p_0 = 200\,\text{kPa}$, $p_0 = 428\,\text{kPa}$. Parametric calibration was performed based on stress paths in $p - q$ plane and compression curves $\varepsilon_v - q$. The adopted value of $\alpha_G = 1.4$ gives satisfactory results, as the initial inclination of stress paths obtained from the laboratory tests and the numerical simulations is consistent. Additionally, the initial stiffness values are a very good match to the test data, in particular for samples consolidated to $p_0 = 200\,\text{kPa}$ and $p_0 = 428\,\text{kPa}$ stress conditions. In contrast, for larger strains the calculated response deviate substantially from the measurements.

The same set of laboratory tests was performed on Todi Clay. Tests were carried out for initial stress conditions of $p_0 = 200\,\text{kPa}$ and $p_0 = 443\,\text{kPa}$. The simulated stress path curves match the experimental results closely, indicating that the chosen anisotropy parameters α_G, β are appropriate. However, the stiffness values do not show the same level of agreement, as the initial stiffness in the simulation is too high.

The influence of bedding plane orientation on material properties

Triaxial compression tests on anisotropic soils can be conducted on samples cut at different orientations relative to the bedding plane. Typically, samples compressed in directions normal (S-sample, $\theta = 0°$) and parallel (P-sample, $\theta = 90°$) to the plane of isotropy are examined. In triaxial test simulations on a single element, only a S-sample can be modeled under axisymmetric conditions, due to its uniform deformation, see Fig. 6.10. In contrast, simulating triaxial compression on a P-sample results in a non-uniform radial strain generation. Such behaviour can be only be modelled as element test assuming three-dimensional calculations on a regular hexahedral element [45]. Samples cut at angles other than $\theta = 0°$ or $\theta = 90°$ are referred to as Z-samples, with $\theta = 45°$ being the most commonly tested orientation. When testing such samples, shearing and non-uniform deformation are already generated during isotropic consolidation. For this reason, mechanical properties of Z-samples cannot be determined through element tests. Instead, they must be analysed by simulating the full triaxial compression test, incorporating the appropriate geometry and boundary conditions [87].

The inclination angle of the plane of isotropy θ has a significant impact on the response of soil in undrained conditions. As shown in Fig. 6.10, the stress path for the S-sample is directed maximally to the left, as the generation of water pressure in the pores during compression is then the greatest. On the other hand, in the case of the P-sample, the pore water pressure is

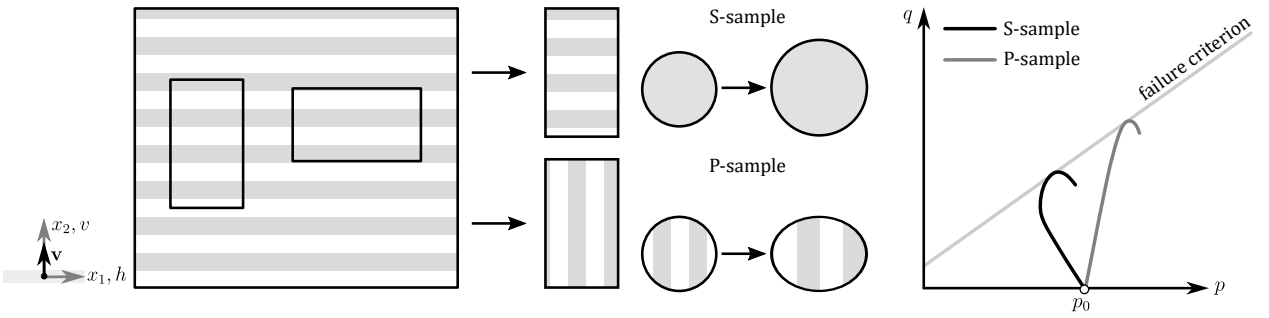

Fig. 6.10: Triaxial compression test conducted on samples cut at different angles relative to bedding plane orientation. Deformation of S-sample is uniform, whereas in case of P-sample, the radial strain generation is influenced by α_G coefficient. Due to differences in pore pressure, the course of the obtained undrained stress paths and the resulting shear strength is dependent on the bedding plane orientation [132, 169]

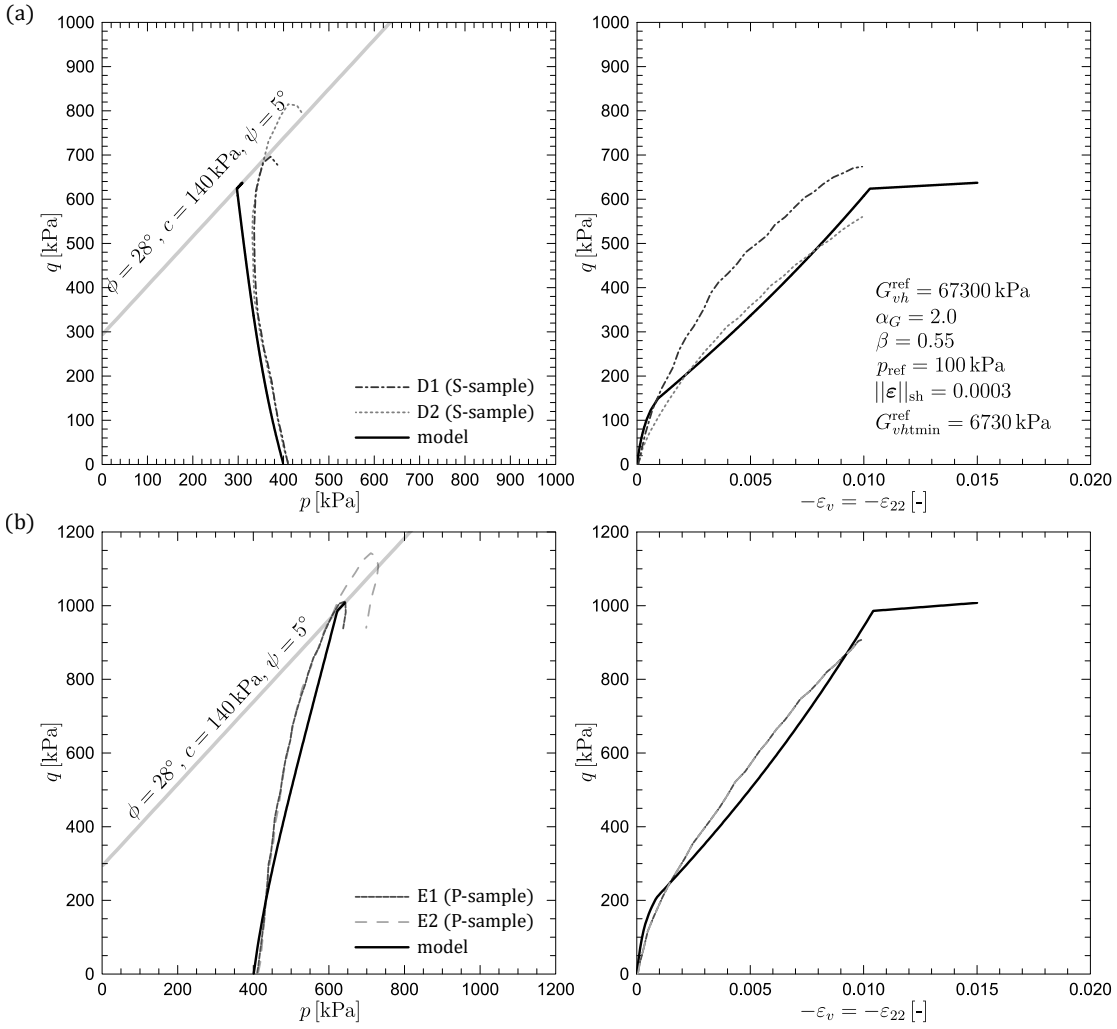

Fig. 6.11: Calibrations of the *AHEBrick* model stiffness and strength parameters compared to the undrained compression test results on London Clay: a) S-samples, b) P-samples [176]

the lowest, resulting in the path being directed maximally to the right. The orientation of the stress paths obtained for intermediate inclinations is within the range defined by $\theta = 0°$ and $\theta = 90°$ [87, 168].

The following parametric calibration is based on the results of triaxial compression tests conducted on S- and P-samples. The microstructure tensor $\mathbf{M}$ is defined according to Eq. 5.3, however, in case of $\theta = 0°$, it simplifies to $\mathbf{M} = \text{diag}(0, 1, 0)$. In Fig. 6.11 the stress paths in $p-q$ plane and compression curves $\varepsilon_v - q$ under undrained conditions are presented for London Clay [176]. The samples were subjected to isotropic consolidation $p_0 = 400\,\text{kPa}$ and then compressed. The calculated stress paths acquired for the adopted anisotropy and strength parameter values show strong consistency with the stress paths obtained from laboratory tests on both S- and

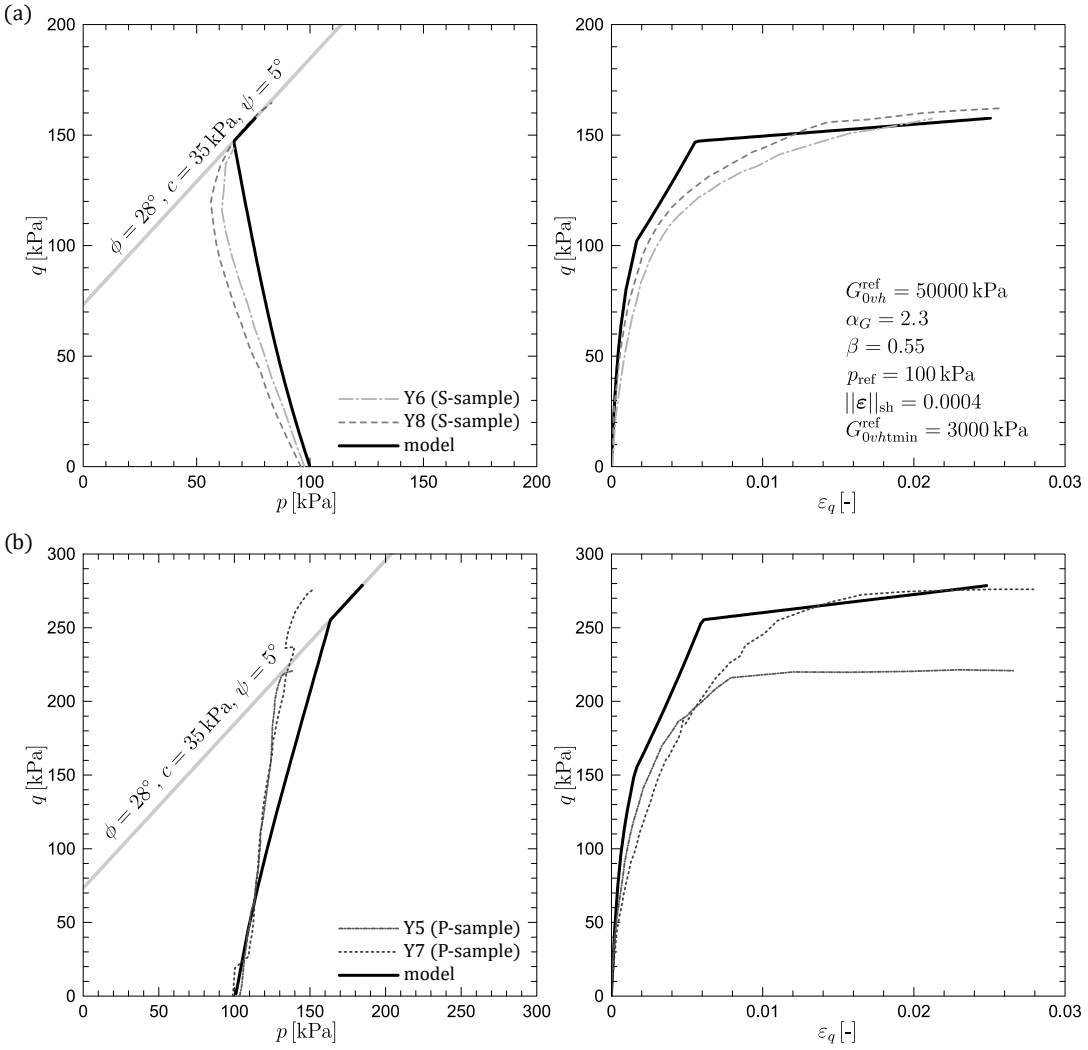

Fig. 6.12: Calibrations of the *AHEBrick* model stiffness and strength parameters compared to the undrained compression test results on Oxford Clay: a) S-samples, b) P-samples [132]

P-samples. The calibrated stiffness parameters also match the test results closely, particularly for the P-sample tests, where the measured and calculated compression curves nearly overlap. Furthermore, the soil stiffness values and the cross-anisotropy coefficient $\alpha_G = 2.0$ correspond well to those determined through the parameter calibration on London Clay shown in Fig. 6.8.

The simulations of triaxial compression tests on Oxford Clay samples, presented in Fig. 6.12, are compared to laboratory data obtained from [132]. Laboratory tests were conducted on two S-samples and two P-samples, isotropically consolidated to $p_0 = 100\,\mathrm{kPa}$. The best agreement between the calculated and measured stress paths was obtained for parameters $\alpha_G = 2.3$ and $\beta = 0.55$. Although the value of parameter $\alpha_G = 2.3$ is relatively high, similar

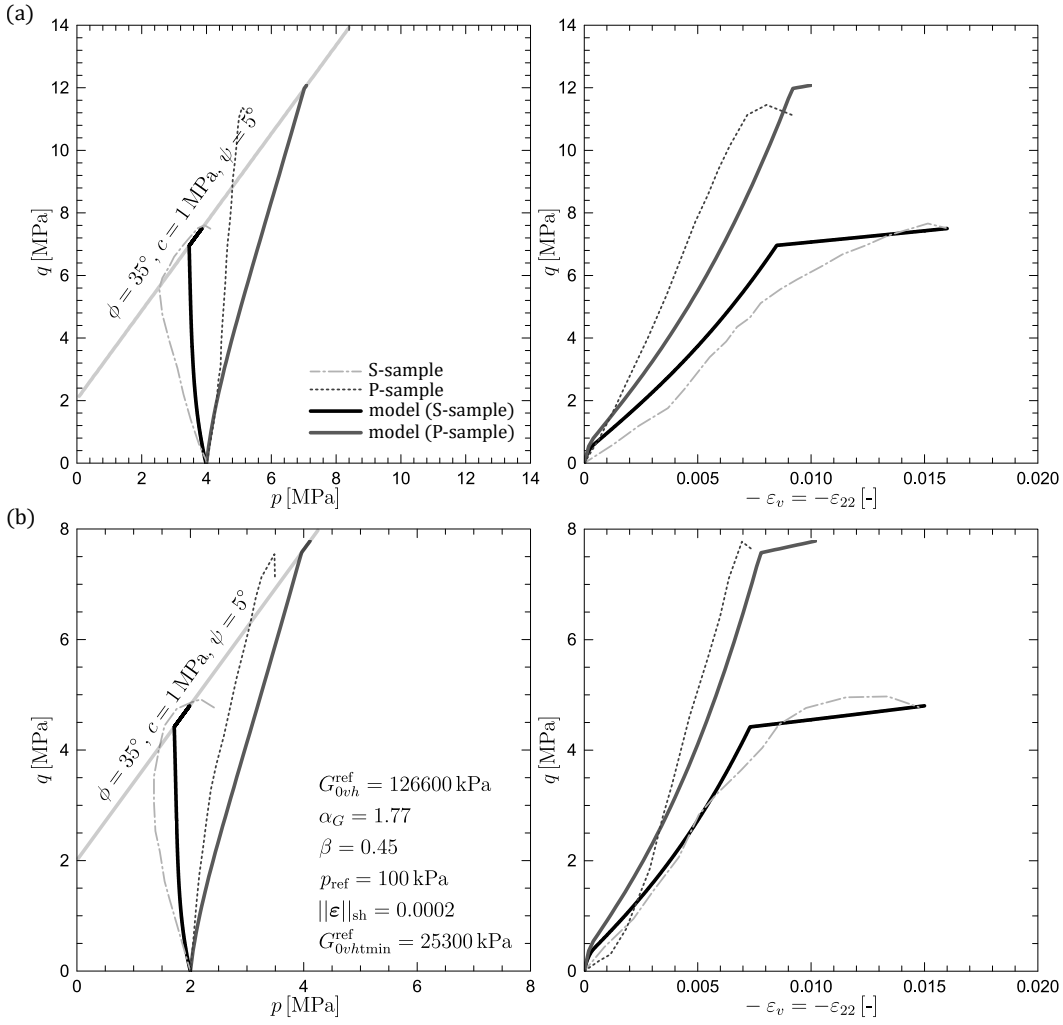

Fig. 6.13: Calibrations of the *AHEBrick* model stiffness and strength parameters compared to the undrained compression test results on Opalinus Clay: a) samples isotropically consolidated to $p_0 = 4.0\,\mathrm{MPa}$, b) samples isotropically consolidated to $p_0 = 2.0\,\mathrm{MPa}$ [87]

value has been reported in [29]. The initial inclination of the stress paths is consistent between the tests and calculations, though the discrepancies become more pronounced along with the increase of deviatoric stress q. In the case of compression curves obtained for the assumed stiffness parameter values, the fit between the calculation and laboratory results is very good, in particular for S-samples, where the soil behaviour is reproduced with high accuracy.

The laboratory tests, illustrated in Fig. 6.13, were performed on Opalinus Clay samples consolidated isotropically to $p_0 = 4\,\mathrm{MPa}$ and $p_0 = 2\,\mathrm{MPa}$ [87]. The adopted strength parameters ϕ and c are quite high, but they correspond well to the values obtained from laboratory tests reported in [168]. The initial inclination of the stress paths, resulting from $\alpha_G = 1.77$ and

$\beta = 0.55$, is consistent with the laboratory data, however, as the value of q increases, the calculated stress paths begin to deviate from the measurements. The remaining parameters were determined on the basis of compression curves. The soil response for the defined values is satisfactory compared to measured curves. Although the assumed value of the initial stiffness G_{vh} is generally high, it remains reasonable, as Opalinus Clay can be classified as both soil and rock.

6.2 Exemplary geotechnical BVPs

In this section the influence of anisotropy on soil-structure interaction is examined by analysing simple geotechnical boundary value problems. The influence of the soil response is investigated for three values of the inherent anisotropy coefficient $\alpha_G = 0.7, 1.0, 2.0$ and three initial stress states $K_0 = 0.5, 1.0, 2.0$. The remaining model parameters are kept constant and are listed in Tab. 6.2. The parameter values $\alpha_G = 0.7$ and $K_0 = 0.5$ do not occur in stiff overconsolidated soils. Nevertheless, they are included in this analysis in order to fully investigate the behaviour of the model.

Table 6.2: Set of the *AHEBrick* model parameters used in the analysis of the exemplary boundary value problems

	Parameter	Clay
Small strain stiffness	G_{vh}^{ref} [kPa]	50000
	β [-]	0.5
	α_G [-]	0.7, 1.0, 2.0, 3.0
	p_{ref} [kPa]	100
Stiffness degradation	$G_{vh\mathrm{tmin}}^{\mathrm{ref}}$ [kPa]	5000
	$\|\|\boldsymbol{\varepsilon}\|\|_{\mathrm{sh}}$ [-]	0.0007
Shear strength criterion	ϕ [°]	27
	c [kPa]	10
	ψ [°]	5
	p_{te} [kPa]	0
Unit weight and initial stress state	γ [kN/m^3]	20.0
	K_0 [-]	0.5, 1.0, 2.0

In order to examine the influence of pure inherent cross-anisotropy on deformation different values of α_G are considered at the isotropic stress state $K_0 = 1.0$. In contrast, stiffness changes, induced by the initial stress conditions K_0, can be investigated considering isotropic microstructure $\alpha_G = 1.0$. Additionally, the *AHEBrick* model is able to simulate pure stress-induced anisotropy if soil microstructure and initial stress state are isotropic ($\alpha_G = 1.0$, $K_0 = 1.0$). In

order to isolate this effect, the comparison to the reference stress-dependent isotropic stiffness is needed. It can be introduced via a hypoelastic law using Hooke's linear elastic stiffness with a fixed Poisson's ratio ν and a reference Young's modulus E^{ref} that increases with mean stress (see Eq. 2.4). Stiffness parameters of hypoelastic isotropic kernel are selected so they correspond to the anisotropic *AHEBrick* material, with isotropic microstructure $\alpha_G = 1.0$, shown in Tab. 6.2: $E^{\text{ref}} = 120000\,\text{kPa}$, $\nu = 0.2$, $m = 0.5$, $p_{\text{ref}} = 100\,\text{kPa}$, $E^{\text{ref}}_{\text{min}} = 0.1 \cdot E^{\text{ref}} = 12000\,\text{kPa}$. In some cases, mixed anisotropy ($\alpha_G \neq 1.0$, $K_0 \neq 1.0$) is examined to check soil response to the most complex conditions.

The findings of the following analyses have also been published in [46] and [101] for cases of tunnel drilling and open-pit excavation.

6.2.1 Tunnel drilling

The influence of stiffness anisotropy on tunneling problems is considered in plane strain and three dimensional conditions. In order to obtain the comparable soil response, the same geometrical, material and flow properties are assumed for both cases. In the used FE code [26], mesh regularisation cannot be performed. Therefore, to prevent mesh-dependent behaviour, a process was used that involved first applying a fine regular mesh throughout the entire domain. Next, the size of elements located furthest from the tunnel was increased until the results changed significantly.

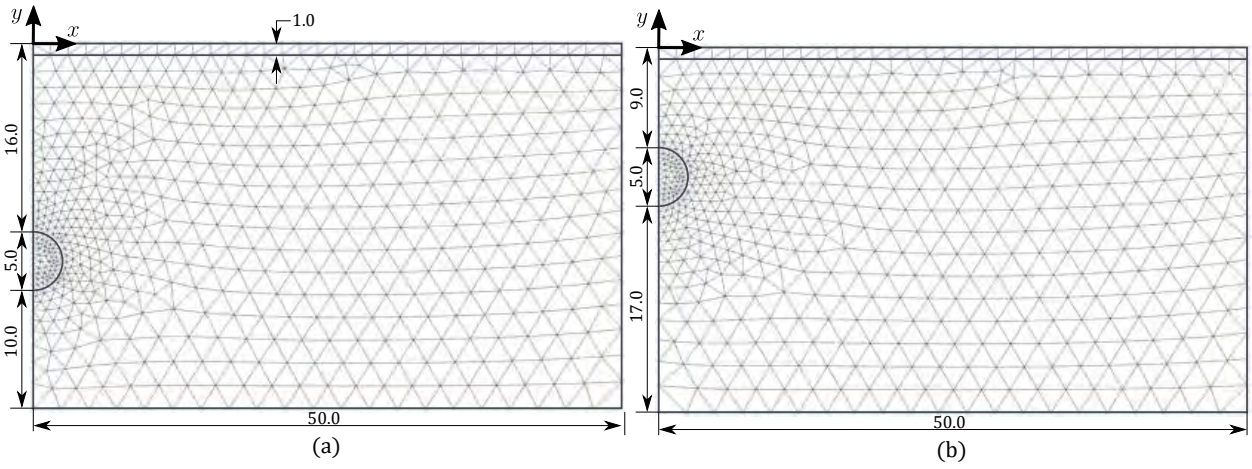

Fig. 6.14: Geometry and FE mesh of two analysed tunnel cases in plane strain conditions: (a) deep tunnel: 1213 15-node triangular elements, 9992 nodes, (b) shallow tunnel: 1162 15-node triangular elements, 9578 nodes

Plane strain model

In plane strain conditions, a 5.0-m-diameter tunnel is modelled at two overburden depths: 16.0 m (deep tunnel) and 9.0 m (shallow tunnel). The geometry of analysed cases is presented in Fig. 6.14. Due to the symmetry, only one half of the problem, with the dimensions of $50.0\,\mathrm{m} \times 31.0\,\mathrm{m}$, is considered. The behaviour of the primary 30.0 m thick clay layer is described with the *AHEBrick* model. The material parameters are presented in Tab. 6.2. In order to avoid the stiffness changes at the low stress level, a drained 1.0 m layer of granular fill at the surface is modeled with a standard Mohr-Coulomb material ($E = 70000\,\mathrm{kPa}$, $\nu = 0.2$, $\phi = 30°$, $c = 3.0\,\mathrm{kPa}$, $\psi = 0.0°$, $\gamma = 18.0\,\mathrm{kN/m^3}$). Around the tunnel face a 0.2 m thick concrete lining is applied (plate elements, $EA = 6 \cdot 10^6\,\mathrm{kN/m}$, $EI = 20 \cdot 10^3\,\mathrm{kNm^2/m}$, $\nu = 0.2$). The groundwater table is located 1.0 m below the surface. No-flow boundary conditions are applied on the bottom and sides of the FE domain and seepage is allowed along the tunnel liner.

The tunnel boring machine (TBM) excavation is simulated via the lining contraction method available in the FE code [26]. In the first calculation phase, the soil and water within the tunnel face are deactivated and the lining is installed by the activation of plate elements.

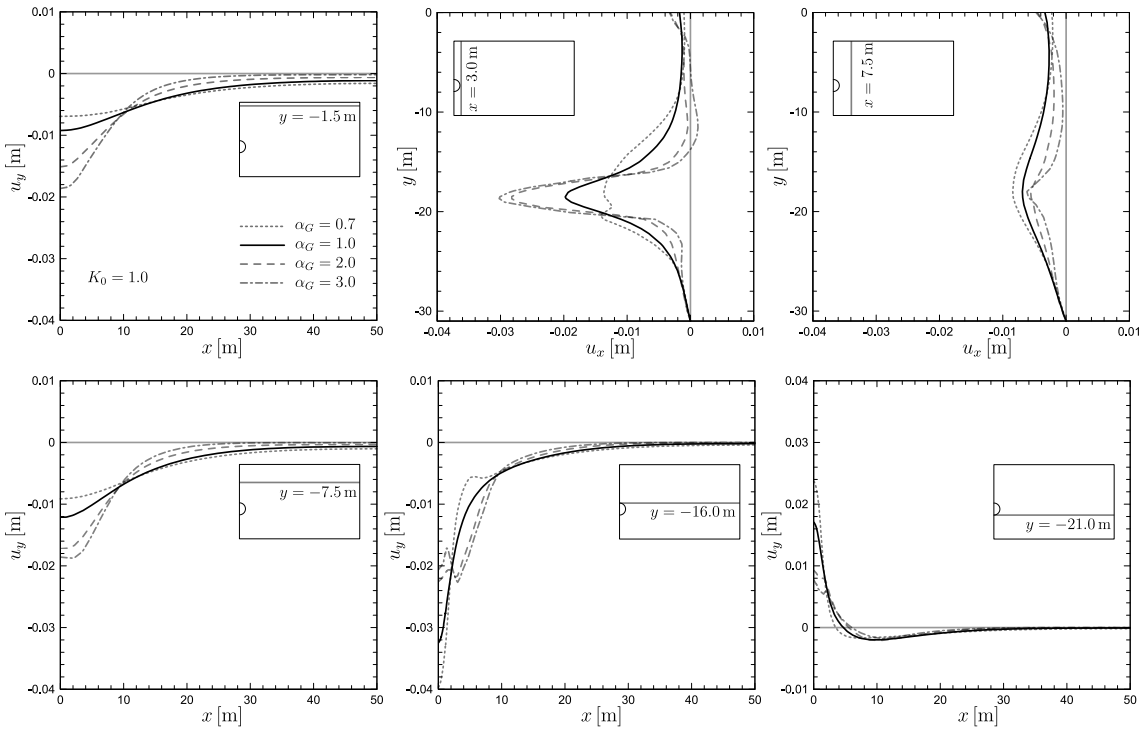

Fig. 6.15: Deep tunnel; the influence of the inherent cross-anisotropy coefficient α_G on the settlement u_y and horizontal displacement component u_x profiles along the selected cross-sections. The initial isotropic stress state $K_0 = 1.0$ is considered

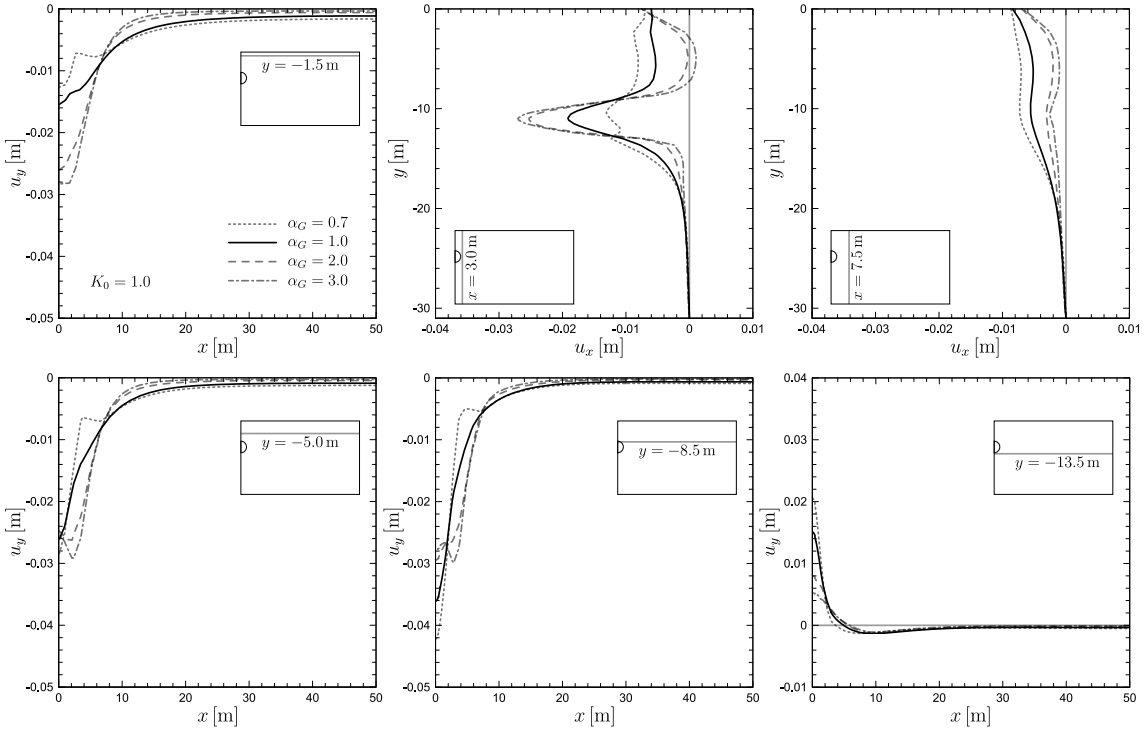

Fig. 6.16: Shallow tunnel; the influence of the inherent cross-anisotropy coefficient α_G on the settlement u_y and horizontal displacement component u_x profiles along the selected cross-sections. The initial isotropic stress state $K_0 = 1.0$ is considered

In the subsequent phase, the lining is uniformly contracted by 1.0 % to mimic tunneling-induced deformation. The numerical simulations are carried out as a plastic calculation type (undrained), for which consolidation and the effect of time are omitted.

The influence of pure initial inherent cross-anisotropy is examined for different values of cross-anisotropy coefficient $\alpha_G = 0.7, 1.0, 2.0, 3.0$, at the isotropic stress state $K_0 = 1.0$. The obtained results are presented in a form of settlement troughs and horizontal displacement profiles for the selected cross-sections. Fig. 6.15 illustrates the obtained deformation for the case of the deep tunnel.

The influence of cross-anisotropy coefficient α_G is obvious. As the value of α_G increases, the surface settlement troughs ($y = -1.5\,\mathrm{m}$) become both deeper and steeper; the same trend holds at $y = -7.5\,\mathrm{m}$. However, directly above the tunnel lining ($y = -16.0\,\mathrm{m}$) the inverse behaviour can be observed - the lower the α_G value is, the steepness and depth of the trough is greater. Moreover, along the cross-section located directly below the tunnel ($y = -21.0\,\mathrm{m}$), the soil heave substantially increases for the low values of α_G. Additionally, the deformation near the tunnel gets noticeably irregular for large values of cross-anisotropy coefficients. In terms of horizontal displacements a pattern is reversed - for the profile closer to the tunnel ($x = 3.0\,\mathrm{m}$),

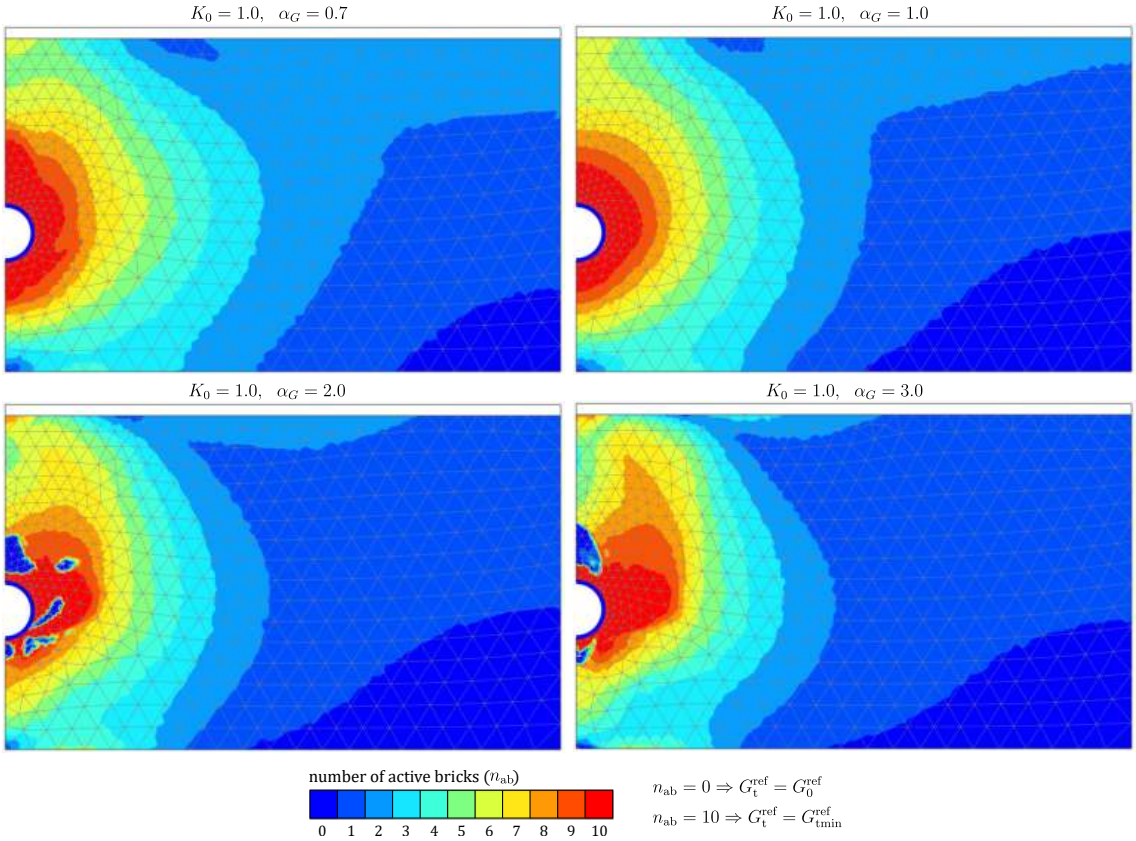

Fig. 6.17: Deep tunnel contraction phase; maps of stiffness degradation for different values of α_G at isotropic stress state $K_0 = 1.0$. The intensity of stiffness degradation is indicated by the number of active bricks n_{ab}

larger α_G value produces greater lateral movement, whereas farther out ($x = 7.5\,\mathrm{m}$) smaller horizontal deformations are obtained with the increase of α_G. Fig. 6.16 shows the influence of pure initial inherent cross-anisotropy on soli deformation induced by the shallow tunnel drilling. The overall deformation patterns and their sensitivity to α_G mirror the results of the deep tunnel analysis, however the settlement troughs are more extensive and less smooth. It is due to the proximity of the tunnel crown to the ground surface which results in the appearance of the localised shear zones.

The influence of pure cross-anisotropy on stiffness degradation is also apparent. The maps of stiffness degradation, after the lining contraction calculation phase, are presented for deep and shallow tunnel analyses in Figs. 6.17 and 6.18, respectively. Each color indicates the number of active bricks n_{ab} that are being pulled, where dark blue means the maximum initial soil stiffness G_{vh}^{ref}, and red means that all 10 bricks are active and the stiffness has reached its minimum value $G_{vh\mathrm{tmin}}^{\mathrm{ref}}$. In the case of a deep tunnel, the region where the minimum stiffness ($n_{\mathrm{ab}} = 10$) is reached, changes its shape proportionally to the value of cross-anisotropy coefficient α_G. When

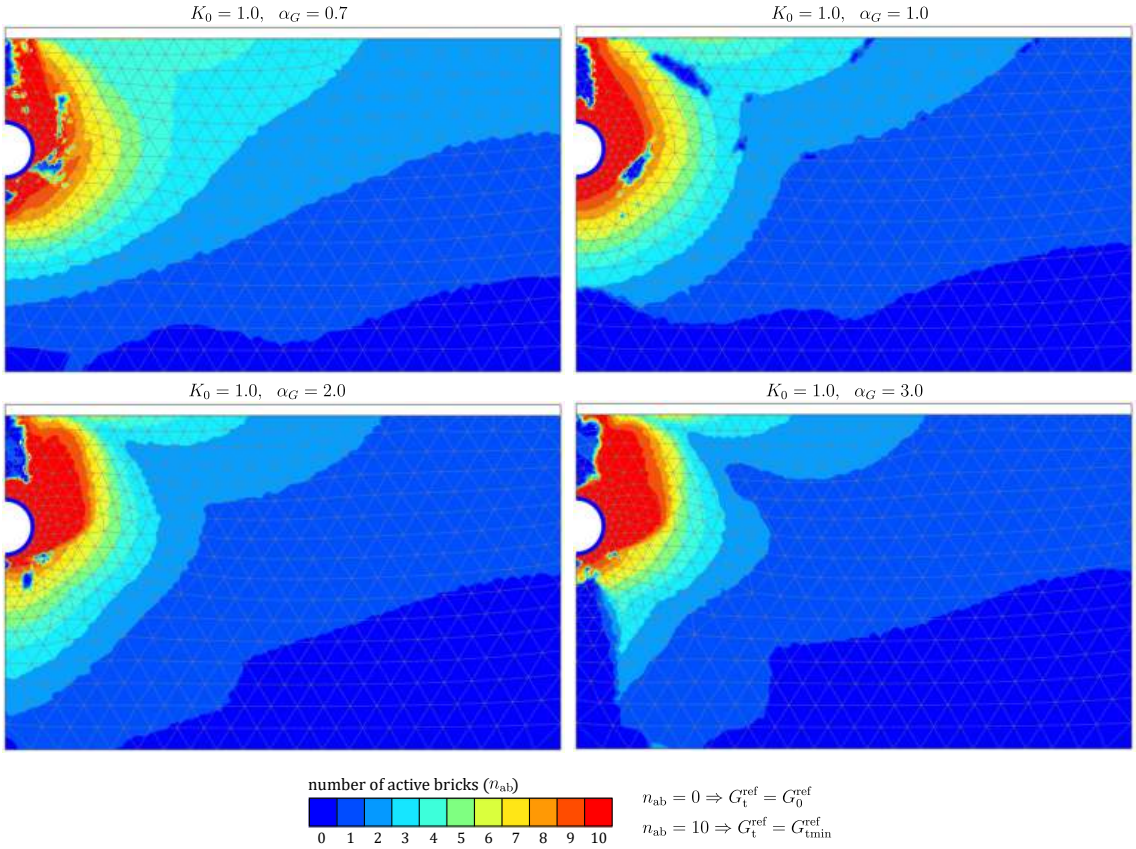

Fig. 6.18: Shallow tunnel contraction phase; maps of stiffness degradation for different values of α_G at isotropic stress state $K_0 = 1.0$. The intensity of stiffness degradation is indicated by the number of active bricks n_{ab}

$\alpha_G = 0.7$, indicating higher stiffness in the vertical direction, this region stretches vertically. For isotropic stiffness $\alpha_G = 1.0$, the region is uniformly distributed. When the horizontal stiffness is higher ($\alpha_G > 1.0$), the area of minimum tangent stiffness $G_{vh\mathrm{tmin}}^{\mathrm{ref}}$ becomes stretched horizontally around the tunnel. This correlation may be the cause of the change in the steepness of the obtained settlement profiles. In addition, for high values of α_G some zones of localised unloading ($n_{\mathrm{ab}} = 0$) occurs, which could explain the irregular shape of settlement troughs in the direct vicinity to the tunnel lining. The stiffness degradation maps, obtained for the shallow tunnel calculations, are characterised by the presence of numerous localised unloading regions that develop, not only in the immediate vicinity of the tunnel, but within whole FE domain. Furthermore, for very high values of cross-anisotropy, $\alpha_G = 3.0$, under the tunnel lining, the unloading occurs up to the bottom boundary of the model.

The influence of initial stress state K_0 on the surface settlement profiles is illustrated for the case of the deep tunnel in Fig. 6.19, and for the shallow tunnel example in Fig. 6.20. The values $K_0 = 0.5, 1.0, 2.0$ are analysed for different anisotropy coefficients $\alpha_G = 0.7, 1.0, 2, 0$. In

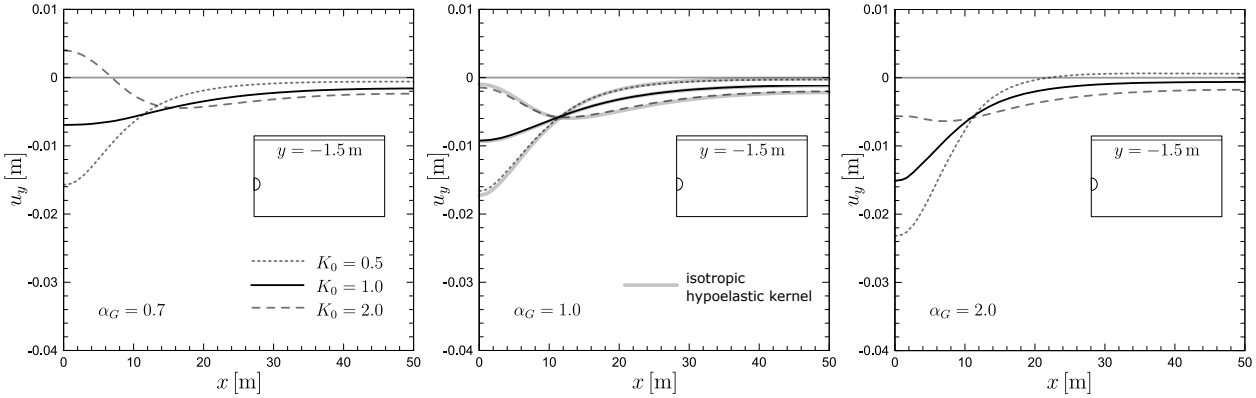

Fig. 6.19: Deep tunnel; the influence of the initial stress state K_0 on the surface settlement u_y profiles. Different values of cross-anisotropic coefficient α_G are considered. The response of the model with purely isotropic hypoelastic stiffness is shown for comparison ($\alpha_G = 1.0$)

all cases, the settlement troughs obtained for $K_0 = 0.5$ show the highest depth and steepness, with the maximum deformation occurring at $K_0 = 0.5$ and $\alpha_G = 2.0$. Conversely, at $K_0 = 2.0$, the troughs arch upwards over the tunnel and heave above the original ground level can be observed for $\alpha_G = 0.7$ in case of the deep tunnel, and for $\alpha_G = 0.7, 1.0$ for the shallow tunnel.

In order to determine the influence of pure stress-induced anisotropy, the comparison of the results obtained from the calculations conducted for the fully isotropic hypoelastic kernel and *AHEBrick* material, that exhibits pure stress-induced anisotropic behaviour ($\alpha_G = 1.0$), has been conducted. Illustrated in Figs. 6.19 and 6.20 settlement profiles nearly overlap, which means that the influence of stress-induced anisotropy on tunnel drilling deformation is negligible and appears to have no practical importance.

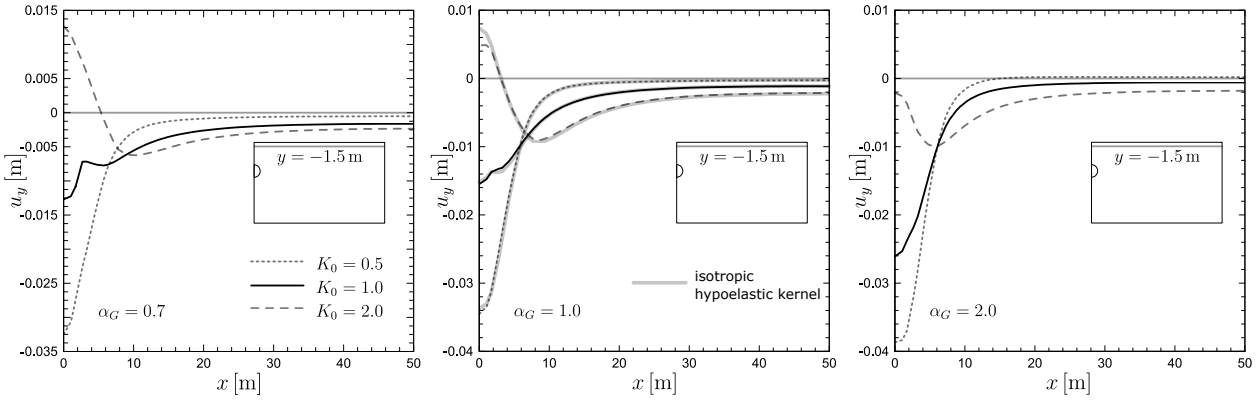

Fig. 6.20: Shallow tunnel; the influence of the initial stress state K_0 on the surface settlement u_y profiles. Different values of cross-anisotropic coefficient α_G are considered. The response of the model with purely isotropic hypoelastic stiffness is shown for comparison ($\alpha_G = 1.0$)

The effect of stress-induced anisotropy is also insignificant in terms of stiffness degradation, shown in Fig. 6.21 (deep tunnel) and Fig. 6.22 (shallow tunnel). The maps obtained for the isotropic hypoelastic kernel analysis are almost identical to that calculated with the *AHEBrick* material model, for $\alpha_G = 1.0$ and $K_0 = 1.0$. Slight differences are apparent in the case of the shallow tunnel - here it can be seen that stress-induced anisotropy is responsible for the appearance of localised shear zones. In general, the largest unloading occurs for $K_0 = 0.5$, and for the shallow tunnel analysis, the soil under the tunnel face achieves its maximum stiffness.

The deformation and bending moment distribution of the deep tunnel lining, subjected to 1% contraction, is presented in Fig. 6.23, for $\alpha_G = 0.7, 1.0, 2.0, 3.0$ and $K_0 = 0.5, 1.0, 2.0$. Under the initial isotropic stress state ($K_0 = 1.0$), the polar graphs of lining deformation and bending moments are distributed horizontally, if $\alpha_G < 1.0$, and vertically for $\alpha_G > 1.0$. In case of

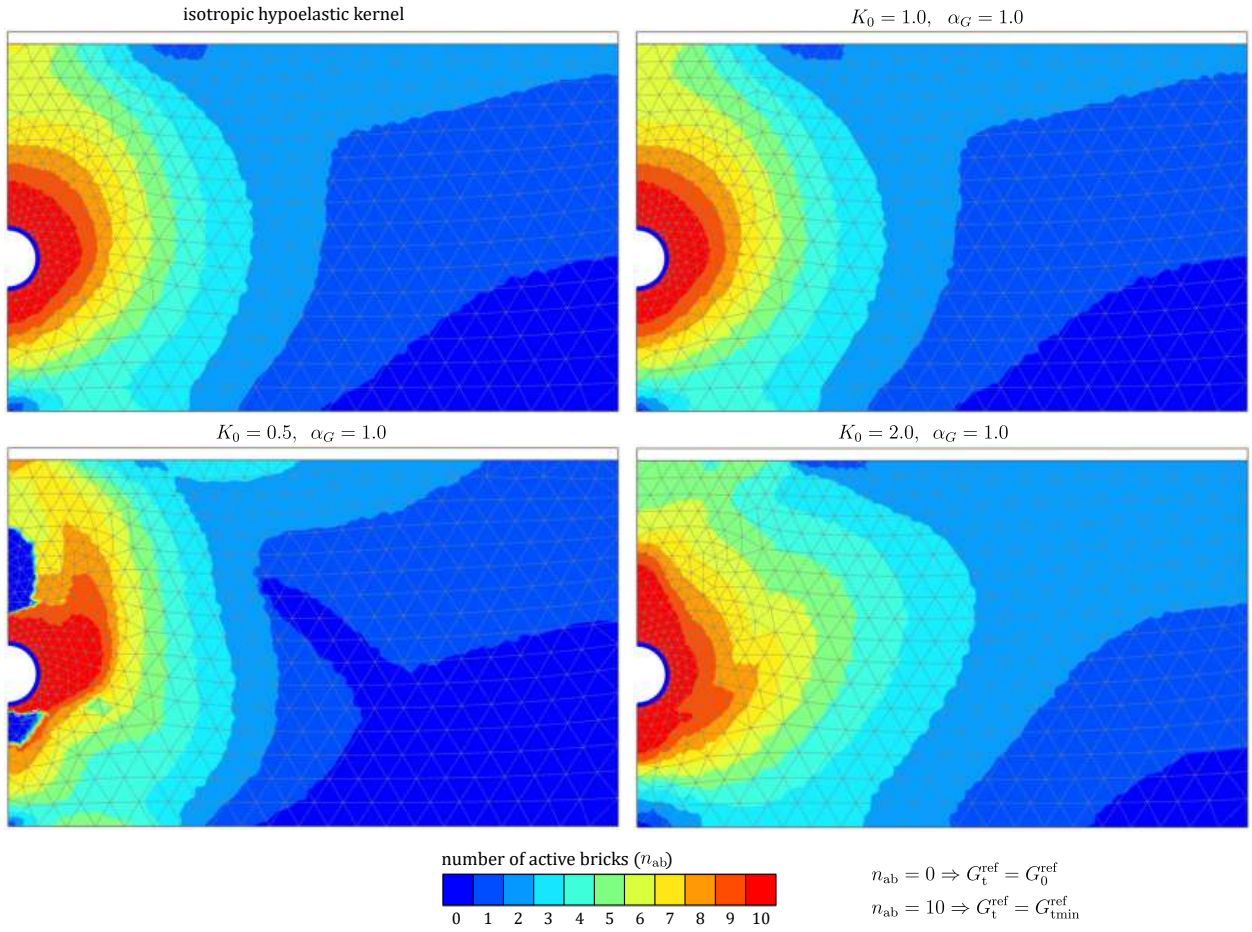

Fig. 6.21: Deep tunnel contraction phase; maps of stiffness degradation for different values of initial stress state K_0 and inherent isotropic material $\alpha_G = 1.0$. The response of the model with purely isotropic hypoelastic stiffness is shown for comparison. The intensity of stiffness degradation is indicated by the number of active bricks n_{ab}

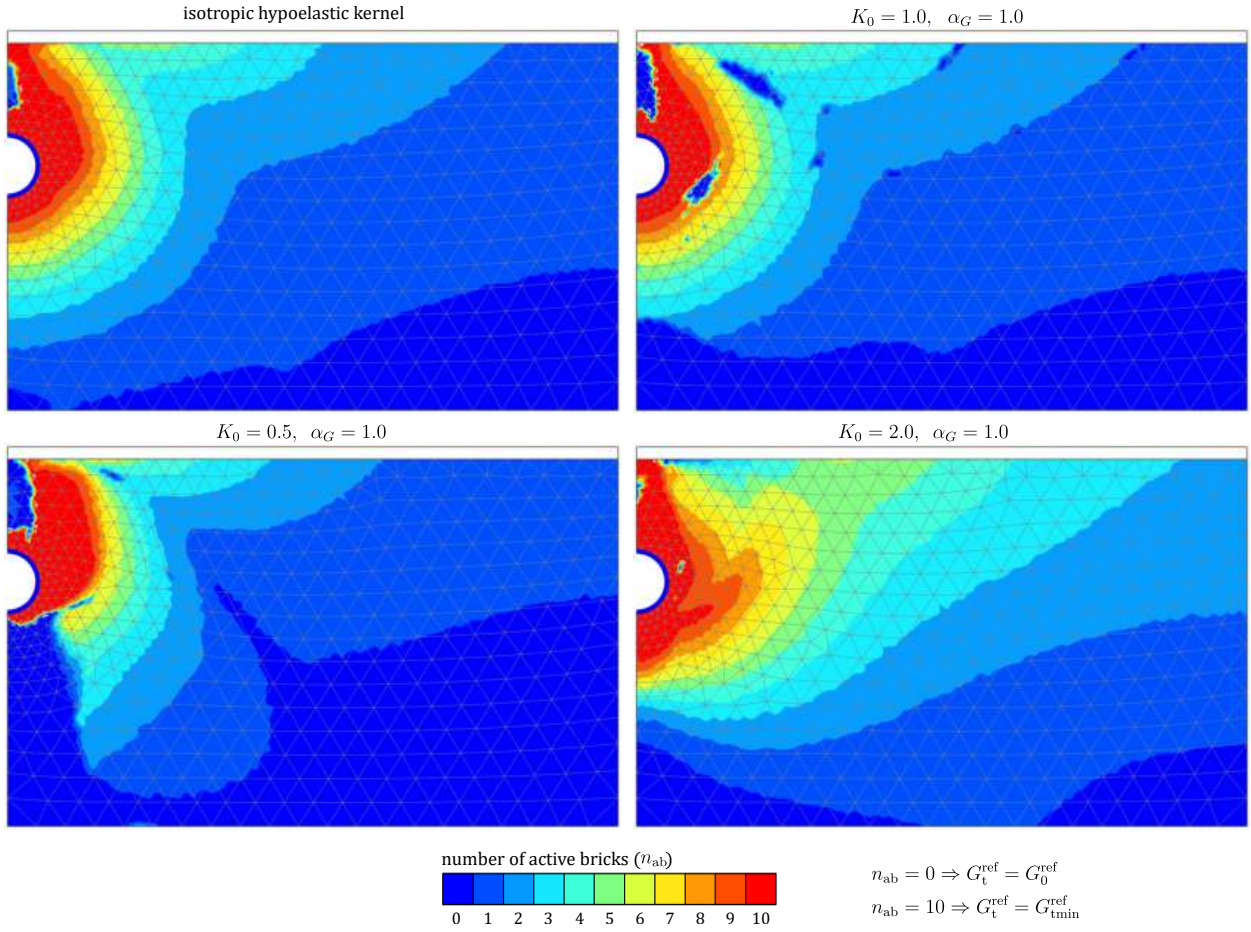

Fig. 6.22: Shallow tunnel contraction phase; maps of stiffness degradation for different values of initial stress state K_0 and inherent isotropic material $\alpha_G = 1.0$. The response of the model with purely isotropic hypoelastic stiffness is shown for comparison. The intensity of stiffness degradation is indicated by the number of active bricks n_{ab}

inherent isotropy ($\alpha_G = 1.0$) the liner contracts uniformly and bending moments are negligible. Given $K_0 = 0.5$, the shape of all graphs is always vertical and this effect is magnified with increase of α_G. If initial stress is higher in horizontal direction ($K_0 = 2.0$), the deformation and bending moment distribution is horizontal for $\alpha_G \leq 1.0$, however for high cross-anisotropy coefficient $\alpha_G = 2.0$, the deflection is nearly isotropic and the obtained moments are very small. The same analysis, conducted for the shallow tunnel is illustrated in Fig. 6.24. The obtained response for $K_0 = 2.0$ is nearly identical to the deep tunnel calculations. For $K_0 = 0.5, 1.0$ the lining deformation and bending moments are smaller and their shape is less pronounced. The biggest differences are seen for $K_0 = 0.5$ and $\alpha_G = 0.7$, as for this case almost no bending moment occurs.

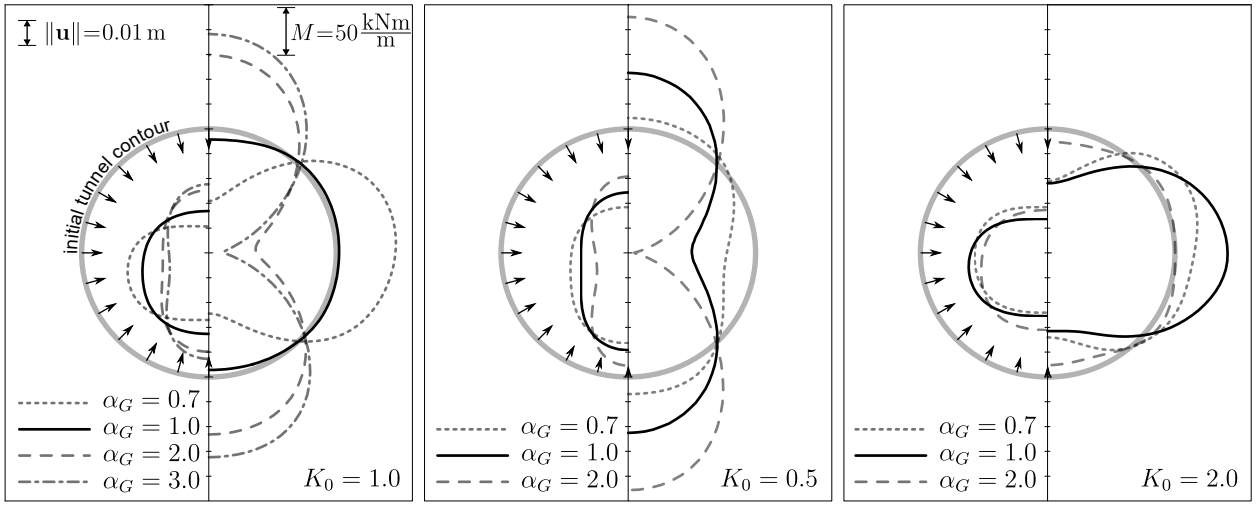

Fig. 6.23: Deep tunnel lining subjected to 1% contraction; the influence of cross-anisotropy coefficient α_G and initial stress conditions K_0 on total deformation $||\mathbf{u}||$ (left side of each graph) and bending moments M (right side of each graph)

3D model

The influence of anisotropy on tunnel induced deformation is also tested for the 3D case. The obtained results pose as a comparison to plane strain analysis. Moreover, the influence of principal stress rotations on deformations at the tunnel face under varying inherent cross-anisotropy coefficient α_G is also examined.

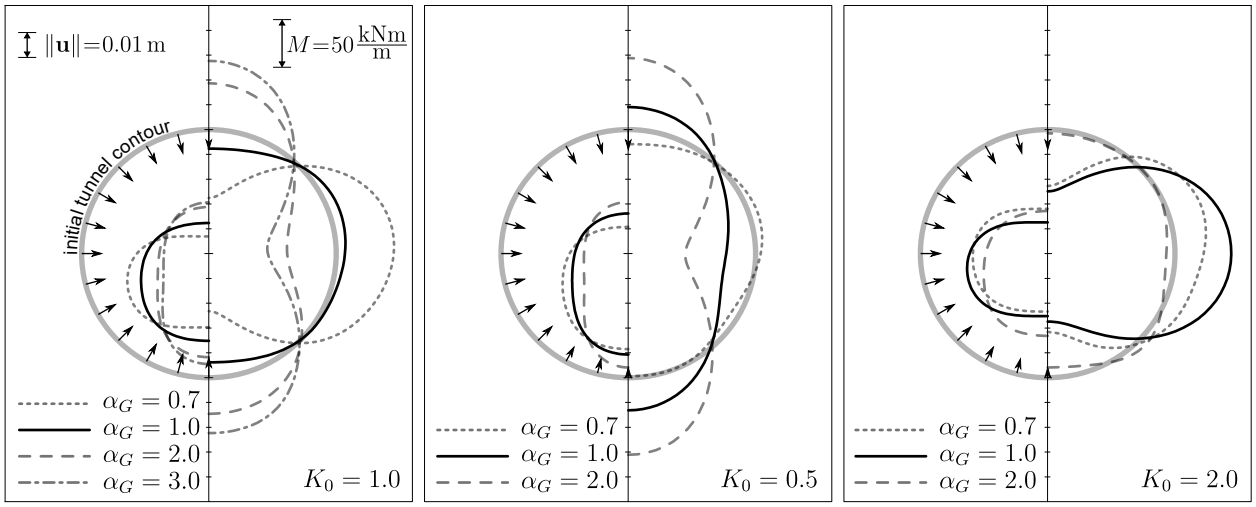

Fig. 6.24: Shallow tunnel lining subjected to 1% contraction; the influence of cross-anisotropy coefficient α_G and initial stress conditions K_0 on total deformation $||\mathbf{u}||$ (left side of each graph) and bending moments M (right side of each graph)

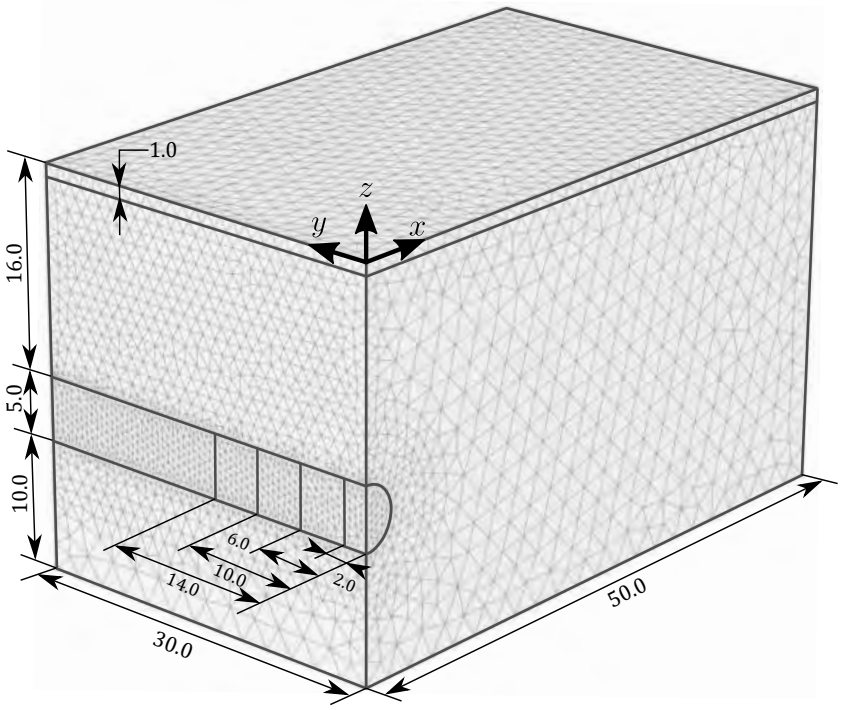

Fig. 6.25: Geometry and FE mesh of the exemplary single deep tunnel problem in 3D conditions, 42538 10-node tetrahedral elements, 67659 nodes. Four lengths of tunnel segments are considered

The geometry of the 3D model, shown in Fig 6.25, is created by the extrusion of the plain strain geometry 30 m along the tunnel axis, while maintaining comparable mesh density. The deep tunnel analysis under initial isotropic stress conditions $K_0 = 1.0$ and three values of inherent cross-anisotropy coefficients $\alpha_G = 0.7, 1.0, 2.0$ is considered. The calculation phases are analogous to the 2D simulations. The lining is modeled as a single segment of length 2 m, 6 m, 10 m, or 14 m (Fig. 6.25), which is then subjected to 1% tunnel contraction. In order to support the tunnel face, distributed horizontal back pressure is applied. Its value increases with along the tunnel depth - 170 kPa at the tunnel crown to 230 kPa at the bottom.

The deformation of the 3D numerical analysis is presented in Fig. 6.26 in a form of settlement troughs and surface plots of the horizontal displacement for the selected cross-sectional planes. The results obtained from 2D calculations, plotted as a dashed line, are shown for the comparison. Just as in 2D model, the depth and the steepness of the settlement troughs is influenced by the value of the cross-anisotropy coefficient α_G. Additionally, the depth of the settlement increases along with the length of the tunnel segment, and for 14 m, the 3D and 2D profiles nearly coincide. Horizontal deformation is shown for a cross-sectional plane located in the tunnel vicinity ($x = 3.0\,\mathrm{m}$). For $\alpha_G = 0.7, 1.0$ the magnitude of the horizontal displacements is not influenced by the segment length, whereas when $\alpha_G = 2.0$ the deformation increases with

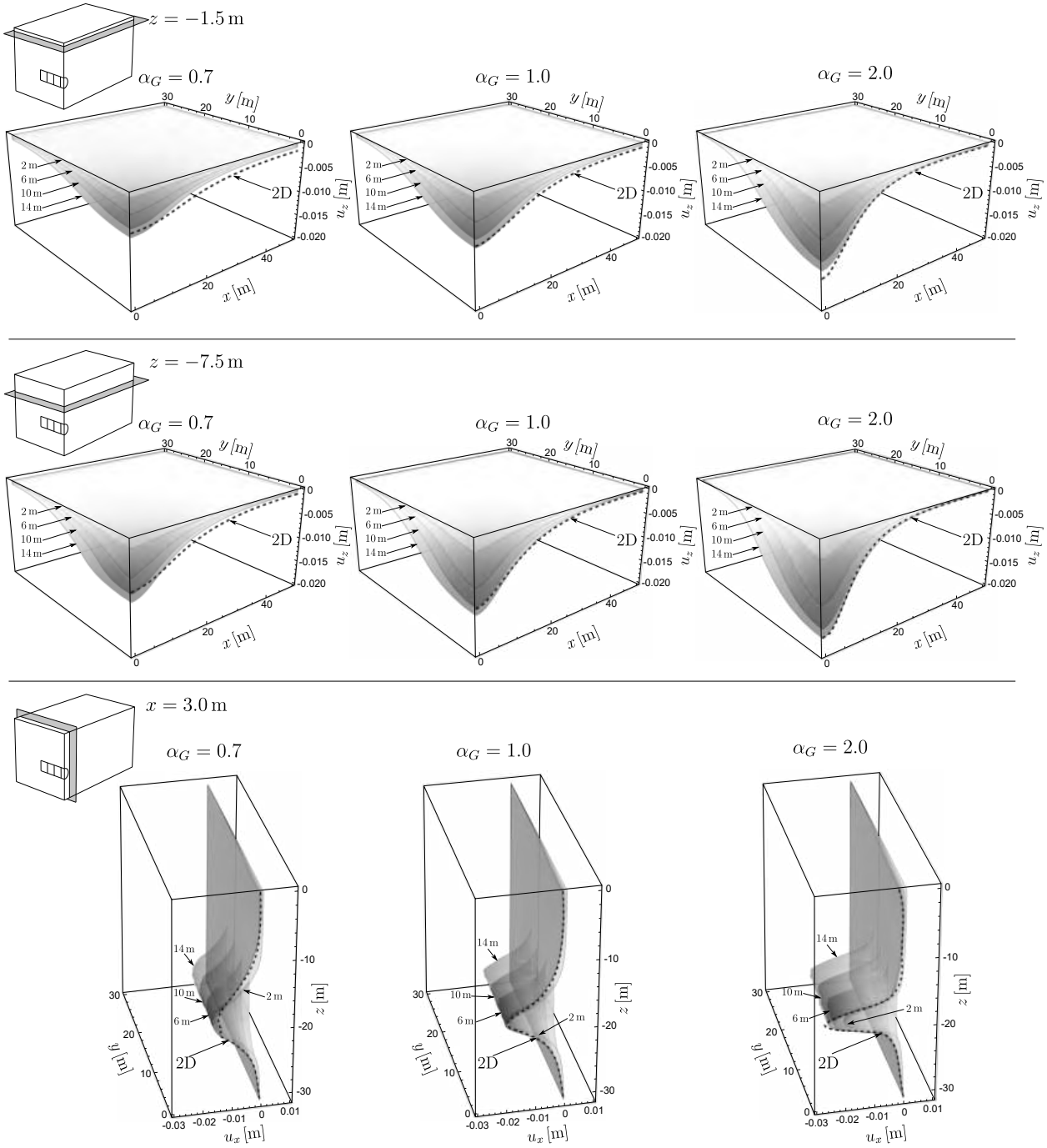

Fig. 6.26: The influence of the inherent cross-anisotropy coefficient α_G on the settlement u_z and horizontal displacement component u_x surface plots in the selected cross-sectional planes obtained in 3D model. The initial isotropic stress state $K_0 = 1.0$ is considered. In each graph, the deformations are shown after 1.0% lining contraction of 2, 6, 10 and 14 m long single tunnel sections. The results from plane strain analysis, plotted as a dashed line, are shown for the comparison

the length of the tunnel. Just as for the settlement troughs, the 3D and 2D analysis are almost the same for the longest segment.

6.2.2 Open-pit excavation

The geometry of the 10-m-depth open-pit excavation problem is presented in Fig. 6.27. The model symmetry is considered, hence, only half of the excavation, with the dimensions of $50.0\,\mathrm{m} \times 20.0\,\mathrm{m}$, is analysed. The mechanical behaviour of a 20.0 m thick undrained stiff clay layer is described with the *AHEBrick* model. The material parameters are presented in Tab. 6.2. To improve slope stability, the value of cohesion has been increased to $c = 20.0\,\mathrm{kPa}$. The groundwater level is set 1.0 m below the ground surface. The groundwater flow boundaries are closed along the symmetry line and the bottom of the FE domain, while a constant water head (-1.0 m) is imposed on the right boundary. Seepage is applied to the model surface and the contour of the excavation.

The calculations are carried out in four phases of excavation and dewatering. The material removal is simulated by deactivating the corresponding soil clusters and dewatering is achieved by setting a new groundwater table at the level of the current excavation bottom, while it stays constant on the right side of the domain ($y = -1.0\,\mathrm{m}$). The first excavation is 1.0 m deep, whereas the remaining 3 are 3.0 m deep each. The numerical calculations are conducted as fully-coupled flow analysis. Considering low value of permeability coefficient, $k_v = k_h = 1 \cdot 10^{-4}\,\mathrm{m/day}$, and the duration of each phase (10 days), the simulation can be assumed as undrained.

The influence of pure inherent cross-anisotropy on the soil deformation induced by open-pit excavation is examined for different values of cross-anisotropy coefficients $\alpha_G = 0.7, 1.0, 3.0$ and isotropic stress conditions $K_0 = 1.0$. In Fig. 6.28 the comparison of the ground movement contours after the excavation is presented. As a reference, the deformed mesh of a isotropic case ($\alpha_G = 1.0$, $K_0 = 1.0$) is considered. The more detailed material response is shown in Fig. 6.29

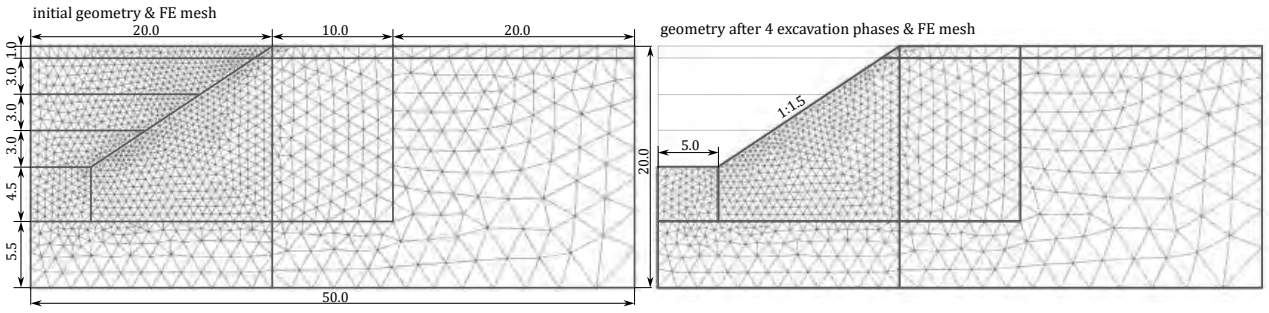

Fig. 6.27: Geometry and FE mesh of the open-pit excavation problem: 2533 15-node triangular elements, 20503 nodes

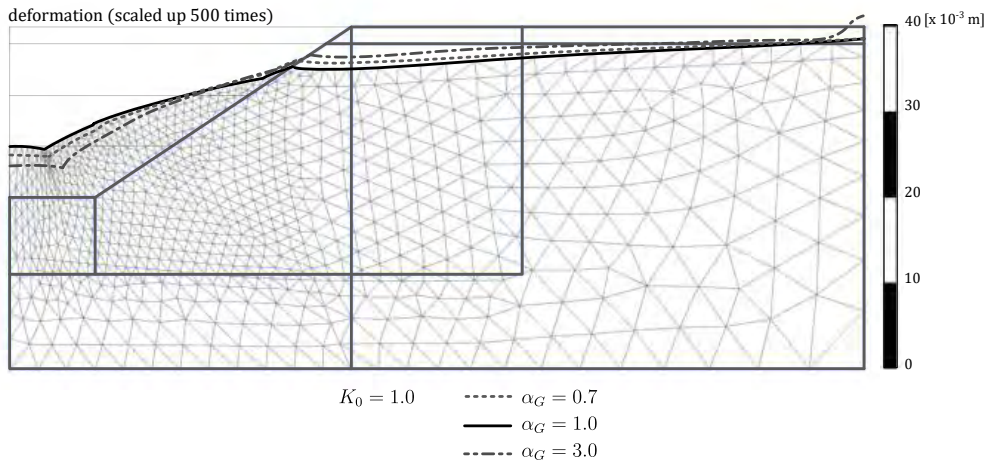

Fig. 6.28: The influence of inherent cross-anisotropy coefficient α_G on soil deformation after 4 excavation phases. The initial isotropic stress conditions $K_0 = 1.0$ are considered

in a form of displacement profiles along the selected vertical ($y = -0.05\,\text{m}$, $y = -5.0\,\text{m}$, $y = -10.05\,\text{m}$, $y = -14.5\,\text{m}$) and horizontal ($x = 5.0\,\text{m}$, $x = 12.5\,\text{m}$, $x = 20.0\,\text{m}$, $x = 30.0\,\text{m}$) cross-sections. The greatest surface settlement, bottom heave, and horizontal displacement of the excavation slope occur in the case of inherent isotropy ($\alpha_G = 1.0$). The response obtained for $\alpha_G = 0.7$ shows significant similarities to isotropic material. The application of high value of cross-anistropy coefficient ($\alpha_G = 3.0$), however, results in the lowest values of settlement and horizontal displacements. Additionally, for this case, a localised heave above the ordinal surface level can be spotted at the right boundary of the FE domain. However, given the range of the considered α_G values, the overall differences of the obtained model behaviour remain relatively small and seem to be insignificant from the practical point of view.

The maps of stiffness degradation, for the selected values of α_G and $K_0 = 1.0$, are presented in Fig. 6.30. In all cases, the lowest stiffness can be observed in the vicinity of the excavation bottom, especially in the area adjacent to the slope. In this region the biggest soil heave occurs. The greatest material strain happens when $\alpha_G = 1.0$, while for $\alpha_G = 3.0$ soil unloading is the most pronounced. Despite those differences, the maps are generally very similar to each other. Hence, inherent cross-anisotropy primarily influences the magnitude of stiffness degradation but does not significantly affect the ground response.

The same set of FE analyses is performed testing the change of the initial stress conditions K_0 of the inherent isotropic material, $\alpha_G = 1.0$. The soil deformation profiles are presented in Fig. 6.31 for $K_0 = 0.5, 1.0, 2.0$. Again, the deformed mesh for the isotropic case ($\alpha_G = 1.0$, $K_0 = 1.0$) is considered as a reference. The obtained excavation bottom heave is comparable for

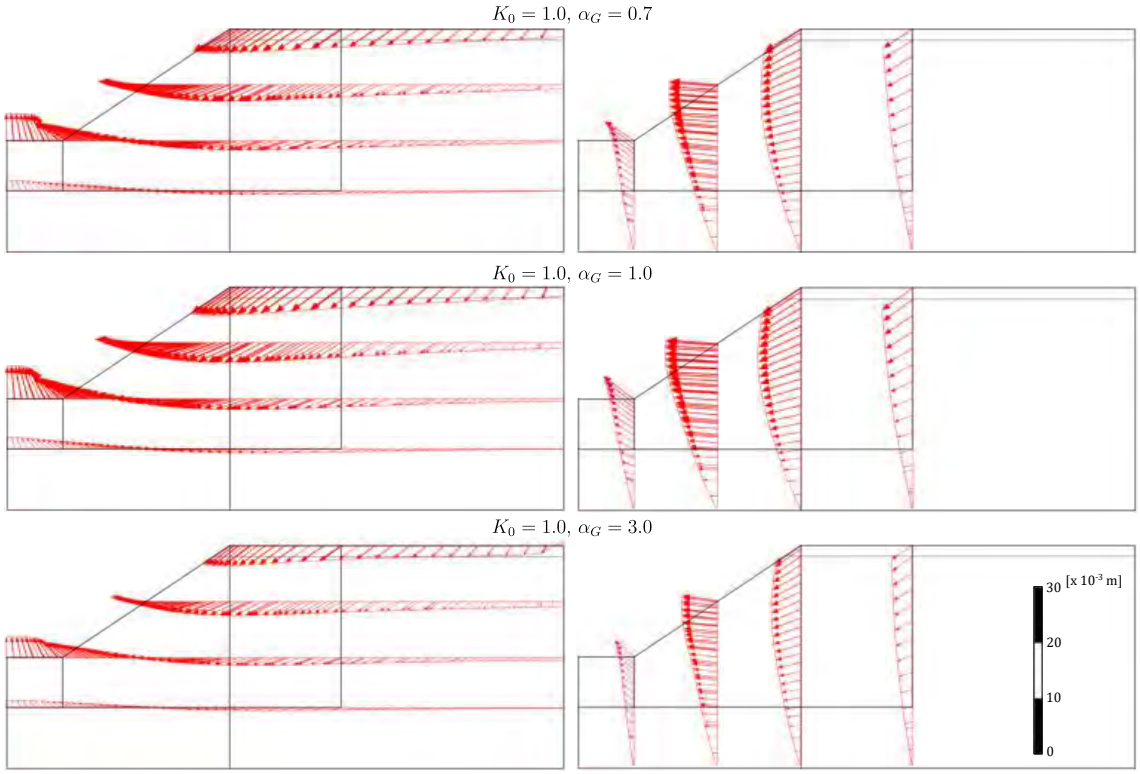

Fig. 6.29: The influence of inherent cross-anisotropy coefficient α_G on displacement profiles for selected vertical and horizontal cross-sections. The initial isotropic stress conditions $K_0 = 1.0$ are considered

all presented cases, though the magnitude of vertical displacement is marginally higher when initial stress predominates in horizontal direction, $K_0 = 2.0$, The slope heave is the greatest for $K_0 = 0.5, 1.0$, while the deeper surface settlement trough is generated when $K_0 = 2.0$. The influence of pure stress-induced anisotropy is tested by the introduction of the reference material with isotropic hypoelastic stiffness, also illustrated in Fig. 6.31 as a ground deformation contour. The obtained results strongly correlate with the isotropic case, which suggests that the effect of stress-induced anisotropy to the open-pit excavation deformation is negligible. Therefore, shown in Fig. 6.32, vertical and horizontal displacement profiles exclude the isotropic hypoelastic kernel model. The material response at the cross-sections furthest from the excavation ($x = 30.0\,\mathrm{m}$ and $y = -14.5\,\mathrm{m}$), show significant similarities across all three analysed examples. Additionally, the magnitude of soil heave at the bottom of the excavation is comparable. Notable differences in ground deformation mainly occur in the vicinity of the excavation slope. The largest horizontal displacement is observed when $K_0 = 2.0$. In the cross-section located at the midpoint of the slope ($x = 12.5\,\mathrm{m}$), the soil settlement is only apparent if the initial horizontal stress is higher.

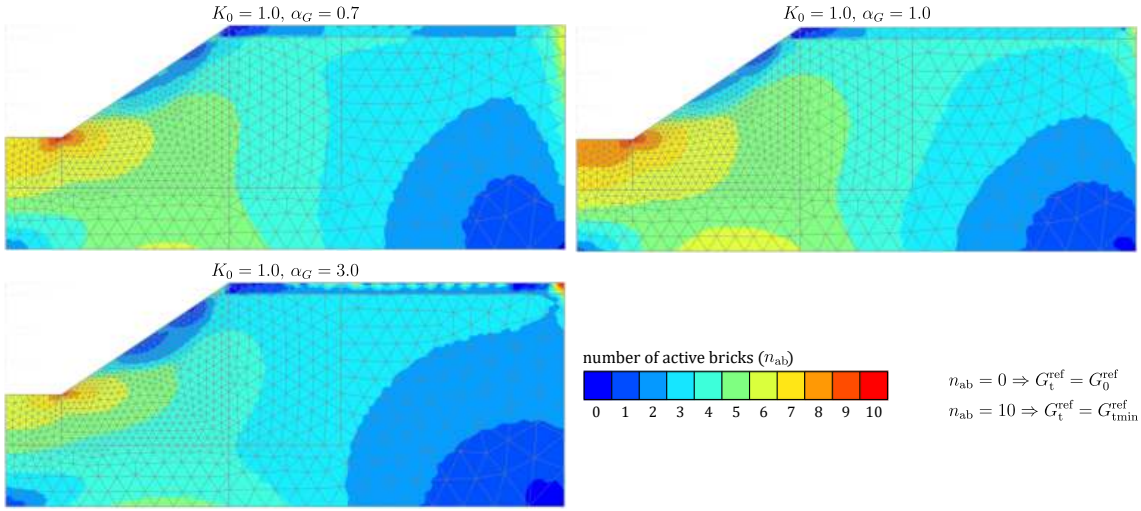

Fig. 6.30: Maps of stiffness degradation for different values cross-anisotropy coefficient α_G at isotropic stress conditions $K_0 = 1.0$, obtained after the last excavation phase. The intensity of stiffness degradation is indicated by the number of active bricks n_{ab}

Furthermore, heave at the excavation bottom near the slope is much smaller for $K_0 = 2.0$, compared to the other two cases, which exhibit almost identical deformation.

Fig. 6.33 illustrates maps of stiffness degradation for the analysed values of K_0. To determine the importance of the pure stress-induced anisotropy on stiffness changes, the response of the isotropic hypoelastic model is shown, as a comparison. No notable differences are observed between two isotropic cases, hence, the influence of stress-induced anisotropy is negligible. Nevertheless, the effect of various K_0 states on stiffness degradation is evident. In all cases,

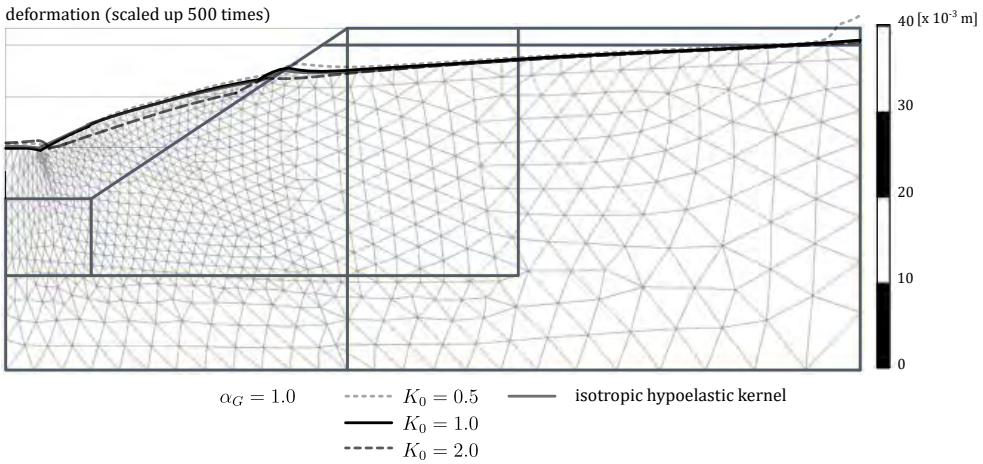

Fig. 6.31: The influence of the initial stress state K_0 on soil deformation after 4 excavation phases. The inherent isotropy $\alpha_G = 1.0$ is considered. The response of the model with purely isotropic hypoelastic stiffness is shown for comparison

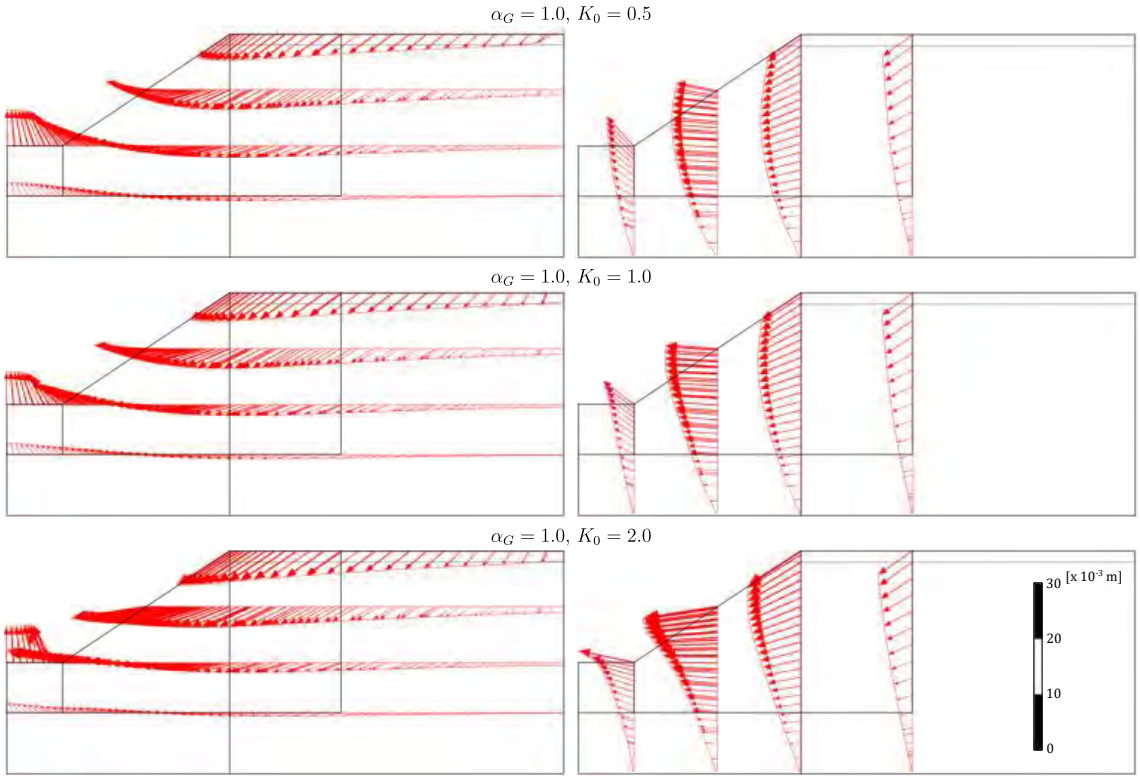

Fig. 6.32: The influence of the initial stress state K_0 on displacement profiles for selected vertical and horizontal cross-sections. The inherent isotropy $\alpha_G = 1.0$ is considered

low stiffness value is obtained at the bottom of the excavation, and for $K_0 = 2.0$, a localized shear zone is clearly visible in this area. Along the excavation slope, a high value of stiffness is observed for $K_0 = 0.5, 1.0$, whereas, if $K_0 = 2.0$, a substantial stiffness degradation occurs. This suggests that, if initial stress is higher in the horizontal direction ($K_0 = 2.0$), the obtained slope heave is caused by horizontal displacement, and otherwise it is a result of soil unloading.

6.2.3 Supported excavation

The simulation of the supported excavation problem is conducted in plane strain conditions. The geometry and FE mesh are presented in Fig. 6.34. Due to the symmetry only a half of the model is calculated. The FE domain measures 80.0 m × 40.0 m, while the excavated area has a width of 15.0 m and a depth of 20.0 m. The excavation is supported by a 25.0-m-long and 1.0-m-thick concrete diaphragm wall, modelled as a plate element: $EA = 30 \cdot 10^6$ kN/m, $EI = 2.5 \cdot 10^6$ kNm^2/m, $\nu = 0.2$. Additionally, at the centre of each excavated cluster a wall support prop is installed (anchor elements, $L_{\text{spacing}} = 3.0$ m, $EA = 2.7 \cdot 10^6$ kN). The mechanical properties of the 39-m-thick clay layer are defined with the *AHEBrick* model and the corresponding material

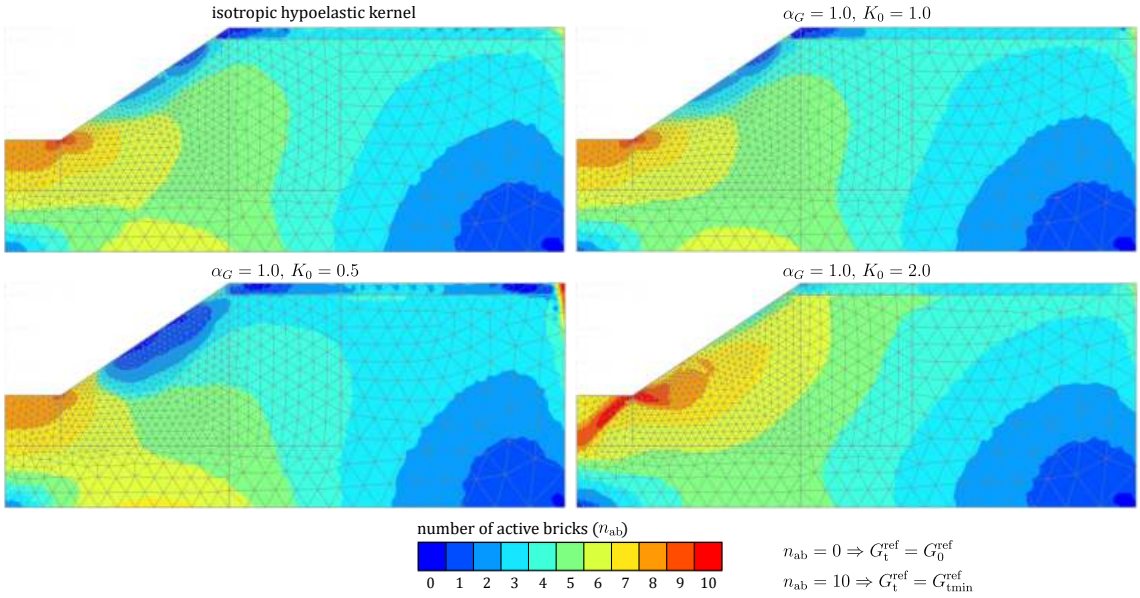

Fig. 6.33: Maps of stiffness degradation for different values of initial stress state K_0 and inherent isotropic material $\alpha_G = 1.0$, obtained after the last excavation phase. The response of the model with purely isotropic hypoelastic stiffness is shown for comparison. The intensity of stiffness degradation is indicated by the number of active bricks n_{ab}

parameters are listed in Tab. 6.2. Analogous to the tunnelling problem simulation, a 1.0-m-thick granular layer is placed above the clay to prevent stiffness variations caused by low stress levels (material parameters are provided in Sec. 6.2.1). The groundwater table is located below the granular fill ($y = -1.0\,\mathrm{m}$). Flow boundaries are closed along the model's axis of symmetry and at the bottom, while the side and top boundaries are open. Seepage is allowed along the diaphragm wall.

The calculations are performed as a fully-coupled flow deformation analysis. In the first phase, the wall installation is simulated by activating the plate elements and enabling the

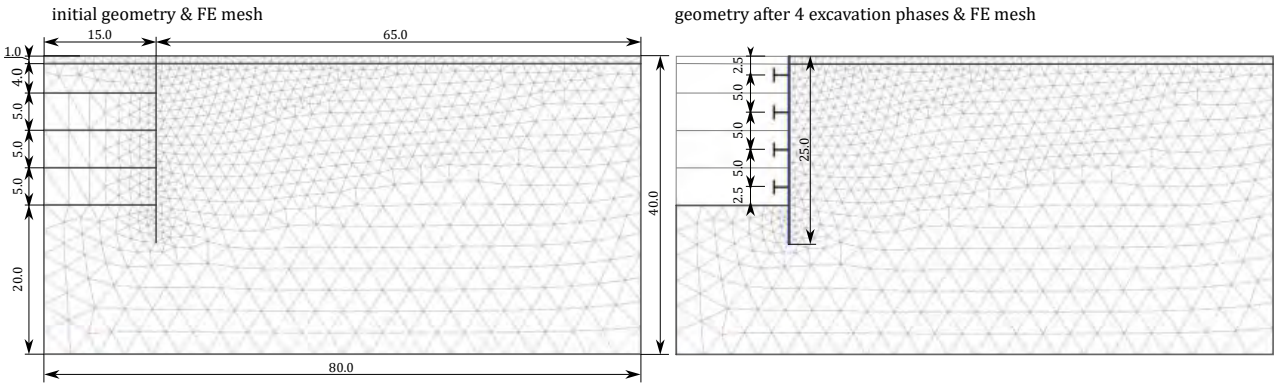

Fig. 6.34: Geometry and FE mesh of the supported excavation problem: 1581 15-node triangular elements, 13128 nodes

interfaces around it. In each subsequent phase, excavation is advanced by 5 m, followed by dewatering and the activation of prop elements. Dewatering is modeled by interpolating the pore water pressure between the initial groundwater level and the current excavation depth for all excavated clusters. Due to the low permeability of the clay layer ($k_v = k_h = 1 \cdot 10^{-4}\,\mathrm{m/day}$) and the short duration of each calculation phase (first phase - 1 day, the remainder - 10 days each), the analysis can be assumed as undrained.

The influence of pure initial inherent cross-anisotropy on soil deformation, induced by the construction of a supported excavation, is examined for different values of cross-anisotropy coefficient $\alpha_G = 0.7, 1.0, 2.0$ and the isotropic stress state $K_0 = 1.0$. The obtained results are presented in Fig. 6.35 in a form of settlement troughs and horizontal displacement profiles for the selected cross-sections. In every case the value of vertical displacement is the highest for the isotropic material, $\alpha_G = 1.0$ and the shape of the settlement troughs is the steepest. The difference in soil response between $\alpha_G = 0.7$ and $\alpha_G = 2.0$, obtained at cross-sections located directly below the granular fill ($y = -1.0\,\mathrm{m}$) and halfway down the diaphragm wall ($y = -10.0\,\mathrm{m}$), is negligible, suggesting that soil, which exhibits anisotropic stiffness produces similar response, regardless the value of α_G. The calculated ground heave directly below the excavation bottom ($y = -20.5\,\mathrm{m}$) and beneath the wall ($y = -25.0\,\mathrm{m}$), is the smallest for $\alpha_G = 0.7$, however, the one for $\alpha_G = 2.0$ is comparable. Additionally, when $\alpha_G \neq 1.0$ the resulting vertical displacement profiles within the excavation area are relatively flat. Horizontal displacement is presented at sections located 5 m and 15 m ($x = 20\,\mathrm{m}$, $x = 30\,\mathrm{m}$) behind the diaphragm wall, as well as at the center of the model ($x = 40\,\mathrm{m}$). In each analysis, the calculated displacement is the greatest for the isotropic case. The differences between $\alpha_G = 0.7$ and $\alpha_G = 2.0$ are minor, though the smallest horizontal displacement profiles are observed for $\alpha_G = 2.0$, despite this case corresponding to the highest horizontal stiffness G_{hh}.

The influence of pure cross-anisotropy on stiffness degradation, presented in Fig. 6.36, is also apparent. In all cases, the minimum stiffness ($n_{\mathrm{ab}} = 10$) is reached near the excavation basin. For $\alpha_G = 1.0$, a substantial reduction in stiffness extends over a large portion of the model. When $\alpha_G = 0.7$, the stiffness degradation at the excavation bottom is the smallest, however, noticeable changes occur in soil located further away from the excavated zone. In contrast, if $\alpha_G = 2.0$, the decrease in stiffness is largely confined to the excavation area. Additionally, when $\alpha_G \neq 1.0$, no significant stiffness degradation near the ground surface occurs, which explains the negligible differences in the calculated settlement troughs. From the obtained maps, it can be concluded that for the example of supported excavation problem, the initial stiffness value, determined by the coefficient α_G, does not strongly influence the overall soil response. Instead,

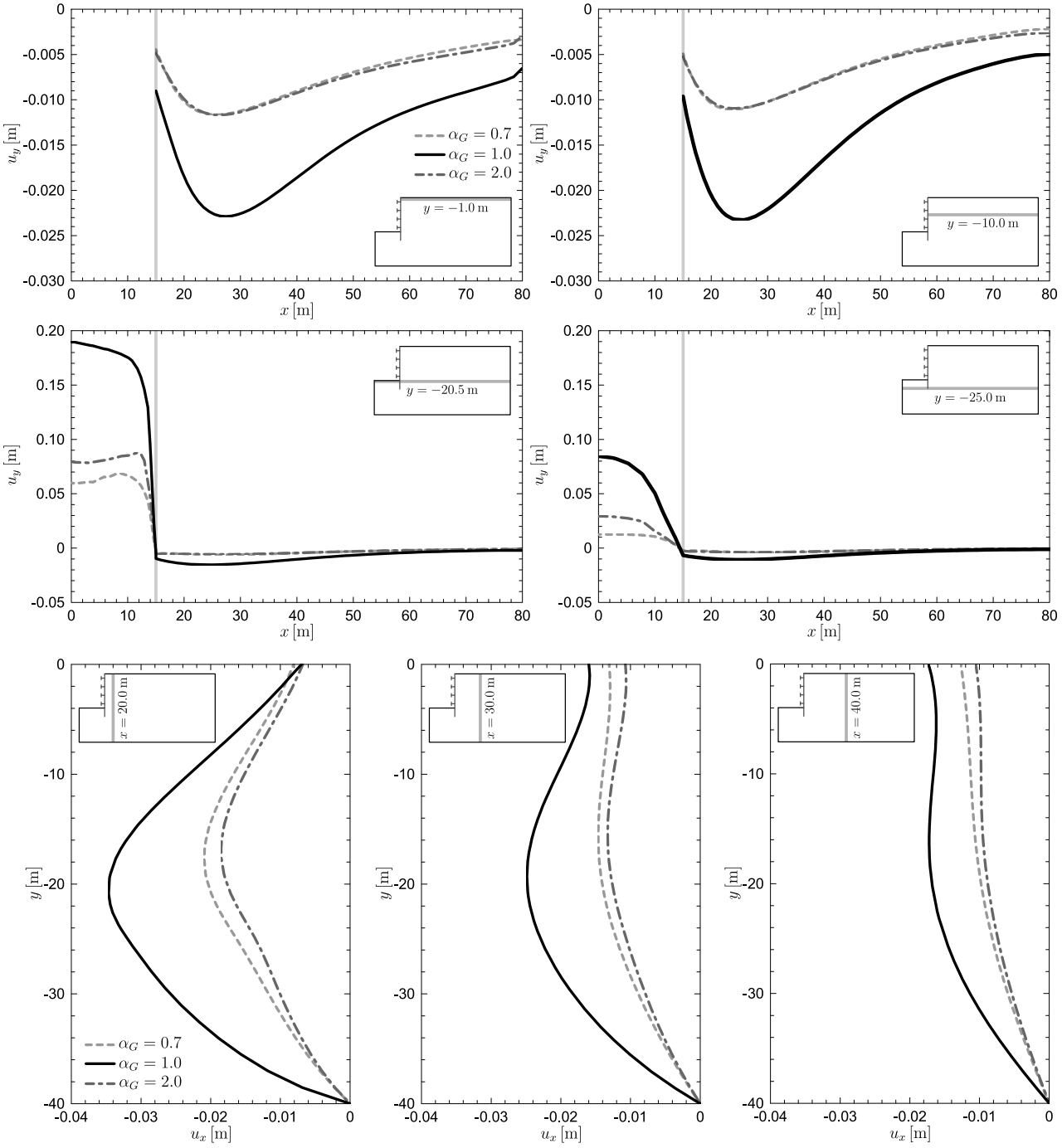

Fig. 6.35: The influence of the inherent cross-anisotropy coefficient α_G on the settlement u_y and horizontal displacement component u_x profiles along the selected cross-sections, induced by the construction of the supported excavation. The initial isotropic stress state $K_0 = 1.0$ is considered

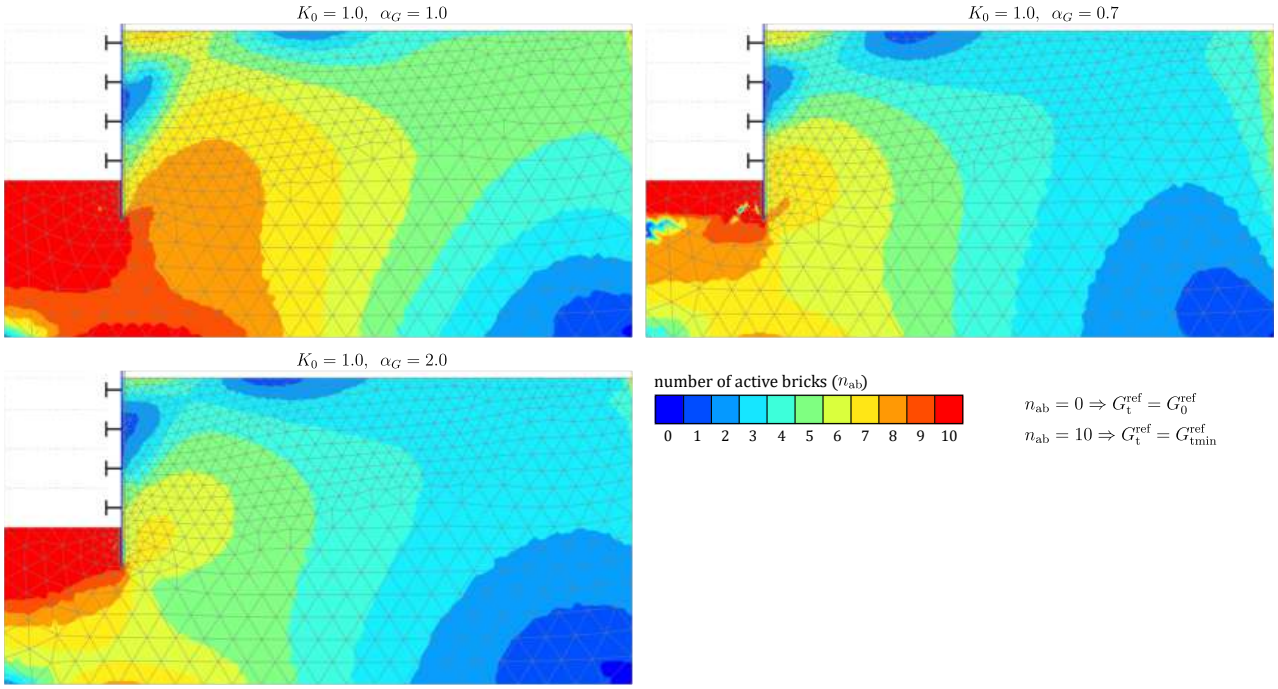

Fig. 6.36: Maps of stiffness degradation for different values of α_G at isotropic stress state $K_0 = 1.0$ obtained for the example of the supported excavation construction. The intensity of stiffness degradation is indicated by the number of active bricks n_{ab}

the rate of strain development and the associated stiffness degradation, which is also dependent on α_G, seem to be more important.

The influence of the initial stress state K_0 on the deformation caused by the construction of a supported excavation was investigated for $K_0 = 0.5, 1.0, 2.0$, assuming an isotropic microstructure, $\alpha_G = 1.0$. Similar to the example shown in Fig. 6.35, the vertical and horizontal displacement profiles, presented in Fig. 6.37, are calculated for selected cross-sections. For cross-sections located at depths $y = -1.0\,\text{m}$ and $y = -10.0\,\text{m}$, the deepest and steepest settlement troughs occur at $K_0 = 2.0$, while the smallest deformation is observed for the isotropic case ($K_0 = 1.0$). At $K_0 = 0.5$, the settlement trough exhibits a gentle slope from the right boundary, however, at a distance of approximately 30 m from the diaphragm wall, a sharp, almost circular decrease in settlement occurs. Soil heave obtained at the excavation bottom (cross-sections $y = -20.5\,\text{m}$ and $y = -25.0\,\text{m}$), is roughly twice as large for $K_0 = 2.0$ than for $K_0 = 0.5, 1.0$, which show very similar results. In case of horizontal displacement profiles, the largest deformation is again associated with $K_0 = 2.0$. The ground movement for $K_0 = 0.5, 1.0$, is comparable down to about half the model depth. Below this depth, however, the displacement u_x becomes

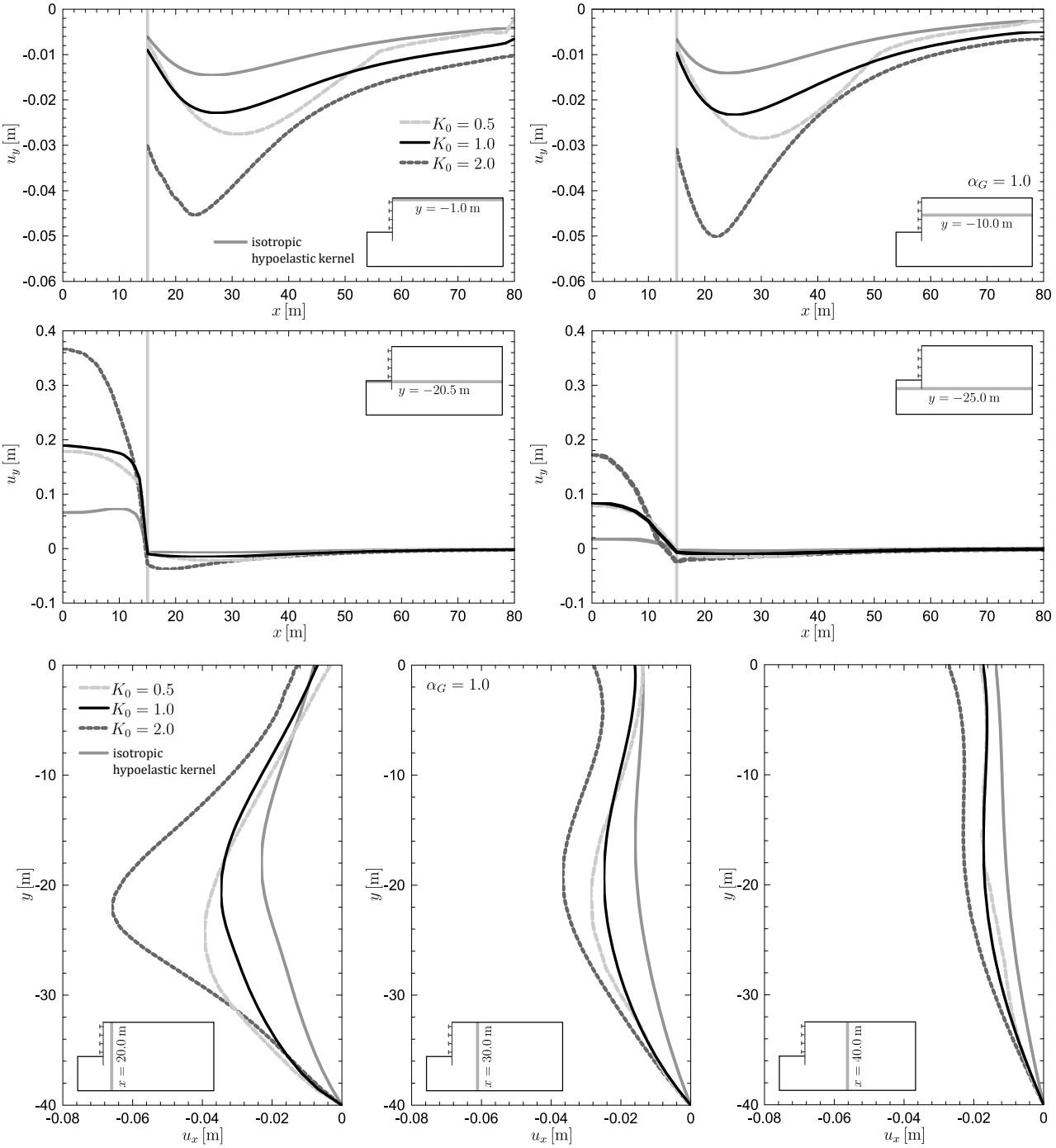

Fig. 6.37: The influence of the initial stress conditions K_0 on the settlement u_y and horizontal displacement component u_x profiles along the selected cross-sections, induced by the construction of the supported excavation. The inherent isotropy $\alpha_G = 1.0$ is considered

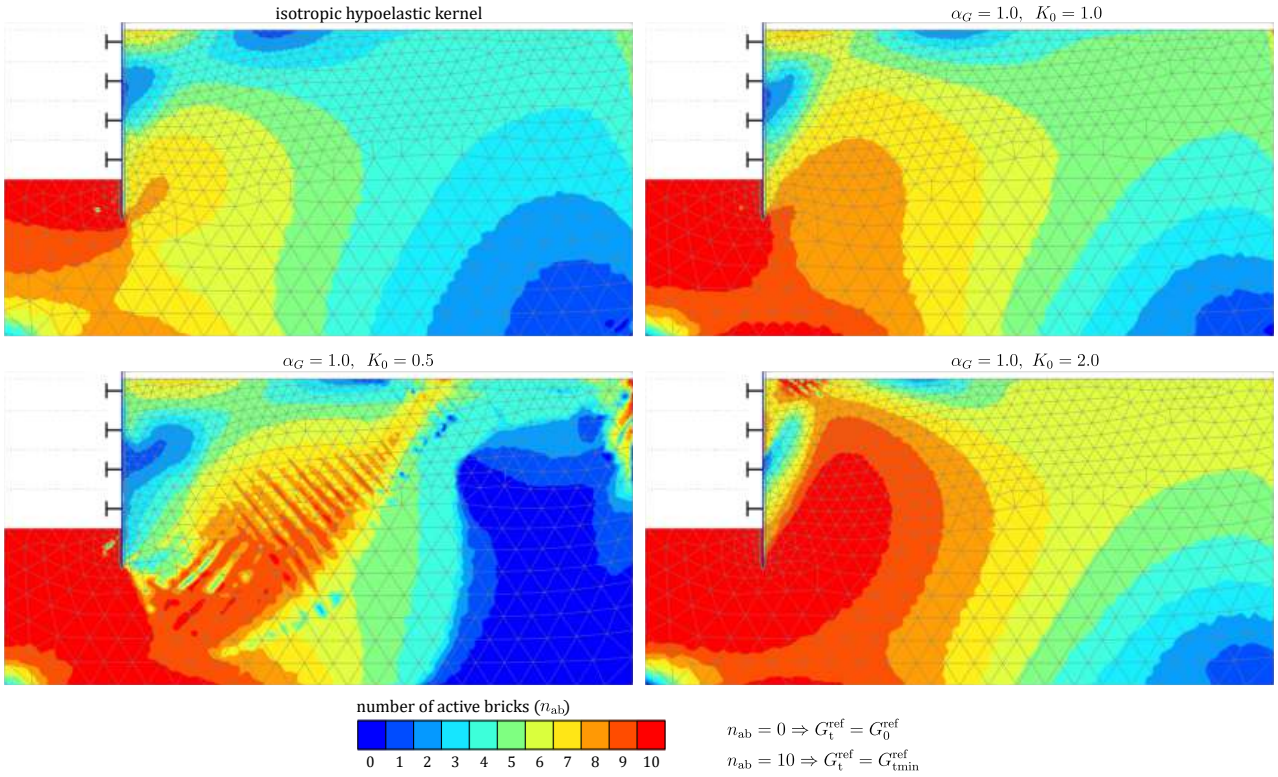

Fig. 6.38: Maps of stiffness degradation for different values of K_0 and isotropic material $\alpha_G = 1.0$ obtained for the example of the supported excavation construction. The intensity of stiffness degradation is indicated by the number of active bricks n_{ab}

greater for $K_0 = 0.5$, although these differences diminish with increasing distance from the excavation.

The influence of pure stress-induced anisotropy is investigated by the comparison of the isotropic *AHEBrick* material to the reference hypoelastic isotropic material. Soil response obtained for hypoelastic model is smaller than for the case of $\alpha_G = 1.0$, $K_0 = 1.0$. This suggests that the importance of stress-induced anisotropy on soil deformation is substantial.

This effect is also evident in the stiffness degradation maps presented in Fig. 6.38. The reduction in stiffness obtained with the hypoelastic model is considerably smaller than in the case of isotropic *AHEBrick* material. In all analysed examples, the maximum stiffness decrease occurs within the excavation area. However, if $K_0 = 2.0$, a pronounced reduction in stiffness extends beyond the excavation zone. For $K_0 = 0.5$, a distinct shear zone develops, marking the path of the slip zone, which may explain the abrupt settlement drop observed in Fig. 6.37.

The horizontal displacement u_x and the bending moment M distribution in the diaphragm wall are presented in Fig. 6.39 for combined cases of α_G and K_0. For each value of K_0, an additional curve is included to represent the behaviour of the hypoelastic model. In terms of

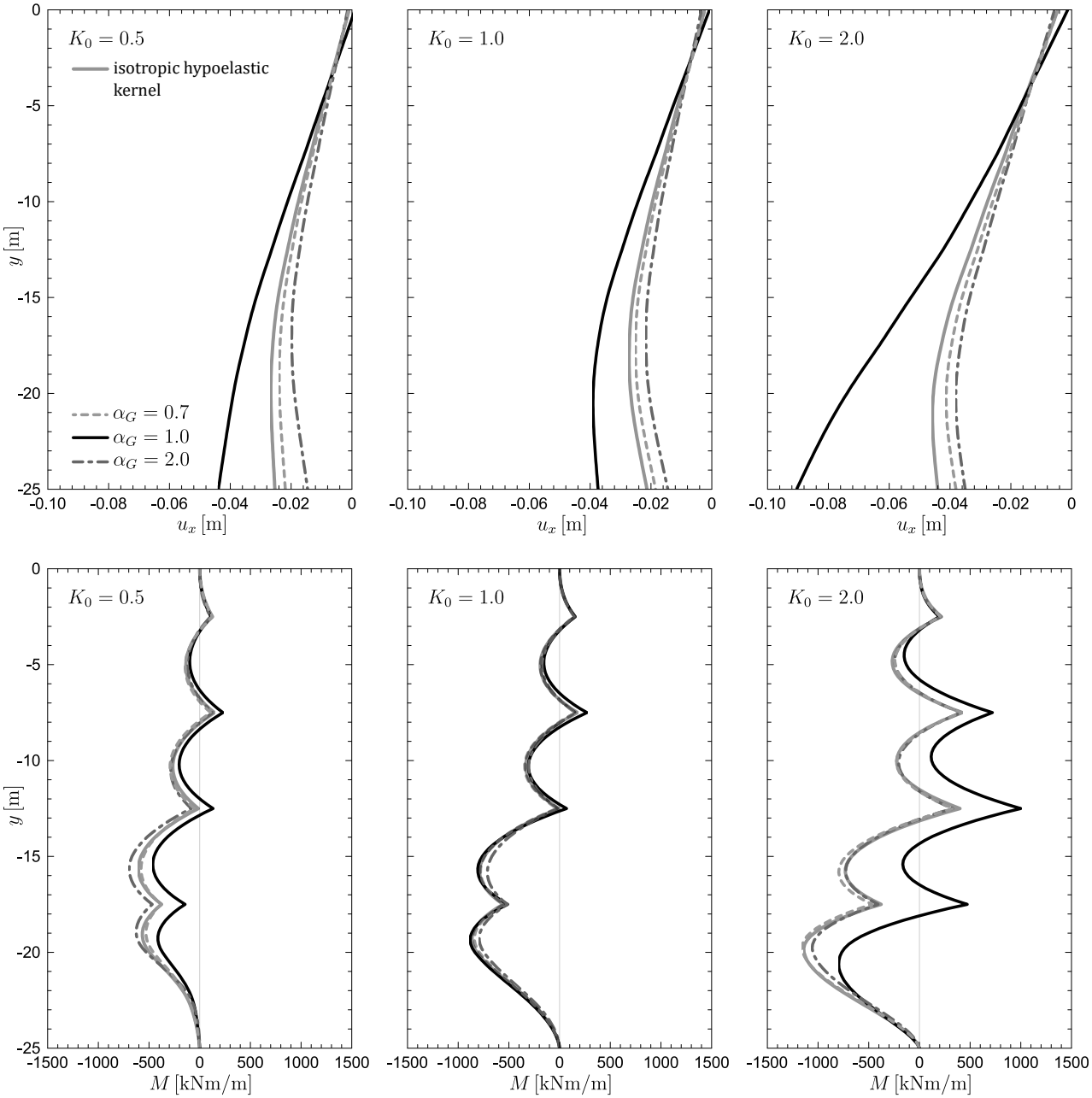

Fig. 6.39: The influence of the inherent cross-anisotropy coefficient α_G and initial stress conditions K_0 on the horizontal displacement u_x and bending moments M in the diaphragm wall

horizontal displacement, the largest values consistently occur for $\alpha_G = 1.0$, while for $\alpha_G \neq 1$ the results are very similar to one another. Taking into consideration a comparison between the soil response for the isotropic *AHEBrick* material ($\alpha_G = 1.0$) and that calculated with the use of the hypoelastic model, it can be concluded that stress-induced anisotropy demonstrates the greatest influence on soil behavior in supported excavation cases. Moreover, this influence appears to increase with higher values of initial stress levels. Overall, the obtained wall deflection is substantially higher when initial horizontal stress exceeds the vertical one. In contrast, no notable differences can be distinguished between horizontal displacement profiles calculated at $K_0 = 0.5$ and $K_0 = 1.0$.

In the case of bending moment distributions, a clear trend is observed: the extreme values of moments corresponding to the same α_G increase with higher K_0, with a particularly pronounced rise at $K_0 = 2.0$. Comparing responses obtained for isotropic materials, the influence of stress-induced anisotropy becomes significant only under anisotropic initial stress conditions. Conversely, for $K_0 = 1.0$, the bending moments are similar in both shape and magnitude, which indicates the influence of α_G is marginal.

7

Application of the *AHEBrick* model in case studies

In this section the *AHEBrick* model is validated against real geotechnical cases. The purpose of such analysis is to verify the extent to which the adopted material model is able to reflect reality. For this reason, the model geometry and construction procedure are closely based on the data reported in literature. Additionally, values of material properties are obtained through parameter calibration of laboratory test results. The results are then compared to corresponding field measurements. That way the accuracy of the calculations can be determined.

The following analyses concern the cases of twin tunnel construction in London Clay [32, 33], FE and HG-A tunnels in Opalinus Clay [43, 102, 115] and trial open-pit excavation in Oxford Clay [70, 132].

7.1 Twin tunnels of the Jubilee Line Extension in London Clay at St. James Park, London

Launched in 1994, the Jubilee Line Extension Project aimed to extend the underground line by 15 km, from Green Park to the existing British Rail station at Stratford. This project provided an excellent opportunity to conduct a field study on the impact of excavation and tunnel construction on ground response in urban areas. For this reason, a collaborative research programme was established, as described in [31]. Two control sites were designated for the purpose of taking field measurements: one located at St. James's Park and the other at Southwark Park. Both locations are characterised by completely different geological conditions, which allowed for the investigation of the impact of tunnelling on clayey (St. James's Park - London Clay) and granular (Southwark Park - Woolwich and Reading deposits) soils. The sites were equipped with the instrumentation capable of measuring ground movements (surface settlement points, inclinometers and extensometers), as well as water pressure (piezometers) in the vicinity of the tunnels. The full report on the obtained results was published in [32, 33].

Given the nature of this research, out of the two control sites, the example of St. James's Park has been examined. It is a very well documented case study, with field data available in [125, 156]. Additionally, the extensive research on the London Clay mechanical properties, e.g. [56, 57, 67, 122, 124], has been carried out over the years, making this case exceptionally suitable to use as a validation for numerous studies on tunneling simulations and new material models, e.g.[4, 3, 16, 54]. The results of the following analysis have been published in [46].

Geometry and soil conditions

The simulation of the problem is carried out as a plane strain analysis. The model geometry and FE mesh are presented in Fig. 7.1. The dimensions of the FE domain are consistent between the examples found in literature, e.g. [15, 16, 4, 59], and have therefore been used in the presented calculations. Two tunnels, each with a diameter of 4.85 m, were excavated in London Clay using open-face shield and mechanical backhoe methods. A concrete lining, 0.17 m thick,

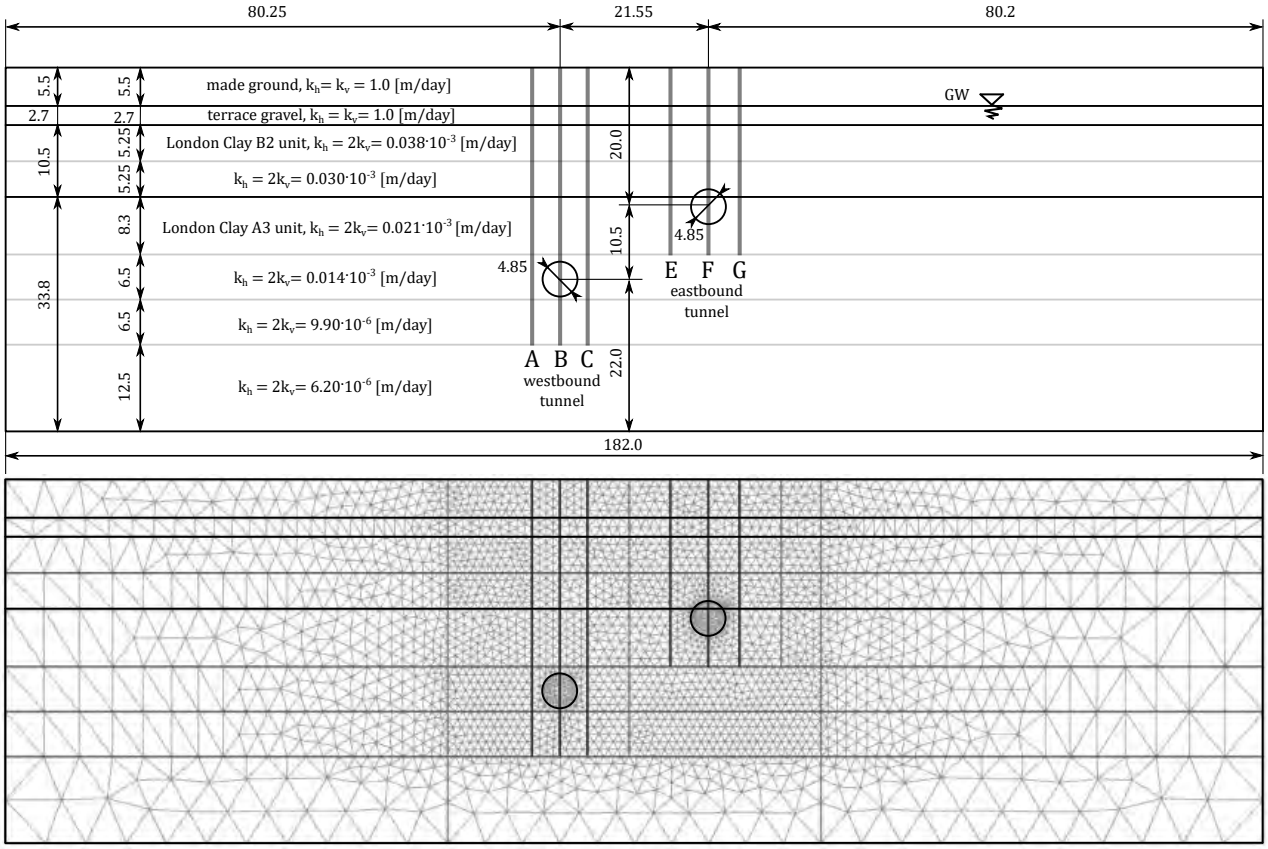

Fig. 7.1: Plane strain geometry and FE mesh of the back analysed case study of the Jubilee Line Extension twin tunnels in London Clay at St James's Park (5682 15-node triangular elements, 45985 nodes). Axes A-C and E-G show the position of measuring instrumentation (electrolevel inclinometers and rod extensometers)

was applied to both tunnels. The tunnel axes are located 30.5 m (westbound) and 20.0 m (eastbound) below the ground surface. Axes A-C and E-G show the placement of the selected measurement instrumentation. Groundwater level is positioned 5.5 m under the ground surface. No-flow conditions are applied at the bottom of the domain, whereas seepage is allowed at the side boundaries and along the tunnel lining.

London Clay deposit is overburdened by 5.5 m of the made ground layer and 2.7 m thick terrace gravel. Following [4, 16], these two materials are defined as:

- made ground - linear elastic model: $E = 5000\,\text{kPa}$, $\nu = 0.3$, $\gamma = 18.0\,\text{kN/m}^3$, $K_0 = 0.5$;
- terrace gravel - Mohr-Coulomb model: $E = 35000\,\text{kPa}$, $\nu = 0.2$, $c = 1\,\text{kPa}$, $\phi = 35°$, $\gamma = 20.0\,\text{kN/m}^3$, $K_0 = 0.5$.

The mechanical properties of the two London Clay units (B2 - 10.5 m thick, and A3 - 33.8 m thick) are simulated with the *AHEBrick* material model. Parameter calibration was carried out via a series of undrained triaxial compression element test based on the laboratory results reported in [56, 67]. The detailed description of the calibration is presented in Sec. 6.1.4 and the obtained results are illustrated in Fig. 6.8.

The initial stress conditions K_0 of London Clay deposits were established taking into consideration the related literature. Despite advances in laboratory and *in situ* testing, the proper determination of K_0 in overconsolidated soils remains a challenge. In the numerical analysis, presented in [4], a constant value of $K_0 = 1.5$ was adopted, following the findings in [69]. Conversely, in [16] and [59], a geological history of London Clay was reconstructed with the use of the kinematic hardening models, which allowed to obtain the depth-dependent K_0 profiles.

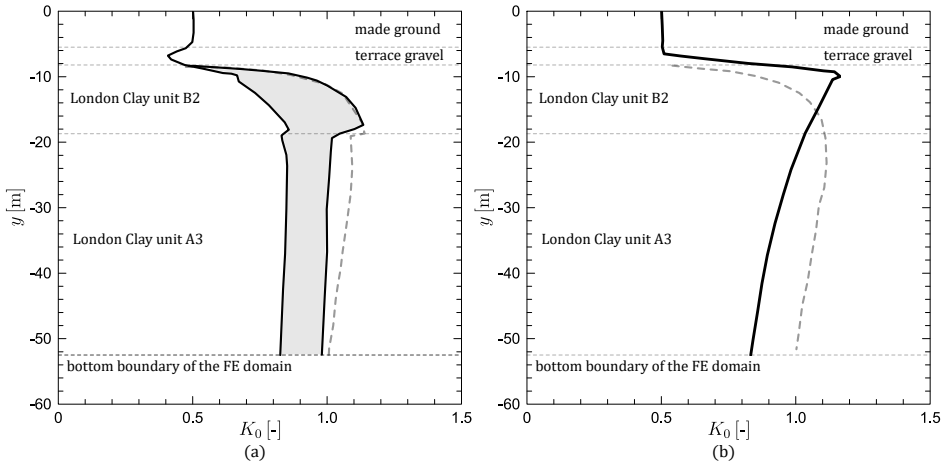

Fig. 7.2: Prediction of K_0 profiles with a use of kinematic hardening models: (a) the area between two bold black lines shows the obtained range for 4 analysed models, after [16], (b) model response presented as a bold black line, after [59]. The expression by Mayne and Kulhawy [109] (gray bold dashed line) introduced as a comparison

These profiles are illustrated in Fig. 7.2. In both cases, for unit A3, the K_0 value ranges from 0.85 to 1.0, while for B2 unit this the variation is more pronounced, spanning from 0.5 to 1.2. Given that the *AHEBrick* model is designed to simulate the behaviour of anisotropic stiff overconsolidated soils, it is not well suited to properly reproduce normally consolidated stress conditions. Therefore, the initial isotropic stress state $K_0 = 1.0$ has been adopted for both B2 and A3 units.

The *AHEBrick* model parameters for B2 and A3 units of London Clay are listed in Tab. 7.1. Following [4], the values of permeability coefficients for London Clay and cover soils are shown in Fig. 7.1. London Clay exhibits anisotropic permeability, which decreases with depth. Hence, each London Clay unit has been subdivided into smaller layers to properly represent its flow properties.

Table 7.1: Parameters of the London Clay B2 and A3 units simulated with the *AHEBrick* model

	Parameter	London Clay B2	London Clay A3
Small strain stiffness	G_{vh}^{ref} [kPa]	48080	70000
	β [-]	0.5	0.5
	α_G [-]	2.0	2.0
	p_{ref} [kPa]	100	100
Stiffness degradation	$G_{vh\mathrm{tmin}}^{\mathrm{ref}}$ [kPa]	2000	7000
	$\|\|\boldsymbol{\varepsilon}\|\|_{\mathrm{sh}}$ [-]	0.0009	0.0004
Shear strength criterion	ϕ [°]	30	28
	c [kPa]	15	55
	ψ [°]	5	5
	p_{te} [kPa]	0	0
Unit weight and initial stress	γ [kN/m^3]	20.0	20.0
	K_0 [-]	1.0	1.0

Calculations

The construction of WB and EB tunnels is simulated analogously to the one described in Sec. 6.2.1. First, the soil elements and pore water pressure are deactivated within the tunnel face. The tunnel lining is installed by activating plate elements ($EA = 4.7 \cdot 10^6$ kN/m, $EI = 1.1 \cdot 10^4$ kNm^2/m) and is next subjected to contraction. The applied values of the contraction are based on the volume loss method. This approach assumes that the volume loss (v_{L}), measured at the ground surface, corresponds to the deformation of the soil, that surrounds tunnel, moving into its boundary. Such value is typically expressed as a percentage of the tunnel's theoretical volume [15]. Generally, the calculations are conducted assuming the undrained conditions of

defined soil deposits. In the utilised FE code [26], this behaviour is simulated by assigning a high bulk modulus to the pore water. This results in the development of excess pore pressure, effectively preventing changes in volumetric strain. Reported in [125], the prescribed values of tunnel contraction are 3.3% and 2.9% in case of westbound and eastbound tunnel, respectively.

In the numerical analysis the following calculation phases were conducted:

1. Initial phase - introduction of the state variables, K_0 stress conditions, hydrostatic water conditions;
2. Construction of the WB tunnel, application of 3.3% tunnel contraction (undrained phase);
3. Consolidation phase $\Delta t = 256\,\text{days}$;
4. Construction of the EB tunnel, application of 2.9% tunnel contraction (undrained phase);
5. Consolidation phase $\Delta t = 415\,\text{days}$;
6. Consolidation phase $\Delta t = 3440\,\text{days}$;
7. Consolidation phase $\Delta t = 1831\,\text{days}$.

The included consolidation phases align with the actual site schedule.

Results

Fig. 7.3 shows the separate surface settlement troughs obtained immediately after the construction of the WB and EB tunnels. The results of the initial analysis - assuming undrained conditions for all soil layers - are represented by the solid bold black line (curve no. 1). The comparison of the obtained soil response to the actual field measurements [125, 156] show the high degree of agreement.

The cover soils, however, are non-cohesive and coarse-grained, so the assumption of undrained conditions is not appropriate. Consequently, a second analysis was performed in which undrained conditions were applied only to the London Clay layer, while the remaining soil layers were treated as drained. The contraction values remained unchanged, 3.3% and 2.9% for WB and EB tunnels, respectively. The resulting settlement troughs, shown as curve no. 2, are too deep, exceeding the measured settlements at the tunnel centerline by 15% for the WB tunnel and 21% for the EB tunnel.

Recommended in [125], contraction values are considered to be unusually high [86, 155]. Therefore, the third analysis was conducted using the updated contraction values: 2.8% for westbound tunnel and 2.4% for eastbound tunnel. The surface settlement profiles, represented by curve no. 3, show the best agreement with the field data.

Following these findings, the remaining results exclude the case with all soils defined as undrained (analysis no. 1). The comparison between the calculated vertical and horizontal

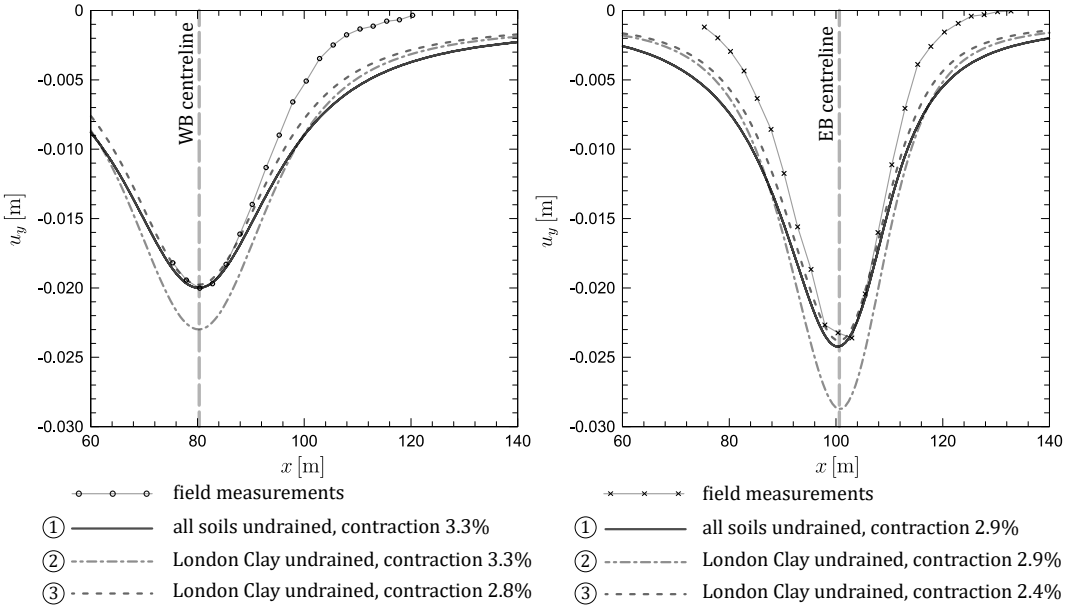

Fig. 7.3: Surface settlement profiles following the separate construction of the westbound (left) and eastbound (right) tunnels, showing a comparison between field measurements [125, 156] and the calculation results. Different behaviour of cover soils and tunnel contraction values are considered

displacement components, obtained immediately after the undrained calculation phases of WB and EB tunnel construction, and the corresponding field measurements along selected vertical axes are presented in Figs. 7.4 and 7.5. Both examples of drained cover soil analyses are considered. The soil deformation of the calculated cases is slightly higher compared to the measurements, especially considering the horizontal displacement component. However, the overall material response show great similarities to the field data. In addition, the differences between results obtained from analyses 2 and 3 appear to be marginal from the practical point of view.

The cumulative long-term settlement troughs, located 5.0 m below the ground surface, are presented in Fig. 7.6. In this analysis the case of the reduced contraction values is considered. The obtained soil response is shown as a total settlement value after each calculation phase, including consolidation before and after the EB tunnel construction. These results are compared to the field measurements found in [16]. The calculated soil deformation show a satisfactory correlation with the field data only during the construction of WB and EB tunnels. However, the settlement induced by ground consolidation is grossly underestimated. It is especially prominent after 15.5 years (5686 days) from the EB tunnel construction - the calculated settlement troughs are nearly two times smaller than the measured ones. Furthermore, the insignificant differences

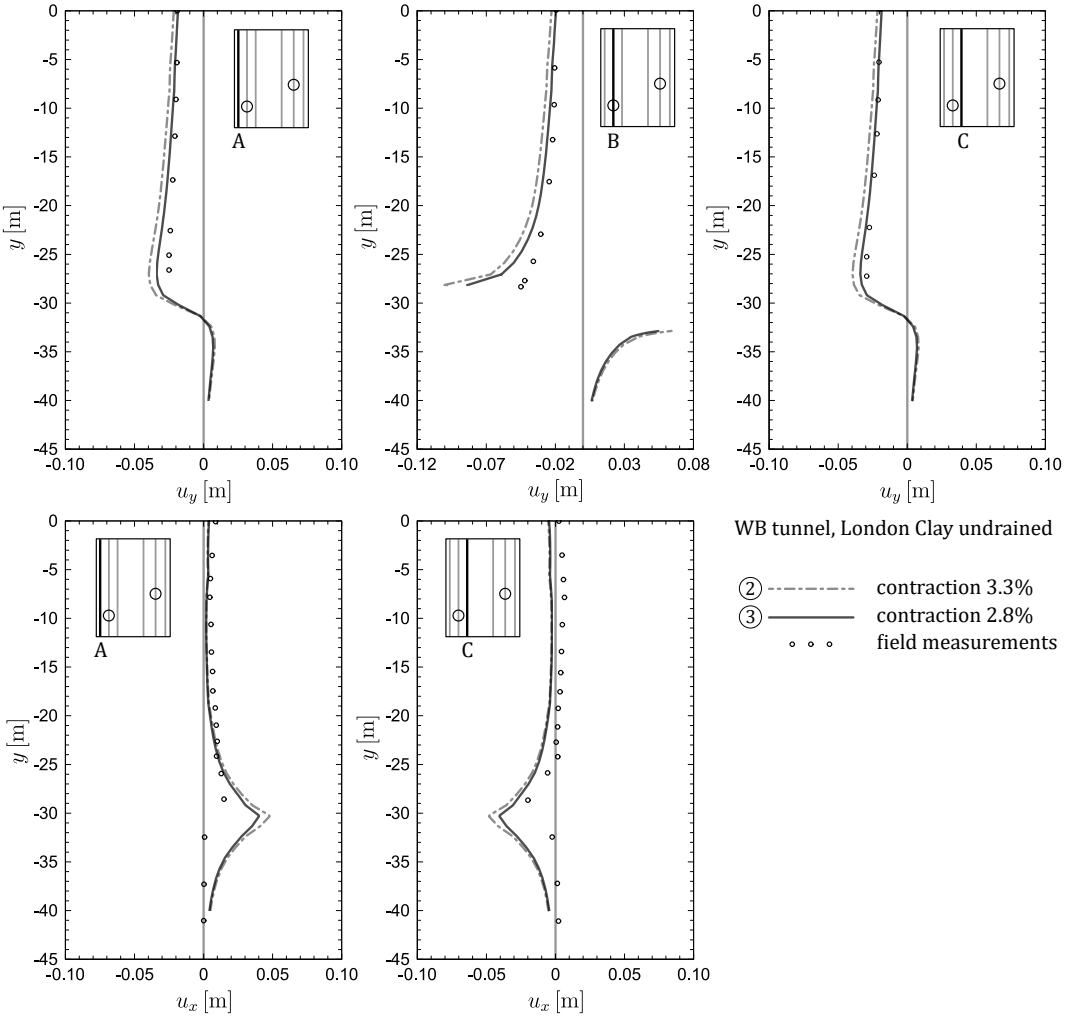

Fig. 7.4: The comparison of the field data [125] and the calculated vertical u_y (axes A,B,C) and horizontal u_x (axes A,C) displacement components, obtained immediately after the westbound tunnel construction

between two last calculation phases indicate that the settlement stabilises after the period of 15 years, whereas this tendency is not observed in the real case.

Conclusions

Considering surface settlement troughs and displacement changes in the tunnel vicinity, the results of the twin tunnel construction analysis show very good match to the measurements. Both the depth and the shape of the calculated displacement profiles are comparable to field data, suggesting that the *AHEBrick* model is capable of correctly simulating anisotropic stiffness. The deformation obtained for short-term and undrained conditions is especially agreeable, which from a practical perspective is desirable, as the most critical differential displacement

occur during that time. Nevertheless, the final settlement values are strongly correlated with the assumed contraction values and flow conditions. Ultimately, in order to reflect the actual state, a very good geotechnical survey must be carried out beforehand. In contrast, long-term settlement values are significantly underestimated, which means the model improvement is needed.

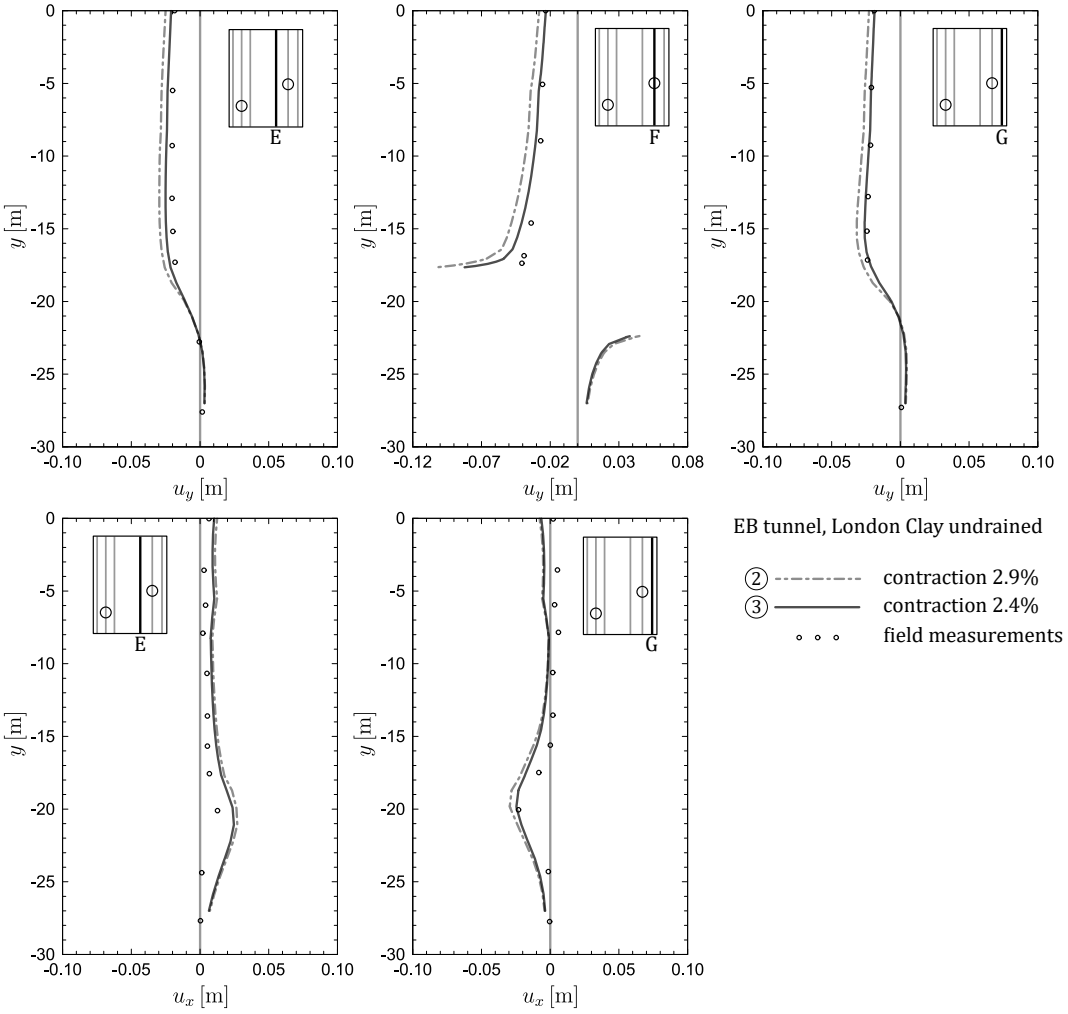

Fig. 7.5: The comparison of the field data [125] and the calculated vertical u_y (axes E,F,G) and horizontal u_x (axes E,G) displacement components, obtained immediately after the eastbound tunnel construction

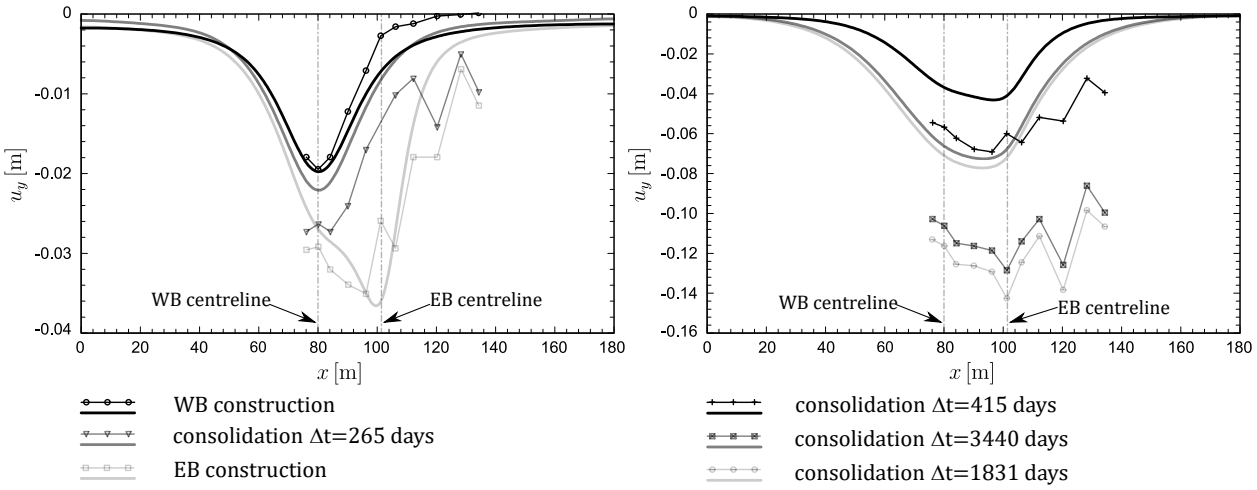

Fig. 7.6: The comparison between the measured [16] (lines with markers) and calculated (solid lines) cumulative long-term total settlements profiles u_y, obtained for the cross-section located 5.0 m under the surface. The case of the reduced contraction values (analysis 3) is taken into consideration. The graph on the left depicts the soil response during the construction of the WB and EB tunnels, while the graph on the right shows the settlements following the construction of the EB tunnel

7.2 FE and HG-A tunnels in Opalinus Clay at Mt. Terri Rock Laboratory, Switzerland

Numerous studies are currently being conducted with the aim of investigating soil suitability for storing nuclear waste products. This type of research is being conducted at the Underground Rock Laboratory (URL) in Mt Terri, Switzerland. It is a very extensive research project run by the international consortium of various organisations from different countries, operating under the auspices of the Swiss Federal Office for the Environment. The entire laboratory centre is built in Opalinus Clay deposits. Over the years, research has been conducted there to determine the hydrogeological, geochemical and geotechnical properties of this soil and its suitability to store nuclear waste. The layout of the laboratory is presented in Fig 7.7. It is located 300 m below the ground surface and it consists of various well-equipped and well-documented trial tunnels. In this section two tunnels are analysed: the FE and HG-A tunnels (marked in the figure).

Opalinus Clay is a heavily overconsolidated stiff clay, considered as a transitional material between soil and rock [21]. Due to its complex geological history, Opalinus Clay is characterised by pronounced bedding planes, often inclined to the horizontal direction. Hence, considering its structure, it exhibit anisotropic stiffness and strength properties. This material has been thoroughly tested in laboratory conditions, e.g. [51, 168, 169]. Additionally, an in-depth study

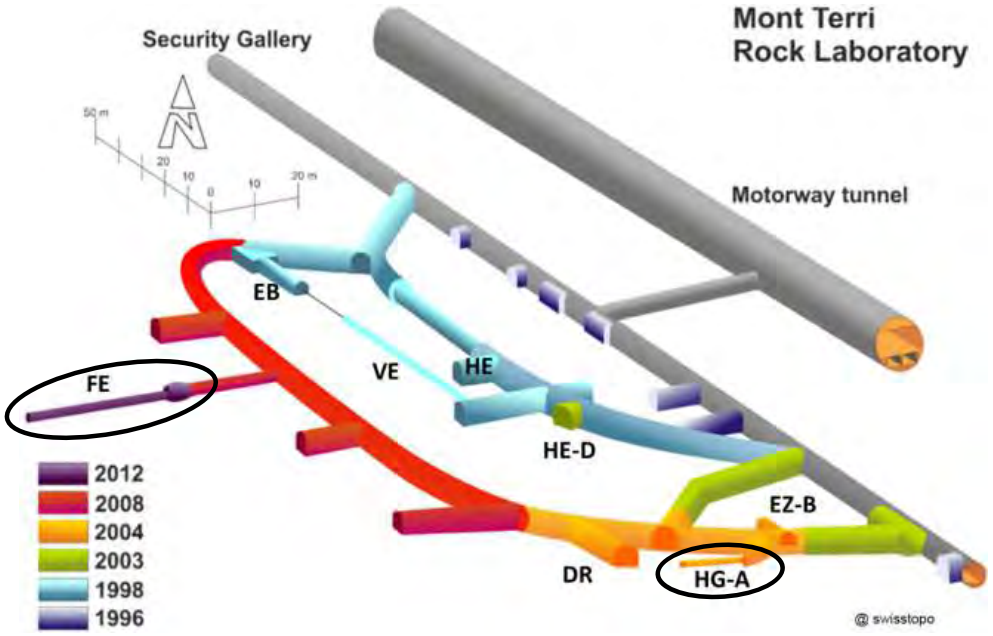

Fig. 7.7: The layout of the Mt. Terri Underground Rock Laboratory (the picture is the property of the Federal Office of Topography swisstopo [116]). The FE and HG-A tunnels are analysed in this section

of the material's mechanical properties was carried out by the National Cooperative for the Disposal of Radioactive Waste (Nagra), and the results of their experiments are presented in an extensive set of technical reports.

The Opalinus Clay tunnelling cases are often used in order to validate constitutive models which introduce strength anisotropy, e.g. [77, 98, 102]. By conducting back analyses of the tunneling problems with the use of the *AHEBrick* material model, this will allow to determine whether a model that accounts only for stiffness anisotropy can still produce satisfactory results when simulating a material with both anisotropic stiffness and strength.

The mechanical properties of the Opalinus Clay deposits are simulated with the *AHEBrick* material model. The set of the obtained material parameters is presented in Tab. 7.2. The parametric calibration was conducted through undrained triaxial compression element tests based on laboratory data reported in [87]. The results of the analysis are illustrated in Fig. 6.13 and the detailed description of the examinations is presented in Sec. 6.1.4. The material is fully saturated. The soil permeability is very small and exhibits anisotropy in directions normal and parallel to the bedding plane arrangement. However, the *AHEBrick* is not able to simulate anisotropic permeability if material's plane of isotropy is inclined to the horizontal direction. Hence, the average value of hydraulic conductivity $k_x = k_y = 0.0173 \cdot 10^{-6}\,\mathrm{m/day}$ [105] is adopted.

Table 7.2: Parameters of the Opalinus Clay simulated with the *AHEBrick* model

	Parameter	Opalinus Clay
Small strain stiffness	G_{vh}^{ref} [kPa]	126600
	β [-]	0.45
	α_G [-]	1.77
	p_{ref} [kPa]	100
Strain degradation	$G_{vh\mathrm{tmin}}^{\mathrm{ref}}$ [kPa]	25300
	$\|\|\boldsymbol{\varepsilon}\|\|_{\mathrm{sh}}$ [-]	0.0002
Shear strength criterion	ϕ [°]	35
	c [kPa]	1000
	ψ [°]	5
	p_{te} [kPa]	1
Unit weight	γ [kN/m^3]	24.7

Due to high depths, the ground surface is not modelled. The field stress applied in the calculations corresponds to the in-situ stress conditions [43], which values, defined for the model's global axis, are: $\sigma_{yy} = 6.5\,\mathrm{MPa}$ in vertical direction, $\sigma_{xx} = 4.5\,\mathrm{MPa}$ in horizontal direction and $\sigma_{zz} = 2.5\,\mathrm{MPa}$ (out of plane). Initial stress conditions are posed as constant within the analysed geometry, i.e. no gradients of effective stress and pore pressure are considered ($\gamma = \gamma_{\mathrm{w}} = 0\,\mathrm{kN/m^3}$). Within the domain a very high stress level occurs, hence all external boundaries are constrained. The groundwater flow is boundaries are open and seepage is allowed along the tunnel circumference. In the FE code [26], it is possible to chose the type of excess pore water pressure calculations. For cases of a material being subjected to considerable stresses, the use of Biot's effective stress concept is recommended. The applied parameter values are: bulk modulus of water $K_{\mathrm{w}} = 1.0\,\mathrm{GPa}$, Biot's pore pressure coefficient $\alpha_{\mathrm{Biot}} = 1.0$.

7.2.1 FE tunnel

The main motivation behind the construction of the Full-scale Emplacement (FE) tunnel was to investigate the coupled effect of the thermo-hydro-mechanical response of soil to the tunnel drilling [115]. The FE tunnel, 50 m long and 3 m in diameter, was excavated using a pneumatic hammer and a roadheader [102]. The plane of isotropy of the Opalinus Clay deposit is inclined $\theta = 33°$ to the horizontal direction. The geometry of the problem, shown in Fig. 7.8, was adopted from [77, 98, 102]. The dimensions of the square FE domain are $50.0\,\mathrm{m} \times 50.0\,\mathrm{m}$. The centre point of the tunnel is located in the middle of the model. The Fig. 7.8 shows the selected field measurement equipment: two 6-m-long extensometers (EXT-01, EXT-02) in directions normal and parallel to the bedding plane arrangement, two inclinometers (INCL-10, INCL-11) located above the tunnel face and two piezometers (BFEA-02, BFEA-05). The tunnel is divided

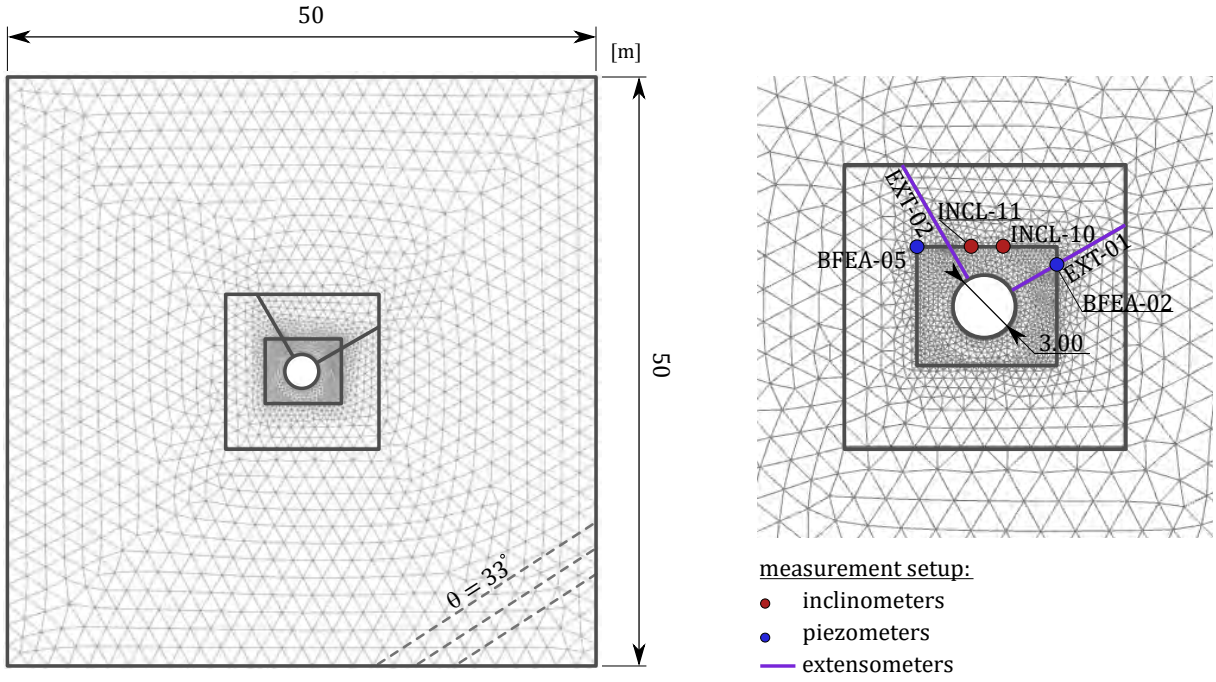

Fig. 7.8: Geometry and FE mesh of the FE tunnel drilling problem (4754 15-node triangular elements, 38265 nodes). Red dots and purple lines represent the selected measurement devices (inclinometers, piezometers and extensometers)

into four sections: access section, plug section, test section and interjacent sealing section. The analysis concerns soil response in the test section. In this section the shotcrete lining, with thickness of 0.16 m, was applied.

Calculations

The numerical analysis consists of the following calculation phases:

1. Initial phase, field stress conditions;
2. Tunnel drilling, $\Delta t = 1$ day;
3. Consolidation phase, fresh shotcrete, $\Delta t = 12$ days;
4. Consolidation phase, stiff shotcrete, $\Delta t = 77$ days.

All calculation phases are performed as consolidation analysis. Individual selected cross-sections within the test section are analysed, therefore the duration of tunnelling is assumed to be 1 day. The tunnel construction procedure is analogous to that given in Sec. 6.2.1. The duration of the consolidation phases correlates with the times given in [102, 115]. The first consolidation phase simulates short-term deformation of soil. During this phase, shotcrete lining is applied, which material properties correspond to the stiffness of the fresh shotcrete. Long-term deformation is considered during the 77-day consolidation phase. In this phase, cured

shotcrete is taken into account. Mechanical parameters of the shotcrete lining are adopted from [152]:

- fresh shotcrete: $EA = 2912\,\mathrm{kN/m}$, $EI = 6.21\,\mathrm{kNm^2/m}$, $\nu = 0.2$;
- cured shotcrete: $EA = 4592\,\mathrm{kN/m}$, $EI = 9.80\,\mathrm{kNm^2/m}$, $\nu = 0.2$.

Results

During construction, tunnel deformation was continuously monitored at selected convergence measurement sections. The analysed cross-section (C4) was located at TM27.6 (27.6 m "tunnel metre"). In this section, five observation points (P1-P5) were installed [102, 115]. Presented in Fig. 7.9, measured tunnel lining convergences over a 90-day period are compared with the corresponding calculated displacement. The presented deformation is scaled by a factor of 20. Overall, the results show very good qualitative and quantitative agreement, particularly at points P2-P4. In contrast, points P1 and P5 deviate significantly from the measurements. This

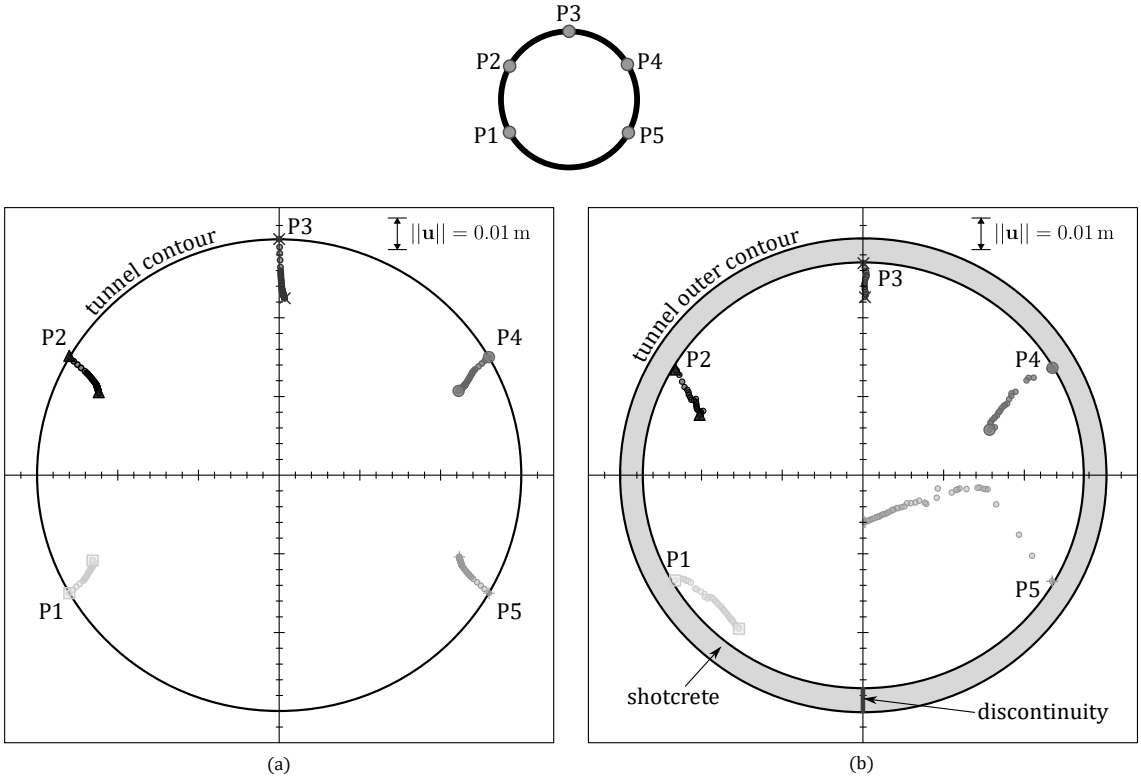

Fig. 7.9: Tunnel lining convergence, obtained at points P1-P5, during a 90-day period: a) calculated deformation compared to b) field data [115]. The deviation from the measurements at points P1 and P5 is attributed to the discontinuity in the tunnel liner

discrepancy is attributed to the failure of the shotcrete invert, which caused a discontinuity in the lower tunnel wall [115].

The measurements of vertical displacement and pore water pressure, shown in Fig. 7.10, were taken at TM31.0 [116]. Monitoring covered boring process of the entire tunnel, however, Fig. 7.10 presents only the changes induced by the excavation at this section. For this reason, the values of settlement are shown starting from zero. Most of the calculated settlement occurs during the tunneling phase, with the remainder resulting from consolidation. In the real case, rapid settlement was observed within the first week. Overall, the final calculated settlements

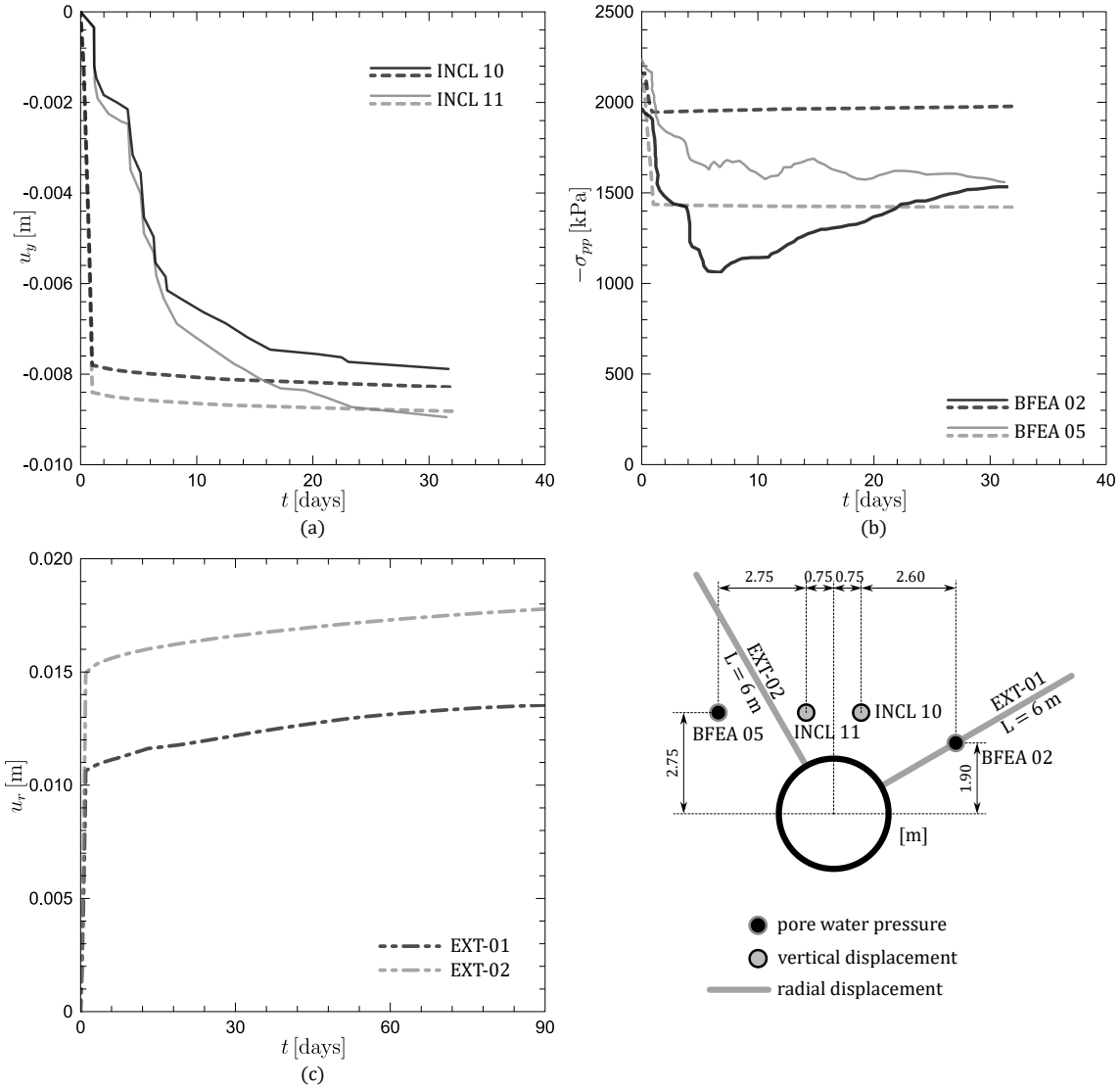

Fig. 7.10: The comparison between calculated and measured [116] settlement: a) u_y, b) pore water pressure σ_{pp}, c) radial displacement u_r at TM31.0 section of the FE tunnel

show good agreement with the measurements, particularly at point INCL-11. At point INCL-10, however, a slight overestimation was noted.

Pore water pressure changes were recorded at two piezometers, BFEA-02, BFEA-05. The initial pressure at the site was approximately $\sigma_{pp} = -2150, \mathrm{kPa}$ and it decreased as excavation progressed. The calculated results show reasonable agreement only at the measurement point BFEA-05, although the magnitudes are too small and any similarity becomes apparent only after 30 days. At point BFEA-02, the calculated values are significantly overestimated.

The calculated radial displacement values differ by approximately 0.005 m. Larger displacements were observed in the direction normal to the plane of isotropy (EXT-02), indicating that the tunnel lining deformation is non-uniform and influenced by the orientation of the bedding planes.

The influence of bedding plane inclination on tunneling induced deformation

The effect of the plane of isotropy inclination angle θ, relative to the horizontal direction, on material response is examined by comparing the analysed case with a reference example, where the bedding plane is horizontal ($\theta = 0°$). The deformation of the tunnel lining for two consolidation phases is presented in Fig. 7.11. The obtained deflection is scaled 40 times. For $\theta = 0°$, the deformation pattern is symmetrical about the y-axis. In contrast, when $\theta = 33°$, the deformation is visibly inclined relative to the plane of isotropy. Due to the bedding plane

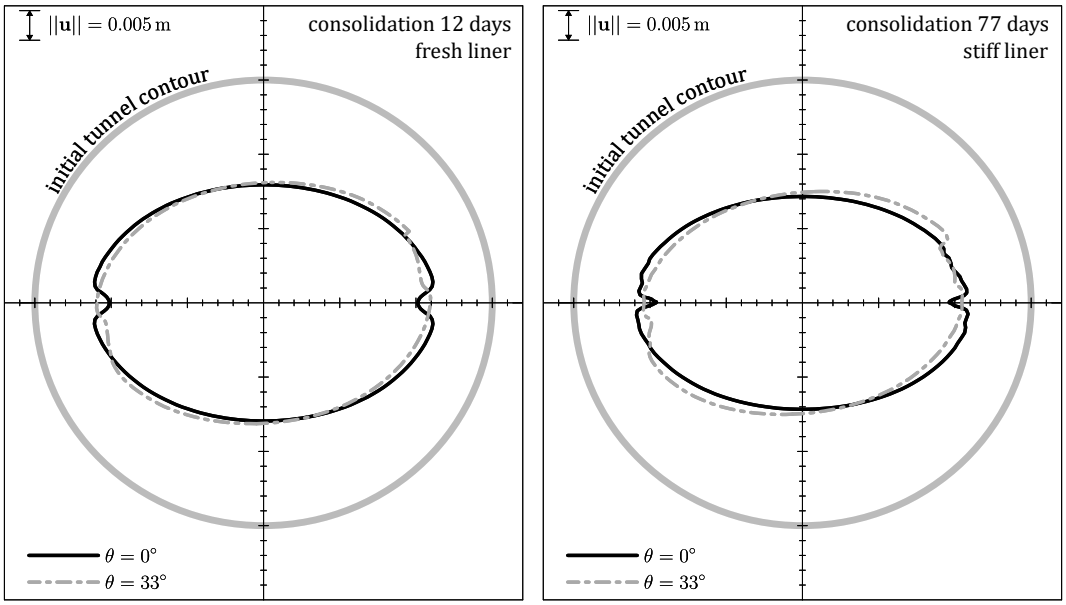

Fig. 7.11: The comparison of tunnel lining deformation for two cases of bedding planes oriented $\theta = 0°$ and $\theta = 33°$ to the horizontal direction

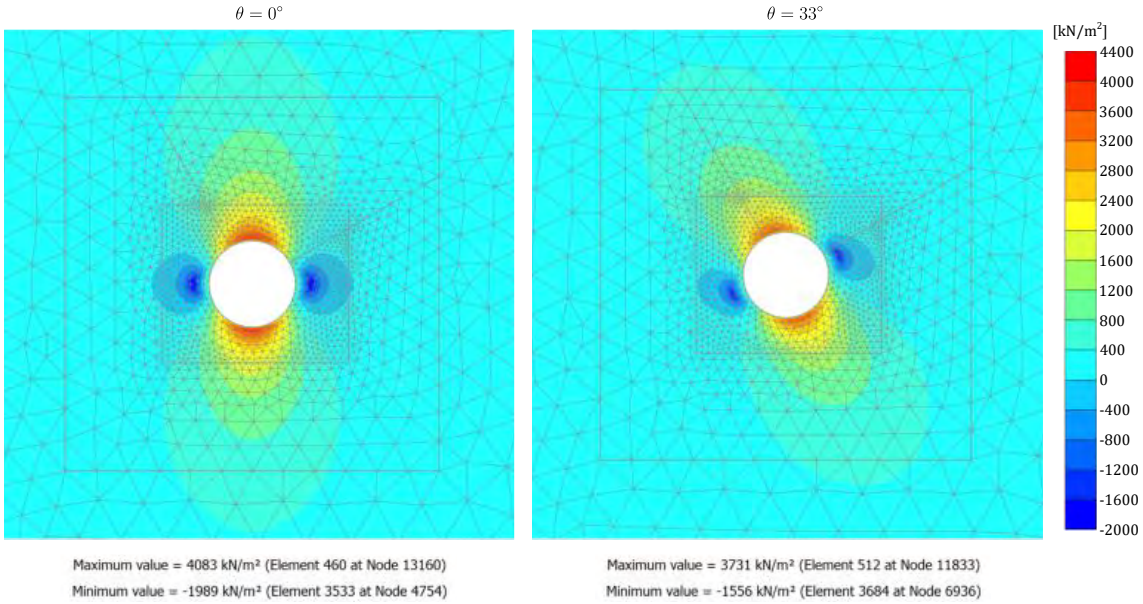

Fig. 7.12: The comparison of excess pore pressure generation, after the tunnel drilling phase, for two cases of bedding planes oriented $\theta = 0°$ and $\theta = 33°$ to the horizontal direction

inclination, the model cannot be simplified by assuming symmetry and analysing only half of it. Furthermore, as consolidation progresses, the inclination of the deformation becomes more pronounced.

The inclination angle of the bedding planes also influences the distribution of pore water pressure. This effect is illustrated in Fig. 7.12, which presents maps of excess pore pressure distribution after the first phase of tunnel excavation. Both the shape of the pressure dispersion and the magnitude of the pore pressures vary with bedding plane orientation. For $\theta = 33°$, the extreme pressure values are approximately 300 kPa lower than in the case of $\theta = 0°$.

The influence of the plane of isotropy inclination is clearly visible in the stiffness degradation maps shown in Fig. 7.13. Considerable reduction in stiffness occurs during the tunnel drilling phase, with the degradation most pronounced along the axis of symmetry defined by the unit vector $\mathbf{v}$. During consolidation, significant unloading develops at the depth of the tunnel face, along the plane of isotropy, as well as directly above and below the tunnel. Overall, stiffness degradation is greater when $\theta = 0°$, whereas unloading induced by consolidation is more pronounced when $\theta = 33°$.

Conclusions

The obtained settlement profiles and lining deformations show a high degree of consistency with the measurements. Significant differences in this case can be attributed to the tunnel

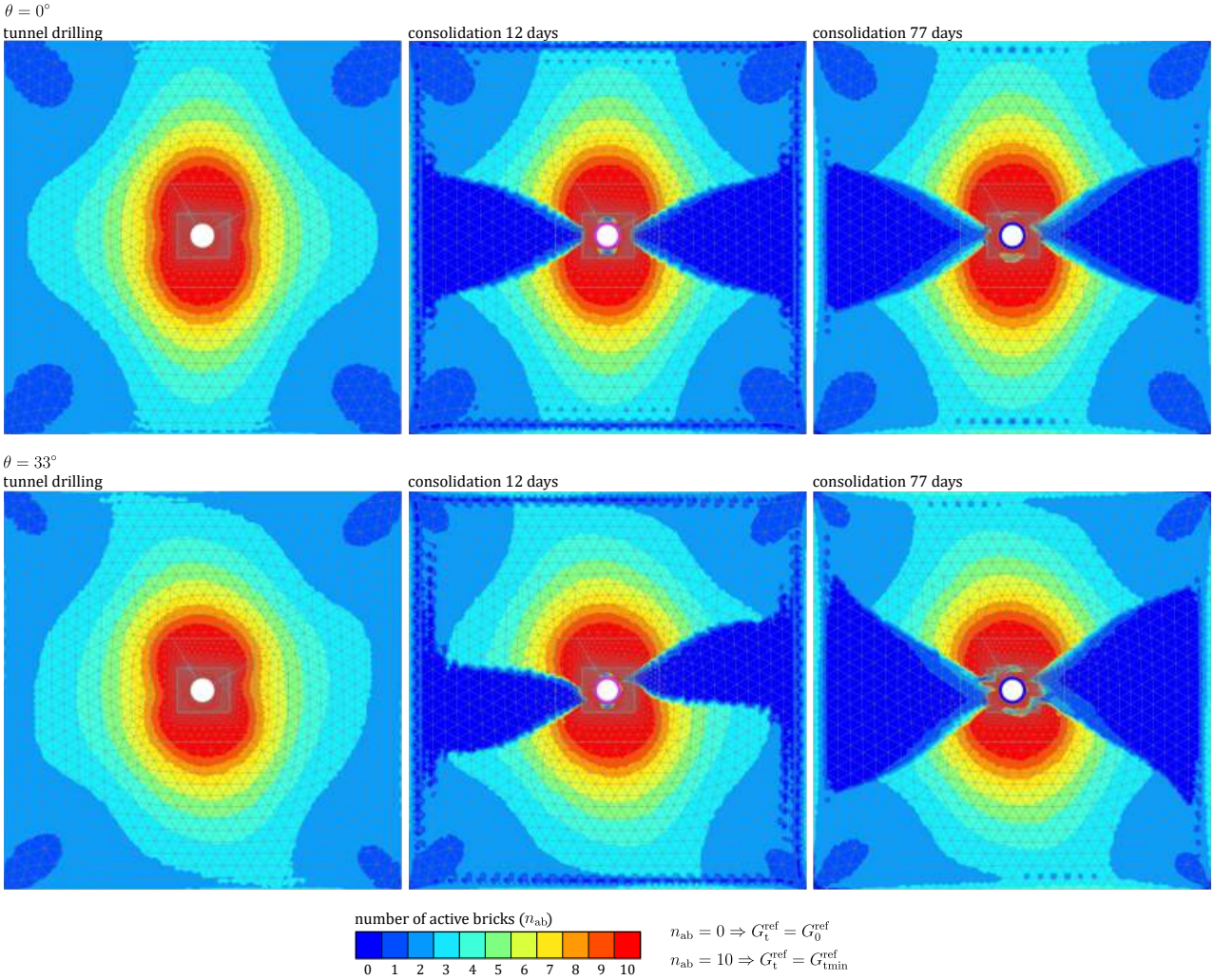

Fig. 7.13: Maps of stiffness degradation obtained for two cases of bedding planes oriented $\theta = 0°$ and $\theta = 33°$ to the horizontal direction. The intensity of stiffness degradation is indicated by the number of active bricks n_{ab}

lining failure. Conversely, the predicted changes in pore water pressure do not align well with the measurements. This inconsistency may be influenced by the selected pore water calculation type in the used FE code [26]. However, these discrepancies may also result from data interpretation, as well as the placement of the measurement devices along the tunnel length. The measurements were recorded throughout the entire construction period of the tunnel, which in the case of plane strain analysis may not always be correctly represented. In this context, it should be considered whether a three-dimensional analysis would have provided more reliable results.

7.2.2 HG-A microtunnel

The HG-A tunnel was constructed to investigate gas leakage and its potential release paths [105]. The tunnel measured 13 m in length and had a diameter of 1.04 m. Excavation was carried out using a micro-TBM auger in Opalinus Clay, where the bedding planes are inclined at $\theta = 45°$ to the horizontal. The geometry of the model and the FE mesh are shown in Fig. 7.14 and are analogous to the analyses reported in [77, 98]. The dimensions of the square domain are 20.0 m × 20.0 m, with the tunnel centre located in the middle. Vertical displacement and pore water pressure were monitored using piezometers (HG-A2, HG-A3) and inclinometers (HG-A5, HG-A7).

Calculations

Similarly to the analysis of the FE tunnel, all calculation phases in HG-A tunnel simulation are consolidation phases:

1. Initial phase, field stress conditions;
2. Tunnel drilling, $\Delta t = 7$ days;
3. Consolidation phase, $\Delta t = 3$ days.

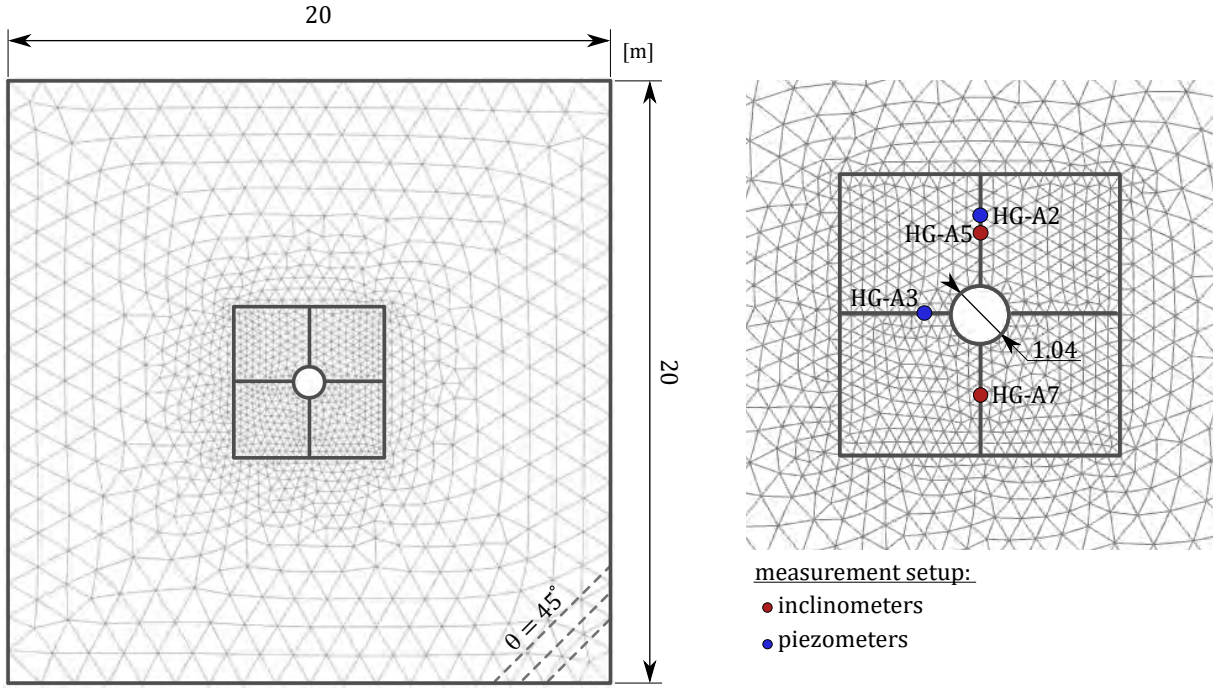

Fig. 7.14: Geometry and FE mesh of the HG-A microtunnel drilling problem (2380 15-node triangular elements, 19185 nodes). Red and blue dots represent the selected measurement devices (inclinometers and piezometers)

4. Consolidation phase, $\Delta t = 90$ days;
5. Consolidation phase, $\Delta t = 100$ days.

The tunnel construction phase corresponds to the actual excavation period, while the subsequent three consolidation phases represent the time during which measurements were recorded [105]. Tunnel drilling was simulated by deactivating the soil cluster and pore water within the tunnel face. The micro-TBM was modelled by introducing plate elements with very high stiffness: $EA = 10.25 \cdot 10^6\,\mathrm{kN/m}$, $EI = 2135\,\mathrm{kNm^2/m}$, $\nu = 0.0$. In order to simulate its removal, the lining was deactivated in the following 3-day consolidation phase. The tunnel lining was not applied in the analysis.

Results

The presented measurement results were obtained from devices located in the test section of the tunnel, which covered its final part (9-13 m). The comparison of measurements and calculations is shown in Fig. 7.15. Solid lines indicate field data and dashed lines define calculation results. Vertical component of displacement is measured at points above and below the tunnel, located at the same distance from the centre point of the tunnel, but the observed response differ. The settlement increases very quickly during the excavation and then stabilises. The obtained heave, however, continuously rises and the displacement does not stabilise during the 200 days of monitoring. These differences may be a result of construction, measurement errors or inconsistencies in the Opalinus Clay deposit. In contrast, the displacement values obtained from the calculations increase slightly during the excavation, but the actual drop is visible after the micro-TBM removal. After that time, the displacements remain at the same level. The obtained displacements are significantly overestimated.

Pore water pressure is measured above and next to the HG-A tunnel. The initial pore water pressure at the tunnel location is $\sigma_{pp} = -900\,\mathrm{kPa}$. The pressure changes measured above the tunnel are generally stable, but there is a significant peak at the beginning and then, about halfway through the observation period, a sudden drop in pressure occurs. The pressure calculated at this point drops rapidly at the beginning due to the tunnel drilling procedure and then stabilises. The results obtained are comparable to the measurements after about 100 days.

The water pressure measured on the side of the tunnel rises rapidly due to the tunnel construction and then dissipates to its initial state during consolidation. The calculations also show a peak in pressure increase, but it is much smaller. During consolidation, the pressure initially drops sharply and then stabilises. Ultimately, the pressure value obtained is too low and becomes comparable at the end of the measurements.

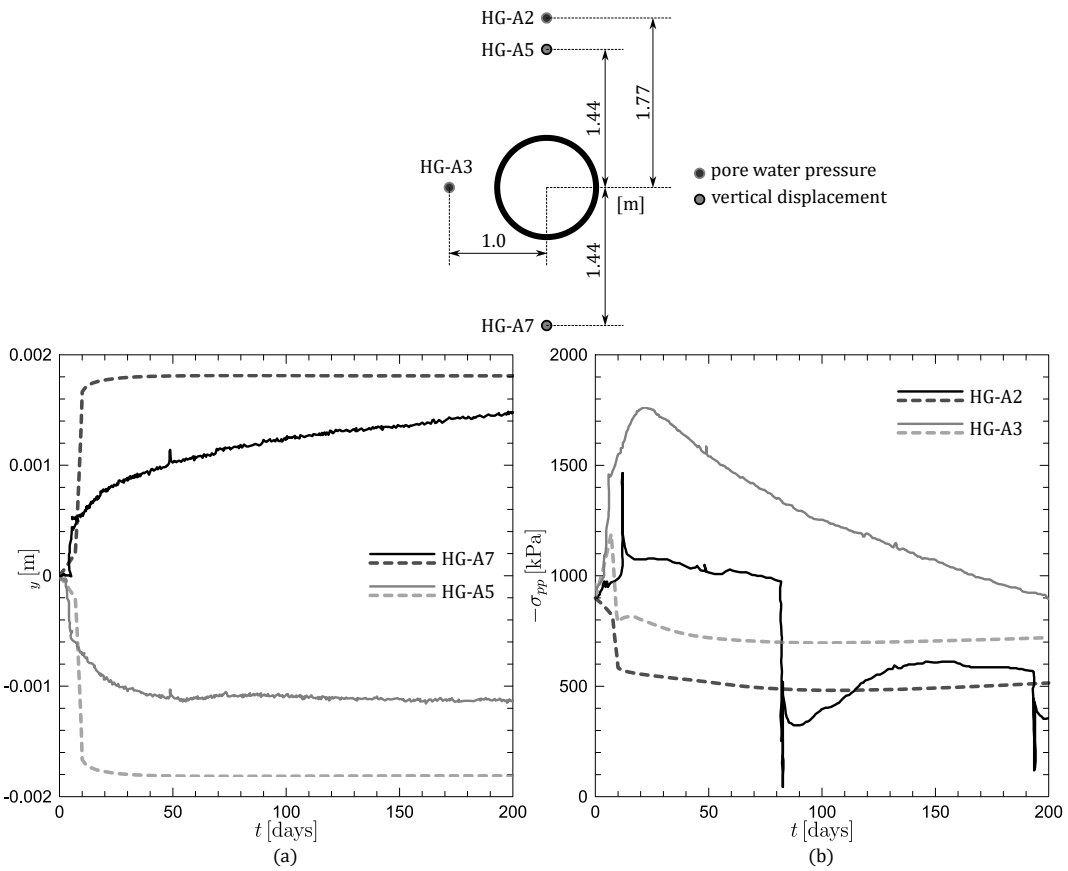

Fig. 7.15: The comparison between calculated and measured [43] settlement: a) u_y, b) pore water pressure σ_{pp} obtained from HG-A tunnel construction

Conclusions

The calculated results show significant discrepancies from the measurements both in terms of the settlement profiles and changes in pore water pressure. The material parameters of Opalinus Clay soil were assumed to be the same for the FE and HG-A tunnel analyses. However, since much greater consistency was achieved for the FE tunnel, this suggests that the soil properties may differ between the sites. Furthermore, these differences could be influenced by the strength anisotropy of Opalinus Clay. As the *AHEBrick* model does not account for strength anisotropy, it should be incorporated and the analyses repeated.

7.3 Open-pit trial excavation in Oxford Clay at Elstow, UK

The ground investigations, carried out in the 1980s, were aimed at finding a suitable location for the storage of low-level nuclear waste. Various locations in the United Kingdom were considered, one of which was in Oxford Clay at Elstow, Hertfordshire. The investigation involved constructing a full-scale excavation, the size of which would correspond to that of the nuclear waste repository, and monitoring ground deformation.

The surface dimensions of the constructed excavation were 38 m × 104 m, with the depth of 10 m. This case was heavily instrumented with extesometers, inclinometers and piezometers, which allowed to measure the obtained horizontal and vertical displacements and pore pressure in the selected points. The field measurement instrumentation and its location is presented in Figs. 7.16 and 7.17, illustrating the geometry of the problem for the plane strain and 3D analyses. Only one half of the excavation is considered, however the displacement measurement points were placed on both sides, symmetric to the excavation axis.

The full course of the experiment and the obtained results were reported in [132] and later in [70]. In [132], the advanced laboratory tests were carried out on Oxford Clay, some of which are presented in Fig. 6.12 in Sec. 6.1.4.

This case of the full scale open-pit trial excavation in Oxford Clay has been used in order to validate the *AHEBrick* model, and the comparative results were published in [101].

Geometry and soil conditions

The numerical analysis includes plane strain and 3D simulations. The total dimensions of the 3D model (Fig. 7.17) are 50.0 m × 166.0 m × 20.0 m. All results are presented for the cross-section $y = 67.5$ m, which dimensions correspond to the plane strain geometry (Fig. 7.16). The groundwater table in located 1.0 m below the ground surface. The groundwater flow conditions of the FE domain are closed at the excavation symmetry line and at the bottom. The side boundaries are defined as a constant water head, located at $y = -1.0$ m in case of plane strain model, and at $z = -1.0$ m for three dimensional analysis. Seepage is allowed at the top of the model and along the excavation slopes.

The 11-m-thick Oxford Clay layer is overburdened by 1.0 m of clayey head deposits and 2.0 m of the Weathered Oxford Clay. Below the Oxford Clay sediment, 4.0 m of Kellaways Sand and 2.0 m of Kellaways Clay are located. The top head deposits layer is described with Mohr-Coulomb model ($E_{\text{oed}} = 60000$ kPa, $\nu = 0.3$, $\phi = 30°$, $c = 10$ kPa, $\gamma = 18$ kN/m^3, $k_v = k_h = 0.01$ m/day, $K_0 = 1.0$). The remaining soils exhibit very high stiffness, hence they are

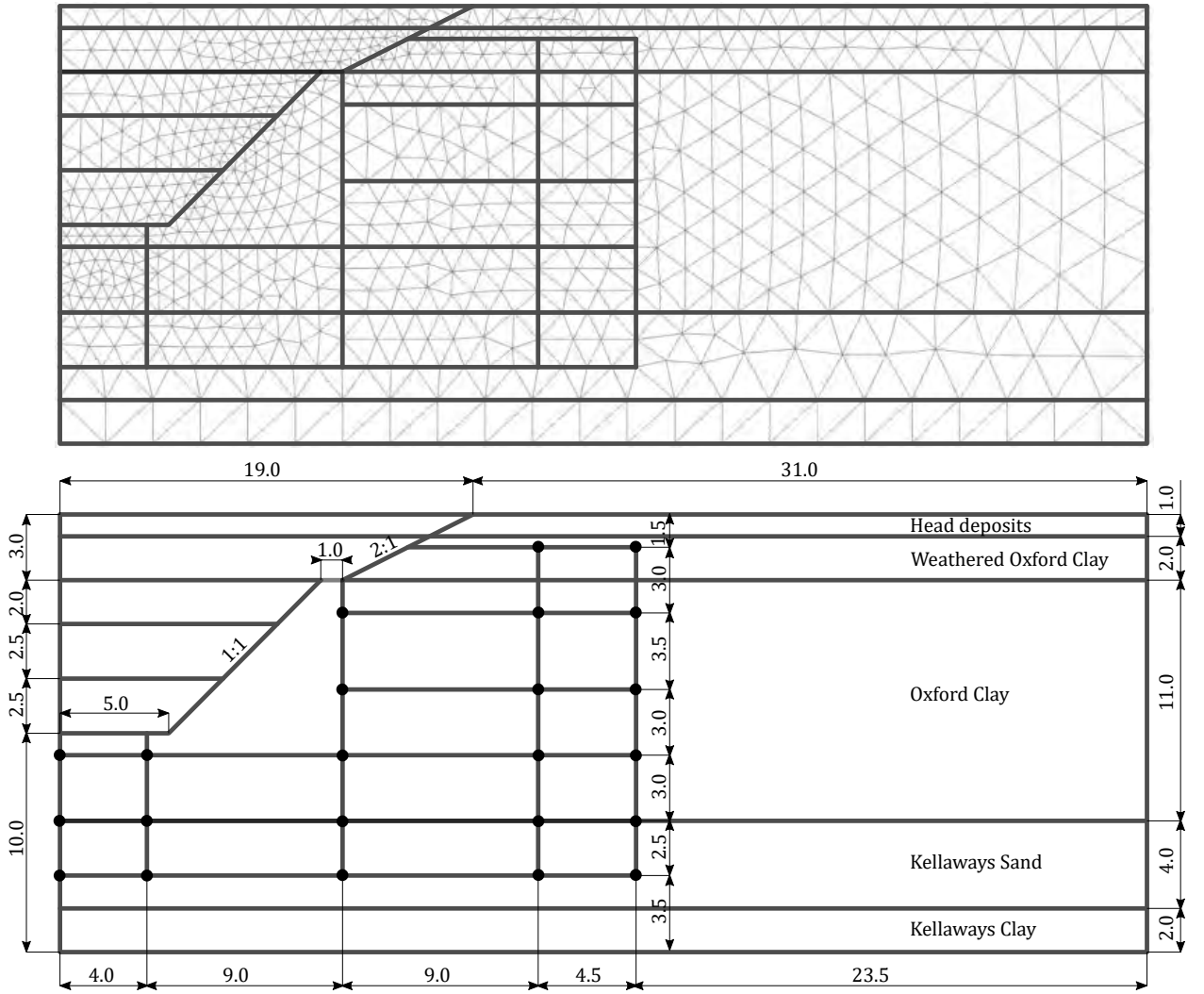

Fig. 7.16: Plane strain geometry and FE mesh of the back analysed case study of the trial excavation in Oxford Clay (1605 15-node triangular elements, 13035 nodes). Black dots represent the location of the displacement measurement points (extensometers and inclinometers)

simulated with the *AHEBrick* model. Material properties are generally adopted from [70, 132]. Since the excavation analysis mainly concerns Oxford Clay, some of the recent laboratory test are taken into consideration [29, 72]. The Oxford Clay parameter calibration is presented in Fig. 7.18. The left-side graph illustrates the material response to the relation between deviatoric and volumetric strain, obtained from triaxial radial tests in drained conditions [132]. The closest fit to the experimental data is achieved for $\alpha_G = 2.3$ and $\beta = 0.4$. The right-side graph shows undrained stress paths in $p - q$ plane [72]. The values of strength parameters are adopted as intermediate values between peak strength envelope and critical state line.

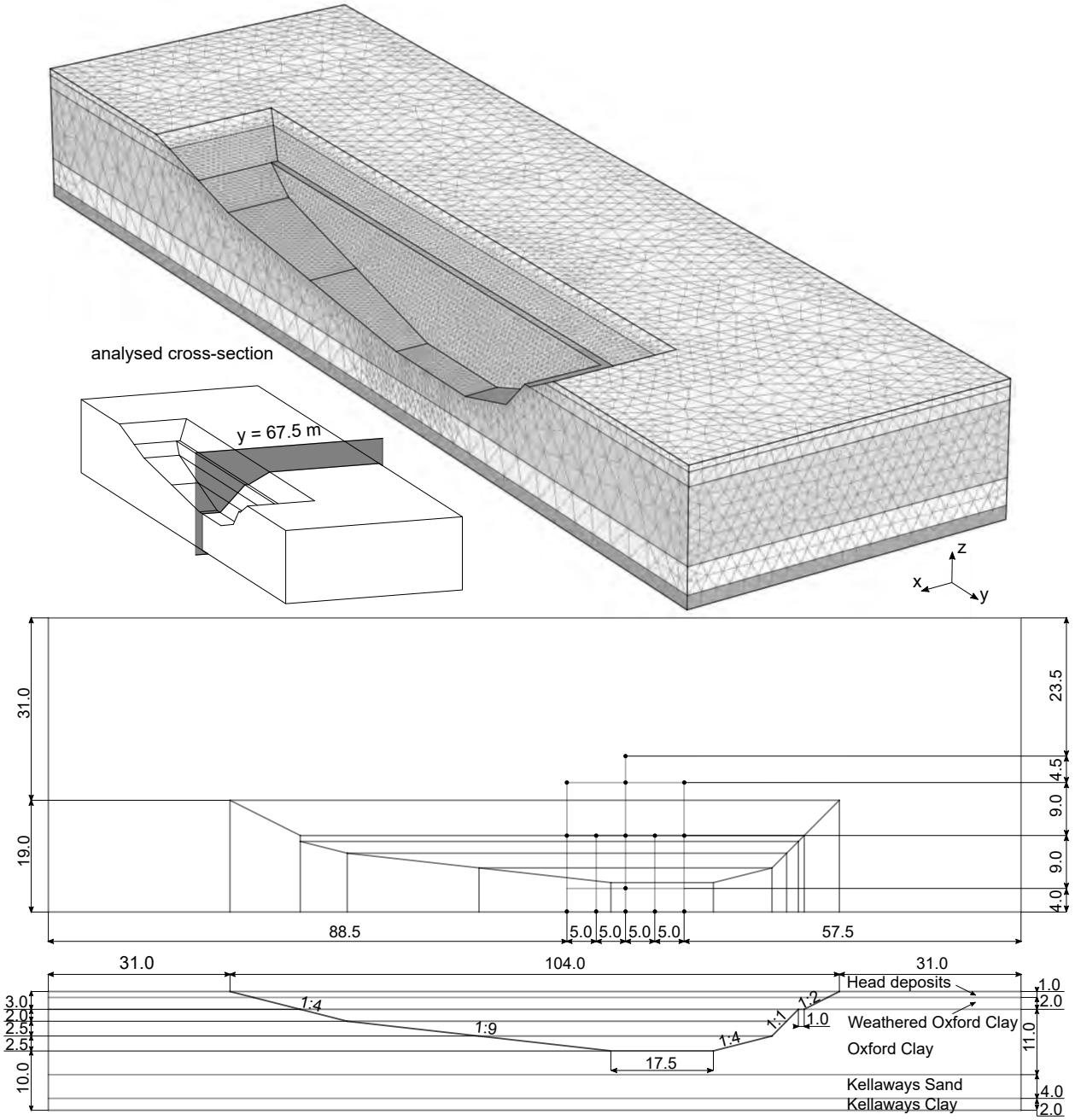

Fig. 7.17: Three dimensional geometry and FE mesh of the back analysed case study of the trial excavation in Oxford Clay (125995 10-node tetrahedral elements, 181357 nodes). Black dots represent the location of the displacement measurement points (extensometers and inclinometers)

Material properties simulated with the *AHEBrick* model are presented in Tab. 7.3. Reported in [70, 132] initial stress conditions are $K_0 = 1.0$ for the head deposits and $K_0 = 5.0$ for the remaining soils. It is an unusually high value, so initial stress state is selected based on findings in [29].

Table 7.3: Parameters of the soil deposits simulated with the *AHEBrick* model

	Parameter	Weathered Oxford Clay	Oxford Clay	Kellaways Clay	Kellaways Sand
Small strain stiffness	G_{vh}^{ref} [kPa]	120000	120000	157300	157300
	β [-]	0.4	0.4	0.5	0.5
	α_G [-]	2.3	2.3	1.7	1.7
	p_{ref} [kPa]	100	100	100	100
Strain degradation	$G_{vh\mathrm{tmin}}^{\mathrm{ref}}$ [kPa]	7000	10000	10000	10000
	$\|\|\boldsymbol{\varepsilon}\|\|_{\mathrm{sh}}$ [-]	0.0005	0.0005	0.001	0.001
Shear strength criterion	ϕ [°]	28	28	30	30
	c [kPa]	50	75	30	20
	ψ [°]	3	3	3	3
	p_{te} [kPa]	1	1	1	1
Flow	$k_v = k_h$ [m/day]	$0.0518 \cdot 10^{-3}$	$0.0518 \cdot 10^{-3}$	$0.0518 \cdot 10^{-3}$	$3.46 \cdot 10^{-3}$
Unit weight and initial stress	γ [kN/m^3]	18.5	17.5	19.5	19.5
	K_0 [-]	1.8	1.8	1.5	1.5

Calculations

The excavation construction is conducted in 4 phases of soil removal and dewatering. In each phase the selected soil cluster is deactivated and the water table is lowered by the introduction of the new global water level, located along the current excavation slope on the left side of the model. On the right side of the domain the water head is kept constant 1.0 m below the ground surface.

The simulation is carried out as fully-coupled flow deformation analysis. The duration of each excavation phase is consistent with the timeline reported for the real case. After the construction two consolidation phases are carried out, the duration of which coincides with the field measurements reading.

The numerical analysis consists of the following calculation phases:

1. Initial phase introduction of the state variables, K_0 stress conditions, hydrostatic water conditions;
2. Excavation of 3-m-thick layer, $\Delta t = 10$ days;
3. Excavation of 2-m-thick layer, $\Delta t = 2$ days;

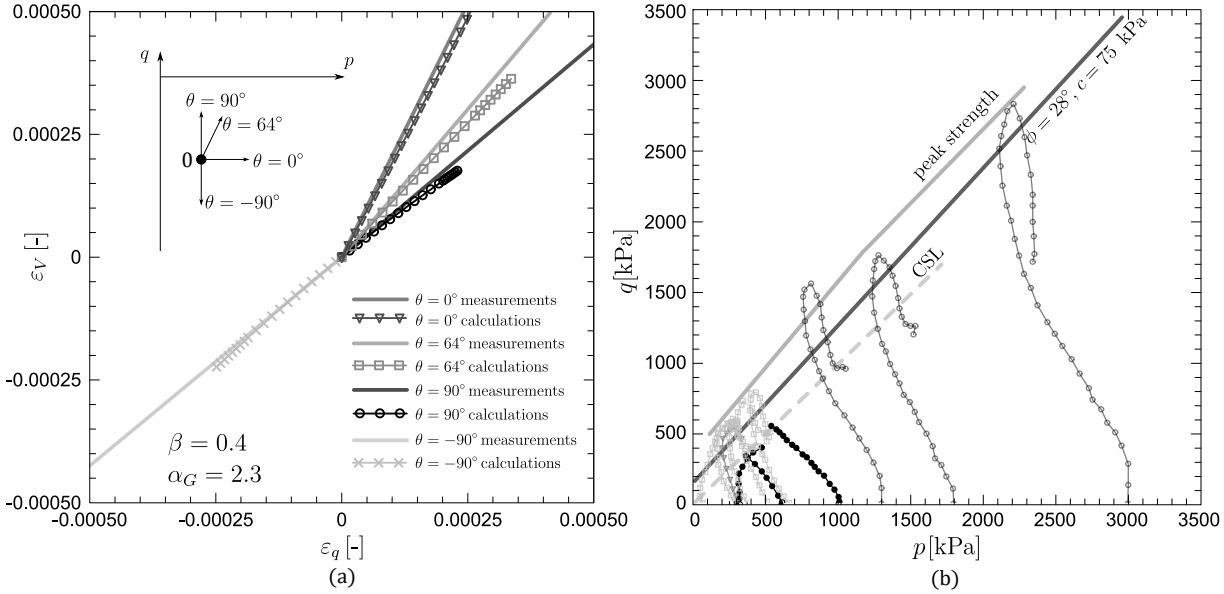

Fig. 7.18: The parameter calibration of the laboratory test data: a) the $\varepsilon_q - \varepsilon_V$ relation obtained from the drained triaxial radial tests [132], b) undrained stress paths in $p - q$ plane [72]

4. Excavation of 2.5-m-thick layer, $\Delta t = 5$ days;
5. Excavation of 2.5-m-thick layer, $\Delta t = 26$ days;
6. Consolidation phase, $\Delta t = 6$ days;
7. Consolidation phase, $\Delta t = 78$ days.

This procedure is the same for both plane strain and 3D simulations.

2D modelling

The results of the plane strain analysis are presented in Fig. 7.19. The figures show a part of the model. The black and blue arrows represent soil displacement obtained from the measurement points, located on the right and left sides of the excavation, respectively [70, 132]. Their values are averaged from the different field instrumentation situated close to each other. The measured deformation was obtained 6 days (two top pictures) and 84 days (two bottom pictures) after the excavation was completed. It should be noted that, despite the assumed symmetry of the structure, the reported field data differ on both sides of the excavation. This suggest that the soil stratification is naturally diverse and the flow conditions may not be uniform.

The soil displacement obtained from the numerical simulation is shown in a form of red vectors, in selected cross-sections. Qualitatively and quantitatively, the calculated results show a better agreement with the deformation measured on the left side of the excavation (blue arrows). The ground heave, achieved in the vicinity the excavation bottom, show great similarities to

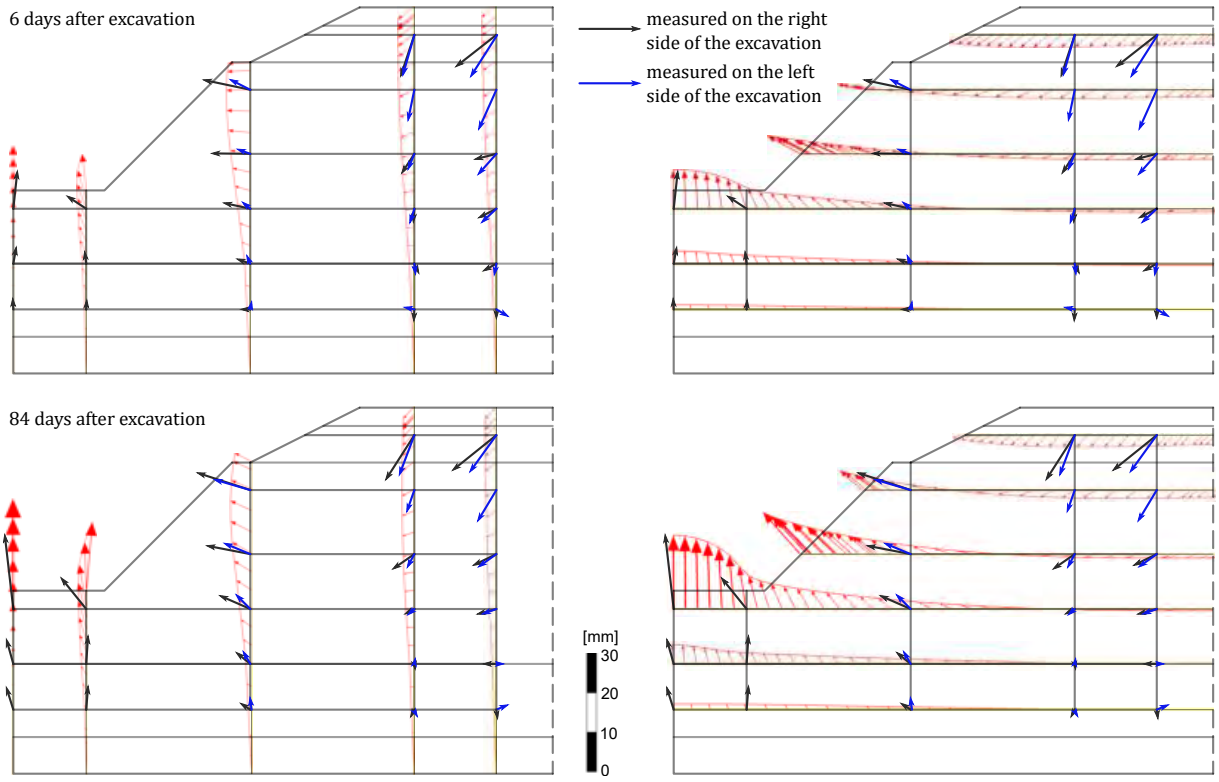

Fig. 7.19: Plane strain analysis; the comparison of the calculated soil deformation and displacement vectors obtained from the measurement points, located on the left (blue arrows) and right (black arrows) sides of the excavation [70, 132]

the field data. Conversely, for the cross-section located near the excavation slope ($x = 13\,\mathrm{m}$), the appropriate soil uplift was not possible to obtain after 6 days. After 84 days, however, it is noticeable, and the inclination of the displacement vectors is nearly identical. The largest discrepancies between calculations and measurements are visible for points located furthest from the excavated area. Here, the calculated displacements are underestimated by almost three times, especially near the ground surface.

3D modelling

The displacement vectors, obtained from the 3D analysis, are shown in Fig. 7.20, for the selected cross-section $y = 67.5\,\mathrm{m}$. For this case, the calculations also show better agreement with the measurements points located on the left side of the excavation. The overall soil deformation in the excavation vicinity show greater similarities to the field data than in the case of the plane strain calculations. However, at the excavation bottom, the results are slightly overestimated. Additionally, the settlement, calculated at the points located further from the axis, is significantly too small, much smaller than for the 2D analysis.

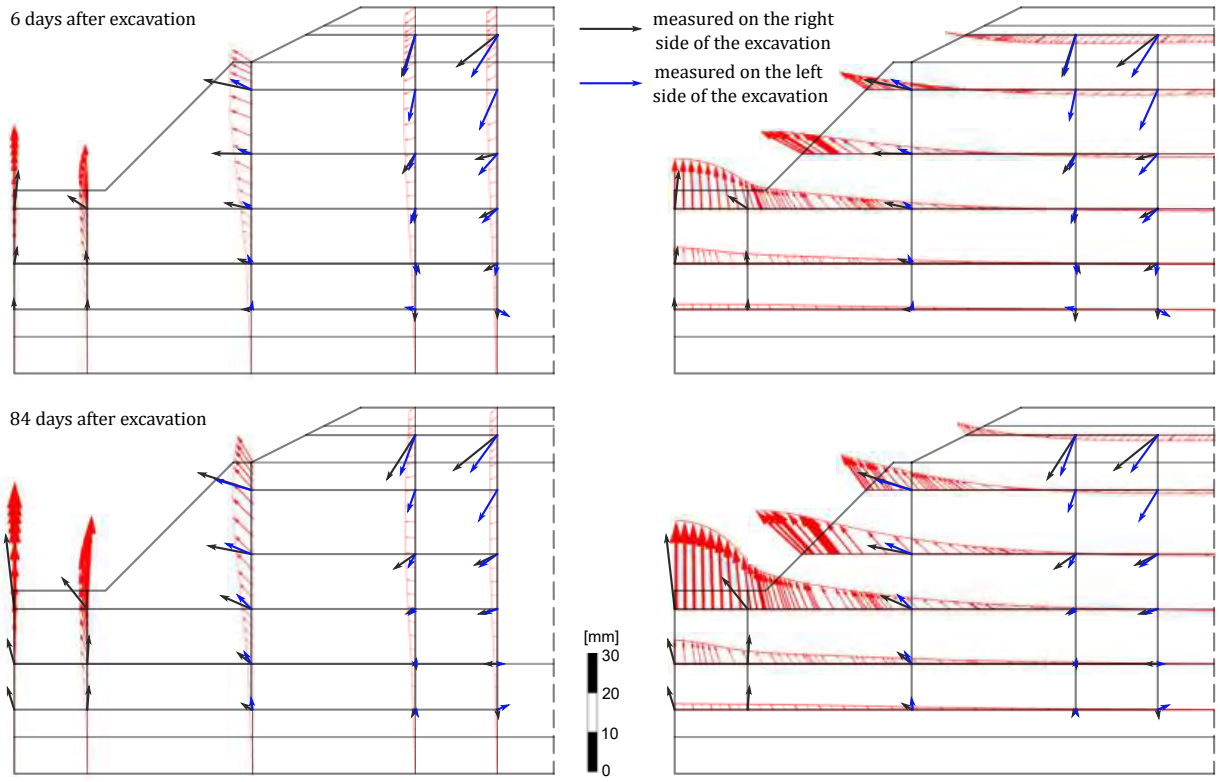

Fig. 7.20: Three dimensional analysis; the comparison of the calculated soil deformation and displacement vectors obtained from the measurement points, located on the left (blue arrows) and right (black arrows) sides of the excavation [70, 132]

In theory, the calculations obtained from plane strain and three dimensional analyses should show a high degree of similarity. It is not applicable in this case because the 3D geometry is not a perfect representation of an extruded 2D FE domain. Additionally, due to the applied fully-coupled flow deformation analysis, differences in soil response are generated by the advanced groundwater flow.

The influence of flow boundary conditions on soil deformation

In order to improve the results, additional numerical analyses has been performed, assuming that water flow is impossible at the sides of the FE domain. The obtained soil response in presented is Fig. 7.21 for the plane strain calculations and in Fig. 7.22 considering 3D modelling. In the both cases, soil heave at the excavation bottom decreased as compared to the previous numerical simulations, which in the case of 3D analysis leads to a perfect match between the calculated displacements and the field measurements. Additionally, the settlement at the points furthest from the excavation increased in comparison to the examples assuming open

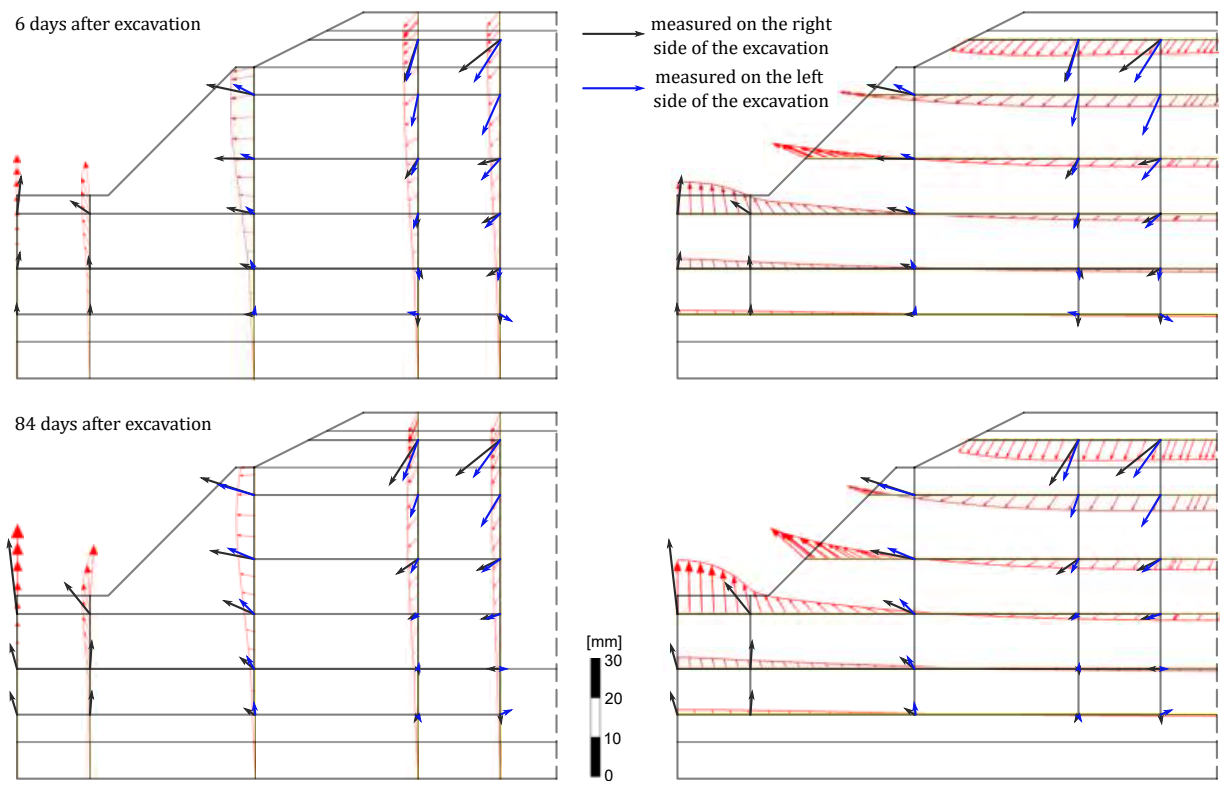

Fig. 7.21: Plane strain analysis; soil deformation obtained from the analysis assuming closed ground water conditions at the sides of the FE domain

flow conditions at side boundaries. Nevertheless, despite the improvement, the displacement values obtained in these points are still too small.

Due to the very low values of isotropic permeability coefficients of clays $k_v = k_h$, most of the water flow occurs in the Kellaways Sand layer. The overall flow intensity is significantly higher considering open boundary conditions. Here, the pore water pressure increases and, in points further from the model axis, the resulting settlement values are lower. In addition, along with the higher groundwater flow rate more water is displaced towards the excavation bottom. By closing off the possibility of water flowing in from the sides, less water moves to the excavated area and ground heave, due to soil unloading, is not as much pronounced.

Conclusions

The results of the analyses show acceptable agreement to the measurements, especially in the vicinity of the excavation bottom. In this area, the predicted displacement profiles show adequate accuracy both in the magnitudes and directions. Any inevitable differences between the calculations and measurements may be attributed to the performance of the *AHEBrick*

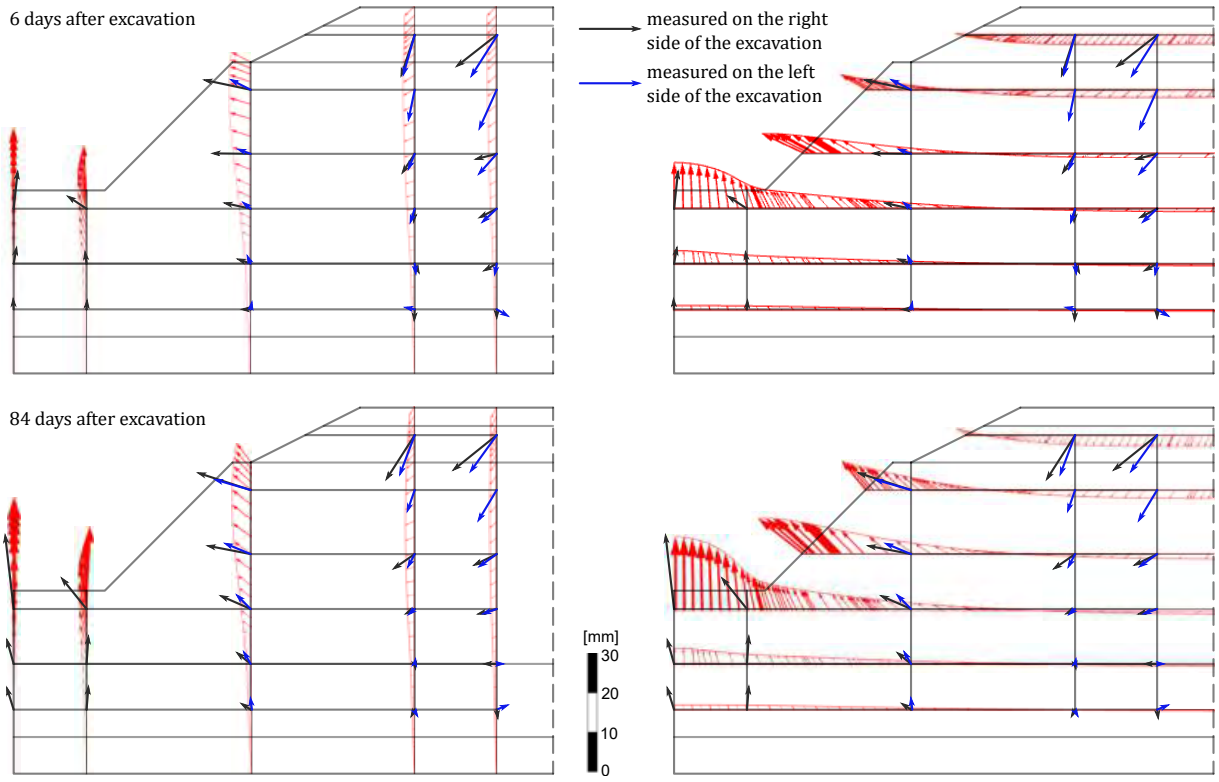

Fig. 7.22: Three dimensional analysis; soil deformation obtained from the analysis assuming closed ground water conditions at the sides of the FE domain

model but also to the limitations of geological surveys, permeability, and groundwater boundary conditions used in the coupled deformation-flow analysis.

8

Conclusions

Stiff overconsolidated soils exhibit anisotropic mechanical properties due to the geological processes that influence soil microstructure. However, the research on stiffness and strength anisotropy is relatively recent, mainly because laboratory testing in this area is complex and requires advanced equipment capable of measuring soil properties in multiple directions.

Although the influence of anisotropy on soil behaviour has been well established, material models available in commercial FE codes are, in most cases, isotropic. This is largely because implementing a robust and consistent framework for anisotropic soil constitutive models continues to be a significant challenge.

This gap is addressed by the *AHEBrick* model, presented in this work. Its structure is simple, following the framework of standard elasto-plastic models. The pre-failure barotropic stiffness is described through an anisotropic hyperelastic stress-strain relation. And nonlinear stiffness degradation is controlled by Brick-type procedure. The conventional isotropic Matsuoka-Nakai shear strength criterion limits admissible stress states. More importantly, the number of required material parameters is not excessive, and the model parameters can be determined using existing experimental testing methods.

The *AHEBrick* model was verified and validated through element test simulations, analysis of the geotechnical BVPs and through back analysis of real geotechnical cases reported in literature. The simulation of laboratory element tests included triaxial compression under both drained and undrained conditions (CID, CIU), drained radial paths, and analyses of how stress history under drained conditions affects material behaviour. In addition, the model was validated through a non-standard parameter calibration, where soil parameters were determined by comparing the simulated soil response with selected experimental data.

Based on these element tests, a parametric study of selected model parameters was carried out (α_G, β, $||\boldsymbol{\varepsilon}||_{\mathrm{sh}}$, K_0). The influence of inherent cross-anisotropy coefficient α_G on stress paths under undrained conditions, and consequently on soil strength, was demonstrated. As the value

of α_G increases, undrained shear strength gets lower. Furthermore, α_G has a very strong influence on stiffness changes under drained conditions. Calibration of the model parameters using laboratory data for selected stiff soils yielded satisfactory results, confirming that the values of the obtained parameters are both consistent and plausible.

The investigations on geotechnical BVPs were carried out for tunnel drilling, open-pit excavation and supported excavation cases. The aim of this research was to examine the impact of anisotropy on the soil-structure response. For this reason, in every case, the homogeneous soil layout, simple geometry and basic flow conditions were considered. Three values of the inherent cross-anisotropy coefficient $\alpha_G = 0.7, 1.0, 2.0$ and three initial stress states $K_0 = 0.5, 1.0, 2.0$ were studied.

Two tunnel drilling examples were analysed: deep tunnel and shallow tunnel. In both cases, the value of the inherent cross-anisotropy coefficient α_G highly influences soil response. Along with the increasing α_G value, the obtained settlement troughs get progressively deeper and steeper. Moreover, stiffness anisotropy influences changes in the tunnel lining. Depending on the assumed values of α_G and K_0, the shape and magnitude of deformation and bending moments are different.

For the open-pit excavation case, the influence of α_G and K_0 on soil behaviour is found to be generally negligible. Only very small differences were observed between the responses of isotropic and anisotropic soils, with the largest deformations occurring at $\alpha_G = 1.0$. Similarly, the largest displacements were obtained when the initial stress state was set to $K_0 = 2.0$. However, from an engineering perspective, these differences are minor and not worth considering.

For the deep supported excavation case, displacements were again larger for isotropic material. However, unlike in the open-pit case, the differences between isotropic and anisotropic soil responses are much more pronounced and cannot be overlooked. Interestingly, when $\alpha_G \neq 1.0$, the soil response is practically identical regardless of whether the horizontal stiffness is greater or smaller than the vertical stiffness. In contrast, when isotropic material is subjected to higher initial horizontal stresses ($K_0 = 2.0$), the resulting settlement troughs and horizontal displacement components are significantly greater than in other cases.

A similar pattern is observed in the displacement and bending moments of the diaphragm wall. Overall, the influence of inherent cross-anisotropy α_G becomes significant only when the soil is subjected to anisotropic initial stress conditions.

In all cases, the influence of α_G and K_0 on stiffness degradation is evident, particularly in the tunnelling and supported excavation examples. Therefore, it can be concluded that the evolution of stiffness is critical in determining the depth and shape of the resulting settlement profiles.

The role of stress-induced anisotropy was also examined by comparing the isotropic case ($\alpha_G = 1.0$, $K_0 = 1.0$) calculated with the *AHEBrick* model to that obtained with the isotropic hypoelastic model. The results indicate that for tunnelling and open-pit excavation the effects of stress-induced anisotropy are negligible. In contrast, for supported excavation, stress-induced anisotropy shows a significant influence and seems to be the major factor generating material deformation.

The back analysis was conducted for the real cases of twin tunnel construction in London Clay, FE and HG-A tunnels in Opalinus Clay and trial open-pit excavation in Oxford Clay. In order to obtain comparable response the model geometry and construction procedure are closely based on the data reported in literature. By analysing the results obtained from simulations of real geotechnical cases, the following conclusions can be drawn:

- The implemented stiffness anisotropy provides a good representation of soil behaviour, particularly under undrained conditions. From the engineering perspective, the agreement between model response and field measurements is especially valuable for short-term deformations, as the most critical differential displacement occurs during this stage.
- Considering long-term soil response, the results obtained from the calculations are significantly underestimated. Similarly, large discrepancies between model performance and field data are evident in case of Opalinus Clay, as it exhibits characteristics of rock matrix. These results suggest that stiffness anisotropy alone is insufficient for capturing settlements induced by consolidation. Additionally, the *AHEBrick* model is incapable of the proper simulation of rock materials. In such cases, strength anisotropy should also be incorporated to properly reflect soil response.
- In most of the geotechnical problems in preconsolidated fine-grained soils, analysed in this study, the idea of introducing anisotropy only into the elastic part of the material model provides, from an engineering perspective, sufficient accuracy of numerical simulations for predicting deformations. This, therefore, confirms the thesis of the study.
- Finally, to obtain results consistent with experimental evidence, material parameters must be selected with great care, and the applied flow conditions must be thoroughly considered, as both exert a major influence on the magnitude of the simulated soil response.

A

Appendix

A.1 Hyperelastic potential

In this section, the detailed description of all operations conducted in order to calculate tangent compliance matrix from the hyperelastic potential (Eq. 5.9) are provided.

The hyperelastic potential used in the AHEBrick model is based on the isotropic model proposed by Vermeer [163]:

$$W(\boldsymbol{\sigma}) = \frac{3p_{\text{ref}}^{1-\beta}}{2G_0^{\text{ref}}(1+\beta)} \left[\frac{2}{3}Q(\boldsymbol{\sigma})\right]^{\frac{1+\beta}{2}}, \tag{A.1}$$

defined as a function of a stress invariant $Q(\boldsymbol{\sigma})$:

$$Q(\boldsymbol{\sigma}) = \frac{1}{2}\text{tr}\,\boldsymbol{\sigma}^2 = \frac{1}{2}\sigma_{ab}\sigma_{ab}. \tag{A.2}$$

In order to incorporate inherent anisotropy into the formulation, the introduction of the joint invariant of stress and microstructure is needed [23, 24]:

$$Q_M(\boldsymbol{\sigma}, \mathbf{M}) = \frac{1}{2}\text{tr}\,(\boldsymbol{\sigma}^2 \cdot \mathbf{M}) = \frac{1}{2}M_{ab}\sigma_{bc}\sigma_{ca}. \tag{A.3}$$

Following findings in [23, 24], the mixed invariant of stress and microstructure is obtained:

$$\begin{aligned}\overline{Q}(\boldsymbol{\sigma}, \mathbf{M}) = c_1 Q + c_2 Q_M = \frac{1}{2}(c_1\sigma_{ab}\sigma_{ab} + c_2 M_{ab}\sigma_{bc}\sigma_{ca}) = \\ = \frac{1}{2}(c_1\delta_{ac}\sigma_{bc}\delta_{bc}\sigma_{ca} + c_2 M_{ab}\sigma_{bc}\sigma_{ca}) = \\ = \frac{1}{2}(\overbrace{c_1\delta_{ab} + c_2 M_{ab}}^{m_{ab}})\sigma_{bc}\sigma_{ca} = \frac{1}{2}m_{ab}\sigma_{bc}\sigma_{ca}.\end{aligned} \tag{A.4}$$

Parameters c_1 and c_2 are the material constants in the *AHEBrick* model. The isotropic potential from Eq. A.1 can be then modified to account for inherent and stress-induced anisotropy by replacing stress invariant $Q(\boldsymbol{\sigma})$ with mixed invariant $\overline{Q}(\boldsymbol{\sigma}, \mathbf{M})$:

$$\overline{W}(\boldsymbol{\sigma}, \mathbf{M}) = \frac{3p_{\text{ref}}^{1-\beta}}{2\,G_0^{\text{ref}}(1+\beta)} \left(\frac{2}{3}\overline{Q}(\boldsymbol{\sigma}, \mathbf{M})\right)^{\frac{1+\beta}{2}}. \tag{A.5}$$

In order to obtain tangent compliance tensor the second derivative of the modified potential function needs to be calculated.

A.1.1 First derivative

The secant stress-strain relation is obtained by the differentiation of the stress-based potential in Eq. A.5:

$$\varepsilon_{ij}^{\text{e}} = \frac{\partial \overline{W}(\boldsymbol{\sigma}, \mathbf{M})}{\partial \sigma_{ij}} = \frac{3p_{\text{ref}}^{1-\beta}}{2\,G_0^{\text{ref}}(1+\beta)} \frac{\partial \left[\left(\frac{2}{3}\overline{Q}\right)^{\frac{1+\beta}{2}}\right]}{\partial \sigma_{ij}}, \tag{A.6}$$

where partial derivative $\frac{\partial \left[\left(\frac{2}{3}\overline{Q}\right)^{\frac{1+\beta}{2}}\right]}{\partial \sigma_{ij}}$ is calculated as follows:

$$\begin{aligned}
\frac{\partial \left[\left(\frac{2}{3}\overline{Q}\right)^{\frac{1+\beta}{2}}\right]}{\partial \sigma_{ij}} &= \overbrace{\frac{2}{3}\frac{1+\beta}{2}\overline{Q}^{\frac{1+\beta}{2}-1}\frac{1}{2}}^{\text{C}=const} m_{ab}\frac{\partial(\sigma_{bc}\sigma_{ca})}{\partial \sigma_{ij}} = \\
&= \text{C}m_{ab}\left(\frac{\partial \sigma_{bc}}{\partial \sigma_{ij}}\sigma_{ca} + \frac{\partial \sigma_{ca}}{\partial \sigma_{ij}}\sigma_{bc}\right) = \\
&= \text{C}m_{ab}\left(\frac{1}{2}[\sigma_{ca}\delta_{bi}\delta_{cj} + \sigma_{ca}\delta_{bj}\delta_{ci} + \sigma_{bc}\delta_{ci}\delta_{aj} + \sigma_{bc}\delta_{cj}\delta_{ai}]\right) = \\
&= \frac{1}{2}\text{C}(\sigma_{aj}\delta_{bi}m_{ab} + \sigma_{ai}\delta_{bj}m_{ab} + \sigma_{bi}\delta_{aj}m_{ab} + \sigma_{bj}\delta_{ai}m_{ab}) = \\
&= \frac{1}{2}\text{C}(\sigma_{aj}m_{ai} + \sigma_{ai}m_{aj} + \sigma_{bi}m_{bj} + \sigma_{bj}m_{bi}) = \\
&= \text{C}(\sigma_{aj}m_{ai} + \sigma_{bi}m_{bj}),
\end{aligned} \tag{A.7}$$

The final expression of $\frac{\partial \left[\left(\frac{2}{3}\overline{Q}\right)^{\frac{1+\beta}{2}}\right]}{\partial \sigma_{ij}}$ is obtained using the provided relation:

$$\frac{\partial \sigma_{ij}}{\partial \sigma_{kl}} = \frac{1}{2}(\delta_{ik}\delta_{jl} + \delta_{il}\delta_{jk}) = I_{ijkl}. \tag{A.8}$$

In the end, the secant stress-strain relation takes the following form:

$$\begin{aligned}\varepsilon_{ij}^{\mathrm{e}} &= \frac{p_{\mathrm{ref}}^{1-\beta}}{2G_0^{\mathrm{ref}}}\left(\frac{2}{3}\overline{Q}\right)^{\frac{\beta-1}{2}}\frac{1}{2}(\sigma_{aj}m_{ai}+\sigma_{bi}m_{bj}) = \\ &= \frac{p_{\mathrm{ref}}^{1-\beta}}{2G_0^{\mathrm{ref}}\left(\sqrt{\frac{2}{3}\overline{Q}}\right)^{\beta-1}}\frac{1}{2}(\sigma_{aj}m_{ai}+\sigma_{bi}m_{bj}) = \\ &= \frac{1}{4\overline{G}_0}(\sigma_{aj}m_{ai}+\sigma_{bi}m_{bj}),\end{aligned} \tag{A.9}$$

where

$$\overline{G}_0 = G_0^{\mathrm{ref}}\left(\frac{\sqrt{\frac{2}{3}\overline{Q}(\boldsymbol{\sigma},\mathbf{M})}}{p_{\mathrm{ref}}}\right)^{1-\beta}. \tag{A.10}$$

A.1.2 Second derivative

Tangent compliance tensor C_{ijkl}^{t} is obtained by the differentiation of the formulation shown in Eq. A.9.

$$C_{ijkl}^{\mathrm{t}} = \frac{\partial^2\overline{W}(\boldsymbol{\sigma},\mathbf{M})}{\partial\sigma_{ij}\partial\sigma_{kl}} = \frac{p_{\mathrm{ref}}^{1-\beta}}{4G_0^{\mathrm{ref}}}\frac{\partial\left[\left(\frac{2}{3}\overline{Q}\right)^{\frac{\beta-1}{2}}(\sigma_{aj}m_{ai}+\sigma_{bi}m_{bj})\right]}{\partial\sigma_{kl}}, \tag{A.11}$$

where

$$\begin{aligned}\frac{\partial\left[\left(\frac{2}{3}\overline{Q}\right)^{\frac{\beta-1}{2}}(\sigma_{aj}m_{ai}+\sigma_{bi}m_{bj})\right]}{\partial\sigma_{kl}} &= \overbrace{\frac{\partial\frac{2}{3}\overline{Q}^{\frac{\beta-1}{2}}}{\partial\sigma_{kl}}}^{\mathrm{I}}(\sigma_{aj}m_{ai}+\sigma_{bi}m_{bj})+ \\ &+\frac{2}{3}\overline{Q}^{\frac{\beta-1}{2}}\overbrace{\frac{\partial(\sigma_{aj}m_{ai}+\sigma_{bi}m_{bj})}{\partial\sigma_{kl}}}^{\mathrm{II}}.\end{aligned} \tag{A.12}$$

Partial derivatives, denoted as I and II, are calculated in a following way:

$$\begin{aligned}\mathrm{I} &= \frac{\beta-1}{2}\left(\frac{2}{3}\overline{Q}\right)^{\frac{\beta-1}{2}-1}\frac{1}{3}m_{ab}\left(\frac{\partial\sigma_{bc}}{\partial\sigma_{kl}}\sigma_{ca}+\frac{\partial\sigma_{ca}}{\partial\sigma_{kl}}\sigma_{bc}\right) = \\ &= \frac{\beta-1}{2}\left(\frac{2}{3}\overline{Q}\right)^{\frac{\beta-3}{2}}\frac{1}{6}(\sigma_{al}m_{ak}+\sigma_{ak}m_{al}+\sigma_{bk}m_{bl}+\sigma_{bl}m_{bk}) = \\ &= \frac{\beta-1}{2}\left(\frac{2}{3}\overline{Q}\right)^{\frac{\beta-3}{2}}\frac{1}{3}(\sigma_{al}m_{ak}+\sigma_{bk}m_{bl}),\end{aligned} \tag{A.13}$$

$$\begin{aligned}\mathrm{II} &= \left[m_{ai}\left(\frac{\partial\sigma_{aj}}{\partial\sigma_{kl}}\right)+m_{bj}\left(\frac{\partial\sigma_{bi}}{\partial\sigma_{kl}}\right)\right] = \frac{1}{2}(\delta_{jl}m_{ki}+\delta_{jk}m_{li}+\delta_{il}m_{jk}+\delta_{ik}m_{lj}) = \\ &= (\delta_{jl}m_{ki}+\delta_{il}m_{jk})^{\mathrm{symm}}.\end{aligned} \tag{A.14}$$

Finally, the second stress derivative of the anisotropic hyperelastic potential $\overline{W}(\boldsymbol{\sigma}, \mathbf{M})$ gives the following tangent compliance tensor $\mathbf{C}^{\mathrm{t}}$:

$$
\begin{aligned}
C^{\mathrm{t}}_{ijkl} &= \frac{1}{4\overline{G}_0}\left[\frac{(\beta-1)(\sigma_{al}m_{ak}+\sigma_{bk}m_{bl})(\sigma_{aj}m_{ai}+\sigma_{bi}m_{bj})}{4\overline{Q}} + (\delta_{jl}m_{ki}+\delta_{il}m_{jk})^{\mathrm{symm}}\right] = \\
&= \frac{1}{4\overline{G}_0}\overbrace{\left[(\delta_{jl}m_{ki}+\delta_{il}m_{jk})^{\mathrm{symm}} - (1-\beta)\frac{(\sigma_{al}m_{ak}+\sigma_{bk}m_{bl})(\sigma_{aj}m_{ai}+\sigma_{bi}m_{bj})}{4\overline{Q}}\right]}^{A_{ijkl}} = \\
&= \frac{1}{4\overline{G}_0}A_{ijkl}. \qquad \text{(A.15)}
\end{aligned}
$$

References

1. Aagaard, B. Strength anisotropy of rocks. Master's thesis, Norwegian Institute of Technology, 1976.
2. Abelev, A. V., and Lade, P. V. Characterization of failure in cross-anisotropic soils. *Journal of Engineering Mechanics 130*, 5 (2004), 599–606.
3. Addenbrooke, T. I. *Numerical analysis of tunnelling in stiff clay.* PhD thesis, Imperial College London, 1996.
4. Addenbrooke, T. I., Potts, D. M., and Puzrin, A. M. The influence of pre-failure soil stiffness on the numerical analysis of tunnel construction. *Géotechnique 47*, 3 (1997), 693–712.
5. Al-Tabbaa, A. *Permeability and stress strain response of speswhite kaolin.* PhD thesis, University of Cambridge, 1987.
6. Al-Tabbaa, A., and Muir Wood, D. An experimentally based *bubble* model for clay. In *Numerical Models in Geomechanics - NUMOG III* (Niagara Falls, 1989), Pande and Pietruszczak, Eds., pp. 91–99.
7. Allirot, D., Boehler, J., and Sawczuk, A. Irreversible deformations of an anisotropic rock under hydrostatic pressure. *International Journal of Rock Mechanics and Mining Sciences and Geomechanics Abstracts 14*, 2 (1977), 77–83.
8. Amorosi, A., Rollo, F., and Houlsby, G. T. A nonlinear anisotropic hyperelastic formulation for granular materials: comparison with existing models and validation. *Acta Geotechnica 15*, 1 (2020), 179–196.
9. Arthur, J. R. F., and Menzies, B. K. Inherent anisotropy in a sand. *Géotechnique 22*, 1 (1972), 115–128.
10. Atkinson, J. H. *The deformation of undisturbed London Clay.* PhD thesis, University of London, 1973.

11. Atkinson, J. H. Anisotropic elastic deformations in laboratory tests on undisturbed London Clay. *Géotechnique 25*, 2 (1975), 357–384.
12. Atkinson, J. H., Richardson, D., and Stallebrass, S. E. Effect of recent stress history on the stiffness of overconsolidated soil. *Géotechnique 40*, 4 (1990), 531–540.
13. Atkinson, J. H., and Sallfors, G. Experimental determination of soil properties. In *10th ECSMFE* (1991), p. 915–956.
14. Attewell, P. B., and Farmer, I. W. Ground deformations resulting from shield tunnelling in London Clay. *Canadian Geotechnical Journal 11*, 3 (1974), 380–395.
15. Avgerinos, V. *Numerical investigation of tunnelling beneath existing tunnels*. PhD thesis, Imperial College London, 2014.
16. Avgerinos, V., Potts, D. M., and Standing, J. R. The use of kinematic hardening models for predicting tunnelling-induced ground movements in London Clay. *Géotechnique 66*, 2 (2016), 106–120.
17. Bauer, G. E., Shields, D. H., Mcrostie, G. C., and Scott, J. D. Predicted and observed footing settlements in a fissured clay. In *Proceedings of Conference on Performance of Building Structures* (1976), London: Pentech Press, pp. 287–302.
18. Bennett, R. H., O'Brien, N. R., and Hulbert, M. H. *Determinants of Clay and Shale Microfabric Signatures: Processes and Mechanisms*. Springer New York, 1991, ch. 2, pp. 5–32.
19. Benz, T. *Small-strain stiffness of soils and its numerical consequences*. PhD thesis, University of Stuttgart, 2007.
20. Benz, T., Vermeer, P., and Schwab, R. A small-strain overlay model. *International Journal for Numerical and Analytical Methods in Geomechanics 33* (2009), 25–44.
21. Bjerrum, L. The third terzaghi lectures; progressive failure in slopes of overconsolidated plastic clay and clay shales. *Journal of the Soil Mechanics and Foundations Division 93*, 5 (1967), 1–49.
22. Bjerrum, L. Problems of soil mechanics and construction on soft clays and structurally unstable soils (collapsible, expansive and others), State of the Art Report, Session 4. In *Proceedings of the 8th International Conference on Soil Mechanics and Foundation Engineering* (Moscow, 1973), Tsytovich and Chetyrkin, Eds., vol. 3, pp. 111–160.
23. Boehler, J.-P., and Sawczuk, A. Equilibre limite des sols anisotropes. *Journal de Mecanique 3* (1970), 5–33.
24. Boehler, J.-P., and Sawczuk, A. On yielding of oriented solids. *Archives of Mechanics 27* (1977), 185–206.

25. Boyce, H. R. A non-linear model for the elastic behaviour of granular materials under repeated loading. In *Proceedings of the International Symposium on Soils under Cyclic and Transient Loading* (Swansea, Wales, 1980), Pande and Zienkiewicz, Eds., pp. 285–294.
26. Brinkgreve, R. B. J., Kumarswamy, S., Swolfs, W. M., Zampich, L., and Ragi Manoj, N. *Plaxis finite element code for soil and rock analyses*. Plaxis bv, Bentley Systems, Incorporated, 2019.
27. Brinkgreve, R. B. J., Swolfs, W. M., and Engin, E. *Plaxis 2D Material Models Manual*. Plaxis.
28. Broch, E. Estimation of strength anisotropy using the point-load test. *International Journal of Rock Mechanics and Mining Sciences and Geomechanics Abstracts 20*, 4 (1983), 181–187.
29. Brosse, A., Hosseini Kamal, R., Jardine, R. J., and Coop, M. R. The shear stiffness characteristics of four Eocene-to-Jurassic UK stiff clays. *Géotechnique 67*, 3 (2017), 242–259.
30. Brosse, A. M., Jardine, R. J., and Nishimura, S. The undrained shear strength anisotropy of four Jurassic-to-Eocene stiff clays. *Géotechnique 67*, 8 (2017), 653–671.
31. Burland, J., Mair, R., Linney, L., Jardine, F., and Standing, J. A collaborativel research programme on subsidence damage to buildings: prediction, protection and repair. In *Geotechnical Aspects of Underground Construction in Soft Ground* (1996).
32. Burland, J., Standing, J., and Jardine, F. *Building response to tunnelling. Case studies from construction of the Jubilee Line Extension, London. Volume 1: Projects and methods*. CIRIA, 2001.
33. Burland, J., Standing, J., and Jardine, F. *Building response to tunnelling. Case studies from construction of the Jubilee Line Extension, London. Volume 2: Case studies*. CIRIA, 2001.
34. Burland, J. B. "Small is beautiful" - the stiffness of soils at small strains, 9th Laurits Bjerrum Memorial Lecture. *Canadian Geotechnical Journal 26*, 4 (1989), 499–516.
35. Burland, J. B., and Moore, J. The measurement of ground displacement around deep excavation. In *Proceedings of the Symposium on Field Instrumentation* (1973).
36. Burland, J. B., Rampello, S., Georgiannou, V. N., and Calabresi, G. A laboratory study of the strength of four stiff clays. *Géotechnique 46*, 3 (1996), 491–514.
37. Callisto, L. *Studio sperimentale su un'argilla naturale: il comportamento meccanico dell'argilla di Pisa*. PhD thesis, University of Rome 'La Sapienza', 1996.
38. Casagrande, A., and Carillo, N. Shear failure of anisotropic materials. In *Proceedings of Boston Society of Civil Engineers* (1944), vol. 31, pp. 74–87.

39. Clarke, S. D. *Enhancement of the BRICK constitutive model to incorporate viscous soil behaviour*. PhD thesis, University of Sheffield, 2009.
40. Clayton, C. R. I. Stiffness at small strain: research and practice, 50th Rankine Lecture. *Géotechnique 61*, 1 (2011), 5–37.
41. Clayton, C. R. I., and Heymann, G. Stiffness of geomaterials at very small strains. *Géotechnique 51*, 3 (2001), 245–255.
42. Cole, K. W., and Burland, J. B. Observation of retaining wall movements associated with a large excavation. In *5th European Conf. Soil Mech. Found. Eng.* (1972), pp. 445–453.
43. Corkum, A., and Martin, C. Modelling a mine-by test at the Mont Terri Rock Laboratory, Switzerland. *International Journal of Rock Mechanics and Mining Sciences 44*, 6 (2007), 846–859.
44. Cudny, M. *Some aspects of the constitutive modelling of natural fine grained soils*. Habilitation Monograph, Faculty of Civil and Environmental Engineering, Gdańsk University of Technology. Wydawnictwo IMOGEOR, 2013.
45. Cudny, M., Lisewska, K., and Truty, A. Incorporation of cross-anisotropic small-strain stiffness into Hardening Soil model. submitted to Acta Geotechnica, 2025.
46. Cudny, M., Lisewska, K., Winkler, M., and Marcher, T. Modelling tunnelling-induced deformation in stiff soils with a hyperelastic-plastic anisotropic model. *Acta Geotechnica* (2024).
47. Cudny, M., and Staszewska, K. A hyperelastic model for soils with stress-induced and inherent anisotropy. *Acta Geotechnica 16* (2021), 1–19.
48. Cudny, M., and Truty, A. Refinement of the Hardening Soil model within the small strain range. *Acta Geotchnica 15*, 8 (2020), 2031–2051.
49. Díaz-Rodríguez, J. A., and López-Molina, J. A. Strain thresholds in soil dynamics. In *Proceedings of the 14-th World Conference on Earthquake Engineering* (Beijing, 2008).
50. Duveau, G., Shao, J. F., and Henry, J. P. Assessment of some failure criteria for strongly anisotropic geomaterials. *Mechanics of Cohesive-frictional Materials 3* (1998), 1–26.
51. Favero, V., Ferrari, A., and Laloui, L. Anisotropic behaviour of opalinus clay through consolidated and drained triaxial testing in saturated conditions. *Rock Mechanics and Rock Engineering 51* (2018), 1305–1319.
52. Fioravante, V., and Capoferri, R. On the use of multi-directional piezoelectric transducers in triaxial testing. *Geotechnical Testing Journal 24*, 3 (2001), 243–255.

53. Franklin, J. A. Suggested method for determining point load strength. *International Journal of Rock Mechanics and Mining Sciences and Geomechanics Abstracts 22*, 2 (1985), 51–60.
54. Franzius, J., Potts, D., and Burland, J. B. The influence of soil anisotropy and K_0 on ground surface movements resulting from tunnel excavation. *Géotechnique 55*, 3 (2005), 189–199.
55. Gajo, A. Hyperelastic modelling of small-strain stiffness anisotropy of cyclically loaded sand. *International Journal for Numerical and Analytical Methods in Geomechanics 34* (2010), 111–134.
56. Gasparre, A. *Advanced laboratory characterisation of London Clay*. PhD thesis, Imperial College, London, 1990.
57. Gasparre, A., Nishimura, S., Minh, N. A., Coop, M. R., and Jardine, R. J. The stiffness of natural London Clay. *Géotechnique 57*, 1 (2007), 33–47.
58. Graham, J., and Houlsby, G. T. Anisotropic elasticity of a natural clay. *Géotechnique 33*, 2 (1983), 165–180.
59. Grammatikopoulou, A., Zdravkovic, L., and Potts, D. M. The influence of previous stress history and stress path direction on the surface settlement trough induced by tunnelling. *Géotechnique 58*, 4 (2008), 269–281.
60. Gryczmański, M. State of the art in modelling of soil behaviour at small strains. *Architecture, Civil Engineering, Environment - ACEE 2*, 1 (2009), 61–80.
61. Gudehus, G., and Mašín, D. Graphical representation of constitutive equations. *Géotechnique 59*, 2 (2009), 147–151.
62. Hardin, B. O., and Blandford, G. E. Elasticity of particulate materials. *Journal of the Geotechnical Engineering Division, ASCE 115*, 6 (1989), 788–805.
63. Hardin, B. O., and Drnevich, V. P. Shear modulus and damping in soils: design equations and curves. *Journal of the Soil Mechanics and Foundations Division, ASCE 98*, SM7 (1972), 667–692.
64. Hettler, A., and Danne, S. Strain response envelopes for low cycle loading processes. In *Proceedings of the 18th International Conference on Soil Mechanics and Geotechnical Engineering* (Paris, 2013), Elsevier, pp. 1491–1494.
65. Heymann, G., Clayton, C. R. I., and Reed, G. T. Laser interferometry to evaluate the performance of local displacement transducers. *Géotechnique 47*, 3 (1997), 399–405.
66. Hight, D. W., Bennell, J. D., Chana, B., Davis, P. D., Jardine, R. J., and E., P. Wave velocity and stiffness measurements of the crag and lower london tertiaries at sizewell. *Géotechnique 47*, 3 (1997), 451–474.

67. Hight, D. W., Gasparre, A., Nishimura, S., Minh, N. A., Jardine, R. J., and Coop, M. R. Characteristics of the London Clay from the Terminal 5 site at Heathrow Airport. *Géotechnique 57*, 1 (2007), 3–18.
68. Hight, D. W., Gens, A., and Symes, M. J. The development of a new hollow cylinder apparatus for investigating the effects of principal stress rotation in soils. *Géotechnique 33*, 4 (1983), 355–383.
69. Hight, D. W., and Higgins, K. G. An approach to the prediction of ground movements in engineering practice: Background and application. In *Proceedings of the First International Conference on Pre-failure Deformation Characteristics of Geomaterials* (Sapporo, 1995), M. Shibuya and Miura, Eds., vol. 2, pp. 909–945.
70. Hird, C. C., and Pierpoint, N. D. Stiffness determination and deformation analysis for a trial excavation in oxford clay. *Géotechnique 47*, 3 (1997), 665–691.
71. Hoek, E. Strength of jointed rock masses. *Géotechnique 33*, 3 (1983), 187–223.
72. Hosseini, R. K., Coop, M. R., Jardine, R. J., and Brosse, A. The post-yield behaviour of four Eocene-to-Jurassic UK stiff clays. *Géotechnique 64*, 8 (2014), 620–634.
73. Houlsby, G. T., Amorosi, A., and Rojas, E. Elastic moduli of soils dependent on pressure: a hyperelastic formulation. *Géotechnique 55*, 5 (2005), 383–392.
74. Houlsby, G. T., Amorosi, A., and Rollo, F. Non-linear anisotropic hyperelasticity for granular materials. *Computers and Geotechnics 115* (2019), 1–11.
75. Hueckel, T., Tutumluer, E., and Pellegrini, R. A note on non-linear elasticity of isotropic overconsolidated clays. *International Journal for Numerical and Analytical Methods in Geomechanics 16* (1992), 603–612.
76. Ismael, M. *Inherent strength and stiffness anisotropy of laminated rocks*. PhD thesis, Bergakademie Freiberg University of Technology, 2018.
77. Ismael, M., Konietzky, H., and Herbst, M. A new continuum-based constitutive model for the simulation of the inherent anisotropy of Opalinus Clay. *Tunnelling and Underground Space Technology 93* (2019).
78. Iwan, W. D., Tatsuoka, F., and Takagi, Y. On a class of models for the yielding behaviour of continuous and composite systems. *Journal of Applied Mechanics, ASME 34*, 3 (1967), 612–617.
79. Jamiolkowski, M., Lancellotta, R., and Lo Presti, D. C. F. Remarks on the stiffness at small strains of six Italian clays. In *Proceedings of the First International Conference on Pre-failure Deformation Characteristics of Geomaterials* (Sapporo, 1995), M. Shibuya and Miura, Eds., pp. 817–836.

80. Janbu, N. Soil compressibility as determined by oedometer and triaxial test. In *Proceedings of the 3rd European Conference on Soil Mechanics and Foundation Engineering* (Wiesbaden, 1963), pp. 19–25.
81. Jardine, R. J. *Investigations of Pile-soil Behaviour, with Special Reference to the Foundations of Offshore Structures*. PhD thesis, Imperial College London, 1985.
82. Jardine, R. J. Some observations on the kinematic nature of soil stiffness. *Soils and Foundations 32*, 2 (1992), 111–124.
83. Jardine, R. J., Zdravkovic, L., and Porovic, E. Panel contribution: Anisotropic consolidation including principal stress axis rotation: Experiments, results and practical implications. In *Proceedings of 14th ICSMFE* (1999), A A Balkema, pp. 2165–2168.
84. Jeremić, B., and Sture, S. Implicit integrations in elastoplastic geotechnics. *Mechanics of Cohesive-frictional Materials 2* (1997), 165–183.
85. Jovičić, V., and Coop, M. R. The measurements of stiffness anisotropy in clays with bender element tests in triaxial apparatus. *Geotechnical Testing Journal 21*, 1 (1998), 3–10.
86. Jovičić, V., Jurečić, N., and Vilhar, G. Modelling the structure and anisotropy of London Clay using the SA BRICK Model. *Applied Sciences 13*, 2 (2023), 1–26.
87. Khaledi, K., Winhausen, L., Jalali, M., and Amann, F. Constitutive modeling of clay shales in undrained conditions and its experimental verification for Opalinus Clay. *International Journal of Rock Mechanics and Mining Sciences 171* (2023).
88. Kirkgard, M., and Lade, P. Anisotropic three-dimensional behavior of a normally consolidated clay. *Canadian Geotechnical Journal 30*, 5 (1993), 848–858.
89. Kirkgard, M. M., and Lade, P. V. Anisotropy of normally consolidated San Francisco Bay mud. *Geotechnical Testing Journal 14*, 3 (1991), 231–246.
90. Knittel, L., Wichtmann, T., Niemunis, A., Huber, G., Espino, E., and Triantafyllidis, T. Pure elastic stiffness of sand represented by response envelopes derived from cyclic triaxial tests with local strain measurements. *Acta Geotechnica* (2020).
91. Kreigel, H. J., and Weisner, H. H. Problems of stress-strain conditions in subsoil. In *Proceedings of 8th ICSMFE* (1973), pp. 133–141.
92. Kuwano, R., Connolly, T. M., and Kuwano, J. Shear stiffness anisotropy measured by multi-directional bender element transducers. In *Pre-failure Deformation Characteristics of Geomaterials* (1999).
93. Lade, P. V. Elasto-plastic stress-strain theory for cohesionless soil with curved yield surfaces. *International Journal of Solids and Structures 13* (1977), 1019–1035.

94. Lade, P. V. Modeling failure in cross-anisotropic frictional materials. *International Journal of Solids and Structures 44*, 16 (2007), 5146–5162.
95. Lade, P. V. Failure criterion for cross-anisotropic soils. *Journal of Geotechnical and Geoenvironmental Engineering 134*, 1 (2008), 117–124.
96. Lade, P. V., and Kirkgard, M. M. Effects of stress rotation and changes of b-values on cross-anisotropic behavior of natural, K_0-consolidated soft clay. *Soils and Foundations 40*, 6 (2000), 93–105.
97. Landon, M. M., and DeGroot, D. J. *Measurement of Small Strain Shear Modulus Anisotropy on Unconfined Clay Samples Using Bender Elements*. ASCE, 2006, pp. 1–6.
98. Le, A., and Nguyen, T. Hydromechanical response of a bedded argillaceous rock formation to excavation and water injection. *Canadian Geotechnical Journal 52*, 1 (2015), 1–17.
99. Lehane, B. M., and Simpson, B. Modelling glacial till under triaxial conditions using a BRICK soil model. *Canadian Geotechnical Journal 37*, 5 (2000), 1078–1088.
100. Lings, M. L., Pennington, D. S., and Nash, D. F. T. Anisotropic stiffness parameters and their measurement in a stiff natural clay. *Géotechnique 50*, 2 (2000), 109–125.
101. Lisewska, K., and Cudny, M. Influence of soil anisotropic stiffness on the deformation induced by an open pit excavation. *Archives of Civil Engineering 4* (2023), 141–156.
102. Lisjak, A., Garitte, B., Grasselli, G., Müller, H., and Vietor, T. The excavation of a circular tunnel in a bedded argillaceous rock (Opalinus Clay): Short-term rock mass response and FDEM numerical analysis. *Tunnelling and Underground Space Technology 45* (2015), 227–248.
103. Love, A. E. H. *A treatise on the mathematical theory of elasticity*. Cambridge University Press, 4th ed., 1st ed. in 1892, 1959.
104. Mair, R. J. Developments in geotechnical engineering research: applications to tunnells and deep excavation, unwin memorial lecture. *Proceedings of ICE, Civil Engineering 93* (1993), 27–41.
105. Marschall, P., Distinguin, M., Shao, H., Bossart, P., Enachescu, C., and Trick, T. Creation and evolution of damage zones around a microtunnel in a claystone formation of the Swiss Jura Mountains. In *SPE International Symposium and Exhibition on Formation Damage Control* (2006).
106. Matsuoka, H., and Nakai, T. A new failure criterion for soils in three dimensional stresses. In *Proceedings of the IUTAM Symposium on Deformation and Failure of Granular Materials* (Delft, 1982), P. Vermeer and H. J. Luger, Eds., Balkema, pp. 253–263.

107. Matthews, M. C., Hope, V. S., and Clayton, C. R. I. The use of surface waves in the determination of ground stiffness profiles. *Proceedings of ICE, Geotechnical Engineering 119* (1996), 84–95.
108. Mašín, D., and Rott, J. Small strain stiffness anisotropy of natural sedimentary clays: review and a model. *Acta Geotechnica 9*, 2 (2014), 299–312.
109. Mayne, P. W., and Kulhawy, F. H. K_0-OCR relationships in soil. *Journal of the Geotechnical Engineering Division, ASCE 108*, GT6 (1982), 851–872.
110. McConnachie, I. Fabric changes in consoliated kaolin. *Géotechnique 24*, 2 (1974), 207–222.
111. Mitaritonna, G., Amorosi, A., and Cotecchia, F. Experimental investigation of the evolution of elastic stiffness anisotropy in a clayey soil. *Géotechnique 64*, 6 (2014), 463–475.
112. Mitchell, J. K., and K., S. *Fundamentals of Soil Behavior*, 3 ed. Wiley, 2005.
113. Mróz, Z. On the description of anisotropic workhardening. *Journal of the Mechanics and Physics of Solids 15* (1967), 163–175.
114. Mukabi, J. N., Ampadu, S. K., Tatsuoka, F., Sato, T., and Hirose, K. Small strain stiffness and elasticity of clays in monotonic loading triaxial compression. In *Proceedings of the Symposium on Triaxial Testing Methods, JSSMFE, Tokyo* (1991), pp. 257–64.
115. Müller, H. R., Garitte, B., Vogt, T., Köhler, S., Sakaki, T., Weber, H., Spillmann, T., Hertrich, M., Becker, J. K., Giroud, N., Cloet, V., Diomidis, N., and Vietor, T. Implementation of the Full-scale Emplacement (FE) Experiment at the Mont Terri Rock Laboratory. *Swiss Journal of Geosciences 110*, 1 (2017), 287–306.
116. Nagra. Implementation of the Full-scale Emplacement Experiment at Mont Terri: Design, construction and preliminary results. Tech. Rep. 15-02, Nagra, 2019.
117. Nemat-Nasser, S., and Hori, M. *Overall Properties of Heterogeneous Materials*. Applied Mathematics and Mechanics. Elsevier, 1993.
118. Niemunis, A. *Theoretische Bodenmechanik mit* Mathematica. IBF KIT, 2019.
119. Niemunis, A., and Cudny, M. On hyperelasticity for clays. *Computers and Geotechnics 23* (1998), 221–236.
120. Niemunis, A., and Cudny, M. Discussion on "Dynamic soil-structure interaction: A three-dimensional numerical approach and its application to the Lotung case study". Poor performance of the HSS model. *Computers and Geotechnics 98* (2018), 243–245.
121. Niemunis, A., and Staszewska, K. Pure cross-anisotropy for geotechnical elastic potentials. *Acta Geotechnica* (2021).

122. Nishimura, S. *Laboratory study on aniosotropy of natural London Clay.* PhD thesis, Imperial College London, 2005.
123. Nishimura, S. Cross-anisotropic deformation characteristics of natural sedimentary clays. *Géotechnique 64*, 12 (2014), 981–996.
124. Nishimura, S., Minh, N. A., and Jardine, R. J. Shear strength anisotropy of natural London Clay. *Géotechnique 57*, 1 (2007), 49–62.
125. Nyren, R. *Field measurements above twin tunnels in London Clay.* PhD thesis, Imperial College London, 1998.
126. Oda, M. Initial fabrics and their relations to mechanical properties of granular material. *Soils and Foundations 12*, 1 (1972), 17–36.
127. Ohde, J. Zur theorie der druckverteilung im baugrund. *Der Bauingenieur 20* (1936), 451–459.
128. Parés, J. M. Sixty years of anisotropy of magnetic susceptibility in deformed sedimentary rocks. *Frontiers in Earth Science 3* (2015).
129. Pennington, D. S., Nash, D. F. T., and Lings, M. L. Anisotropy of G_0 shear stiffness in Gault Clay. *Géotechnique 47*, 3 (1997), 391–398.
130. Pestana, J. M., and Whittle, A. Formulation of a unified constitutive model for clays and sands. *International Journal for Numerical and Analytical Methods in Geomechanics 23* (1999), 1215–1243.
131. Pickering, D. J. Anisotropic elastic parameters for soil. *Géotechnique 20*, 2 (1970), 217–233.
132. Pierpoint, N. D. *The prediction and back analysis of excavation behaviour in Oxford Clay.* PhD thesis, University of Sheffield, 1996.
133. Pietruszczak, S., and Mróz, Z. Formulation of anisotropic failure criteria incorporating a microstructure tensor. *Computers and Geotechnics 26* (2000), 105–112.
134. Pietruszczak, S., and Mróz, Z. On failure criteria for anisotropic cohesive-frictional materials. *International Journal for Numerical and Analytical Methods in Geomechanics 25* (2001), 509–524.
135. Pietruszczak, S., and Pande, G. N. Description of soil anisotropy based on multilaminate framework, Short communication. *International Journal for Numerical and Analytical Methods in Geomechanics 25* (2001), 197–206.
136. Piriyakul, K. *Anisotropic stress-strain behaviour of Belgian Boom clay in the small strain region.* PhD thesis, Ghent University, 2006.

137. Puzrin, A. M., and Burland, J. B. Kinematic hardening plasticity formulation of small strain behaviour of soils. *International Journal for Numerical and Analytical Methods in Geomechanics 24* (2000), 753–781.
138. Puzrin, A. M., and Burland, J. B.and Strandind, J. R. Simple approach to predicting ground displacements caused by tunnelling in undrained anisotropic elastic soil. *Géotechnique 62*, 4 (2012), 341–352.
139. Ramamurthy, T., Venkatappa Rao, G., and Singh, J. Engineering behaviour of phyllites. *Engineering Geology 33*, 3 (1993), 209–225.
140. Ratananikom, W., Likitlersuang, S., and Yimsiri, S. An investigation of anisotropic elastic parameters of Bangkok Clay from vertical and horizontal cut specimens. *Geomechanics and Geoengineering 8* (2013), 15–27.
141. Richardson, D. *Investigations of treshold effects in soil deformations*. PhD thesis, City University, London, 1988.
142. Santos, J. A., and Correia, A. G. Reference threshold shear strain of soils. its application to obtain a unique strain-dependent shear modulus curve for soil. In *Proceedings of the 15th International Conference on Soil Mechanics and Geotechnical Engineering* (Istanbul, Turkey, 2001), vol. 1, Balkema, pp. 267–270.
143. Schanz, T., Vermeer, P. A., and Bonnier, P. G. The Hardening Soil model: Formulation and verification. In *Beyond 2000 in Computational Geotechnics - 10 Years of Plaxis* (1999), Balkema: Rotterdam, pp. 1–16.
144. Schwehr, K., Tauxe, L., Driscoll, N., and Lee, H. Detecting compaction disequilibrium with anisotropy of magnetic susceptibility. *Geochemistry, Geophysics, Geosystems 7*, 11 (2006).
145. Shibuya, S., and Mitachi, T. Small strain shear modulus of clay sedimentation in a state of normal consolidation. *Soils and Foundations 34*, 4 (1994), 67–77.
146. Shirley, D. J., and Hampton, L. D. Shear-wave measurements in laboratory sediments. *The Journal of the Acoustical Society of America 63*, 2 (1978), 607–613.
147. Simpson, B. Retaining structures: displacement and design, 32nd Rankine Lecture. *Géotechnique 42*, 4 (1992), 541–576.
148. Simpson, B., Atkinson, J. H., and Jovičić, V. The influence of anisotropy on calculations of ground settlements above tunnels. In *Geotechnical Aspects of Underground Construction in Soft Ground* (1996), Mair and Taylor, Eds., Balkema: Rotterdam, pp. 591–594.
149. Simpson, B., O'Riordan, N. J., and Croft, D. D. A computer model for the analysis of ground movements in London clay. *Géotechnique 29*, 2 (1979), 149–175.

150. Sivakumar, V., Doran, I. G., Graham, J., and Johnson, A. The effect of anisotropic elasticity on the yielding characteristics of overconsolidated natural clay. *Canadian Geotechnical Journal 38* (2001), 125–137.
151. Skempton, A. W. The pore-pressure coefficients A and B. *Géotechnique 4*, 4 (1954), 143–147.
152. Smaniotto, S., Neuner, M., Dummer, A., Cordes, T., and Hofstetter, G. Experimental study of a wet mix shotcrete for primary tunnel linings — Part i: Evolution of strength, stiffness and ductility. *Engineering Fracture Mechanics 267* (2022).
153. SoilModels. `https://soilmodels.com`.
154. St. John, H. D. *Field and theoretical studies of the behaviour of ground around deep excavations in London Clay*. PhD thesis, University of Cambridge, 1975.
155. Standing, J. R., and Burland, J. B. Unexpected tunnelling volume losses in the Westminster area, London. *Géotechnique 56*, 1 (2006), 11–26.
156. Standing, J. R., Nyren, R. J., and Burland, J. B. The measurement of ground movements due to tunnelling at two control sites along the jubilee line extension. In *Geotechnical Aspects of Underground Construction in Soft Ground* (1996), Mair and Taylor, Eds., Balkema: Rotterdam, pp. 751–756.
157. Stokoe, K. H., Hwang, S. K., Lee, J. N. K., and Andrus, R. D. Effects of various parameters on the stiffness and damping of soils at small to medium strains. In *Proceedings of the First International Conference on Pre-failure Deformation Characteristics of Geomaterials* (Sapporo, 1995), M. Shibuya and Miura, Eds., vol. 2, pp. 785–816.
158. Stokoe, K. H., Nasir, S. H., and Andrus, R. D. *In situ* and laboratory measurements of the dynamic properties of cemented granular soils: a case history. In *Proceedings of US/Brasil Geotechnical Workshop, Application of Classical Soil Mechanics to Structured Soils* (Belo Horizonte, 1991), U. o. I. a. U.-C. Alberto S. Nieto, Ed.
159. Tatsuoka, F., and Shibuya, S. Deformation characteristics of soils and rocks from field and laboratry tests. *Report of the Institute of Industrial Science, University of Tokyo;(Japan) 37*, 1 (1992).
160. Trzciński, J., and Wójcik, E. Application of microstructure classification for the assessment of the variability of geological-engineering and pore space properties in clay soils. *Open Geosciences 11*, 1 (2019), 236–248.
161. Tsidzi, K. The influence of foliation on point load strength anisotropy of foliated rocks. *Engineering Geology 29* (1990), 49–58.
162. Vakili, A., Albrecht, J., and Sandy, M. Rock strength anisotropy and its importance in underground geotechnical design. In *Proceedings of Third Australasian Ground*

Control In Mining Conference (AusRoc 2014) (2014).

163. Vermeer, P. A. A five constant model unifying well established concepts. In *Constitutive Relations of soils* (Rotterdam, 1985), D. Gudehus and Vardoulakis, Eds., Balkema, pp. 175–197.
164. Vermeer, P. A. *Non-Associated Plasticity for Soils, Concrete and Rock*. Springer Netherlands, 1998, pp. 163–196.
165. Waffenschmidt, T., Menzel, A., and Kuhl, E. Anisotropic density growth of bone - A computational micro-sphere approach. *International Journal of Solids and Structures 49* (2012), 1928–1946.
166. Ward, W. H., Samuels, S. G., and Gutler, M. E. Futher studies of the properties of london clay. *Géotechnique 9*, 2 (1959), 321–344.
167. Whittle, A. J., and Kavvadas, M. J. Formulation of MIT-E3 constitutive model for overconsolidated clays. *Journal of Geotechnical Engineering, ASCE 120*, 1 (1994), 173–198.
168. Wild, K., and Amann, F. Experimental study of the hydro-mechanical response of Opalinus Clay – Part 1: Pore pressure response and effective geomechanical properties under consideration of confinement and anisotropy. *Engineering Geology 237* (2018).
169. Wild, K., and Amann, F. Experimental study of the hydro-mechanical response of Opalinus Clay – Part 2: Influence of the stress path on the pore pressure response. *Engineering Geology 237* (2018).
170. Wilson, M., and Wilson, L. Clay mineralogy and shale instability: An alternative conceptual analysis. *Clay Minerals 49* (2014).
171. Wittke, W. *Rock Mechanics: Theory and Applications with Case Histories*, 1 ed. Springer, 1990.
172. Wroth, C. P. In situ measurement of initial stresses and deformation characteristics. In *Proceedings of the Conference on In Situ Measurement of Soil Properties* (1975), ASCE Geotechnical Special Publication, pp. 181–230.
173. Xiao, Y., Zhang, Z., and Wang, J. Granular hyperelasticity with inherent and stress-induced anisotropy. *Acta Geotechnica 15*, 3 (2020), 671–680.
174. Yamakawa, Y. Hyperelastic constitutive models for geomaterials: Extension of existing models to include finite strains and their comparison. *Computers and Geotechnics 143* (2022).
175. Yamashita, S., Hori, T., and Suzuki, T. Anisotropic stress-strain behavior at small strains of clay by triaxial and bender element tests. In *Proceedings of the Second Japan-*

U.S. Workshop on Testing, Modeling, and Simulation in Geomechanics (2005), ASCE Geotechnical Special Publication, pp. 44–57.

176. Yimsiri, S. *Pre-failure deformation characteristics of soils : anisotropy and soil fabric*. PhD thesis, University of Cambridge, 2001.
177. Yimsiri, S., and Soga, K. Cross-anisotropic elastic parameters of two natural stiff clays. *Géotechnique 61*, 9 (2011), 809–814.
178. Zdravković, L., and Jardine, R. J. Undrained anisotropy of K_0-consolidated silt. *Canadian Geotechnical Journal 37*, 1 (2000), 178–200.
179. Zdravković, L., Potts, D. M., and D.W., H. The effect of strength anisotropy on the behaviour of embankments on soft ground. *Géotechnique 52*, 6 (2002), 447–457.
180. Zwanenburg, C. *The influence of anisotropy on the consolidation behaviour of peat*. PhD thesis, Delft University of Technology, 2005.